Morphology and polymorphism of TiO_2 nanoparticles prepared in premixed stagnation flames

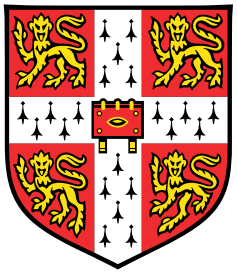

Manoel Yohanes Manuputty

Department of Chemical Engineering and Biotechnology
University of Cambridge

This dissertation is submitted for the degree of
Doctor of Philosophy

Churchill College

September 2019

Declaration

I hereby declare that except where specific reference is made to the work of others, the contents of this dissertation are original and have not been submitted in whole or in part for consideration for any other degree or qualification in this, or any other university. This dissertation is my own work and contains nothing which is the outcome of work done in collaboration with others, except as specified in Appendix A.

This dissertation contains approximately 58,000 words, 71 figures, and 18 tables. Some of the work in this dissertation has been published or submitted for publication:

1. **Manuputty, M. Y.**, Akroyd J., Mosbach S., Kraft M. (2017). Modelling TiO_2 formation in a stagnation flame using method of moments with interpolative closure. *Combustion and Flame* 178: 135–47. doi:10.1016/j.combustflame.2017.01.005

2. **Manuputty, M. Y.**, Dreyer J. A. H., Sheng Y., Bringley E. J., Botero M. L., Akroyd J., Kraft M. (2019). Polymorphism of nanocrystalline TiO_2 prepared in a stagnation flame: Formation of the TiO_2-II phase. *Chemical Science* 10: 1342–50. doi:10.1039/C8SC02969E

3. **Manuputty, M. Y.**, Lindberg C. S., Botero M. L., Akroyd J., Kraft M. (2019). Detailed characterisation of TiO_2 nano-aggregate morphology using TEM image analysis. *Journal of Aerosol Science* 133: 96–112. doi:10.1016/j.jaerosci.2019.04.012

4. Lindberg, C. S., **Manuputty, M. Y.**, Buerger P., Akroyd J., Kraft M. (2019). Numerical simulation and parametric sensitivity study of titanium dioxide particles synthesised in a stagnation flame. *Journal of Aerosol Science* 138: 105451. doi:10.1016/j.jaerosci.2019.105451

5. **Manuputty, M. Y.**, Lindberg C. S., Dreyer J. A. H., Akroyd J., Edwards, J., Kraft M. Understanding the anatase-rutile stability in flame made TiO_2. *Submitted to Combustion and Flame*.

Manoel Yohanes Manuputty

September 22, 2019 (approved corrections February 7, 2020)

Morphology and polymorphism of TiO_2 nanoparticles prepared in premixed stagnation flames

Manoel Yohanes Manuputty

This thesis investigates the morphology and polymorphism of TiO_2 nanoparticles prepared in premixed stagnation flames in order to understand the factors controlling the formation of the particles. Computational models are developed and experimental measurements are performed to characterise the effect of varying process conditions on the particle properties. The model predictions and the experimental results are critically assessed to gain insights into the fundamental processes involved in particle formation.

A univariate particle model is implemented in a flame solver to simulate TiO_2 particle formation from titanium tetraisopropoxide (TTIP) in a stagnation flame reactor. The particle model is solved using the method of moments with interpolative closure (MoMIC) and is fully coupled with the gas-phase chemistry and flow models. The model predictions are compared against literature data which reveals a good agreement for particle size but some discrepancy in particle geometric standard deviation (GSD). This suggests that the particle morphology is more complex that is assumed by the univariate particle model.

The morphology of TiO_2 particles is characterised experimentally using transmission electron microscopy (TEM) image analysis and mobility measurements. The analysis allows a quantification of the particle sphericity. The detailed particle morphology is simulated using a post-processing method with a stochastic population balance solver. The model predictions show an excellent agreement with measurements for both particle size and GSD. The model is subsequently used to quantify the uncertainties in the measured particle morphology.

The phase composition of the experimentally produced TiO_2 particles is analysed. The results demonstrate a high sensitivity of the phase composition to the premixed gas equivalence ratio, especially for near-stoichiometric mixtures. Metastable phases TiO_2-B and TiO_2-II are identified which provide new insights into the phase formation mechanism. It is suggested that TiO_2-II is a pre-rutile phase and it is formed through sub-oxide intermediates, TiO_{2-x}.

The sensitivity of phase composition to the flame dilution is investigated experimentally for stoichiometric flames. The results demonstrate a strong influence of the flame dilution on anatase-rutile stability. Different hypotheses to explain the origin of this sensitivity are evaluated using the stochastic population balance solver with a size-dependent transformation model. The analysis suggests that the nascent particle composition may play a more important role in the anatase-rutile stability than the particle size.

This thesis is dedicated to my loving parents, Richard and Judith.

Acknowledgements

I am indebted to so many people in the four year period leading up to this thesis. I am deeply grateful for the continuing guidance and the endless support from my supervisor Prof. Markus Kraft. I would also like to thank Dr. Jethro Akroyd and Dr. Sebastian Mosbach who have been providing practical assistance since my very first day in the computational modelling (CoMo) group. I especially appreciate their constructive criticisms on the earlier versions of the work that goes into this thesis as well as their encouragement along the way.

Most of this thesis would not have been possible without the earlier works by the past and current CoMo and CARES members. Dr. Edward Yapp and Dr. Sebastian Schmutzhard provided the indispensable help with the flame code. Dr. Philip Buerger's work on the TTIP decomposition mechanism laid the foundation for the TiO_2 modelling studies. Dr. Maria Botero, Dr. Weijing Wang, Dr. Sheng Yuan, and Dr. Jochen Dreyer have been incredibly helpful with the experimental work and the data analysis. The collaborative modelling work with Casper Lindberg has been an important highlight of this thesis.

My gratitude further extends to all the other CoMo members who have enriched my PhD experience overall, both in Cambridge and Singapore. I cherish the countless conversations we had over tea, coffee, beer, and all kinds of beverages. Special thanks to Angiras Menon and Dr. Edward Yapp who have provided valuable feedback on the draft of this thesis. I am extremely grateful for all the support staff in Cambridge CARES who made sure that all my day-to-day activity runs smoothly.

I would also like to acknowledge the generous financial assistance from the Singapore National Research Foundation (NRF), CMCL Innovation, Trinity-Henry Barlow Scholarship, and CMEDT/MCSC Cambridge Bursary.

Finally, I thank my family and friends in Indonesia, UK, Singapore, and beyond who have been my constant support all these years. You are the reason I am who I am today.

Table of contents

List of figures

List of tables

Chapter 1

Introduction

1.1 Motivation

Flame synthesis of aerosols is an important process in large scale manufacturing of functional powders including carbon black and ceramic materials [182]. Today titanium dioxide or TiO_2 is the most important ceramic material produced through flame synthesis. The global production capacity of pigmentary TiO_2 is nearly 8 million tonnes annually, mainly through the continuous high temperature chloride process [230]. Titanium dioxide is used in many emerging applications (e.g., photocatalysis, photovoltaics), in addition to the more conventional ones (e.g., pigments). This has led to increased research interests in preparation methods of TiO_2 with novel structure and properties.

Flame synthesis offers a continuous and scalable way to prepare TiO_2 nanoparticles for specialised applications. One of the attractions of flame synthesis is the ability to tune the properties of particles produced by controlling a range of operating conditions. For example, numerous studies since the 1970s have documented the procedures to prepare TiO_2 nanoparticles with wide range of properties, including size, polydispersity, morphology, composition, and crystallinity in lab-scale flame reactors [184, 71, 5, 125]. While the relationship between synthesis conditions and particle properties is largely established, the fundamental mechanisms of TiO_2 particle formation during flame synthesis are not well understood. Consequently, the optimisation of flame synthesis processes has been mostly empirical. One key step that is currently still an active research area is the precursor-to-particle conversion stages, i.e. inception stages. The understanding of these early stages is essential as they are expected to significantly impact the particle morphology and crystallinity of TiO_2.

Different experiments have been devised to investigate the fundamental processes of TiO_2 formation in flame. This typically involves lab-scale reactors with well defined configurations that are accessible for experimental characterisation. Wang and coworkers [146, 221, 155, 222, 168, 135] demonstrated the use of a premixed stretch-stabilised stagnation flame to prepare ultrafine crystalline TiO_2. This configuration results in a very short particle residence time (< 5 ms) and uniform time-temperature profiles which makes it an ideal test case for studying the early stages of particle formation and growth. In addition, the particle size and crystallinity of the prepared TiO_2 can be easily tuned by controlling the process variables such as premixed gas mixture composition and precursor concentration. For example, previous studies have shown that particles prepared in oxygen-rich flames are mostly anatase while oxygen-lean flames favour rutile formation [108, 155]. Lastly, the laminar flow and the simple geometry of the reactor configuration make it amenable to modelling studies.

Modelling studies of particle formation provide a powerful tool to examine complex processes that are not easily observed through experimental measurements. However, the insights gained from computational modelling of particle formation are often limited due to the simplifying assumptions required to make the model solvable. With the increase in computing power in the past decade, more computationally expensive models can now be used to describe particle formation in flame conditions with a much greater detail. The state-of-the-art particle models contain complex and realistic description of particle morphology and composition. The model complexity, at least in principle, allows it to be used to investigate processes such as crystal structure formation and multi-particle sintering in real synthesis conditions. Nevertheless, many of the process rates and model parameters are unknown and difficult to derive from first principles. Thus, comparison of model predictions against experimental measurements is indispensable to evaluate these unknown model parameters and to gain deeper insights into the fundamental processes of particle formation. However, interpretation of experimental measurements is often challenging which may limit what can be learned from this comparison.

The **objective of this thesis** is to investigate the morphology and polymorphism of TiO_2 nanoparticles in order to better understand the physical mechanisms of their formation, especially in the early stages. This is accomplished through a combination of experimental and modelling studies. In this thesis, the premixed stagnation flame configuration is chosen as the test system with titanium tetraisopropoxide (TTIP) as the precursor. The experimental invetigations focus on the morphological and structural characterisations of TiO_2 prepared in varying process conditions. This thesis also examines the modelling methodology, interpretation of experimental measurements, and their comparison against state-of-the-art computational model predictions.

1.2 Novel aspects of this thesis

This thesis presents the following **novel contributions**:

- A new implementation of a TiO_2 particle model based on the method of moments with interpolative closure (MoMIC) is presented. The MoMIC-based particle model is fully coupled with a detailed hydrocarbon chemistry mechanism and a one-dimensional flow approximation to simulate the TiO_2 formation from TTIP in a premixed stagnation flame. The model predictions, assuming a simple one-step reaction mechanism of TTIP decomposition, compare favourably against previously reported experimental measurements. The effects of different process parameters are investigated in detail. The findings have been published in Ref. [140].

- Experimental characterisation of nano-aggregate morphology of TiO_2 prepared in a premixed stagnation flame is performed. The mobility measurements and TEM image analysis are combined to evaluate detailed morphological features of the particles which have not been resolved before. The effects of varying equivalence ratio and precursor loading on particle morphology are investigated. The resulting dataset is compared to the detailed particle model coupled with an extensive TTIP decomposition mechanism. The findings have been published in Refs. [142] and [133].

- Identification of crystal phases of TiO_2 prepared in premixed stagnation flames with varying mixture equivalence ratio is performed using independent experimental methods. In addition to anatase, rutile and TiO_2-B phases, the formation of the metastable phase TiO_2-II is demonstrated for the first time in flame synthesis conditions. The formation of metastable phases and their dependence on the oxidising environment offers new insights into the phase formation and transformation mechanisms of TiO_2 nanoparticles in flames. The findings have been published in Ref. [141].

- The effect of argon dilution on the anatase-rutile composition is investigated experimentally for flames with stoichiometric mixture. The origin of the sensitivity of anatase-rutile composition is examined by comparison between measurements and predictions from an extended detailed particle model. The simple size-dependent models from the literature are shown to be inadequate. It is proposed that the composition of the nascent particles is the key in understanding TiO_2 phase formation mechanism. The findings have been submitted for publication.

1.3 Structure of this thesis

The remainder of this thesis is structured as follows. Chapter 2 presents relevant background material to set the context of this thesis. It covers the general properties and polymorphism of TiO_2. It is followed by a short description of flame synthesis in general and stagnation flame reactors in particular for nanoparticle preparation. The background also covers various characterisation methods for both particle morphology and polymorphism/crystallinity, as well as the modelling approaches for particle population dynamics. Lastly a literature review of important particle processes relevant to TiO_2 particle formation in flame is given with a focus on precursor chemistry, particle growth, and phase transformation.

Chapters 3 and 4 are concerned with the morphology of TiO_2 nanoparticles prepared in a stagnation flame synthesis. Chapter 3 outlines the implementation of a flame simulation methodology with coupled gas-phase chemistry, flow dynamics, and particle models. The particle formation is described with the method of moments with interpolative closure (MoMIC) in which spherical particle morphology is assumed. The experimental measurements reported by Tolmachoff et al. [221] are used as the test case. In Chapter 4, new experimental measurements are performed to investigate the detailed morphological properties of the prepared TiO_2 nanoparticles. The results are then compared against the simulation using a detailed particle model which takes into account the complex morphology resulting from aggregation and sintering processes.

Chapters 5 and 6 are concerned with the polymorphism of TiO_2 nanoparticles prepared in a stagnation flame synthesis. Chapter 5 presents new experimental characterisations of TiO_2 polymorphism as a function of the mixture equivalence ratio. This confirms the rutile stabilisation over anatase in oxygen lean environments. The measurements identify two new metastable phases, one of which has never been reported before. The implications of these metastable phases on phase transformation mechanism are discussed. Chapter 6 reports new measurements aimed at quantifying phase composition of TiO_2 as a function of flame dilution for stoichiometric mixtures. A new detailed particle model is then used to investigate various possible physical mechanisms to explain the experimental observation.

Chapter 7 summarises the conclusions of this thesis and suggests areas for future investigation. A bibliography can be found at the end, along with appendices containing supplemental information on the experimental details and the thermodynamics analysis of TiO_2 phase stability.

Chapter 2

Background

This chapter presents a broad overview of the general concepts and relevant works in the literature that set the context for the rest of this thesis. In the first section, general properties of TiO_2 are outlined including its crystal structure modifications (polymorphs) and their stabilisation mechanisms. In the second section, a general description of flame synthesis of nanoparticles is given with a narrowed focus on the stagnation flame reactor which is used as a test reactor in this thesis. Next, the working principles and challenges of various characterisation methods for particle morphology and polymorphism are summarised in the third section. Lastly, the fourth section discusses some general particle population balance models and numerical methods as well as the current state of the literature on TiO_2 particle formation stages. These include the precursor (TTIP) chemistry, particle morphological evolution, and crystal phase transformation.

2.1 General overview of TiO_2

Titanium dioxide, also referred to as TiO_2, titania or titanium (IV) oxide (used interchangeably in this thesis), is one of the most studied transition metal oxides. It is mainly produced from the naturally occuring mineral ilmenite after its discovery in 1791 by William Gregor [194]. Industrially, ilmenite is converted to TiO_2 through either the chloride process (with intermediate titanium tetrachloride, $TiCl_4$) or the sulfate process (with intermediate titanyl sulfate, $TiOSO_4$).

TiO_2 is part of a very complex Ti-O family of compounds as illustrated by the phase diagram in Fig. 2.1. Despite its chemical formula, TiO_2 is a reducible or non-stoichiometric oxide and maintains its structure (rutile) over a range of oxygen composition, i.e. $TiO_{1.96-2.00}$ [9]. The reduced rutile TiO_{2-x} exhibits various types of defects, including doubly charged oxygen vacancies, Ti^{3+} and Ti^{4+} interstitials, and planar defects or the so called crystallographic shear planes (CSPs) [56]. The crystallographic shear structure is the main mechanism for the formation of the homologous Magnéli series Ti_nO_{2n-1}, with $n \geq 4$ [37, 247].

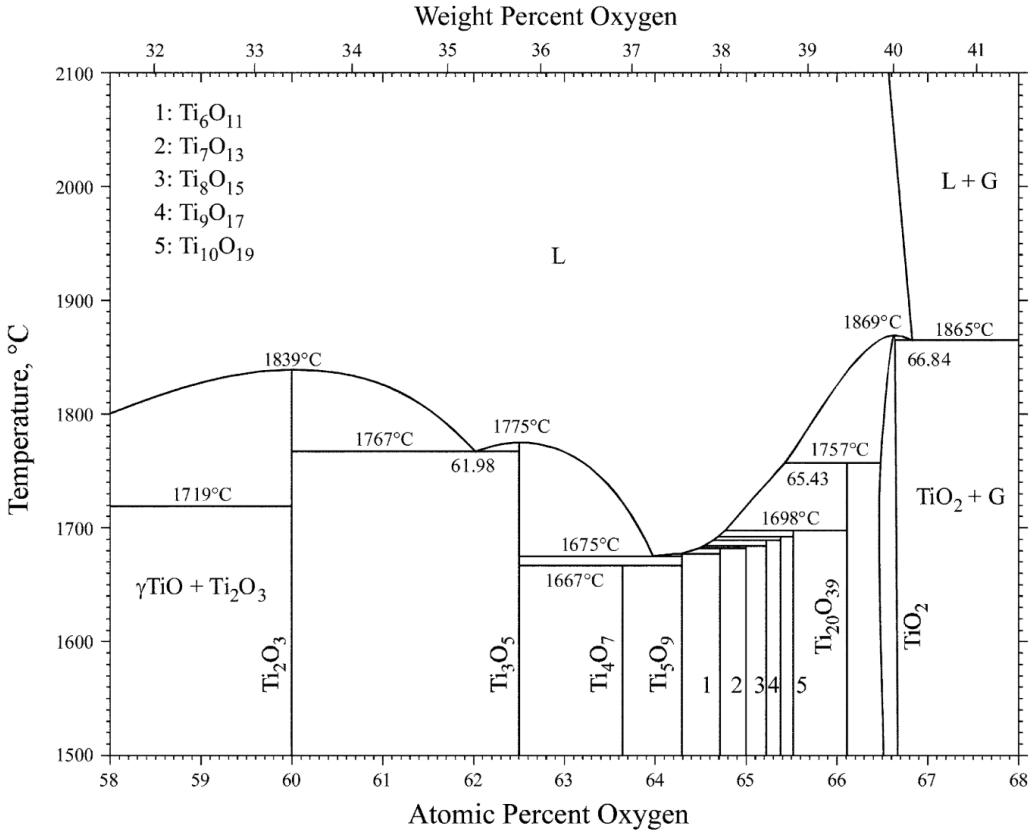

Figure 2.1: *Ti-O phase diagram for 58–68 at.% oxygen at 1 atm. Reprinted from Okamoto [172] with permission from Springer Nature.*

2.1.1 Properties and applications

TiO_2 is used in a wide range of applications among which pigment is the most commercially important with worldwide production capacity of 7.7 million tonnes in 2018 [230]. TiO_2 pigment is nowadays used as the base of virtually all paints owing to its high refractive index. The high refractive index also makes TiO_2 thin films ideal for optical coating applications such as in anti-reflective coatings and frequency selective filters [145, 40].

TiO_2 is an intrinsic wide bandgap semiconductor and thus is capable of producing electron-hole pairs when irradiated. This gives rise to its important use in photocatalysis, photovoltaics, and gas sensing. The field of photocatalysis is an especially important use of TiO_2 with some pioneering works in 1970s. Fujishima and Honda [77] demonstrated a photosensitised (or photocatalysed) electrolytic oxidation of water with TiO_2 electrode. Separately, Formenti et al. [71] reported the photocatalytic oxidative properties of TiO_2 aerosols toward hydrocarbons. The same principle is utilised in solar to electrical energy conversion or photovoltaics [72], photo-assisted degradation of organic molecules [112], and photo-induced superhydrophilicity [262].

One of the challenges of TiO_2 is its low quantum yield for the conversion of solar energy due to the relatively large bandgap. Thus, the improvement of solar efficiency has become an important and active research area. This can be achieved through a variety of strategies, including the use of colloidal suspensions of TiO_2 [245], addition of dye molecules in dye-sensitised solar cells (DSSCs) [179], or introduction of defects or nanostructure to control the bandgap [68]. This has subsequently led to the shift of research interests from bulk TiO_2 to nanosized TiO_2 with novel structure.

2.1.2 Polymorphism of TiO_2

Titanium dioxide exists in at least twelve different structure modifications or polymorphs or phases, eight of which are shown in Fig. 2.2. In addition, at least three different non-crystalline or amorphous phases have been reported [258]. All of the crystalline polymorphs share the same building block of (distorted) octahedron unit in which Ti^{4+} ion is coordinated to six O^{2-} ions, with the exception of 7-coordinated Ti in Baddeleyite [196]. Rutile is thermodynamically the most stable phase for bulk TiO_2 although other metastable phases are routinely found in nature or prepared synthetically. For example, anatase and brookite are commonly reported in fine-grained or nano-sized samples [167], TiO_2-II is found in nature as a mixture with rutile [202, 156], while TiO_2-B is found as lamellae in natural anatase crystals [12] in metamorphic rocks.

All structure modifications of TiO_2 except for rutile are considered metastable from a bulk thermodynamic point of view at 1 atmospheric pressure. Nevertheless, many of these metastable phases have been prepared and retained through a range of synthesis routes. Four examples of these are anatase, brookite, TiO_2-B and TiO_2-II which are discussed below. The formation of these phases can be explained from either a thermodynamics or kinetics point of view.

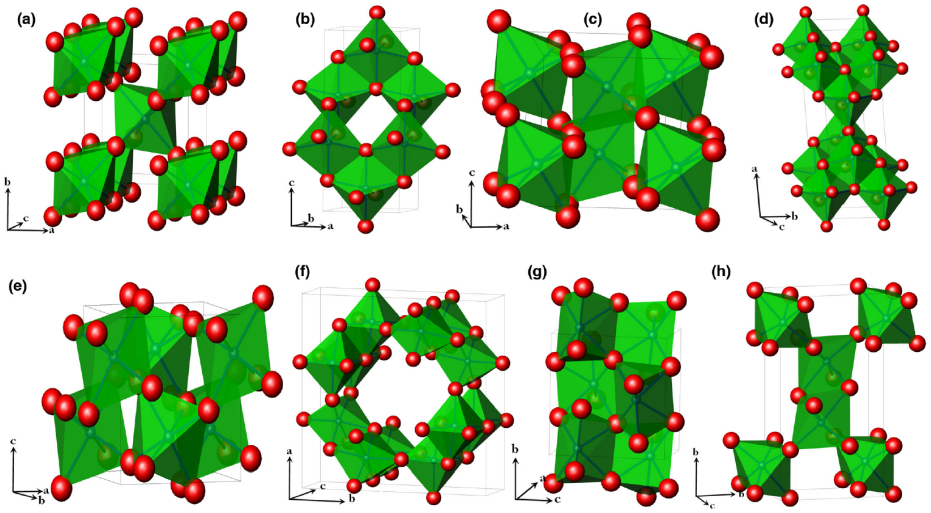

Figure 2.2: *Eight of at least twelve known modifications/polymorphs of TiO_2: (a) Rutile, (b) anatase, (c) bronze or TiO_2-B, (d) brookite, (e) columbite or TiO_2-II, (f) hollandite or TiO_2-H, (g) baddeleyite or TiO_2-III, and (h) ramsdellite or TiO_2-R. Not shown: TiO_2-OI, TiO_2-OII, cubic TiO_2, η-TiO_2. Reprinted from Aravindan et al. [11] with permission (CC BY NC ND).*

Thermodynamic stability

The common occurence of metastable phases, especially anatase and brookite, in nanosized particles is often attributed to surface energetic effects [167, 258]. Anatase and brookite have been reported to have lower surface enthalpies compared to rutile based on calorimetry measurements of nanosized particles, i.e. rutile: 2.2 ± 0.2 J/m^2, brookite: 1.0 ± 0.2 J/m^2, anatase: 0.4 ± 0.2 J/m^2 [187]. The higher surface energy of rutile is also predicted by theoretical studies based on atomistic and molecular dynamics simulations although the exact values vary depending on the exposed crystallographic planes and the chemical environments.

The interplay between bulk and surface energetics leads to a size-dependent stability [258]. Zhang and Banfield [255] used a simple thermodynamic description of the change in Gibbs free energy of the anatase-rutile transformation, $\Delta G^\circ_{A\to R}$, for spherical particles that takes into account the surface energy contribution as follows (derivation in Appendix C.1),

$$\Delta G^\circ_{A\to R} = \Delta G^\circ_{f,R} - \Delta G^\circ_{f,A} + 2(2t+3)\frac{M}{d}\left(\frac{\gamma_R}{\rho_R} - \frac{\gamma_A}{\rho_A}\right), \tag{2.1}$$

where ΔG°_f, γ, and ρ are the standard Gibbs free energy of formation, surface free energy, and mass density of anatase (subscript A) and rutile (subscript R), t is the ratio of surface stress to surface free energy, M is the molar mass of TiO_2, d is the particle diameter. Using the average surface energies derived from atomistic simulations, they calculated a crossover

stability size between anatase and rutile of 14–15 nm which is largely consistent with earlier experimental data [88]. Using a similar analysis with surface enthalpies, size-dependent stabilities for anatase (< 11 nm), brookite (11–35 nm), and rutile (> 35 nm) can also be calculated [256].

Theoretical studies predicted a similar size-dependent crossover size albeit with varying values depending on the method and particle morphologies assumed. For example, using molecular dynamics Naicker et al. [165] reported an anatase-rutile stability crossover at 2.5 nm for spherical particles (brookite is less stable at any size) while Zhou and Fichthorn [271] reported crossover sizes of ∼2.9 nm for faceted particles and ∼4.1 nm for spherical particles. Using *ab initio* methods, Barnard and Zapol [15] predicted crossover sizes of 9.3 nm for faceted and 2.6 nm for spherical particles.

The discrepancies in the crossover size obtained from experiments and theoretical studies highlight the challenge in accurately predicting the energetics of nanoparticles. Nanoparticle surfaces are known to undergo atomic relaxation to minimise the surface energies, sometimes exhibiting a core-shell structure with an amorphous shell and a crystalline core [220, 259]. In addition, surface modifications such as hydroxylation and hydrogenation significantly affect the surface properties of crystalline TiO_2 [14, 15]. These factors are usually dependent on the preparation methods and are challenging to be properly characterised.

Further, the bulk and surface energetics crystalline TiO_2 is also influenced by the concentration of defects [56]. For example, at low oxygen chemical potential, the formation of oxygen vacancies or Ti interstitials in rutile structures is thermodynamically favourable [131, 44]. The effect of the oxygen defects on the bulk energetics can be seen from the melting point of TiO_{2-x} which decreases with increasing x in the Ti-O phase diagram, shown in Fig. 2.1. Similarly, introduction of dopants strongly affects the interplay between bulk and surface energies such as demonstrated for Nb-doped TiO_2 [51].

Kinetic stability

A metastable phase/structure can be stabilised "kinetically" or trapped in a local equilibrium state despite there being lower-energy alternatives due to an energy barrier of transformation.

The nucleation of crystal phase from melt involves an energy barrier (or critical nucleation energy) according to the classical homogeneous nucleation theory [4]. Thus, a metastable phase can nucleate if its critical nucleation energy, which is governed by the solid-liquid interfacial energy, is lower than that of a thermodynamically stable phase. For example, McPherson [151] argued that this effect explains the formation of the metastable γ-Al_2O_3

instead of the thermodynamically stable α-Al_2O_3 from a supercooled melt. Similarly, Li and Ishigaki [126] suggested that anatase nuclei have a lower nucleation energy barrier than rutile nuclei in a supercooled melt. Thus the metastable anatase will form kinetically from melt with a high degree of undercooling (or high cooling rate).

The reconstruction of the atomic arrangement during a solid-state phase transformation also involves an energy barrier. Thus, a metastable phase can form due to a close topotactic or orientational relationship with the initial structure. This is especially common in TiO_2 due to the similarity in the building block of its polymorphs, i.e. 6-coordinated Ti. Two examples of the kinetically stabilised phase transformation are noted here. The first is the formation of TiO_2-B and transformation of TiO_2-B to anatase. The second is the oxidation of α-Ti_3O_5 to TiO_2-II.

Formation of TiO_2-B and transformation of TiO_2-B to anatase TiO_2-B was first prepared by Marchand et al. [143] by hydrolysis of $K_2Ti_4O_9$ followed by filtration and thermolysis. The intermediate in this process was identified as $(H_2O)Ti_4O_7(OH)_2$ which undergoes a series of topotactic dehydroxylations to form TiO_2-B [223]. In this case, a common structural block of two 2-multiple octahedral ribbons sharing corners is present in $K_2Ti_4O_9$, $(H_2O)Ti_4O_7(OH)_2$, and TiO_2-B.

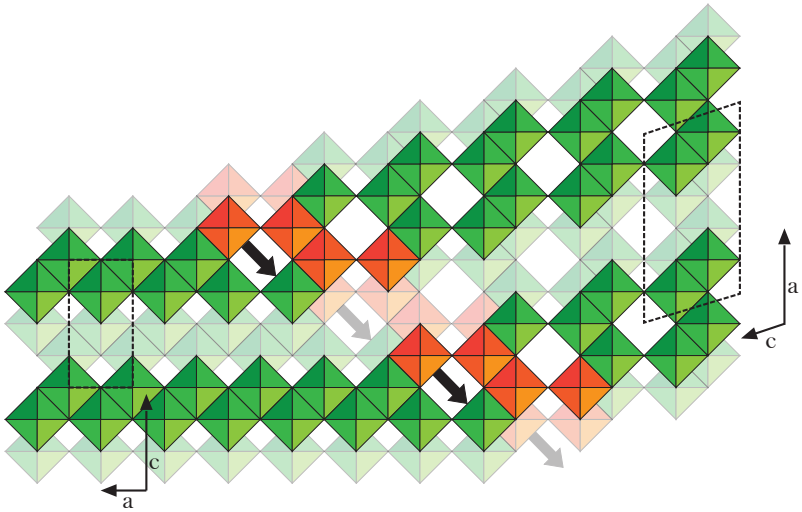

Figure 2.3: *Idealised octahedra diagram showing the transformation step from TiO_2-B (right) to anatase (left) through a crystallographic shear of $(\bar{2}\ 0\ 1)_B$ planes, highlighted in orange, in $[\bar{2}\ 0\ \bar{3}]_B$ direction by one octahedron edge, as shown by arrows. Adapted from Tournoux et al. [223] with permission from Elsevier.*

Upon heating at a temperature higher than 550°C, TiO_2-B slowly transforms to anatase. The transformation can be explained by the close structural relationship between these two phases. In particular, the transformation can be viewed as resulting from a crystallographic shear of $(\bar{2}\ 0\ 1)_B$ planes in the $[\bar{2}\ 0\ \bar{3}]_B$ direction [33, 223]. This is illustrated in Fig. 2.3. The shear is analogous to the formation of Magnéli phases from rutile structure [9] albeit with elimination of both anionic and cationic vacancies (thus maintaining the stoichiometry).

Formation of TiO_2-II from α-Ti_3O_5 TiO_2-II is an orthorhombic high-pressure phase of TiO_2 isostructural with α-PbO_2 [205]. Although pure TiO_2-II is only thermodynamically stable at high pressure conditions, experiments and first-principles studies have shown that it can be retained at ambient pressure as a metastable phase [154].

TiO_2-II was first prepared at atmospheric pressure conditions by Grey et al. [87]. They dissolved α-Ti_3O_5 in sulphuric acid at elevated temperatures and obtained TiO_2-II as fine crystallites. Upon further heating above 370°C, the TiO_2-II was converted to rutile. The electron microscopy studies show that the TiO_2-II forms thin plates parallel to $(1\ 0\ 1)_{II}$. Thus it was suggested that TiO_2-II was formed through solid state transformation instead of precipitation from solution. It was further pointed out that the (1 1 0) planes of α-Ti_3O_5 are closely matching the (1 0 1) planes in TiO_2-II. Thus the transformation requires only small displacements of atoms in the α-Ti_3O_5 lattice.

Interestingly, TiO_2-II has also been prepared in more recent experiments without using high pressure conditions. The first is through ball milling of anatase particles in which TiO_2-II crystals are observed on the surface of anatase particles [17, 79]. It was suggested that contact forces from the particle-particle impacts are responsible for the transformation. The second is through atomic layer deposition (ALD) using $TiCl_4$ and H_2O as precursor [1]. It was suggested that a non-stoichiometric surface layer is formed during deposition cycles which can be an intermediate for TiO_2-II, similar to α-Ti_3O_5 in Grey et al.'s study [87]. This is further supported by the observation that the relative amount of TiO_2-II in the ALD-grown films is related to the water vapour concentration [2].

2.2 Flame synthesis

Flame synthesis here refers to the formation of ultrafine particles from gases in flames. The use of flame synthesis to prepare ceramic or metal oxide aerosols first gained interest following the development of industrial production of fumed silica in the 1940s called Aerosil

[181]. One of the key attractions of flame synthesis over its wet-chemistry based counterparts is the fact that no additional expensive processes such as filtering, drying, and calcination are typically required.

Ulrich and coworkers pioneered the investigations of the particle formation processes in flame synthesis by studying SiO_2 formation from $SiCl_4$ [226–228]. Formenti et al. [71] subsequently demonstrated preparation of various metal oxides (Al_2O_3, Fe_2O_3, GeO_2, SiO_2, TiO_2, V_2O_5, ZrO_2) from metal chloride vapours in a H_2/O_2 burner. Many authors have since demonstrated that the properties of flame-made particles can be controlled by various process variables including flame configuration or burner type, precursor molecule, system temperature, gas composition, additives, dopants, as well as external electric fields.

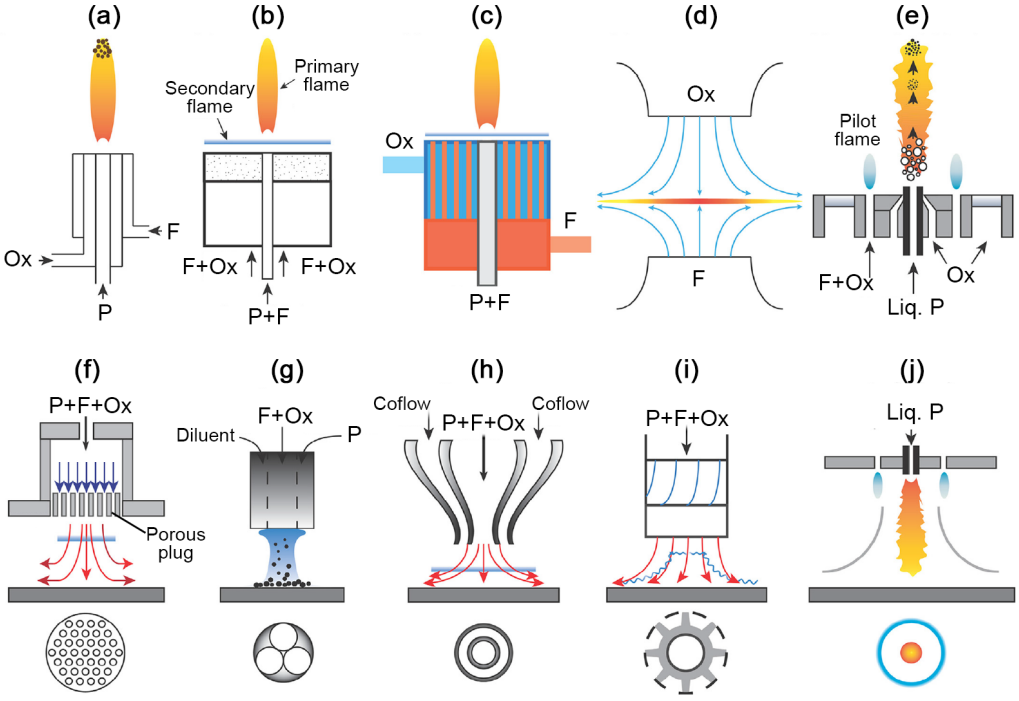

Figure 2.4: *A schematic of various flame reactor configurations for nanoparticle synthesis: (a) Multi-annulus diffusion flame, (b) central diffusion with premixed flat flame or McKenna burner, (c) central diffusion with multi-channel diffusion flame or Hencken burner, (d) counterflow diffusion flame, (e) flame spray pyrolysis, (f) burner-stabilised stagnation flame, (g) inner tube-stabilised stagnation flame, (h) divergence-stabilised stagnation flame, (i) swirl-stabilised stagnation flame, (j) flame spray with stagnation surface.* P, F, *and* Ox *denote precursor, fuel, and oxidiser. Adapted from Li et al. [125] with permission from Elsevier.*

In the past few decades, the research has intensified with emphasis on nanosized particles, including TiO_2 nanoparticles. This is motivated by the potential applications of novel and functional flame-made nanomaterials for use in a variety of technologies [116, 182, 212, 213].

At the same time, significant efforts have been made to better understand the fundamental processes of particle formation in order to better control the synthesis process to prepare materials with the desired properties.

Figure 2.4 shows a wide range of burner configurations that have been studied for flame synthesis of ceramic materials such as "free-jet" burners (a-e), including co-flow diffusion, McKenna, and Hecken flat flames, counterflow diffusion burner, flame spray pyrolysis, and premixed stagnation burners (f-i), including burner-stabilised, stretch stabilised, and swirl stabilised flames [125]. The burner configuration is especially important as it largely dictates the operational windows of operation and affects the temperature-time profiles of the particles.

One useful strategy to study the particle formation in flame synthesis is by performing experimental studies using well-defined burners, usually with simple flow conditions and a simple geometry which allow for easier characterisation. These are often complemented by the development of comprehensive computational models to interpret and gain deeper insights from the experimental observations. One such flame configuration that is useful for flame synthesis study is the stagnation flame configuration.

Stagnation flame reactor

A stagnation flame configuration is widely used in laboratory scale reactors for combustion studies (Fig. 2.4(f-i)). The flow geometry results in a planar and strained flame which is useful to evaluate combustion models. The quasi one-dimensional flow profile can be described by a reduced hydrodynamic equation, allowing for easier coupling with computationally expensive transport and kinetic models [158, 107]. This kind of flame can be operated under low-pressure conditions to stretch the reaction zone although atmospheric pressure flames are also common. In addition, the one-dimensional flow field results in uniform particle properties (narrow distirbution) which is often desired.

Stagnation flames can be generated in either opposed-jet or jet-wall configurations. The opposed-jet configuration, i.e. Fig. 2.4(d), is normally operated as a diffusion flame where the fuel and oxidiser are issued separately in opposing streams and a stagnation point is created between the two nozzles. In a jet-wall configuration, Fig. 2.4(f-i), the fuel and oxidiser are usually premixed and the stagnation point is created on the wall. Thus stagnation flames with a jet-wall configuration are often referred to simply as premixed stagnation flames. In both of these configurations, the flow domain is short and the boundary conditions are well defined, which are useful for modelling studies. The opposed jet flow configuration was

historically employed for studying aerosol formation in flames [159, 96, 248]. However, the jet-wall configuration is now more widely used for material synthesis as the surface is useful for sample collection and for controlling the substrate temperature [125]. The heat-loss to the wall also helps stabilise the flames.

The premixed stagnation flame includes the so called burner stabilised stagnation flame (BSSF, Fig. 2.4(f)) and divergence stabilised stagnation flame (DSSF, Fig. 2.4(h)). These differ in the flame stabilisation location, i.e. at the burner nozzle for BSSF or on the stagnation surface for DSSF. For metal oxide synthesis, clogging of the burner nozzle is usually an issue in BSSFs due to the use of a porous plug. The DSSFs, on the other hand, employ jet nozzles with high gas velocity which results in the flame (and particles) forming away from the burner. The DSSFs can be operated under a wide range of equivalence ratios but is limited by the high strain induced by the temperature gradient which could lead to flame extinction. In addition, the proximity to the surface usually results in non-adiabatic flames.

More recently, Wang and coworkers demonstrated the use of DSSFs to prepare ultrafine (< 10 nm) TiO_2 nanoparticles [221, 155]. The small particle size is a consequence of the very short flame residence time. The particles can be collected using a rotating stagnation surface. This is termed the flame stabilised on a rotating surface (FSRS) reactor. The rotation of the stagnation surface cools the substrates and minimise further particle growth/sintering once the particles are collected. This type of flame is suitable for studies focusing on the early stages of particle formation as the particles formed in flame are quickly quenched by the high cooling rate near the surface.

2.3 Particle characterisation

Characterisations of particles prepared in flames are important to understand the underlying physical processes of particle dynamics and to provide reference data for model testing. However, flame characterisations in general are inherently challenging due to the high temperature conditions and short characteristic time scales of important processes, e.g., particle formation and chemical reactions. In depth reviews on characterisation techniques for gas-phase nanoparticles have been provided by Li et al. [125] and Dreier and Schulz [59]. In this section, the general working principles and challenges of some characterisation techniques for particle morphology and crystallinity are described.

Particle morphology is a typical target for characterisation. The particle morphology here refers to the size and shape/geometry of the particles. An important combination often

used to characterise particle morphology is electron microscopy and electrical mobility measurements. The electron microscopy methods are generally more time-consuming but provide direct observation of particle morphology. On the other hand, electrical mobility measurements allow for fast analysis of particle morphology although the interpretation of the measured quantity is more challenging. Thus, these two methods are often used together to investigate the morphology of flame-made particles including soot [176, 47, 53] and TiO_2 [266, 218].

Particle crystallinity (or phase) is an important property of flame-made nanoparticles, especially for inorganic materials such as TiO_2. The particle crystallinity here refers to the atomic arrangement within the particles. The crystallinity is important because it directly impacts the electrical, optical, and mechanical properties of the material. An important characterisation method is the diffraction or scattering based techniques such as electron diffraction or powder x-ray diffraction.

2.3.1 Morphological descriptors

The morphology of flame made nanoparticles varies from simple spherical shapes to complex aggregate structures depending on the synthesis conditions. A meaningful description of the morphological features of these nanoparticles is the first step to understand the particle formation processes. Here, some morphological descriptors typically used in the aerosol community are described.

The simplest particle shape is a sphere which is common in high temperature synthesis conditions although faceted particles are not uncommon for crystalline materials at later stages of growth. Spherical particles can be simply described by their diameter, d. The number averaged or volume averaged mean is often reported to describe the particle population. In addition, the polydispersity of the particle size is an important property that is often described by the standard deviation (SD), or geometric standard deviation (GSD) if the underlying population is lognormally distributed.

In many cases, especially in later growth stages, the flame-made nanoparticles take a more complex morphology termed agglomerate or *aggregate*. Aggregates can be seen as a collection of interconnected spherical *primary particles* that form a complex three-dimensional structure. These structures are challenging to describe and various morphological properties are often used. Some of the useful descriptors of aggregates include the number of primary particles per aggregate, N_{pri}, and the overlap parameter, C_{ov}, which is a measure of the level of sintering between primary particles in an aggregate [30].

Aggregates with a large number of primary particles are often considered fractal-like, i.e. their structures at different scales are statistically equivalent (self similar) [102]. In such structures, a characteristic power law scaling relationship applies between the primary particle diameter, the number of constituent primary, and the radius of gyration, R_g:

$$N_{\text{pri}} = k_f \left(\frac{R_g}{d} \right)^{D_f}, \tag{2.2}$$

where k_f is the fractal prefactor and D_f is the fractal dimension [214, 114]. The gyration radius is a geometrical descriptor of the aggregates, given by

$$R_g = \frac{\int \rho(r) r^2 \mathrm{d}r}{\int \rho(r) \mathrm{d}r}, \tag{2.3}$$

where $\rho(r)$ is the radial mass density distribution. Projection of a fractal structure is also a fractal and thus a scaling relationship similar to Eq. 2.2 can also be written for the aggregate projected area [153, 53]. Similarly, a scaling relationship for aggregate mobility size has also been described [176, 207]. Thus, k_f, D_f, and various fractal descriptors can be used to describe an aggregate morphology. It is important, however, to note that these are only truly valid in the $N_{\text{pri}} \to \infty$ limit [102, 207]. The fractal dimension D_f is a useful descriptor as it can be used to classify the aggregate formation mechanism, i.e. particle-cluster, or cluster-cluster aggregation [171, 152].

2.3.2 Sampling methods

Sampling or collection of flame-made nanoparticles is an important part of non-optical based particle characterisations.

For electron microscopy measurements, various sampling techniques can be employed. For example, the particles can be directly collected from the flame through a rapid insertion technique (thermophoretic collection), from an aerosol sampling line (impaction collection), or from redispersion or transfer of collected particles on to the substrates (collection by settling) [118]. The thermophoretic and impaction collections are useful to investigate the aggregate structure of the particles in flame while the redispersion technique often results in artificial aggregation.

For mobility measurements, a probe is often used to sample and carry the sampled gas (through a sampling line) to the instruments. This is challenging because at high temperature and high particle concentration, further reactions and coagulation can lead to particle loss and

alter the particle size distribution during sampling [24]. In addition, diffusive particle losses of small particles to the wall of the probe and along the sampling line result in a bias towards larger particle size. In order to minimise these particle losses, a sampling system often referred to as dilution sampling or dilution probe, is usually used to immediately quench and dilute the sampled gas. This is often called the primary dilution stage. In addition, a secondary dilution is often necessary for mobility measurements because of the instrument limitation.

For stagnation flame configurations, a dilution sampling system can be integrated into the stagnation surface, i.e. *in situ* sampling probe, as employed by Zhao et al. [267]. This allows for rapid quenching of sampled particles while minimising the perturbation to the flow [105]. In this system, samples are extracted from the flame via a small orifice and immediately quenched with dilution gas, usually nitrogen. Zhao et al. [267] performed a systematic characterisation of such sampling methods and demonstrated that the particle losses can be minimised when the dilution ratio is sufficiently high. Nevertheless, the sampling orifice can be clogged due to the deposition of the sampled particles and thus frequent cleaning is often required. In addition, the flow through orifice may introduce a notable impact on the local flow field, temperature, and particle residence time [195].

2.3.3 Transmission electron microscopy

Electron microscopy is widely used for particle imaging. The imaging can be accomplished with two different operation methods, i.e. transmission or scanning methods. For ultrafine nanoparticles (< 50 nm), a transmission electron microscopy (TEM) is usually more suitable due to its superior resolution. In TEM, a beam of high energy electrons is used to illuminate the sample and the transmitted beam is recorded on a detector [244].

Particle sampling followed by TEM analysis has been extensively used to investigate the size distributions and morphology of particles in flames. The TEM imaging allows a direct observation of particle morphology in two-dimensional projection as shown in Fig. 2.5. The aggregate structure and the individual primary particles can be easily observed. A quantitative analysis can be performed by using image analysis algorithms to calculate various projected morphological properties [114]. The sampling can also be done at different locations along the flame to understand how the particle morphology evolves.

Nevertheless, some aspects need to be carefully considered when performing the analysis of particle morphology through TEM images. First, a quantitative analysis requires a large number of images to produce statistically meaningful results. Second, the number of

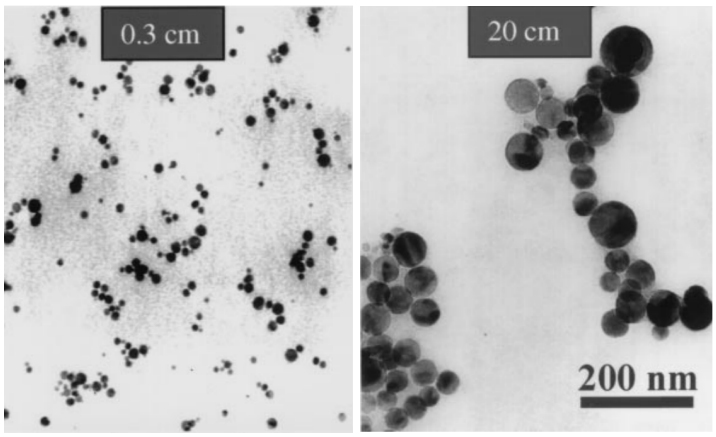

Figure 2.5: *Examples of TEM images of TiO_2 particles generated in a $CH_4/O_2/N_2/Ar$ premixed flame with TTIP precursor reported by Arabi-Katbi et al. [10]. The TEM sampling was performed by a rapid insertion technique (thermophoretic sampling) at 0.3 cm and 20 cm away from the burner. Adapted with permission from Elsevier.*

particles per image (or image coverage) needs to be low enough in order to minimise particle overlapping. Third, the sampling method may result in size-dependent collection efficiency which alters the particle distirbution. It is therefore important to compare the TEM-derived morphology against other measurement methods.

2.3.4 Mobility measurements

Electrical mobility measurements are routinely used to characterise particle size distributions in flame synthesis reactors [207]. Different instruments are available commercially including the electrical aerosol analyser (EAA), the scanning mobility particle sizer (SMPS), differential mobility spectrometer (DMS). The general principles of these instruments remain the same although they differ in their time response and spectral resolution. More in depth descriptions of these instruments is beyond the scope of this chapter.

A typical mobility analyser has three main components: charger, classifier, and detector. The sample first passes through an aerosol charger which applies a charge on the particles. The charged particles then pass through a classifier where they are separated based on their electrical mobility. Lastly, the number of particles are detected using the particle detector. These measurements can be operated semi-continuously which allows for fast analysis of particle mobility.

Electrical mobility The electrical mobility, Z, describes the ability of a charged particle to move through a medium in response to an external electrical field. For a particle moving at a constant drift velocity v relative to the fluid, it is subject to two equal and opposing forces: an electrical force equal to zeE (z is the number of charge, e is the elementary charge, E is the electric field) and a drag force F_{drag}. The drag force on a particle in a medium moving with velocity v at low Reynolds number can be written as $F_{\text{drag}} = k_d v$, where k_d is the drag coefficient. The electrical mobility is defined as the ratio of the drift velocity to the magnitude of the electric field, thus $Z = v/E = ze/k_d$.

Spherical particles The dependency of the drag coefficient k_d on the particle radius, r, varies with the flow regime. The flow regime is determined by the Knudsen number, Kn, which is the ratio of the molecular mean free path, λ, to r, i.e. $\text{Kn} = \lambda/r$. In the continuum regime ($\text{Kn} \ll 1$), the drag coefficient is proportional to r as given by the Stokes formula [211],

$$k_d = 6\pi\mu r, \tag{2.4}$$

where μ is the fluid viscosity. For the free molecular regime ($\text{Kn} \gg 1$), the drag coefficient is proportional to r^2 as given by the Epstein formula [66],

$$k_d = -\frac{8}{3}\delta\sqrt{2\pi m_g k_{\text{B}} T} N_g r^2, \tag{2.5}$$

where δ is a numerical factor that depends on the scattering model of gas molecules, m_g is the mass of the gas molecule, k_{B} is the Boltzmann constant, T is the temperature, and N_g is the number density of the gas. Between these two limits, the Stokes-Cunningham formula [50] gives an empirical relationship for all Kn:

$$k_d = \frac{6\pi\mu r}{C_c} \tag{2.6}$$

$$C_c = 1 + \text{Kn}[A + B\exp(-E/\text{Kn})], \tag{2.7}$$

where C_c is the slip correction factor or Cunningham correction which is a function of Kn, and A, B, E are empirical parameters. Eq. 2.6 collapses to the Stokes formula in the continuum regime ($\text{Kn} \to 0$ limit).

In the free molecular regime, the drag coefficient is not only defined by the particle size r but also by the scattering process between gas molecules and the particles, i.e. diffuse or specular scattering (this is contained in δ in Eq. 2.5). Eq. 2.6 was shown to be consistent with Epstein's

formula assuming 90% diffuse and 10% specular scattering in the free molecular regime (Kn$\rightarrow\infty$ limit) [128]. However, as a particle approaches the size of a molecule, the scattering process becomes more specular. Therefore, in the limit of rigid-body collisions, Eq. 2.6 tends to overpredict the drag force of small particles. This is supported by experimental evidence that the mobility diameter based on the Cunningham correction is about 20% larger than the value measured by transmission electronic microscopy. In order to account for the diffuse to specular transition, Li and Wang [128] proposed a generalised formulation of drag force in the free molecular regime using a momentum accomodation function. This formulation was shown to explain the discrepancy between the mobility and microscopy sizes [129].

Non-spherical particles The interpretation of electrical mobility for non-spherical particles is non-trivial. The initial approach had been to use the expression in Eqs. 2.6 and 2.7 where r is replaced by the volume equivalent spherical radius, r_v. This arbitrary approximation, however, incorrectly implies no dependency on particle orientation relative to the flow and thus is limited to particles that are only slightly non-spherical [52]. A more robust method to calculate the drag coefficient of non-spherical particles over all Kn is given by Dahneke [52] and later verified by Zhang et al. [263]. They show that the drag coefficient of non-spherical particles over all Kn regime can be estimated using the orientationally averaged hydrodynamic radius, r_H, and the orientationally averaged projected area, PA [263, 218],

$$k_d = \frac{6\pi\mu r_H}{C_c} \tag{2.8}$$

$$C_c = 1 + \mathrm{Kn}[A + B\exp(-E/\mathrm{Kn})] \tag{2.9}$$

$$\mathrm{Kn} = \frac{\lambda\pi r_H}{\mathrm{PA}}. \tag{2.10}$$

These quantities, however, are shape and structure dependent. Thus, the interpretation of the mobility measurements of non-spherical particles requires an independent characterisation of the particle shape and structure, for example using TEM images.

In the free molecular limit (Kn$\rightarrow\infty$), Eq. 2.8 can be reduced to the so called projected area (PA) approximation, i.e. $k_d \sim$ PA [83]. This is largely consistent with the evidence that the mobility size, d_m is usually within a few percent of the size of projected area equivalent sphere, d_A, from microscopy, i.e. $d_m \sim d_A$, for small aggregates [46, 191].

Another potential issue in the analysis of the mobility of non-spherical particles is the deviation of the charging probability from the charging model based on Fuchs' limiting-sphere theory for sphere [23]. For large aggregates with high aspect ratios, for example, the

particle morpholgy can affect the particle charge distribution from the unipolar diffusion charger commonly used in a mobility sizer [84, 122].

2.3.5 Phase characterisation

The atomic arrangement or the internal structure of inorganic materials can be characterised with different techniques. Some of the most commonly used techniques are described very briefly below, including the high resolution TEM imaging (HRTEM), selected area electron diffraction (SAED) and powder X-ray diffraction (PXRD). These methods are based on the scattering phenomenon of high energy source by the ordered atomic structure of crystalline materials. In these methods, the analysis is performed *ex situ* with the samples collected from the synthesis.

High resolution transmission electron microscopy (HRTEM) is an imaging mode in conventional TEMs, traditionally known as the phase contrast imaging [244]. In this mode, the size of the objective aperture is enlarged compared to a normal imaging mode to allow the central electron beam and a few low index diffracted beams to be collected. The beams form an interference pattern that constitutes a latice image of the specimen. Thus, the HRTEM imaging allows the formation of a real-space image of the crystal lattices which can be interpreted to identify a specific crystal structure. HRTEM, however, only allows identification of local crystal structure, e.g., in a single particle.

Selected area electron diffraction (SAED) is another mode of operation in conventional TEMs. In this mode, diffraction patterns (DPs) formed on the detector from the scattering of electron beams are obtained. For single crystalline materials, the pattern consists of diffraction spots that depend on the crystal structure and the orientation of the electron beam relative to the sample. For polycrystalline materials, a series of concentric rings are formed with relative spacings dependent on the structures. In contrast to HRTEM, the SAED analysis can be performed over a larger scale and thus is suitable for statistical sampling. In addition, diffraction techniques usually require lower beam energy making them suitable for beam-sensitive materials [70].

Powder x-ray diffraction (PXRD) is an established method for structural characterisation of materials [160, 147]. In PXRD, the x-ray beam is scattered by the sample which consists of a large number of crystalline particles in random orientations. The intensity of the scattered x-ray is detected as a function of the scattering angle. The result, often referred to as the XRD patterns, can be analysed to reveal a wealth of information about the atomic structure and microstructure of the analysed materials.

The most widespread use of PXRD is for phase identification. For example, most studies discussed in this chapter rely on the XRD patterns to identify the presence of various polymorphs of TiO_2, e.g., anatase and rutile, in the samples. The qualitative phase identification is usually quite straightforward when only one or two phases exist and the crystal sizes are large (> 20 nm). However, when multiple phases exist, the diffraction patterns can overlap and complicate the identification. For ultrafine particles (< 10 nm), the significant peak broadening effects due to the small size and presence of microstrain, e.g., due to defects, present another challenge.

2.4 TiO_2 particle formation and growth

In this section, general approaches to model the evolution of particle growth are outlined. This is followed by a summary of the current state of the literature on particle processes that affect TiO_2 morphology and polymorphism. This covers the precursor (TTIP) chemistry, particle growth, and phase transformation.

2.4.1 Particle models and numerical methods

The time evolution of a particle distribution, or population balance dynamics, can be described by a general Smoluchowski coagulation equation [206]. Assuming the particle can be described by a discrete quantity such as the number of monomers, the population balance equation can be written as a summation,

$$\frac{\mathrm{d}n_i}{\mathrm{d}t} = \frac{1}{2}\sum_{j=1}^{i-1} \beta_{j,i-j} n_j n_{i-j} - \sum_{j=1}^{N} \beta_{i,j} n_i n_j \tag{2.11}$$

where n_i is the number concentration of particles containing i monomers, $\beta_{i,j}$ is the coagulation kernel describing the rate of coagulation of particles with i and j monomers, and N is the largest i. The first and second terms represent the production and consumption rates of particles with size i, respectively. Thus, the evolution of particle distribution can be completely described by N differential equations.

Particle models The exact form of the population balance equations depends on the choice of how the particles are represented [115]. This is often referred to as the particle model. The simplest models are univariate models where particles are described only by one quantity,

usually mass. In these models, the particle size can be calculated by assuming a constant mass density and a certain particle shape, for example the spherical particle model. A more complex representation is used in bivariate models such as the surface-volume model. In the surface-volume model, the particle surface area is considered an independent quantity from its volume which allows the model to capture a non-spherical particle morphology which is often encountered in nanoparticles. However, the calculation of particle properties in this model like primary particle size, are only possible when certain assumptions are made, e.g., primary particle monodispersity and no primary particle overlap. A more complete description of particle morphology often requires more than two descriptors. In multi-variate models, the particles are described by quantities such as the constituent primary particle sizes, connectivity between these primary particles and the sintering level of primary-primary pairs, chemical compositions, etc. In general the multivariate particle models contain particle descriptions that are closest to real nanoparticles. Thus, they enable the investigation of complex particle processes such as sintering and evolution of particle internal structure. For example, Lindberg et al. [134] described a detailed particle model that resolves the composition, size, and position of each individual primary particle in aggregate particles.

Numerical methods In a real nanoparticle system, N in Eq. 2.11 is a very large number and so an analytical solution is impractical. The numerical methods often employed to solve the population balance equations include moment methods, sectional methods, and Monte-Carlo methods. The choice of numerical method often constrains the type of particle model that can be used.

In moment methods, the particle population is represented by the first few moments of its distribution while the distribution itself remains unknown. Thus, the population balance equations are transformed into a smaller number of differential equations (moment equations) that can be solved more easily. Moment methods have the obvious advantage of being computationally cheap while allowing important properties of particle size distribution to be derived from the tracked moments. However, moment methods are usually constrained to univariate models although extension to bivariate models has been done with some difficulty. Another important challenge of the moment methods is the fact that the moment equations are usually unclosed. The closure of the equations can be done in various ways: imposing a distribution shape (presumed probability density function approaches) such as monodisperse or lognormal distribution [181, 58], interpolation of fractional order moments (MoMIC) [74, 73], quadrature based approximation (QMoM) [150, 144], etc.

In sectional methods, the population distribution is discretised to reduce the number of population balance equations. This is computationally more expensive than moment methods but they allow for more complex representation of particles. One of the issues with sectional methods is numerical diffusion due to the discretisation. This can be minimised with the moving sectional method. The sectional method has been used to model TiO_2 formation by various authors [224, 268].

In Monte Carlo methods, the particle population is represented by an ensemble of stochastic particles [186, 82]. The evolution of particle population is modelled by a series of discrete events or jump processes. The solution of the Monte Carlo methods have been shown to converge to the solution of the population balance equations [65]. The Monte Carlo methods allow for a very complex particle representation. The main disadvantage of these methods is the computational cost which is often prohibitive especially in a system that includes transport. Thus, applications of these methods have been largely confined to simple reactors (batch or plug flow reactors) or in post-processing steps.

2.4.2 Precursor chemistry

Titanium tetrachloride ($TiCl_4$) and titanium tetraisopropoxide ($Ti(OC_3H_7)_4$, TTIP) are two of the most important precursors for TiO_2 synthesis and thus the chemistry of these two compounds have been the focus of numerous studies. In a typical flame synthesis set up, the overall oxidation reactions of these molecules can be written as single-step global reactions as follows,

$$TiCl_4 + O_2 \longrightarrow TiO_2 + 2\,Cl_2 \tag{2.12}$$

$$Ti(OC_3H_7)_4 + 18\,O_2 \longrightarrow TiO_2 + 12\,CO_2 + 14\,H_2O. \tag{2.13}$$

The earlier kinetic experiments have focused on measuring the rates of such global reactions. However, there has been a growing interest in the recent decades to develop a more comprehensive kinetic model comprised of single step-wise elementary reactions. This kind of model is expected to be valid for a wider range of experimental conditions and thus can be used to develop new reactors in addition to optimising exisiting ones. For example, although $TiCl_4$ oxidation was initially studied as a single step reaction [183], detailed kinetic models for this oxidation have been developed based on first-principle calculations. This has been compared against kinetic studies by West et al. [242, 241, 243].

TTIP was initially used as an alternative to $TiCl_4$ to produce TiO_2 at a lower operating temperature [254] such as in chemical vapor deposition. Okuyama and coworkers [173, 174, 197, 166] studied TiO_2 formation from TTIP in hot wall reactors through two main reactions, i.e. thermal decomposition and hydrolysis (with water vapour), shown below. The kinetics of these reactions are usually described as first order with respect to TTIP [173, 104, 261] although some studies have suggested that higher order rates may also be applicable for TTIP thermal decomposition [215, 237].

$$Ti(OC_3H_7)_4 \longrightarrow TiO_2 + 4\,C_3H_6 + 2\,H_2O \tag{2.14}$$

$$Ti(OC_3H_7)_4 + 2\,H_2O \longrightarrow TiO_2 + 4\,C_3H_7OH \tag{2.15}$$

In subsequent studies of TiO_2 formation from TTIP in flames, similar one-step reaction models have been used to describe the precursor consumption and particle inception [224, 268, 137, 161].

In the past decade, more comprehensive decomposition models have been proposed. Figure 2.6 illustrates a detailed, up-to-date TTIP decomposition mechanism in the literature. Shmakov et al. [203] investigated the products from TTIP combustion in a H_2/O_2/Ar flame using molecular beam mass spectrometry. They then proposed a semi-empirical scheme of TTIP decomposition based on step-wise C_3H_6 releases and hydrolysis to form $Ti(OH)_4$ and the subsequent decomposition of $Ti(OH)_4$ to TiO_2. Buerger et al. [34] later proposed a kinetic mechanism based on the analogy between the decomposition of isopropanol and the decomposition of the isopropoxide branches of TTIP. The thermodynamic properties were calculated from first principle to ensure consistency [35]. However, some discrepancies were observed when the proposed mechanism was compared against TTIP ignition delay measurements at 1200–1500 K [3], suggesting important pathways were missing or using isopropanol-based reaction rate constants was unsuitable. More recently, Ershov et al. [67] suggested another important pathway of TTIP decomposition through acetone (C_3H_6O) abstraction which was not considered by Buerger et al. [34]. In this decomposition pathway, TTIP decomposes to form less deoxygenated Ti species, e.g., Ti and TiO, which are consistent with the earlier measurements by Shmakov et al. [203].

Further insights into the initial stages of TiO_2 formation from TTIP have been provided from measurements of sub-2 nm particles in flame conditions by Biswas and coworkers [25, 237, 69, 236, 238]. For example, Fang et al. [69] identified charged species $Ti(OH)_4H^+$, $Ti(OH)_3H^+$, and $TiO(OH)_4^+$ in an atomospheric $CH_4/O_2/N_2$ flame confirming that $Ti(OH)_4$ is one of the main decomposition species which is likely important in particle formation. This is consistent with the predicted thermodynamic stability of $Ti(OH)_4$ [35] as well as

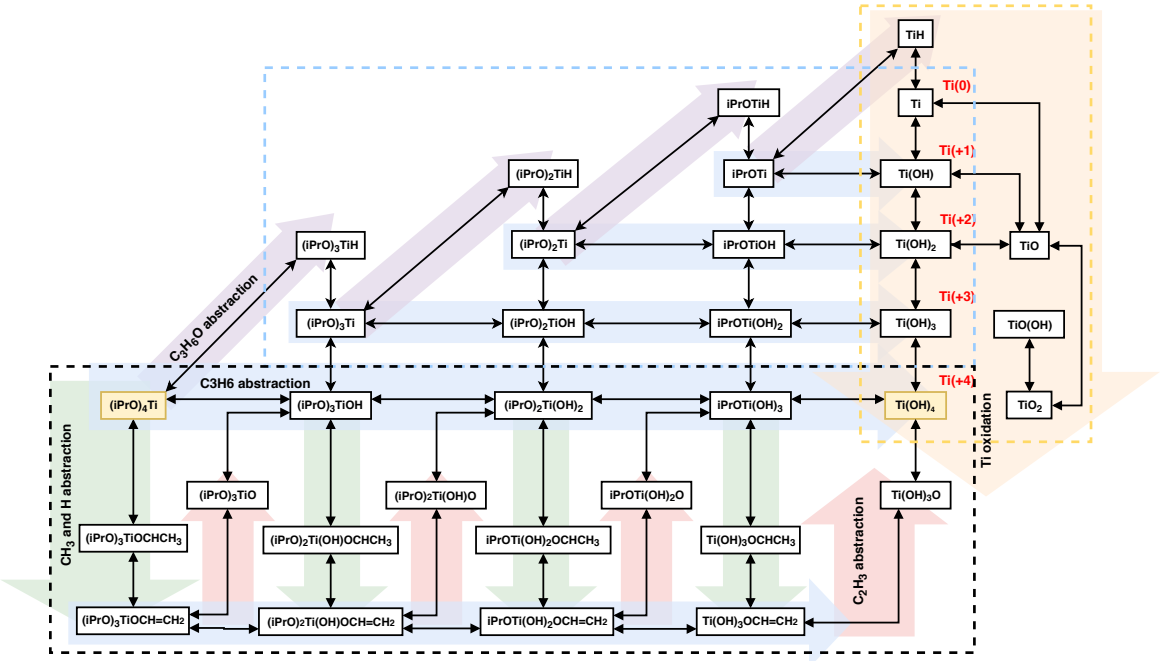

Figure 2.6: *The reaction pathways of TTIP or $(iPrO)_4Ti$: TTIP decomposition through C_3H_6 and CH_3+H abstractions to form $Ti(OH)_4$ calculated by Buerger et al. [34]* ***(black dashed line)****, TTIP decomposition through C_3H_6O abstractions followed by C_3H_6 abstractions to form $Ti(OH)_n$ proposed by Ershov et al. [67]* ***(blue dashed line)****, $Ti(OH)_4$ decomposition to form TiO_xH_y species proposed by Shmakov et al. [203]* ***(yellow dashed line)****. The different reaction types are highlighted with the colored arrows.*

earlier experimental studies [203, 35]. In addition, they observed larger clusters $Ti_nO_xC_yH_z$ ($n = 1$–4) with varying Ti:O ratio suggesting that hydrocarbon fragments (impurities) are also present and may play important roles in the initial particle clustering stages. This is supported by the fact that the early TiO_2 particles, with mobility sizes of 1–1.5 nm, have substantially lower density (1.75 g/cm^3) compared to the bulk TiO_2 (3.8–4 g/cm^3) [236].

2.4.3 Particle growth

Evolution of particle morphology

The evolution of TiO_2 particle sizes and size distributions are controlled by the relative rates of the various particle processes, including *inception*, *surface growth*, *coagulation*, and *sintering*. In this section, the general particle growth stages are described as a function of temperature and residence time [249, 226, 182, 96]. In practice, the particle morphology is also influenced by other factors such as precursor loading [10, 268], burner configuration

[272, 250], dopants [123, 5], and presence of external fields [106, 103]. The particle growth stages are illustrated in Fig. 2.7.

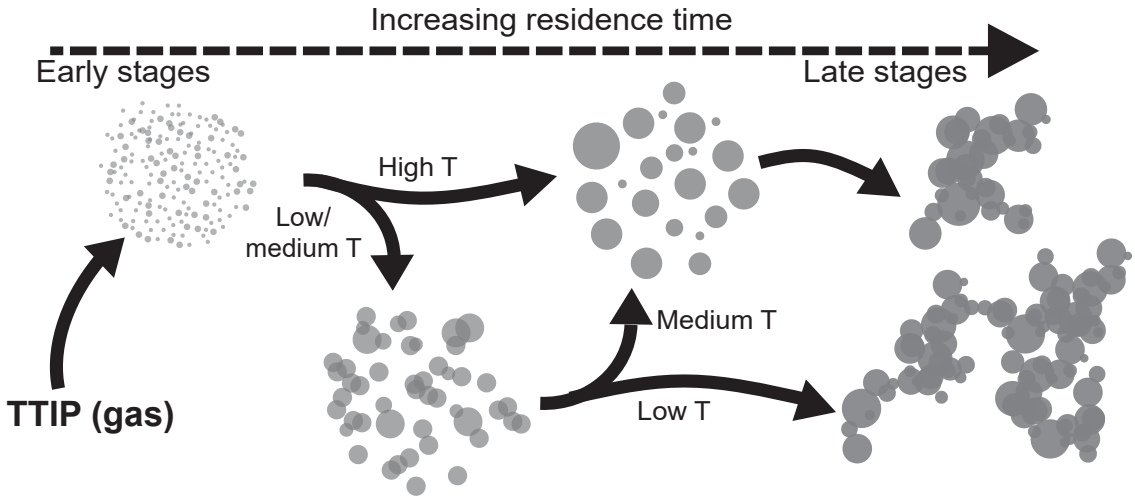

Figure 2.7: *Generalised schematic of the evolution of TiO_2 particle morphology in flame synthesis conditions as a function of residence time and temperature. The typical growth stages at low, medium, and high temperature are shown.*

The early stages include the precursor decomposition and particle inception. Following the particle inception, a large number of small particles with a narrow size distribution are formed. These particles continue to grow through two main processes: coagulation and surface growth. Coagulation is a growth process through collision of particles. The particle collision frequency is given by kinetic gas theory [119]. In the early stages, due to the small size of particles, collided particles fuse to form a larger spherical particle almost instantaneously. This is also termed coalescence. On the other hand, surface growth is a process whereby gas-phase precursor is added to the surface of the particles, either through chemical reaction or condensation of particle monomers. As the surface growth rate depends on the available surface area and precursor concentration, it is usually more dominant in early stages where a high surface area of particles and the gas-phase precursor are available.

Coagulation typically leads to a broadening of the particle size distribution while surface growth tends to narrow the size distribution [225]. Simultaneous inception and coagulation can lead to a bimodality in the particle size distribution although this is not always the case when surface growth or mixing is dominant. Surface growth has been shown to be an important process for TiO_2 formation from TTIP at high temperature. For example, Tsantilis et al. [224] modelled TiO_2 formation in a premixed $CH_4/O_2/N_2$ flame and accounted for surface growth by assuming a surface decomposition of TTIP in addition to the gas-phase

thermal decomposition. They demonstrated that this produces a better agreement with experimental data compared to when no surface growth is accounted for.

After these early stages, three generalised growth pathways are shown in Fig. 2.7 for high, medium, and low temperatures. At this point, precursor conversion is completed and the particle evolution is controlled largely by coagulation and sintering [62, 64, 57]. For high temperature, the sintering rate is usually very fast so an instantaneous coalescence can be assumed and particles remain spherical. This coagulation-controlled growth broadens the size distribution towards the well-known unimodal self-preserving shape with a geometric standard deviation (GSD) of ~ 1.45 [75]. For medium and low temperature, sintering is slower and particle coagulation leads to the formation of small aggregates. As coagulation results in a rapid decrease in particle number, coagulation rate eventually falls off. For medium temperature, sintering eventually overtakes coagulation, leading to formation of spherical particles again. Such particle evolution is consistent with experimental data reported by Hung et al. [96] and Arabi-Katbi et al. [10].

Finally, in the late stages of particle formation, larger particle sizes lead to a dramatically slower sintering [36]. As a result, larger aggregates are formed. The formation of aggregates at this stage is indicated by the broadening of aggregate size distribution towards the self preserving limit. On the other hand, the primary particle size distribution becomes narrower because sintering of smaller particles is faster [119].

Effects of cooling rate and precursor concentration

As noted previously, residence time and temperature profiles play a key role in the particle morphology of TiO_2 particles prepared in flame synthesis reactors. This is especially important in the cooling stage where the particles are collected. Higher cooling rates usually result in more spherical and less aggregated particles as the late stages of particle aggregation are suppressed. The cooling rates in flame synthesis reactors can be controlled using a few strategies. Yang et al. [250] simply used a fast insertion of a thermophoretic sampler to collect particles from the hot reaction zone and limit the particle residence time. Pratsinis and coworkers [240, 239, 217] used a critical flow nozzle to quench particle coagulation/aggregation. Alternatively, a high cooling rate can be achieved by using the stagnation flame configuration with a cooled surface. Wang and coworkers [221, 155, 168, 135] used a stagnation flame configuration where the flame is stabilised on a rotating surface. The rotation acts to cool the surface and induce a high cooling rate. The particle residence time in stagnation flame configurations can also be controlled using swirl (stagnation swirl flames). Using

stagnation swirl flames, the reaction zone can be controlled by varying the burner-to-surface distance [235]. Another strategy is to vary the reactor pressure as it directly affects the particle residence time. For example, Zhao et al. [268] showed that increasing the pressure in a premixed stagnation flame results in larger aggregates with smaller primary particles.

Precursor concentration also affects the particle morphology. Arabi-Katbi et al. [10] showed that increasing the TTIP flow rate results in a larger primary particle size. The higher precursor concentration leads to a higher particle concentration and a higher temperature which favour coagulation and sintering. In contrast, Zhao et al. [268] reported the opposite effect of precursor concentration. In their experiments, increasing precursor concentration resulted in larger aggregates but similar or even slightly smaller primary particles. These contrasting trends are explained by the difference in the temperature between the two experiments, i.e. $\sim$ 2000 K in [10] vs. $\sim$ 1600 K in [268]. At moderate or lower temperature, slower sintering explains the observed insensitivity of primary particle size to the precursor concentration [80]. It is also likely that at lower temperature, increasing precursor concentration results in a higher inception rate relative to surface growth in the early stages, leading to the formation of smaller particles.

2.4.4 Phase transformation

In addition to the evolution of the particle morphology, TiO_2 nanoparticles also undergo a concurrent internal structure evolution. The internal structure evolution occurs through the transition from a non-ordered phase which includes melt or amorphous solid to an ordered/crystalline phase as well as the transformation of one crystalline phase to another. These processes are termed *phase transformation*.

Anatase and rutile

A large proportion of exisiting studies concerning the phase transformation of TiO_2 in gas-phase or flame synthesis, both with TTIP and $TiCl_4$ as precursor, is focused on anatase and rutile. The relative composition of these two phases is often suggested to be a result of an anatase to rutile transformation. This is largely supported by the thermodynamic analysis which predicts anatase to be the more stable phase in nanosized particles as discussed above. The incepted particles in flame synthesis are very small so anatase is usually assumed to be the initial phase formed [91]. As the particle grows larger, eventually rutile becomes the thermodynamically more stable phase which leads to the anatase-rutile transformation.

For this reason, the anatase-rutile transformation is usually observed in grain coarsening experiments (heat treatments of starting anatase particles) [97, 88]. In flames, similar transformation is shown by Liu et al. [136]. They seeded a premixed stagnation flame reactor with anatase particles and observed the anatase-rutile transformation using *in situ* Raman measurements. Similarly, Zhao et al. [265] found that rutile crystallites are usually larger than anatase crystallites in TiO_2 with anatase-rutile mixture prepared in a premixed stagnation flame reactor. This is in agreement with Pratsinis et al. [185] who observed that coarser particles prepared in a diffusion flame reactor (using $TiCl_4$ as a precursor) contain higher rutile content.

The anatase-rutile transformation implies that anatase content will decrease with increasing residence time. This is supported by measurements of samples collected at different heights in a premixed flame synthesis showing the rutile content increasing with height [253, 138]. Further, anatase-rutile transformation is a reconstructive process which involves an energy barrier. Therefore, a temperature dependence is also expected. For example, Vemury et al. [231] suggested that anatase-rutile transformation is inhibited when an electric field is applied because it leads to shorter flame and shorter particle residence time in high temperature zone. Yeh et al. [253] and Ma and Yang [138] also attributed lower anatase content when precursor loading is increased to the increased flame temperature.

Another very common observation that has been reported by numerous authors is the influence of the oxidising environment, e.g., oxygen concentration in the gas mixture, on anatase-rutile composition. It is often argued that anatase-rutile transformation is inhibited in oxygen rich conditions and accelerated in oxygen lean conditions [97]. This is usually attributed to the preferential formation of rutile due to high oxygen vacancy/defect concentration [97] or impurities from fuel or unreacted precursor [109]. For example, a Raman spectra analysis by Li Bassi et al. [130] showed that stoichiometric flame-made particles are usually anatase while those with high oxygen vacancy concentration are usually rutile. Similarly, Akhtar et al. [5] and Li et al. [123] demonstrated that the presence of Al dopant induces oxygen vacancies which enhance the anatase-rutile transformation.

The preferential formation of rutile in oxygen lean environments has been reported for TiO_2 flame synthesis using $TiCl_4$ [272, 193] and TTIP [253, 138, 239, 221, 155], as well as in conventional CVD [111] and plasma-assisted synthesis [127, 98]. This effect was demonstrated clearly by Kho et al. [108] who performed a systematic study of anatase-rutile content using a flame spray pyrolysis. They showed that anatase-rutile content can be tuned by controlling the mixture equivalence ratio (ER) through varying the oxygen gas flow rate and precursor loading. They identified the window for anatase-rutile tunability at

$1.0 < ER < 1.5$. A similar range is also observed in stagnation flame experiments by Liu et al. [135].

Sub-oxides and metastable phases

While the anatase-rutile transformation described above is satisfactory to explain many experimental observations, it only offers an incomplete picture of crystal structure formation of TiO_2 in flames. In particular, the intermediates in the early stages of particle growth are still poorly understood. For example, Liu et al. [136] performed in situ Raman and light scattering measurements in a TTIP doped stagnation flame. Based on the scattering results, the initial particle formation occurs very early near the burner nozzle. However, Raman peaks of anatase only appear much later in the flow. This suggests that the nascent particles are not anatase but possibly amorphous. This is consistent with molecular dynamics simulations that showed that TiO_2 particles with diameter < 2 nm are likely amorphous due to the surface reconstruction effect [258]. In this case, anatase can then nucleate from amorphous TiO_2 as particles grow [257].

Furthermore, the nascent particles are likely to be non-stoichiometric. This is supported by the blue appearance of TiO_2 prepared in highly oxygen lean environments [96] which is indicative of a high oxygen vacancy concentration [31]. Blue TiO_2 powder was also prepared by Teleki and Pratsinis [217] in a TTIP-doped diffusion flame with a quenching nozzle. They observed varying coloration as a function of burner-to-nozzle distance (BND). At moderate BND, they found a peak in the XRD spectrum which is not attributed to anatase or rutile but possibly a Magnéli phase, i.e. a suboxide. The formation of suboxide intermediates are likely to be related to the preferential formation of rutile over anatase in oxygen lean environments.

Lastly, other authors have reported the formation of other metastable phases in flame-made TiO_2. For example, McCormick et al. [146] suggested that brookite is also formed in TiO_2 synthesis using a tubular burner and a rotating sampler. More recently, Riad et al. [189] prepared a mixture of TiO_2-B and anatase using a flame spray pyrolysis process. The amount of metastable TiO_2-B is shown to increase with increasing oxygen mole fraction. The formation of these metastable phases, however, is not clearly understood. Thus, further work is needed to fully understand TiO_2 phase transformations in flame environments and the possible roles of the sub-oxides and metastable phases.

Chapter 3

Modelling TiO_2 formation in a stagnation flame using method of moments

In this chapter, the stagnation flame synthesis of titanium dioxide nanoparticles from titanium tetraisopropoxide (TTIP) is modelled based on a simple one-step decomposition mechanism and one-dimensional stagnation flow. The particle model, which accounts for nucleation, surface growth, and coagulation, is fully-coupled to the flow and the gas phase chemistry and solved using the method of moments with interpolative closure (MoMIC). The model assumes a complete coalescence of particles after coagulation considering the high temperature of typical flames. The model predictions show a good agreement with mobility particle size measurements with varying TTIP loading, although the particle geometric standard deviation (GSD) is underpredicted for high TTIP loading. The particle size is predicted to be sensitive to the sampling location near the stagnation surface in the modelled flame. The sensitivity to the sampling location is found to increase with increasing precursor loading and stagnation temperature. Lastly, the effect of surface growth is evaluated by comparing the result with an alternative reaction model. It is found that surface growth plays an important role in the initial stage of particle growth which, if neglected, results in severe underprediction of particle size and overprediction of particle GSD.

3.1 Background

The use of a stretch-stabilised stagnation flame reactor to prepare highly crystalline and ultrafine TiO_2 nanoparticles has been demonstrated by Wang and coworkers, termed flames stabilised on a rotating surface (FSRS) [221, 222, 155, 168]. In this configuration, a thin flame is typically stabilised approximately 2-5 mm above a cooled surface. The thin flame results in uniform particle time-temperature trajectories radially and thus a narrow particle size distribution. The cooled surface allows for the formation of a steep temperature gradient near the surface and hence a controllable residence time for particle formation. The surface also acts as a substrate for sample collection with adjustable temperature to produce different nanostructures/films.

Previous studies have shown that the particle properties and morphology are easily controlled by a few process variables including flame mixture, precursor loading, and plate temperature. The prepared TiO_2 particles are usually crystalline and spherical with a limited degree of aggregation. The size of the particles can be easily controlled by changing the precursor loading and the residence time. The crystal structure, usually anatase or rutile, is also tunable by varying the flame mixture [155]. Due to the short residence time, the particles are very small, usually < 15 nm. This provides an ideal set up to study the early stage formation of TiO_2 which is still poorly understood.

Furthermore, the flow dynamics of an impinging laminar jet can be captured by a pseudo one-dimensional flow approximation [107]. This allows for simulations with fully coupled flow, chemistry, and particle dynamics to be solved at a reasonable computational cost.

The method of moments is one of the most computationally efficient numerical approaches to solve the population balance equations. The challenge with this method is the difficulty in capturing a complex particle morphology or bimodal size distributions. However, narrow particle size distributions and particle sphericity are usually assumed for the stagnation flame synthesis with short residence times. The use of the method of moments allows coupling with flow dynamics and detailed chemistry to capture the interaction between gas-phase and particle models at relative ease.

The purpose of this chapter is to present an implementation of a moment-based particle model employing a simple reaction mechanism available in literature and to demonstrate the ability to model TiO_2 formation from titanium tetraisopropoxide (TTIP) in FSRS reactors. The predicted results are compared with experimental data obtained from Tolmachoff et al. [221]. The model is used to investigate the effects of important process variables, including

precursor loading and stagnation temperature, and to explain the experimentally observed trends of particle size in terms of relative rates of the particle processes modelled.

3.2 Computational details

Figure 3.1 presents a schematic of the flame solver presented in this chapter. The gas-phase reaction, flow, and particle models are fully coupled within the flame solver. The flame solver and the corresponding models are implemented in the *k*inetics® software package [49]. The flow, gas-phase reaction, and particle models are described below.

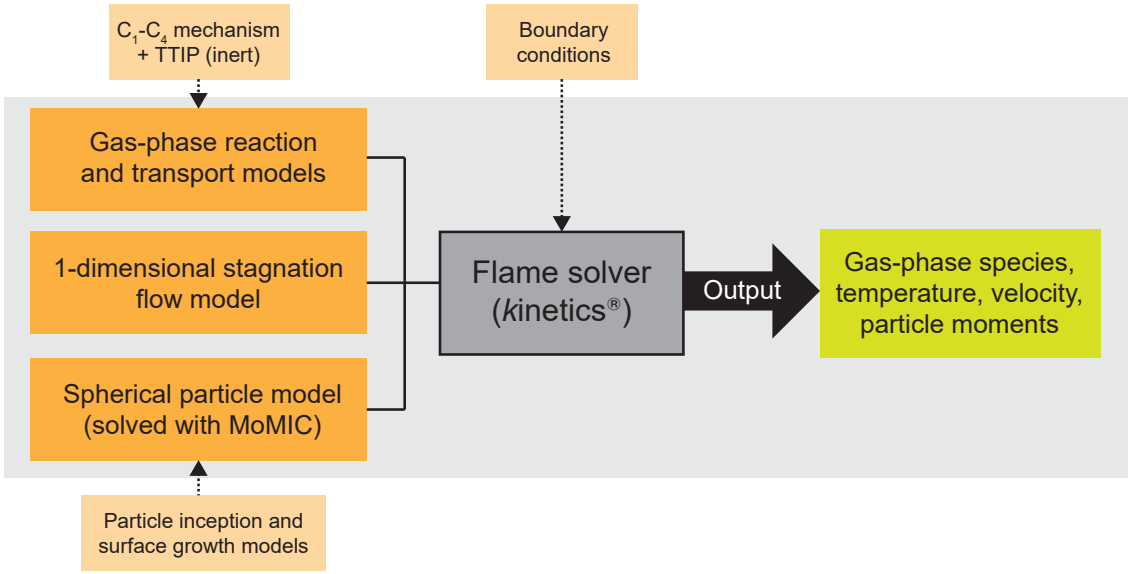

Figure 3.1: *Schematic of the modelling method used in this chapter. The grey box denotes the general model framework.*

3.2.1 Stagnation flow model

The flow in the burner is assumed to be an axisymmetric stagnation flow. It is modelled using a pseudo one-dimensional approximation, illustrated in Fig. 3.2, by introducing a streamfunction of the form

$$\Psi(z,r) = r^2 U(z), \tag{3.1}$$

where z is the axial distance from the nozzle, r is the radial distance from the burner centerline, and $U(z)$ is the axial component of the streamfunction. The axial velocity, u_z, and radial

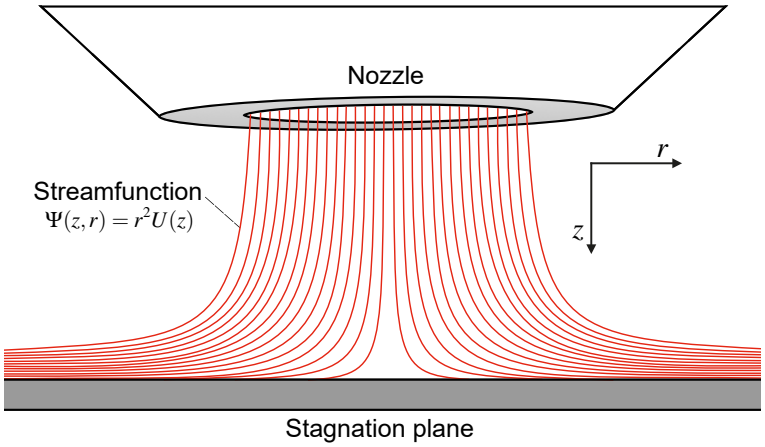

Figure 3.2: *Diagram of a one-dimensional stagnation flow with streamlines shown in red.*

velocity, u_r, are given by

$$u_z = \frac{2U(z)}{\rho} \tag{3.2}$$

$$u_r = -\frac{r}{\rho}\frac{\mathrm{d}U(z)}{\mathrm{d}z}, \tag{3.3}$$

where ρ is the gas mixture density.

By introducing the streamfunction assumption, the Navier-Stokes equations are reduced to a set of one-dimensional ordinary differential equations [more on derivation in 107],

$$\frac{\mathrm{d}\Lambda}{\mathrm{d}z} = 0 \tag{3.4}$$

$$\Lambda - 2\frac{\mathrm{d}}{\mathrm{d}z}\left(\frac{UG}{\rho}\right) + \frac{3G^2}{\rho} + \frac{\mathrm{d}}{\mathrm{d}z}\left[\mu\frac{\mathrm{d}}{\mathrm{d}z}\left(\frac{G}{\rho}\right)\right] = 0, \tag{3.5}$$

where Λ is the radial pressure-gradient eigenvalue, G is $\mathrm{d}U/\mathrm{d}z$, and μ is the gas mixture viscosity. Equations (3.4) and (3.5) are the eigenvalue and momentum equations for one-dimensional stagnation flow, respectively. Next, assuming the temperature, T, and the species mole fractions, Y_k, are radially uniform, the additional governing equations for T and Y_k are given as

$$2U\frac{\mathrm{d}T}{\mathrm{d}z} - \frac{1}{c_p}\frac{\mathrm{d}}{\mathrm{d}z}\left(\kappa_g\frac{\mathrm{d}T}{\mathrm{d}z}\right) + \frac{\rho}{c_p}\sum_{k=1}^{K} Y_k c_{p,k} V_k \frac{\mathrm{d}T}{\mathrm{d}z} + \frac{1}{c_p}\sum_{k=1}^{K} h_k \dot{\omega}_k + \frac{1}{c_p}\dot{Q}_{\mathrm{rad}} = 0 \tag{3.6}$$

$$2U\frac{\mathrm{d}Y_k}{\mathrm{d}z} + \frac{\mathrm{d}}{\mathrm{d}z}(\rho Y_k V_k) - W_k\dot{\omega}_k = 0 \quad (k = 1, K), \tag{3.7}$$

where c_p is the mixture specific heat, κ_g is the mixture thermal conductivity, $\dot{Q}_{\text{rad}}$ is the gas radiation term in the optically-thin limit [204], K is the number of gas-phase species, Y_k, $c_{p,k}$, h_k, $\dot{\omega}_k$, V_k and W_k are the mole fraction, the specific heat, the molar enthalpy, the molar production rate, the multicomponent diffusion velocity, and the molar mass of species k, respectively. The gas radiation term is calculated according to Barlow et al. [13], including the radiation from H_2O, CO_2, CO, and CH_4.

This model has been used to simulate various combustion systems successfully before. The simplified flow governing equations reduces the computational power required. This is an attractive benefit for cases where coupling with complex and computationally expensive reacting systems is necessary [252, 41].

3.2.2 Gas-phase reaction model

The combustion chemistry and transport data of the gas species are described by the USC Mech II hydrocarbon kinetic model which includes 111 species and 784 reactions [234]. TTIP is added as an extra inert species. TTIP thermodynamic data is obtained from first-principle calculations by Buerger et al. [35] while the transport data is estimated from the transport data for large hydrocarbons [229]. The approximation of the transport data is deemed acceptable given the relatively low loading of TTIP simulated in this work.

3.2.3 Particle model

Inception and surface growth

In this work, the simple one-step reaction proposed by Okuyama et al. [174] is used to describe the overall rate of TTIP consumption with first order reaction rate constant, k_1, given by

$$k_1 = 3.96 \times 10^5 \exp\left(\frac{-8479.7\ \text{K}}{T}\right)\ \text{s}^{-1}. \tag{3.8}$$

The overall reaction is assumed to include both gas-phase decomposition and surface reaction of TTIP. The surface reaction rate is described by the first-order rate model proposed by Battiston et al. [16] with rate constant, k_2, derived by Tsantilis et al. [224],

$$k_2 = 1 \times 10^{11} \exp\left(\frac{-15155.16\ \text{K}}{T}\right)\ \text{cm/s}. \tag{3.9}$$

The rate of the gas-phase decomposition of TTIP is calculated from the difference between the overall and surface reaction rates. When the surface reaction rate exceeds the overall rate, the gas-phase decomposition rate is set to zero and the surface reaction rate is calculated from the overall rate instead. In summary, the chemical reactions modelled leading to TiO_2 formation are

$$\mathrm{Ti(OC_3H_7)_{4(g)}} \xrightarrow{k_g} \mathrm{TiO_{2(s)} + 4C_3H_{6(g)} + 2H_2O_{(g)}}$$
$$\mathrm{Ti(OC_3H_7)_{4(g)} + (TiO_2)_{i-1(s)}} \xrightarrow{k_s} \mathrm{(TiO_2)_{i(s)} + 4C_3H_{6(g)} + 2H_2O_{(g)}}.$$

The gas-phase reaction rate constant, k_g, and the surface reaction rate constant, k_s, are given by

$$k_g = \begin{cases} k_1 - Ak_2 & \text{for } k_1 \geq Ak_2 \\ 0 & \text{for } k_1 < Ak_2 \end{cases} \tag{3.10}$$

$$k_s = \begin{cases} k_2 & \text{for } k_1 \geq Ak_2 \\ k_1/A & \text{for } k_1 < Ak_2, \end{cases} \tag{3.11}$$

where A is the total surface area of the particles per unit volume. Considering the relatively low loading of TTIP simulated in this study, these reactions are excluded from the temperature source term calculation in Eq. (3.6).

A similar model was used by Tsantilis et al. [224] and was shown to result in excellent agreement with experimental data. In addition, this reaction rate model was shown to sufficiently describe the overall TTIP consumption in a H_2/O_2 stagnation flame experiment conducted by Korobeinichev et al. [113]. A more recent study of TTIP decomposition in an aerosol reactor [237] also supported the first-order overall rate as proposed by Okuyama et al. [174] for high temperature conditions.

Method of moments

The particle population is described by the number density moments of the size distribution, M_r, which are defined as

$$M_r = \sum_{i=1}^{\infty} i^r N_i \tag{3.12}$$

$$\mu_r = \frac{M_r}{M_0}, \tag{3.13}$$

where r is the order of the moment, N_i is the number density of particles with i TiO_2 monomers, and μ_r are the reduced moments. The method of moments has been widely used to simplify population balance models in areas such as aerosol science, materials science, and cell biology. Hulburt and Katz [95] were some of the first to develop the method of moments to model particles in inhomogeneous flow in 1964. Frenklach and Harris [74] later extended the method to use interpolation to provide closures in the method of moments with interpolative closure (MoMIC), used in this work.

While complete reconstruction of the full particle size distribution requires the knowledge of all moments, a number of relevant properties such as number density, area density, mass density, and average diameter, can be inferred from the first few moments alone. These population properties are given by

$$\text{Number density} = M_0 \tag{3.14}$$

$$\text{Area density} = A_1 M_{2/3} \tag{3.15}$$

$$\text{Mass density} = m_1 M_1 \tag{3.16}$$

$$\text{Average diameter} = d_1 \frac{M_{1/3}}{M_0}, \tag{3.17}$$

where A_1, m_1 and d_1 are the surface area, the mass, and the diameter of a single TiO_2 monomer, respectively. The surface area and diameter A_1 and d_1 are calculated from m_1 using the bulk density of rutile.

The accuracy of the interpolation used in MoMIC depends on the number of moments. Six moments are normally used, in this case the zeroth to fifth order moments. Thus, the particle population is tracked by only six moment equations. This provides an computationally efficient approach without having to make any prior assumptions about the particle size distribution shape.

The spherical particle model, which assumes an instantaneous coalescence, is imposed by the choice of the method of moments model. This assumption is motivated by the fact that the temperature in the combustion zone is much higher than the melting point of bulk TiO_2 ($\sim$ 1900 K) which leads to rapid sintering. In cases where particles form an aggregate structure, a more detailed particle model, which accounts for aggregation and sintering, is required [157, 163, 89].

The particle model is coupled to the flow and the gas-phase chemistry through transport equations describing the convection, thermal diffusion, size-dependent molecular diffusion and moment source terms. The transport equation for the r^{th}-moment is given in logarithmic form as

$$2U\frac{\mathrm{d}}{\mathrm{d}z}\left(\frac{1}{\rho}\right)+\frac{2U}{\rho}\frac{\mathrm{d}\log M_r}{\mathrm{d}z}+\frac{2}{\rho}\frac{\mathrm{d}U}{\mathrm{d}z}-\frac{2G}{\rho}+v_{T,z}\frac{\mathrm{d}\log M_r}{\mathrm{d}z}+\frac{\mathrm{d}v_{T,z}}{\mathrm{d}z}- \frac{1}{M_r}\frac{\mathrm{d}}{\mathrm{d}z}\left[\rho D_{p,1}\frac{\mathrm{d}}{\mathrm{d}z}\left(\frac{M_{r-2/3}}{\rho}\right)\right]-\frac{\dot{M}_r}{M_r}=0, \quad (3.18)$$

where $D_{p,1}$ is the Brownian diffusion coefficient of TiO_2 monomer, $v_{T,z}$ is the thermophoretic velocity, and $\dot{M}_r$ is the moment source terms. The formulations for $D_{p,1}$ and $v_{T,z}$ [232] are given as follows,

$$D_{p,1}=\frac{3}{2\rho}\left(1+\frac{\pi\alpha_T}{8}\right)^{-1}\sqrt{\frac{\bar{W}k_{\mathrm{B}}T}{2\pi N_{\mathrm{A}}}}\left(\frac{1}{d_1^2}\right) \quad (3.19)$$

$$v_{T,z}=-\frac{3}{4}\left(1+\frac{\pi\alpha_T}{8}\right)^{-1}\frac{\mu}{\rho}\frac{\mathrm{d}\log T}{\mathrm{d}z}, \quad (3.20)$$

where α_T is the thermal accommodation factor which represents the fraction of gas molecules undergoing a diffuse scattering and is usually taken to be 0.9 [76], $\bar{W}$ is the average molar mass of the gas mixture, k_{B} is the Boltzmann constant, and N_{A} is the Avogadro number.

The moment source terms, $\dot{M}_r$, describe the evolution of the moments according to particle processes, including inception, surface growth, and coagulation,

$$\dot{M}_r=\dot{M}_r^{\mathrm{in}}+\dot{M}_r^{\mathrm{sg}}+\dot{M}_r^{\mathrm{coag}}, \quad (3.21)$$

where $\dot{M}_r^{\mathrm{in}}$ and $\dot{M}_r^{\mathrm{sg}}$ represent the moment source terms due to the inception and surface growth described in the reaction model. With the reaction model described in Section 3.2.3,

these terms are given as

$$\dot{M}_r^{\text{in}} = k_g C_{\text{TTIP}} N_{\text{A}} \qquad \text{for } r \geq 0 \tag{3.22}$$

$$\dot{M}_r^{\text{sg}} = \begin{cases} 0 & \text{for } r = 0 \\ k_s A_1 C_{\text{TTIP}} N_{\text{A}} \sum_{k=0}^{r-1} \binom{r}{k} \mu_{k+\frac{2}{3}} M_0 & \text{for } r \geq 1, \end{cases} \tag{3.23}$$

where C_{TTIP} is the TTIP molar concentration in the gas-phase. The moment source term due to inception is independent of the moment order, r, because the smallest particle in the population is assumed to have $i = 1$ (i.e. a TiO_2 monomer).

The moment source term due to the coagulation, $\dot{M}_r^{\text{coag}}$, follows the formulation proposed by Pratsinis [181],

$$\dot{M}_r^{\text{coag}} = \begin{cases} \dfrac{G_r^{\text{c}} G_r^{\text{f}}}{G_r^{\text{c}} + G_r^{\text{f}}} & \text{for } r \neq 1 \\ 0 & \text{for } r = 1, \end{cases} \tag{3.24}$$

where G_r^{c} and G_r^{f} are the moment source terms due to the coagulation in the continuum and free-molecular regimes, respectively. The coagulation source term in the continuum regime for spherical particles is given as [derivation in 73]

$$G_r^{\text{c}} = \begin{cases} -K_{\text{c}} \left(1 + \mu_{\frac{1}{3}} \mu_{-\frac{1}{3}} + K_c' [\mu_{-\frac{1}{3}} + \mu_{\frac{1}{3}} \mu_{-\frac{2}{3}}]\right) M_0^2 & \text{for } r = 0 \\ 0 & \text{for } r = 1 \\ \dfrac{1}{2} K_{\text{c}} \sum_{k=1}^{r-1} \binom{r}{k} \left(\beta_1^{\text{c}}(r,k) + K_{\text{c}}' \beta_2^{\text{c}}(r,k)\right) M_0^2 & \text{for } r \geq 2 \end{cases} \tag{3.25}$$

$$K_{\text{c}} = \frac{2 k_{\text{B}} T}{3\mu} \tag{3.26}$$

$$K_{\text{c}}' = 2.514 \lambda \left(\frac{\pi \rho_{\text{TiO}_2}}{6 m_1}\right)^{\frac{1}{3}} \tag{3.27}$$

$$\beta_1^{\text{c}}(r,k) = \mu_{k+\frac{1}{3}} \mu_{r-k-\frac{1}{3}} + 2\mu_k \mu_{r-k} + \mu_{k-\frac{1}{3}} \mu_{r-k+\frac{1}{3}} \tag{3.28}$$

$$\beta_2^{\text{c}}(r,k) = \mu_{k+\frac{1}{3}} \mu_{r-k-\frac{2}{3}} + \mu_k \mu_{r-k-\frac{1}{3}} + \mu_{k-\frac{1}{3}} \mu_{r-k} + \mu_{k-\frac{2}{3}} \mu_{r-k+\frac{1}{3}}, \tag{3.29}$$

where λ is the mean free path and ρ_{TiO_2} is the bulk density of rutile titania.

The coagulation source term in the free-molecular regime for spherical particles is given as [derivation in 73]

$$G_r^{\mathrm{f}} = \begin{cases} -\frac{1}{2} K_{\mathrm{f}} \left({}^{\frac{1}{2}} f_{0,0} \right) M_0^2 & \text{for } r = 0 \\ 0 & \text{for } r = 1 \\ \frac{1}{2} K_{\mathrm{f}} \sum_{k=1}^{r-1} \binom{r}{k} \left({}^{\frac{1}{2}} f_{k,r-k} \right) M_0^2 & \text{for } r \geq 2 \end{cases} \tag{3.30}$$

$$K_{\mathrm{f}} = \varepsilon_{i,j} \left(\frac{6 k_{\mathrm{B}} T}{\rho_{\mathrm{TiO_2}}} \right)^{\frac{1}{2}} \left(\frac{3 m_1}{4 \pi \rho_{\mathrm{TiO_2}}} \right)^{\frac{1}{6}} \tag{3.31}$$

$${}^{l} f_{x,y} = \sum_{i=1}^{\infty} \sum_{j=1}^{\infty} \frac{i^x j^y}{\sqrt{ij}} (i+j)^l \left(i^{\frac{1}{3}} + j^{\frac{1}{3}} \right)^2 \frac{N_i N_j}{M_0^2}, \tag{3.32}$$

where $\varepsilon_{i,j}$ is the size-dependent collision enhancement factor due to attractive or repulsive inter-particle forces. In this case, a constant multiplier, ε, is assumed to replace the size-dependent enhancement factor as normally done for soot coagulation [92]. The enhancement factor used in this study is 2.64 as calculated by Zhang et al. [264] considering both the van der Waals and the dipole-dipole interaction of TiO_2 particles in the free-molecular regime at high temperature. The enhancement factor used for soot is only slightly lower, 2.2 [92].

Interpolative closure for moments

Finally, closures for the fractional moment terms are obtained from the Lagrange interpolation (or extrapolation in case of negative order moments) among the known values of whole order moments as prescribed by Frenklach et al. [73],

$$\log \mu_p = L_p \left(\log \mu_0, \log \mu_1, \ldots, \log \mu_{r_{\max}} \right) \qquad \text{for } p > 0 \tag{3.33}$$

$$\log \mu_p = L_p \left(\log \mu_0, \log \mu_1, \log \mu_2 \right) \qquad \text{for } p < 0. \tag{3.34}$$

The function ${}^{\frac{1}{2}} f_{x,y}$ is estimated by a logarithmic Lagrange interpolation between evaluations of the grid function,

$${}^{m} f_{x,y} = \sum_{k=0}^{m} \binom{m}{k} \left(\mu_{k+x+\frac{1}{6}} \mu_{m+y-k-\frac{1}{2}} + 2 \mu_{k+x-\frac{1}{6}} \mu_{m+y-k-\frac{1}{6}} + \mu_{k+x-\frac{1}{2}} \mu_{m+y-k+\frac{1}{6}} \right), \tag{3.35}$$

for $m \in \mathbb{N}_0$, using the parameterisation

$$m = 0, ..., n-1 \tag{3.36}$$

$$n = \min(4, U - \max(x, y)) \quad \text{with } U \in \{3, ..., 6\}, \tag{3.37}$$

where U is the number of moments evolution equations being solved, six in this case, such that $r = 0, ..., U-1$ [6].

3.2.4 Boundary conditions

The set of governing equations in Eqs. (3.4)–(3.7) and (3.18) represent a fully-coupled system of fluid flow, gas-phase chemistry, and particles. The equations are solved as a boundary value problem by specifying a set of boundary conditions at the burner nozzle and stagnation surface.

The boundary conditions at $z = 0$ (nozzle) are given as

$$U(0) = \frac{\rho_0 u_0}{2} \tag{3.38}$$

$$G(0) = 0 \tag{3.39}$$

$$T(0) = T_0 \tag{3.40}$$

$$\rho(0) Y_k(0) V_k(0) = \rho_0 u_0 (Y_{k,0} - Y_k(0)) \qquad \text{for } k = 1, ..., K \tag{3.41}$$

$$\log M_r(0) = 0 \qquad \text{for } r = 0, ..., 5, \tag{3.42}$$

where u_0, ρ_0, T_0, and $Y_{k,0}$ are the exit velocity, density, temperature, and mole fraction of species k of the gas mixture in the nozzle, respectively. The formulation of the boundary condition of the species mole fraction, Y_k, allows for a back-diffusion into the nozzle which leads to $Y_{k,0} \neq Y_k(0)$. As the particles are supposed to be non-existent in the initial gas mixture in the nozzle, M_r should be zero. However, as the moments are tracked in a log-space, $\log M_r$, this boundary condition is not feasible. Instead, $\log M_r(0) = 0$ is used, corresponding to a negligible but non-zero particle concentration. This choice is justified by the fact that the high temperature region is located far from the nozzle, which results in an insensitivity to the choice of $\log M_r(0)$.

The boundary conditions at $z = L$ (stagnation plane) are given as

$$U(L) = 0 \tag{3.43}$$

$$G(L) = 0 \tag{3.44}$$

$$T(L) = T_s \tag{3.45}$$

$$\rho(L)Y_k(L)V_k(L) = 0 \qquad \text{for } k = 1,...,K \tag{3.46}$$

$$\frac{\mathrm{d}\log M_r(L)}{\mathrm{d}z} = 0 \qquad \text{for } r = 0,...,5, \tag{3.47}$$

where T_s is the stagnation temperature.

3.2.5 Numerical methods

The boundary-value problem, described in Section 3.2.4, is solved using a damped Newton search algorithm to obtain the steady-state solution [similar to 86].

The convergence criterion is specified by setting a tolerance level which controls the grid refinement to resolve the regions with large magnitudes of the gradient and curvature of the dependent variables. Using the solution-adapted grid refinement, convergence is achieved with 250–300 grid points for the nozzle-stagnation plate separation distance, $H = 1.27$ cm, and 400–450 grid points for $H = 3.4$ cm. By way of comparison, Modak et al. [161] used only around 200 grid points for $H = 3.4$ cm with a similar flame.

3.3 Experimental details

The experimental conditions in Tolmachoff et al. [221] are used in all simulations in this work except where otherwise stated. The initial molar composition of the gas mixture is 3.96% C_2H_4, 26.53% O_2, and 69.51% Ar (corresponding to an equivalence ratio of $\phi = 0.45$) while TTIP loading is varied from 10–2000 ppm. The other boundary conditions are specified as

$$u_0 = 429 \text{ cm/s}$$

$$T_0 = 423.15 \text{ K}$$

$$T_s = 400 - 1600 \text{ K}.$$

3.4 Results and discussion

3.4.1 Flame location

In the experimental study by Tolmachoff et al. [221], the distance between the stagnation surface and the nozzle, L, is 3.4 cm and the nozzle exit diameter, d_{nozzle}, is 1 cm. This high L/d_{nozzle} ratio is an important parameter to consider because ideal one-dimensional stagnation flow equations assume an infinitely wide nozzle exit diameter ($L/d_{\text{nozzle}} \approx 0$). As a result of the high L/d_{nozzle} ratio, a free-jet region with a plug flow velocity profile is formed upstream of the flame. This free-jet region is not captured by the parabolic solution of the one-dimensional stagnation flow model [20, 19].

The best solution to this problem is to specify boundary conditions downstream of the free-jet region where the flow can be modelled as a one-dimensional stagnation flow [20]. However, this would require the knowledge of the full velocity profile which could only be determined experimentally or with rigorous fluid dynamics simulations.

An alternative solution is to fit the predicted temperature profile to the experimental measurements [221, 113]. This is done by specifying a computational distance, H, that excludes the free-jet region such that $H < L$. In other words, the one-dimensional stagnation flow behaviour is assumed to start at the end of the free-jet region. Nevertheless, this approach requires an accurate temperature profile which is not available due to the large uncertainty in the reported temperature measurement [221].

In this work, information about the flame location is used to determine the computational distance, H. It is assumed that OH-chemiluminescence is responsible for the experimentally observed luminosity of the flame. This is a reasonable assumption given that the non-sooting, lean flame is used where particle radiation could be neglected. The peak luminosity is observed at 0.29 ± 0.03 cm from the substrate [221]. The distance $H = 1.27$ cm is chosen such that the location of the OH peak predicted by the model coincides with the experimentally observed peak luminosity (this is illustrated in Fig. 3.3).

Without taking into account the existence of the free-jet region, the calculation of the one-dimensional stagnation flame with $H = 3.4$ cm would result in the flame located almost 1 cm away from the stagnation surface. This is significantly different from the experimental observation and leads to a much longer particle residence time in the combustion zone. The maximum temperature is also higher due to a smaller heat loss to the stagnation plate.

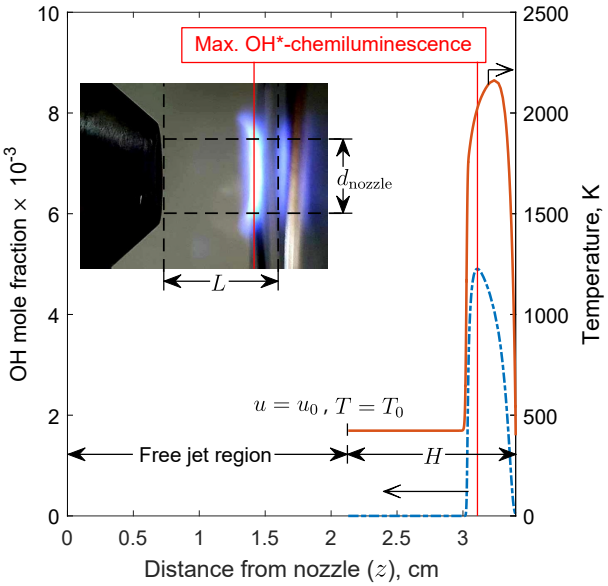

Figure 3.3: *Simulated temperature and OH-mole fraction profiles showing the free-jet region upstream of the flame (306 ppm TTIP, $H = 1.27$ cm, $T_s = 400$ K). The inset illustrates the experimental setup and does not correspond to any specific simulation presented in the figure. It shows a flat undoped flame stabilized near the stagnation surface rotating at 300 rpm. The vertical solid lines indicate the location of max. OH-chemiluminescence.*

3.4.2 Flame structure

Figure 3.4 shows the steady-state solution for an undoped flame. The results are plotted with $z = 0$ being the location of the nozzle (as for all figures in this work). The stagnation surface is located at $z = 3.378$ cm, instead of 3.4 cm, in order to allow comparison with measurement and calculation done by Tolmachoff et al. [221].

Figure 3.4(a) shows the simulated temperature profile for an undoped flame as well as the experimental measurements and calculation reported by Tolmachoff et al. While the authors do not explicitly state whether the measurements are conducted with a doped or undoped flame, given that direct comparison is made with undoped flame simulations in their work, it is assumed here that the measurements are performed for an undoped flame. This is consistent with the current work as the simulated maximum temperature ($T_{max} = 2123.8$ K) shows an excellent agreement with the experiment ($T_{max} = 2124 \pm 50$ K). The simulated temperature profile also shows an acceptable agreement given the spatial uncertainty of the measurement.

A similar trend is shown for both experimental and simulated temperature profiles. Initially, the temperature is constant, equal to the gas temperature in the nozzle. At $z \sim 3.0$ cm the

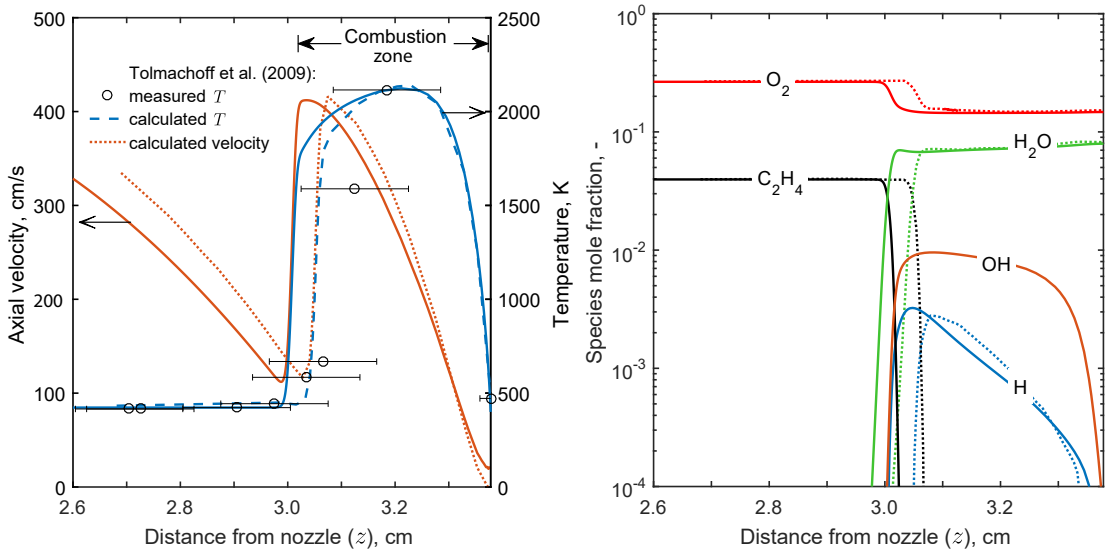

Figure 3.4: *Calculated undoped flame structure with $H = 1.27$ cm and $T_s = 400$ K: (a) Temperature and axial velocity profiles, (b) Major species mole fractions. The results form this work are shown with solid lines. The temperature measurement (symbol) and calculated flame structure from [221] are included (broken lines).*

temperature starts to increase sharply, reaching a maximum temperature at $z \sim 3.25$ cm. This high temperature region is subsequently referred to as the combustion zone. The width of the combustion zone is predicted to be slightly less than 0.4 cm which is consistent with the experimental observation. Near the stagnation surface, there is a rapid decrease in the temperature as a result of heat loss to the plate.

In doped flames, the decomposition of TTIP releases the gaseous fuel propene, C_3H_6. This results in an increasing maximum temperature with increasing TTIP loading (around 120 K difference between 0 and 1070 ppm). The effect of TTIP loading is discussed further in Section 3.4.5.

The axial velocity calculated in Fig. 3.4(a) is the total of the convective and thermophoretic velocities. The axial velocity initially decreases to 113 cm/s at $z = 3.0$ cm due to flow divergence. At the edge of the combustion zone, the axial velocity increases sharply as a result of the thermal expansion. It is noted that at the stagnation surface, the axial velocity is not zero (≈ 23 cm/s), corresponding to the thermophoretic velocity. The velocity profile calculation by Tolmachoff et al. only considers convective velocity and thus a zero velocity is shown at the stagnation surface.

Overall, the leading edge of combustion zone calculated by Tolmachoff et al. appears shifted ~ 0.5 cm closer to the stagnation surface compared to the current work. This suggests that

a computational distance, $H < 1.27$ cm is employed although no exact value is reported. Presumably, the peak of H atom concentration is used by Tolmachoff et al. to determine the flame location, in contrast to the assumption used in this work (see Section 3.4.1).

The calculated major species profiles are shown in Fig. 3.4(b). A similar shift towards the stagnation surface is observed for the calculated profiles by Tolmachoff et al. Both H and OH profiles start to increase sharply at $z = 3.0$ cm, where the temperature increases rapidly. It is noted that the H mole fraction reaches a maximum slightly before OH mole fraction, explaining the difference in computational distance employed by Tolmachoff et al.

Effect of rotation surface

This section examines the effect of the off-centered rotating disk on the flame structure. This is done by constructing a potential stagnation flow with similar axial velocity and temperature profiles to those of the simulated flame boundary layer in Fig. 3.4(a). The analytical solutions for an off-centered potential stagnation flow (assuming constant properties) on a rotating disk are available following the approach by Wang [233]. Thus, the effect of rotation on such flows can be easily assessed.

Potential flow on rotating stagnation boundary

Briefly, in a Cartesian coordinates (x, y, z) a potential flow impinges on a rotating disk along the z axis whose rotation axis is located at $x = b, y = 0$. The boundary conditions at the potential source ($z = \infty$) and on the surface ($z = 0$) are written as

$$u(\infty) = ax, \qquad v(\infty) = ay, \qquad w(\infty) = -2az, \qquad T(\infty) = T_1 \tag{3.48}$$

$$u(0) = -\Omega y, \qquad v(0) = \Omega(x-b), \qquad w(0) = 0, \qquad T(0) = T_0, \tag{3.49}$$

where (u, v, w) are the velocity components, T is the temperature which is only a function of z, a is the strength of the stagnation flow, and Ω is the angular velocity of the surface.

The following similarity transformations are introduced,

$$u = axf'(\eta) - \Omega y g(\eta) + b\Omega k(\eta) \tag{3.50}$$

$$v = ayf'(\eta) + \Omega x g(\eta) + b\Omega h(\eta) \tag{3.51}$$

$$w = -2\sqrt{a\nu} f(\eta) \tag{3.52}$$

$$\eta = \sqrt{a/\nu} z, \tag{3.53}$$

such that the governing equations are reduced to

$$f''' + 2ff'' - (f')^2 + \alpha^2 g^2 + 1 = 0 \tag{3.54}$$
$$g'' + 2fg' - 2gf' = 0 \tag{3.55}$$
$$h'' + 2fh' - hf' - \alpha kg = 0 \tag{3.56}$$
$$k'' + 2fk' - kf' + \alpha hg = 0 \tag{3.57}$$
$$T'' + 2\mathrm{Pr} fT' = 0, \tag{3.58}$$

where $\alpha = \Omega/a$, ν is the kinematic viscosity, and Pr is the fluid Prandtl number. The boundary conditions now become

$$f(0) = f'(0) = 0, \quad f'(\infty) = 1 \tag{3.59}$$
$$g(0) = 1, \quad g(\infty) = 0 \tag{3.60}$$
$$h(0) = 1, \quad h(\infty) = 0 \tag{3.61}$$
$$k(0) = 0, \quad k(\infty) = 0 \tag{3.62}$$
$$T(0) = T_0, \quad T(\infty) = T_1. \tag{3.63}$$

For a given α, the functions f and g are first solved from Eqs. 3.54 and 3.55 with the boundary conditions in Eqs. 3.59 and 3.60. Next, h and k are solved from Eqs. 3.56 and 3.57 with the boundary conditions in Eqs. 3.61 and 3.62. Finally the temperature profile T is solved from Eq. 3.58 with the boundary conditions in Eq. 3.63. Similar to Wang [233], shooting algorithms (tolerance level of $1 \times 10{-}6$) using Runge-Kutta numerical integration in MATLAB.

Deviation of the flame structure

Figure 3.5 shows the axial velocity and temperature profiles of a potential stagnation flow with $a = 1000\ \mathrm{s}^{-1}$, $T_0 = 400$ K and $T_1 = 2100$ K (no rotation, $\Omega = 0$). Here the thermal properties of air at 1000 K are assumed ($\mathrm{Pr} = 0.7092$ and $\nu = 1.133 \times 10^{-4}\ \mathrm{m^2\,s^{-1}}$). This is found to reasonably represent the flow structure of the simulated boundary layer, approximately 0.1 cm from the surface, from the full flame simulation.

Subsequently, the particle trajectories can be integrated from the solved velocity components taking into account the thermophoretic velocity according to Eq. 3.20. Figure 3.6 shows the trajectories for various α (or equivalently Ω) with the starting points at $z = 1$ mm. Here the rotation axis is located at $x = -120$ mm corresponding to the experimental setup of Tolmachoff et al. [221]. For non-rotating case (Fig. 3.6, left), the trajectories are symmetric

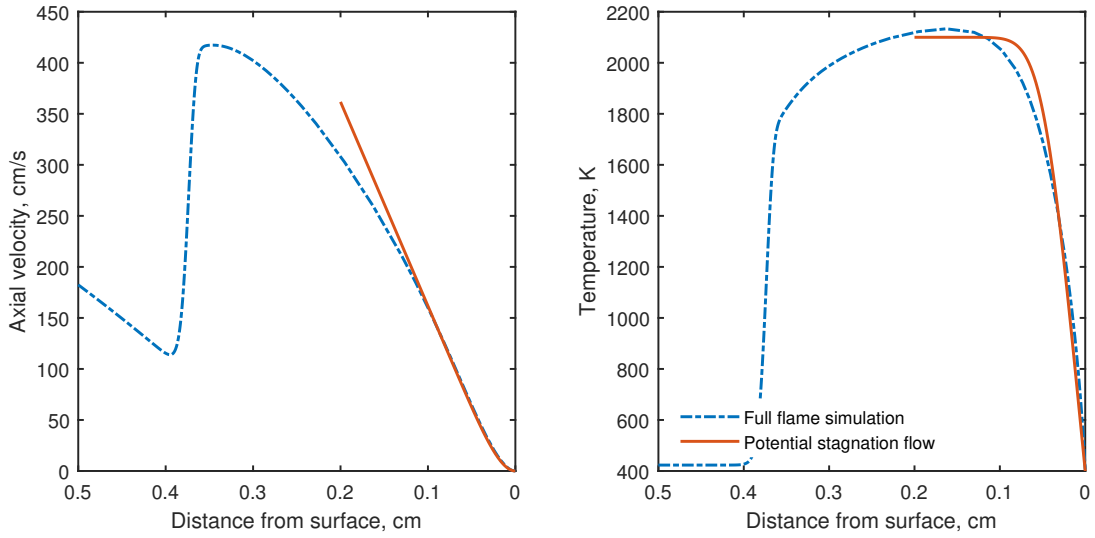

Figure 3.5: *Axial velocity (left) and temperature (right) profiles from the full flame simulation and the potential stagnation flow with* $a = 1000\ s^{-1}$, $T_1 = 2100\ K$, $\Omega = 0$ *(no rotation) to approximate the boundary layer (0.1 cm from the surface).*

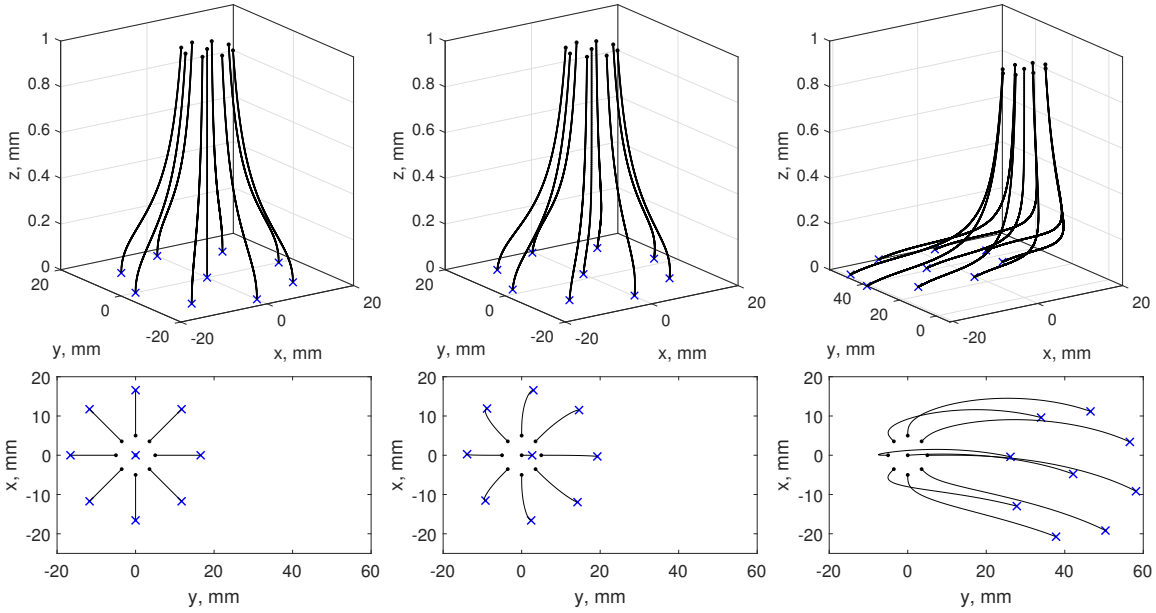

Figure 3.6: *The integrated particle trajectories (accounting for thermophoretic velocity) for* $\alpha = 0$ *(no rotation, left), 0.0314 (*$\Omega = 300$ *rpm, middle), 0.5 (*$\Omega = 4800$ *rpm, right). Top: 3D view, bottom: 2D view from* $+z$ *axis. The start points (at* $z = 1$ *mm) are denoted by black dots while the end points (at* $z = 0$ *mm) are denoted by blue crosses. The rotation axis is located at* $x = -120$ *mm similar to the set up used by Tolmachoff et al. [221].*

around the flow axis and diverging as the particles approach the surface. Due to the strong thermophoretic velocity near the surface, the particles are eventually deposited on the surface.

As α increases (Fig. 3.6, middle and right), the surface rotation results in an induced flow near the surface. As the 2D projection shows, the particle trajectories can be seen as a superposition of the diverging flow due to the stagnation flow and the rotation-induced shift on the xy plane.

As the residence time and temperature are highly relevant to the particle growth, the deviation of these quantities is quantified as a function of the rotation speed ($\alpha = \Omega/a$) in Fig. 3.7. Here the deposition time is defined as the particle residence time while the deposition temperature is the time-average temperature within the boundary layer ($0 \leq z \leq 1$ mm). Fig. 3.7 shows that the deviation of the deposition time and temperature increases as α increases (increasing rotation speed Ω or decreasing potential flow strength a). However, the deviation is negligible ($\approx 0.2\%$) for $\alpha < 0.3$. Here the rotating speed of 300 rpm (31.4 rad s^{-1}) corresponds to $\alpha = 0.0314$, denoted by the dashed line in Fig. 3.7, given $a = 1000$ s^{-1}.

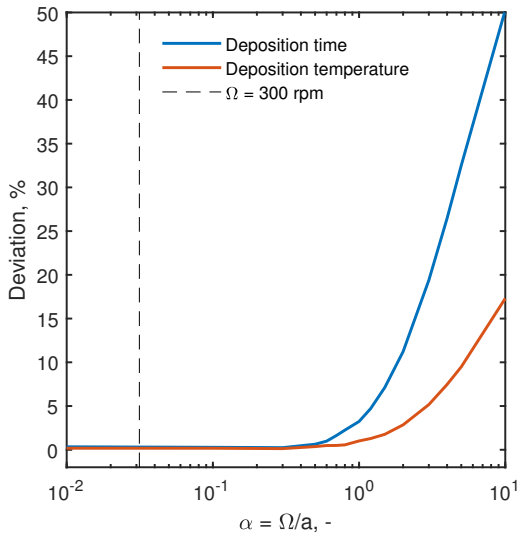

Figure 3.7: *Deviation in the deposition time and deposition temperature as a function of* α *relative to the non-rotating case* ($\alpha = 0$)*. The dashed line denotes* $\Omega = 300$ *rpm as used by Tolmachoff et al. [221].*

It is noted, however, that the potential stagnation flow assumption invoked in the analysis here implies an infinite flow cross section. When the flow is finite, as is the case in the actual experimental setup, entrainment of surrounding air induced by the rotating boundary is expected to be significant, affecting the deposition time and temperature. This is especially likely when the rotation rate is very high in which case the induced flow on xy plane results in significant shift of flow trajectories away from the potential source (the flame) as shown for $\alpha = 0.5$ in Fig. 3.6 (right panel). Thus, the deviation in Fig. 3.7 is best taken as a lower limit.

The effects of the air entrainment due to the finite flow corresponding to the same experimental conditions discussed here have recently been discussed by Hu et al. [94]. They performed a computational fluid dynamics (CFD) simulation of the flame used by Tolmachoff et al. [221] and analysed the deviation in the flame structure due to the air entrainment induced by the surface rotation. As the rotation speed increases, more air is entrained by the rotation and thereby affecting the flame temperature and particle residence time near the surface. Similar to the analysis here, the deviation is found to increase with increasing rotation speed or decreasing flame stretch rate (related to the stagnation flow strength discussed in this section). For the same flame conditions as discussed here, the average deviation for the case with $\Omega = 300$ rpm is estimated to be $\approx 0.2\%$ for deposition time and $\approx 1.0\%$ for deposition temperature (Fig. 13(b) in [94]). Therefore, the effect of the rotating boundary in this cases is not expected to be significant.

3.4.3 Particle moments and TTIP profiles

Figure 3.8 shows the evolution of particle size moments in the combustion zone. Before the combustion zone, the moments are virtually constant showing little to no particle processes occuring. The sharp increase in all particle moments, M_0–M_5, shows the formation of particles inside the combustion zone. Initially, all moments are similar in magnitude which is indicative of the nucleation of TiO_2 monomers. As the surface growth and coagulation rates increase, the higher order moments increase more sharply compared to the lower order moments. Near the stagnation surface, the higher order moments increase while the zeroth order moment, M_0, decreases slightly. This is due to the coagulation.

Similar to the particle moments, Fig. 3.8 shows that the TTIP mole fraction is constant before the combustion zone. The TTIP mole fraction decreases in the combustion zone as it is consumed by the inception and surface growth. Close to the stagnation surface ($z > 3.3$ cm), the TTIP mole fraction approaches zero, showing that TTIP is almost completely converted to TiO_2 in this region. This is expected considering the high temperature in the combustion zone.

3.4.4 Particle size and GSD

Tolmachoff et al. [221] shows that the particle size distributions follow a log-normal distribution for all TTIP loadings considered. The fitted particle size distribution is described by its median particle size, $\langle d_p \rangle$, and geometric standard deviation, GSD. In the current work, the

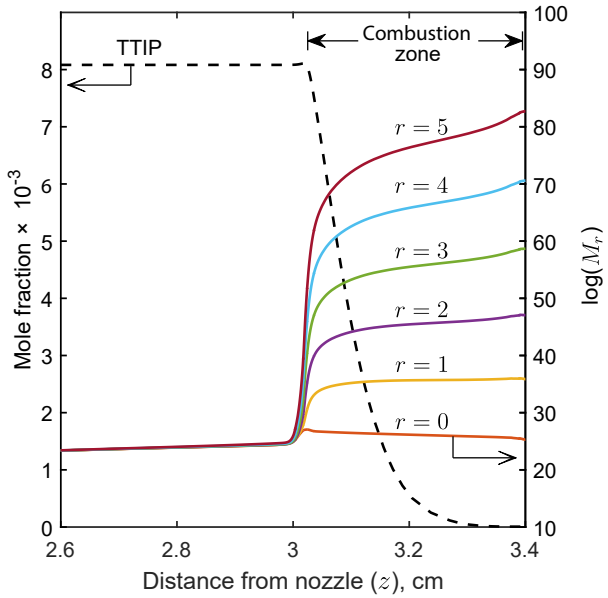

Figure 3.8: *Simulated particle moments, M_r, evolution (r = moments order) and TTIP mole fraction profiles for 1070 ppm TTIP loading ($H = 1.27$ cm, $T_s = 400$ K).*

parameters $\langle d_p \rangle$ and GSD are calculated using the following relations [162],

$$\langle d_p \rangle = \frac{d_p}{\sqrt{1 + \frac{\mathrm{SD}^2}{d_p^2}}} \tag{3.64}$$

$$\mathrm{GSD} = \exp\sqrt{\log\left(1 + \frac{\mathrm{SD}^2}{d_p^2}\right)}, \tag{3.65}$$

where d_p and SD are the mean and the standard deviation of the particle size distribution calculated from the reduced particle moments, respectively,

$$d_p = d_1 \mu_{\frac{1}{3}} \tag{3.66}$$

$$\mathrm{SD} = d_1 \sqrt{\mu_{\frac{2}{3}} - \mu_{\frac{1}{3}}^2}. \tag{3.67}$$

Before comparing the model predictions to the experimental data, it is important to consider two aspects of the experimental work performed by Tolmachoff et al. [221] which affect the particle size measurements, namely stagnation plate rotation and stagnation temperature.

The particle size measurements are reported for both stationary and rotating stagnation plate configurations, employing different particle sampling techniques. A scanning mobility

particle sizer (SMPS) is used to measure the particle mobility diameter in stationary stagnation plate cases with the sampling probe mounted inside the plate. On the other hand, a transmission electron microscopy (TEM) sample collected using a rapid insertion probe is used to measure the primary particle diameter in the rotating stagnation plate cases.

The rotation, combined with four equally spaced cold jets placed at the back of the stagnation plate, is intended to cool the stagnation surface. With a total cooling jet volumetric flow of 40 l/min, the stagnation plate temperature, T_s, is shown to be stabilized at ~ 400 K for the rotational speed in the range 100–600 rpm. Without rotation (i.e. 0 rpm), the absence of convective cooling leads to T_s reaching as high as ~ 1000 K although no measurements are reported.

Non-rotating stagnation surface

Taking into account the lack of convective cooling, the temperature of the stationary stagnation surface is assumed to be 1000 K. The simulated particle median size at the stagnation surface ($\delta_s = 0$) with $T_s = 1000$ K, presented in Fig. 3.9(a), shows a good agreement with the experimental data. For ease of comparison, the simulated and experimental $\langle d_p \rangle$ and GSD for the five TTIP loadings tested are also presented in Table 3.1. In general, the particle size is predicted to increase as a function of the TTIP loading.

Table 3.1: *Simulated and experimental median size, $\langle d_p \rangle$, and geometric standard deviation, GSD, assuming $T_s = 1000$ K. (experimental data is taken from Tolmachoff et al. [221])*

TTIP	Experimental data		Simulation result	
(ppm)	$\langle d_p \rangle$, nm	GSD	$\langle d_p \rangle$, nm	GSD
10	4.6	1.19	3.4	1.25
29	6.0	1.21	4.5	1.26
96	7.3	1.29	6.2	1.28
306	8.9	1.34	8.6	1.32
1070	13.0	1.47	12.5	1.35

A similar trend is also observed for particle GSD in Fig. 3.9(b), both in the model prediction and experiment. It is noted that for high TTIP loading, the model underpredicts the particle GSD. This underprediction appears especially significant due to the narrow particle size distributions where the GSD is extremely sensitive to distribution width. This is illustrated in Fig. 3.10, where the log normal density functions for the measured and simulated distributions for $T_s = 1000$ K are compared. It shows a relatively insignificant difference in the

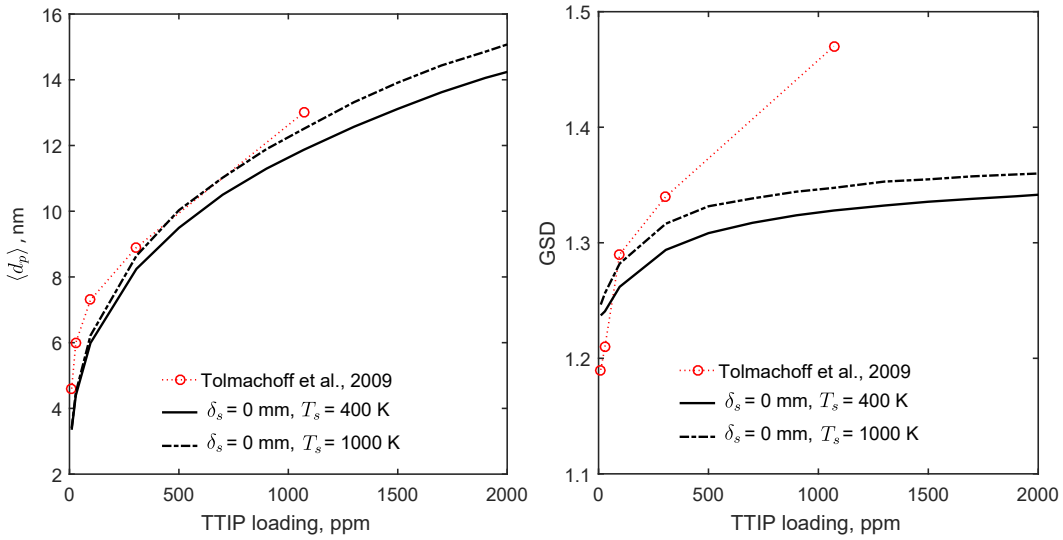

Figure 3.9: *Simulated (a) median and (b) GSD as a function of TTIP loading and surface temperature, T_s at stagnation plate, i.e. $\delta_s = 0$ ($H = 1.27$ cm). Experimental mobility sizes [221] ($L = 3.4$ cm) are shown as a function of TTIP loading for stationary stagnation plate case.*

distribution width given the difference in the GSD. The difference in the GSD can also be interpreted as due to the formation of small aggregated particles which are not accounted for in the spherical model.

Rotating stagnation surface

Tolmachoff et al. show that there is a substantial decrease in primary particle size measured with TEM analysis for the rotating cases compared to the mobility particle size measured with SMPS for stationary case. For instance, in a 1070 ppm TTIP flame, TEM analysis gives median primary particle diameter of 8.5–9.8 nm for 100–600 RPM rotation while SMPS measurement gives median mobility particle diameter of 13 nm. This comparison, however, can only be made under the assumption of complete coalescence of particles, i.e. primary particle diameter is equal to mobility-derived diameter.

Assuming that a complete coalescence occurs, Tolmachoff et al. suggested that the difference can be explained by the difference in the stagnation surface temperature between the rotating and stationary surface cases. Figure 3.9 shows the predicted median particle size and GSD for surface temperature of 400 K. It is shown that there is indeed some decrease in particle

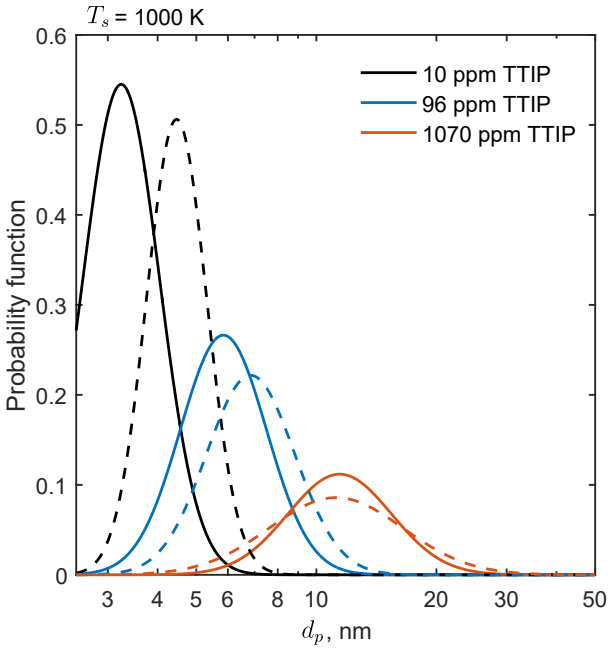

Figure 3.10: *Log-normal probability functions for model prediction (solid lines) and experimental data (dashed lines) for varying TTIP loading.*

size as the surface temperature decreases but it does not seem to be enough to explain the significant discrepancy in the measured particle size.

It is possible that the decrease in the measured particle size is a consequence of a significant level of aggregation in the flame. Compared to the stationary stagnation cases, the gas temperature near the plate for the rotating cases is expected to be significantly lower. This results in a slower particle sintering relative to coagulation, leading to the formation of aggregates. In this case, a more detailed particle model is required to fully capture the effects of aggregation. The presence of aggregation, however, is not directly confirmed in the experiment. The extent of the aggregation and its implications on the interpretation of the experimental data will be investigated in the Chapter 4.

3.4.5 Sensitivity to process variables

Precursor loading

Figure 3.11(a) shows the simulated temperature profiles with varying TTIP loading. Increasing TTIP loading from 10 to 1070 ppm increases $T_{\max}$ from 2130 K to 2240 K due to the release of C_3H_6. Thus, a slight increase in the thermophoretic velocity near the stagnation

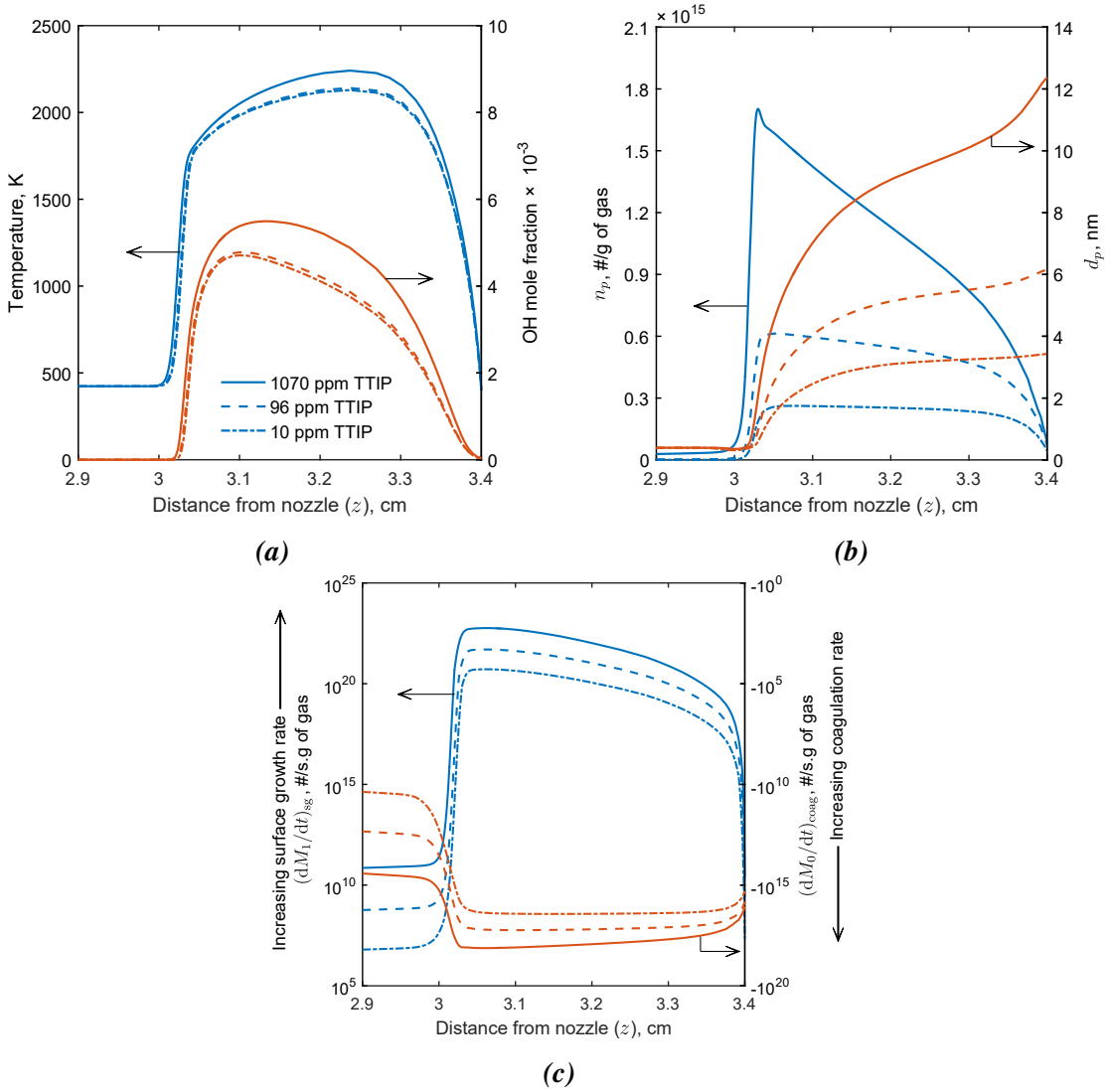

Figure 3.11: *Simulation results with varying precursor loading (10, 96, 1070 ppm TTIP, $H = 1.27$ cm): (a) Temperature and OH mole fraction profiles, (b) mean particle size, d_p, and particle number concentration, n_p, evolution along the flame, and (c) steady-state source terms for M_0 due to coagulation and M_1 due to surface growth.*

surface is expected. The combustion zone and OH profile are slightly broadened, which results in small shifts in the initial temperature increase and OH peak locations. The shift in the OH peak location is from 3.10 to 3.13 cm.

Figure 3.11(b) shows the mean particle size, d_p, and the particle number concentration, n_p. The number concentration, n_p, is normalized by the gas density, ρ, to remove the effect of volume expansion. Initially, n_p increases sharply due to the inception of TiO_2 monomers, especially for high TTIP loading. This is followed by a gradual decrease for high TTIP

loading while almost constant n_p for low TTIP loading. For all cases, d_p increases most sharply at the upstream edge of the combustion zone, at $z \sim 3$ cm, and also near the stagnation surface.

It is noted that the initial growth region in Fig. 3.11(b) starts at around 0.4 cm from the stagnation surface, earlier than that suggested by Tolmachoff et al. [221]. Tolmachoff et al. assume that after the temperature reached 1850 K (at ~ 0.3 cm from stagnation surface), TTIP undergoes a rapid decomposition into Ti atoms which are oxidized and then nucleate. This is in contrast with the kinetically-limited decomposition model employed in this work (Section 3.2.3) and other studies [203, 224]. As a consequence of using this reaction model, the simulated nucleation and surface growth coincide with the onset of the initial temperature increase at the leading edge of the flame (Fig. 3.11(a), ~ 0.4 cm from the stagnation surface). In addition, the difference in modelling assumptions used to determine the computational distance (see Section 3.4.1) results in a slight shift of the flame edge in this work compared to the calculation by Tolmachoff et al.

Figure 3.11(c) compares the coagulation and surface growth rates in the combustion zone. Similar to n_p, the rates are also normalized with ρ. Note that the coagulation rate has the opposite sign to $\mathrm{d}M_0/\mathrm{d}t$ because M_0 decreases with coagulation. As the temperature increases rapidly in the combustion zone, both the surface growth and coagulation rates increase sharply (note the log-scale) because of the high concentration of TiO_2 monomers. As expected, the rates increase with increasing TTIP loading. In this region, the surface growth rate is a few orders of magnitude higher than the coagulation rate. This indicates that surface growth is important in the initial stage of the particle growth.

As the particles flow downstream ($z = 3.05 - 3.35$ cm), the coagulation and surface growth rates decrease due to the consumption of TiO_2 monomers and TTIP, respectively. This is also shown by the steady decrease of n_p and the slower increase in d_p in Fig. 3.11(b).

Near the stagnation surface ($z > 3.35$ cm), both surface growth and coagulation rates start to decrease more sharply due to the steep decrease in the temperature. The surface growth rate decreases much faster than the coagulation rate (surface growth rate drops from 10^{20} to 10^{10} while coagulation rate drops from 10^{17} to 10^{16} /s.g of gas for 1070 ppm loading). Therefore, coagulation becomes more dominant compared to surface growth in this region. This could explain the apparent faster increase in d_p and decrease in n_p for higher TTIP loading.

The coagulation-dominated growth in this region leads to a sensitivity of the particle size to the sampling location near the stagnation surface, which increases with increasing TTIP loading.

Stagnation temperature, T_s

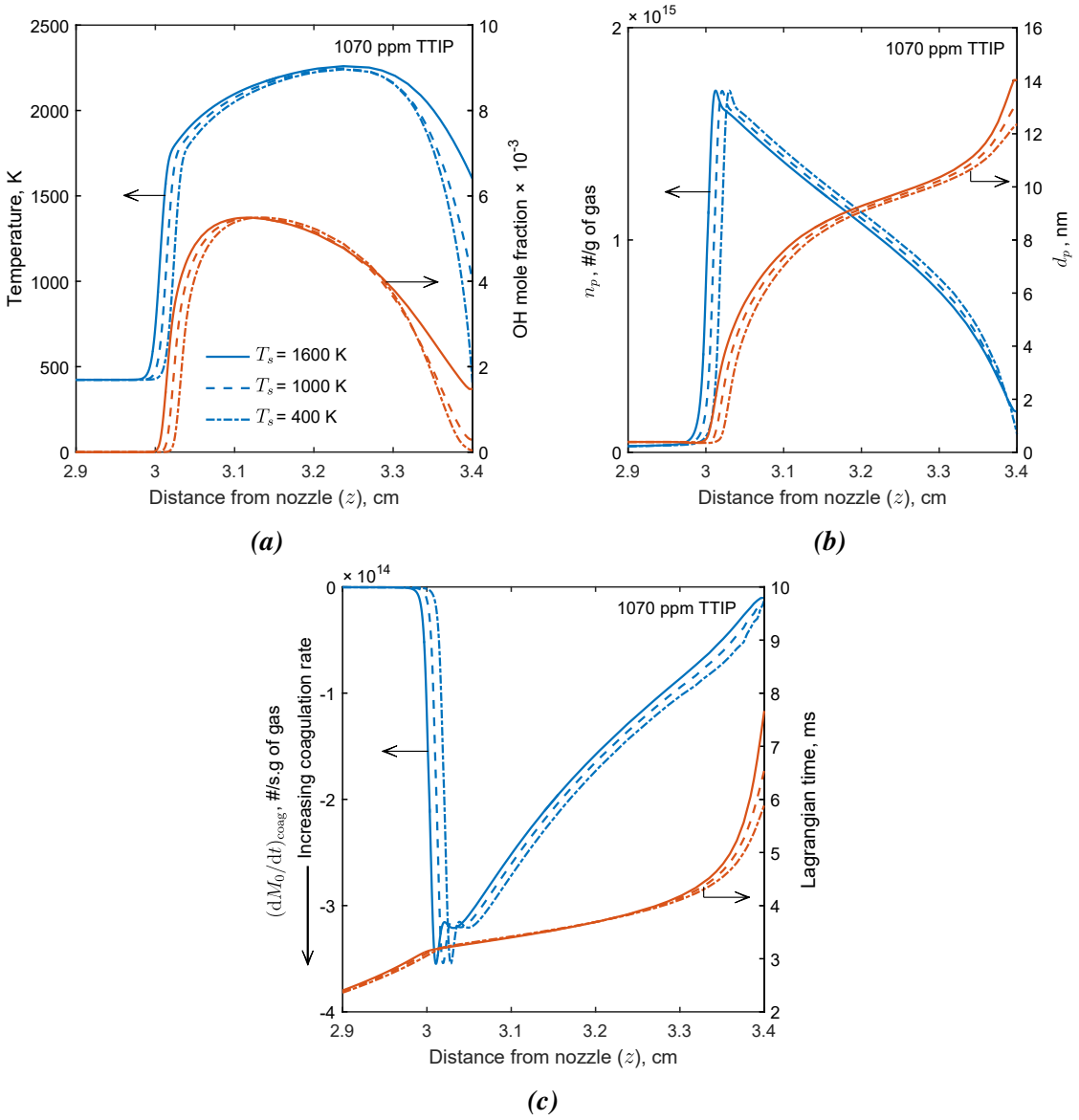

Figure 3.12: *Simulation results with varying stagnation temperature, T_s (400, 1000, and 1600 K), with $H = 1.27$ cm: (a) Temperature and OH mole fraction profiles, (b) mean particle size, d_p, and particle number concentration, n_p, evolution along the flame, and (c) steady-state source terms for M_0 due to coagulation and calculated Lagrangian particle time.*

In order to evaluate the effect of the stagnation temperature, the cases with $T_s = 400$, 1000, and 1600 K are simulated for 1070 ppm TTIP loading. The results are shown in Fig. 3.12.

Figure 3.12(a) shows that increasing T_s broadens the temperature and OH profiles and significantly reduces the temperature gradient near the stagnation surface. $T_{\max}$ increases slightly (2241 K for $T_s = 400$ K, 2260 K for $T_s = 1600$ K) due to the smaller heat loss to the plate. The location of the OH peak shifts slightly from $z = 3.12$ to 3.13 cm (for $T = 400$ and 1600 K, respectively).

As described previously, the nucleation initially dominates at the start of the combustion zone, followed by the surface growth and coagulation. Figure 3.12(b) shows a slight shift in the start of the combustion zone. This leads to an earlier increase (and the subsequent decrease) of n_p for higher T_s. Thus, at $z \sim 3.3$ cm, n_p is lowest for $T_s = 1600$ K (also for coagulation rate in Fig. 3.12(c)).

Near the stagnation surface ($z > 3.3$ cm), there is a sharper increase in d_p for higher T_s despite the lower coagulation rate, as shown in Fig. 3.12(c). This is explained by examining the particle time history near the stagnation surface, calculated from the total of convective and thermophoretic velocities. Higher T_s leads to smaller thermophoretic velocity and consequently, longer residence time near the stagnation surface. As a result, the spatial sensitivity of the particle size is expected to be larger for a higher T_s. A similar trend is also observed for the other TTIP loading.

3.4.6 Role of surface growth

It has been demonstrated that coagulation plays an important role in the post flame region near the stagnation surface. In this section, the role of the surface growth is evaluated by comparing the reaction model described in Section 3.2.3 with a reaction model that assumes no surface growth [161]. Without surface growth, the nucleation rate is equal to the overall TTIP decomposition rate. The gas-phase composition and temperature profiles are identical in both models because of the equal rate of C_3H_6 release, which is governed by the overall reaction rate.

Figure 3.13(a) presents the particle size evolution along the flame for both models (with 96 ppm TTIP loading, $T_s = 400$ K). It shows that without surface growth, the particle size is significantly smaller at all locations in the combustion zone. The most important difference is in the initial growth region at the upstream edge of the combustion zone, which shows a more gradual increase of d_p without surface growth compared to the steep increase of d_p with surface growth. This highlights the important role of surface reaction in the initial growth stage.

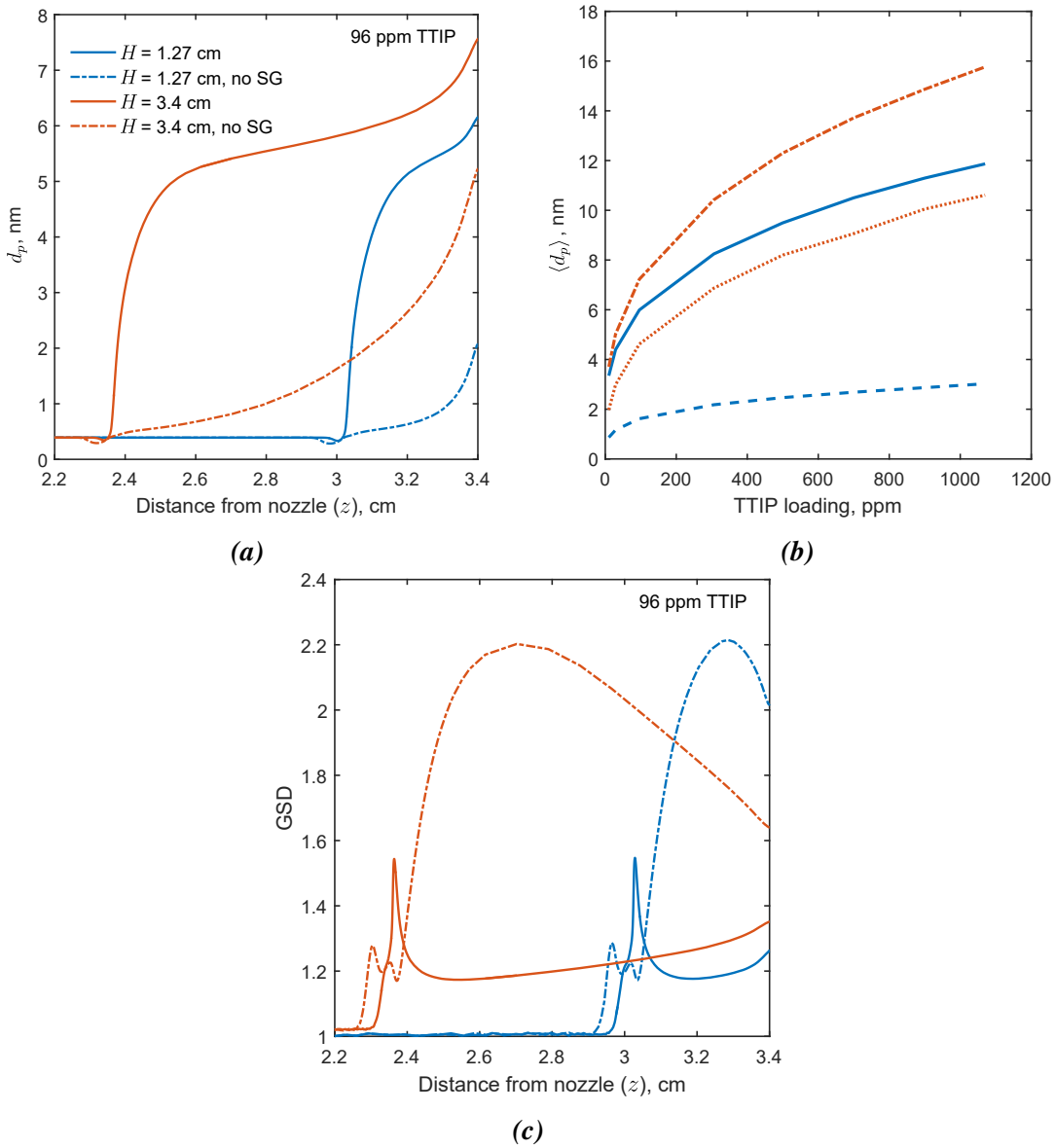

Figure 3.13: *Simulation results with and without surface growth with nozzle-stagnation surface separation distance, H, of 1.27 and 3.4 cm: (a) Mean particle size, d_p, evolution along the flame, (b) median particle size, $\langle d_p \rangle$, at the stagnation surface as function of TTIP loading, and (c) geometric standard deviation, GSD, evolution along the flame.*

Eventually, the slower growth of the particles at the upstream edge of the combustion zone leads to an underprediction of the particle size at the stagnation surface ($z = 3.4$ cm). Figure 3.13(b) shows the particle sizes at $z = 3.4$ cm with and without surface growth for different TTIP loadings, showing a similar trend for all loadings considered in this work.

Figure 3.13(c) shows the calculated GSD profiles for all cases considered by assuming a log-normal distribution. However, in the initial growth region ($z \sim 2.4$ cm for $H = 3.4$ cm and $z \sim 3$ cm for $H = 1.27$ cm) the particle distribution is not expected to follow a log-normal distribution. This results in an unexpected behaviour as shown by peaks and oscillations in the inception region. For the model with surface growth, further growth of particles after the inception region proceeds mainly through surface growth, which explains the slower increase in particle GSD. In contrast, for the model with no surface growth, the particles grow only through coagulation, resulting in rapid increase in the particle GSD (widening of particle distribution). Eventually, the GSD decreases to approach the GSD of a self-preserving size distribution [120]. The calculated GSDs at the stagnation surface indicate significantly broader particle size distribution functions, PSDFs, (with GSD > 1.5) when surface growth is neglected. This is inconsistent with the experimental observation [221].

The original simulations using the model without surface growth by Modak et al. [161] appear to yield a good agreement with experimental data. However, these simulations are performed without correcting the computational distance related to the free-jet region. As discussed earlier in Section 3.4.1, the simulation with $H = 3.4$ cm leads to a significantly wider combustion zone. As a result, the slower particle growth is compensated by the longer particle residence time.

It is noted that the importance of the surface reaction in the initial particle growth stage has been predicted in a study by Tsantilis et al. [224] (for a premixed flat burner). However, particle sampling close to the flat burner face (< 0.5 cm), where particles are newly incepted, is not feasible. In contrast, a stagnation burner configuration allows an experimental investigation of the initial particle growth stage where the masking effect of coagulation is minimized. This results in a high sensitivity to surface growth. Hence, the FSRS setup is a good candidate to investigate the TTIP decomposition kinetics and test more detailed TiO_2 formation models.

3.5 Chapter summary

A spherical particle model describing TiO_2 formation in a stagnation flame reactor is developed by assuming a simple one-step TTIP decomposition reaction and a complete coalescence. In order to compare the simulation results with experimental data, it is important to account for the existence of the free-jet region in the flow. In this work, this is done by matching the location of the simulated OH peak with the experimentally observed flame location. The computational distance used in this work is 1.27 cm.

In general agreement with the experimental observation, the simulated average particle size and standard deviation increase with increasing TTIP loading and stagnation temperature. The model successfully reproduced the average particle sizes measured with a stationary stagnation surface, with $L = 3.4$ cm, as functions of TTIP loading although some discrepancy in the particle GSDs is observed. If complete coalescence and negligible effect of rotation on the flow are assumed, the simulated particle sizes with $T = 400$ K significantly overpredict the particle sizes obtained from the rotating surface experiments. This suggests the presence of a significant aggregation in the rotating surface cases or that the effects of the surface rotation on the flow are not captured in this model.

Coagulation is shown to be a dominant process near the stagnation surface. This leads to a high spatial sensitivity of the particle size to the sampling location near the stagnation surface for high TTIP loading. The sensitivity increases with increasing stagnation temperature because of the longer particle residence time near the stagnation surface.

Further, surface growth is found to play an important role during the initial particle growth at the leading edge of the flame. With decreasing length of combustion zone, surface growth becomes increasingly more important than coagulation in overall. This leads to the formation of particles with a narrow size distribution and a high sensitivity to surface growth. These characteristics make the stagnation flame reactor an attractive experimental tool to investigate and improve on the scarce kinetic data available in literature on TTIP decomposition.

Chapter 4

Morphology of TiO_2 nanoparticles prepared in a stagnation flame

In this chapter, a detailed morphological characterisation is performed on flame synthesised TiO_2 nano-aggregates using transmission electron microscopy (TEM) image analysis and mobility measurements. The size-dependent collection efficiency of the TEM sampling method is accounted for with a simple correction for particle deposition through impaction and diffusion. The TEM-derived sizes show excellent agreement with electrical mobility measurements. Primary particle size, aggregate size, and degree of aggregation distributions are obtained for two different flames and varying precursor loading. The analysis reveals some particle aggregation which is likely to occur only very late in the growth stage, leading to the similarity between the primary particle and spherical particle size distributions. The size distributions are found to be strongly affected by precursor loading but not by flame mixture or maximum temperature. In all cases, approximately 60–70% particles are spherical while the rest form small aggregates. The results are compared to the detailed model predictions. The model is subsequently used to investigate the sensitivity of particle properties to the measurement uncertainties.

4.1 Background

The previous chapter demonstrates the use of a simple particle model to study the TiO_2 nanoparticle formation in a stagnation flame synthesis. While the low dimensionality of the

model allows for easier coupling with the gas chemistry and flow dynamics, the simple description of particle morphology precludes the investigation of processes such as aggregation and sintering.

Using a post-processing methodology recently developed by Lindberg et al. [132], a particle model with a more extensive description of particle structure can be used to resolve the morphology and thus to understand how the particle morphology is affected by various process variables. In the detailed particle model [134], particles are represented as aggregates consisting of connected primary particles which resemble the actual structure of particles in experiments. Thus, the morphological properties can be derived without making assumptions such as the particle size distribution shape. The detailed particle model, however, necessitates a detailed experimental characterisation of particle morphology to properly evaluate the model parameters.

As discussed in the previous chapter, Tolmachoff et al. [221] performed measurements of TiO_2 particles prepared in a stagnation flame reactor and found some discrepancy between particle sizes measured with TEM and a mobility sizer. The authors attributed this discrepancy to the difference in sampling conditions based on the assumption that the particles are spherical. Nevertheless, it is possible that some aggregation occured in the gas phase, as evidenced from the TEM images, resulting in larger mobility sizes. Resolving such morphological information is essential in order to properly interpret the experimental data and evaluate computational models.

The purpose of this chapter is to investigate the morphology of small flame-synthesised TiO_2 aggregates using TEM image analysis and mobility measurements. The analysis allows a quantification of the degree of aggregation in the nanoparticles prepared which explains the discrepancy between TEM derived and mobility sizes reported previously [221]. In this work, varying operating conditions, including temperature and precursor loading, are chosen to evaluate their effects on the synthesised particle morphology, such as primary particle size and the degree of aggregation. The results are compared to the detailed model predictions which reveals a good agreement.

4.2 Experimental details

4.2.1 Flame reactor

Figure 4.1 shows a schematic of the premixed laminar stagnation flame used in this study. Briefly, an aerodynamic nozzle (1.4 cm exit diameter) generated a premixed laminar jet that impinged on a water-cooled stagnation plate. Upon ignition, a thin flame was formed and stabilised by stretch above the stagnation plate. The setup used here is similar to that used in previous studies of titania and soot formation [221, 155, 42].

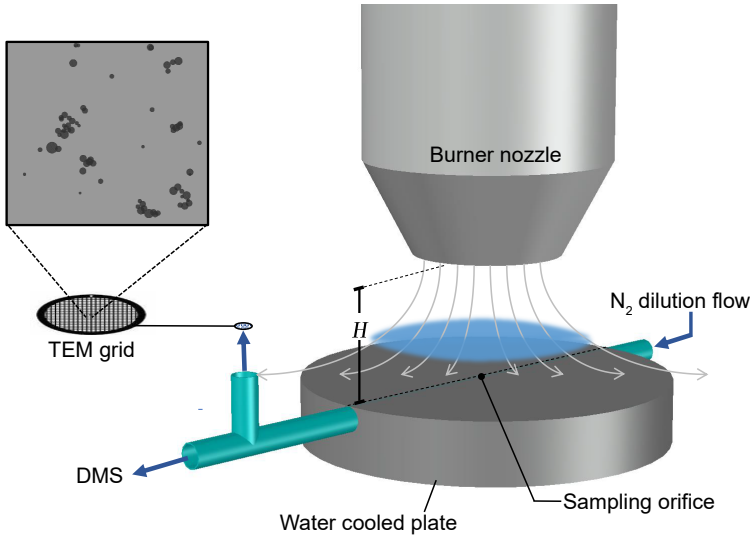

Figure 4.1: *Schematic of the premixed laminar stagnation flame synthesis and particle sampling method used in this study. The burner-stagnation surface separation distance, H, is 1 cm.*

Two different flames were employed in this study with equivalence ratios of $\phi = 0.35$ (3.5% C_2H_4–30% O_2–66.5% Ar) and $\phi = 1.67$ (10.3% C_2H_4–18.5% O_2–71.2% Ar), corresponding to fuel-lean and fuel-rich conditions, respectively. The two different flames were used to investigate the effect of flame temperature with the rich flame being approximately 450 K hotter than the lean flame based on the calculated adiabatic flame temperature ($T_{ad} = 2073$ K and 2542 K, respectively).

The total gas flowrate was 28 standard litre per minutes (slpm), corresponding to 436 cm/s burner exit velocity, with a N_2 sheath flowrate of 20 slpm. The burner-surface separation, H, was 1 cm. The surface temperature, measured with a K-type thermocouple, was stabilised at 503±20 K ($\phi = 0.35$) and 580±20 K ($\phi = 1.67$). For each flame, titanium tetraisopropoxide

(TTIP, Sigma Aldrich, 97%) was injected into the gas line with a syringe pump (Cole-Parmer) at loading rates of 4, 12, and 30 ml/h (corresponding to 194, 582, and 1455 ppm of TTIP). The gas line was heated to 150°C to prevent precursor condensation. Previous studies have shown that the particles synthesised in the lean flame are mainly anatase while particles prepared in the rich flame are mainly rutile [155, 135].

A temperature measurement was performed for the lean flame ($\phi = 0.35$) using the thermocouple scanning method ($d = 75$ μm, S-type, P10R-003, Omega Engineering). In addition, flame photographs are taken with a digital camera (EX-ZR5000, Casio) for flame distance estimation, approximately 3.2±0.2 mm ($\phi = 0.35$) and 4.0±0.2 mm ($\phi = 1.67$). A more detailed description is given Appendix B.5.

4.2.2 Particle characterisation methods

Post-flame gas was sampled through a 0.2 mm orifice on a horizontal sampling probe inside the stagnation plate as shown in Fig. 4.1. The static pressure drop across the orifice was maintained at 4 ± 0.5 mbar under atmospheric pressure. A nitrogen flow of 36 l/min (STP) was used to quench the sampled gas to minimise further reactions after sampling and particle losses due to coagulation and wall deposition. Downstream from the sampling orifice, a needle valve and vacuum pump system was configured to allow 8.5 slpm of the diluted flow to pass to a DMS500 (Cambustion Ltd.) for electrical mobility size measurements.

Simultaneously, the remaining diluted gas was passed through a TEM grid (HC400-Cu, Electron Microscopy Sciences) mounted perpendicular to the flow within the sample line where particles were deposited and subsequently imaged for analysis. The holey carbon grids were chosen to allow sufficient particle collection for analysis. The sampling time for each measurement was 10–15 s. TEM micrographs were obtained with a JEOL JEM-2100F operating at 200 keV.

A more detailed description of the sampling system and the results of the sampling dilution tests are given in Appendices B.1 and B.3.

4.3 Computational details

The stagnation flame is simulated using a two-step methodology as illustrated in Fig. 4.2. In the first step, the flame is modelled using a one-dimensional stagnation flow approximation, coupled to a detailed gas-phase chemistry and a simple population balance model solved

using the method of moments with interpolative closure (MoMIC). This is similar to the methodology outlined in Chapter 3 except a detailed TTIP decomposition mechanism and different inception and surface growth models are used here.

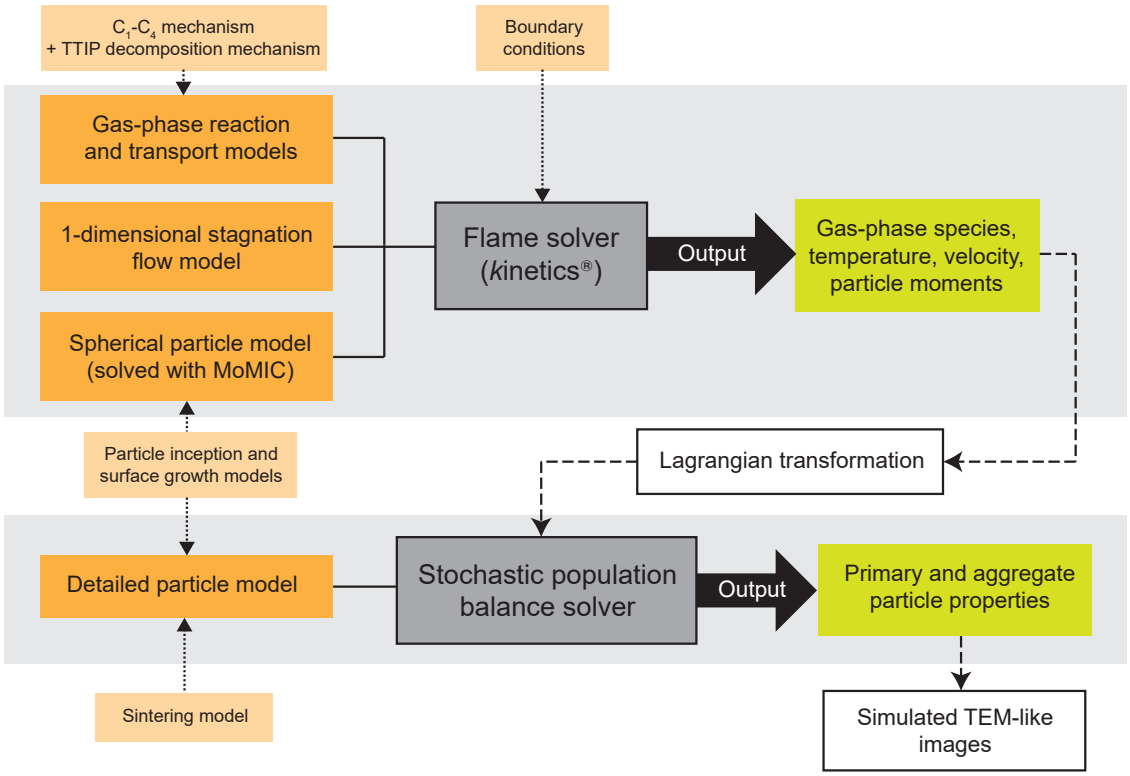

Figure 4.2: *A schematic of the modelling method used in this chapter. The grey boxes denote the general model frameworks.*

In the second step, a stochastic population balance solver is used to post-process the simulation results from the first step. A detailed particle model is implemented in the solver which resolves the detailed morphology of the particles. A detailed description of the two-step methodology has been given by Lindberg et al. [132].

4.3.1 Flame simulation

Gas-phase chemistry model

The chemical reaction model consists of a TTIP decomposition mechanism combined with hydrocarbon combustion chemistry described by the USC-Mech II model [234]. The TTIP mechanism contains 25 Ti species and 61 reactions, and describes the decomposition of

TTIP to titanium (IV) hydroxide ($Ti(OH)_4$) through the C_3H_6 and CH_3 abstraction pathways identified by Buerger et al. [34] as well as dissociation reactions of $Ti(OH)_4$ as proposed by Shmakov et al. [203] which are assumed to be barrierless.

Particle inception and surface growth

In the previous chapter, a simple one-step decomposition mechanism of TTIP as proposed by Tsantilis et al. [224] was assumed for both inception and surface growth. While the model was shown to be successful in reproducing the experimentally measured particle sizes, the simple model does not contain any description of precursor decomposition to species other than TiO_2. A more detailed mechanism with elementary reactions is required to study the effect of the synthesis conditions on particle composition/stoichiometry which may be of interest for TiO_2 synthesis (this is discussed in Chapter 6). In this chapter, the particle inception and surface growth reactions are modelled as collision-limited processes (with collision rates from the kinetic theory of gases) with $Ti(OH)_4$ as the collision species. The inception (in) and surface growth (sg) reactions can be written as

$$2\,Ti(OH)_4 \xrightarrow{k_{in}} (TiO_2)_2 + 2\,H_2O \tag{4.1}$$

$$Ti(OH)_4 + (TiO_2)_i \xrightarrow{k_{sg}} (TiO_2)_{i+1} + H_2O, \tag{4.2}$$

where the rates k_{in} and k_{sg} are the inception and surface growth rates.

The rate k_{in} can be calculated by the free molecular collision kernel,

$$k_{in} = \varepsilon \sqrt{\frac{\pi k_B T}{m_{Ti(OH)_4}}} (2 d_{Ti(OH)_4})^2, \tag{4.3}$$

where $m_{Ti(OH)_4}$ and $d_{Ti(OH)_4}$ are the mass and collision diameter of $Ti(OH)_4$, ε is the collision enhancement factor taken as 2.64 [264], k_B is the Boltzmann constant, and T is the temperature. The collision diameter is taken from the optimised geometry calculated in [35], $d_{Ti(OH)_4} = 0.5128$ nm. The moment source term due to inception, $\dot{M}_r^{in}$, can be written as

$$\dot{M}_r^{in} = \frac{1}{2} k_{in} C_{Ti(OH)_4} N_A 2^r \text{ for } r \geq 0, \tag{4.4}$$

where $C_{Ti(OH)_4}$ is the molar concentration of $Ti(OH)_4$, and N_A is the Avogadro constant. The factor 2^r comes from the fact that each inception reaction adds 2 units of TiO_2 to the particle.

The rate k_{sg} is estimated using the free-molecular coagulation rate between spherical particles of size i and j [73], in which $Ti(OH)_4$ is approximated by a spherical particle containing 1 TiO_2 unit, i.e. $j = 1$. Assuming $i \gg j$,

$$k_{sg} = K_f \sqrt{\frac{1}{i} + \frac{1}{j}} (i^{1/3} + j^{1/3})^2 \approx K_f i^{2/3}, \tag{4.5}$$

where K_f is given by Eq. 3.31, i is the size of the particle involved in the surface growth. Similar to Eq. 3.23, the moment source term due to surface growth, $\dot{M}_r^{sg}$, can now be written as

$$\dot{M}_r^{sg} = \begin{cases} 0 & \text{for } r = 0 \\ C_{Ti(OH)_4} N_A K_f \sum_{k=0}^{r-1} \binom{r}{k} \mu_{k+\frac{2}{3}} M_0 & \text{for } r \geq 1, \end{cases} \tag{4.6}$$

where M_r and μ_r are the r-th order moment and fractional moment (see Eqs. 3.12 and 3.13).

Boundary conditions

The one-dimensional stagnation flow formulation invokes a constant eigenvalue assumption which is only valid for a specific set of conditions [27, 100]. This results in the predicted flame front being shifted compared to the experiments. This can be circumvented by imposing the boundary conditions – if these are known – near the flame instead of at the nozzle exit as done by Bergthorson and Dimotakis [18]. Alternatively, Bouvet et al. [27] show that the 1D solution approximates the 2D solution when an appropriate radial velocity gradient (or jet spreading rate) at the nozzle exit is imposed to recover the same flame front position as in the 2D simulation.

The same approach is used here in which the boundary conditions are specified according to the experimental conditions and appropriate axial velocity gradients are chosen to reproduce the experimental flame standing distance for each case. An arbitrary assumption is made in this work to define the experimental standing distance using the location of the point at which the flame intensity is half of the maximum intensity (Appendix B.5). This is shown to coincide with the simulated peak of H concentration for the undoped $\phi = 0.35$ flame when the flame distance is constrained by the temperature measurement – this is discussed further in Section 4.5.5. Thus the jet spreading rates are adjusted to match the simulated peak of H concentration with the flame distance estimated from the flame photographs for all other cases.

The boundary conditions including burner exit temperature (T_0), velocity (u_0), velocity gradient (a_0), and the plate temperature (T_s) are summarised in Table 4.1.

Table 4.1: *Boundary conditions imposed at nozzle exit (1 cm) and stagnation surface.*

Case	T_0 (K)	u_0 (cm/s)	a_0 (1/s)	T_s (K)
$\phi = 0.35$, undoped	423.15	436	-245	503
$\phi = 0.35$, 4 ml/h TTIP	423.15	436	-230	503
$\phi = 0.35$, 12 ml/h TTIP	423.15	436	-185	503
$\phi = 0.35$, 30 ml/h TTIP	423.15	436	-99	503
$\phi = 1.67$, undoped	423.15	436	-185	580
$\phi = 1.67$, 4 ml/h TTIP	423.15	436	-185	580
$\phi = 1.67$, 12 ml/h TTIP	423.15	436	-215	580
$\phi = 1.67$, 30 ml/h TTIP	423.15	436	-280	580

4.3.2 Stochastic population balance simulation

A comprehensive description of the detailed particle model and the numerical methods are presented elsewhere [134], so only a brief summary is given here. At the end of the simulation, detailed descriptors of primary particles and aggregates, as well as TEM-like images are generated.

Detailed particle model

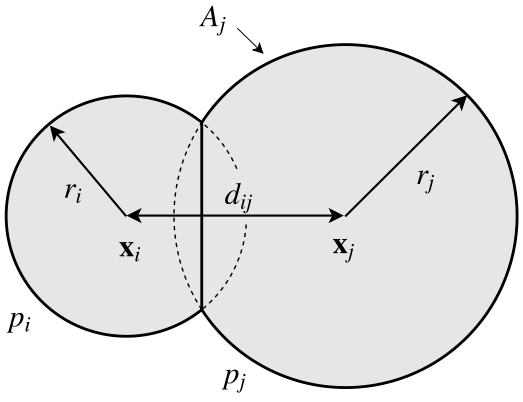

Figure 4.3: *An illustration of the detailed particle model type space.*

The type space of the detailed particle model is illustrated in Fig. 4.3. The type space is the mathematical description of a particle. An aggregate particle is composed of polydisperse

primary particles modelled as overlapping spheres. Each primary particle, p_i, is characterised by its composition η_i, radius r_i, and position of the primary centre $\mathbf{x}_i$. The degree of overlap between two neighbouring primaries, p_i and p_j, is then resolved by their centre to centre separation, $d_{ij} = |\mathbf{x}_i - \mathbf{x}_j|$.

Inception and surface growth processes are modelled according to the models implemented in the flame solver (see above).

An aggregate is formed when two particles stick together as a result of a collision. The rate of collision is calculated using the transition regime coagulation kernel [177]. The orientations of the colliding particles and point of contact following the collision are determined by a ballistic cluster-cluster aggregation with a random impact parameter [101].

Neighbouring primaries undergo sintering in which the primary centres approach each other, increasing their overlap. The mass of each individual primary is conserved by increasing the primary radii. The sintering model follows the approach of Eggersdorfer et al. [63] with the rate evaluated using a grain boundary diffusion model. Once sufficiently sintered, two primaries are assumed to coalesce to form a single primary. The threshold for coalescence is chosen to be

$$\frac{R_{ij}}{r_i} > 0.95, \tag{4.7}$$

where R_{ij} is the neck radius and $r_i \leq r_j$. It should be noted that the particle model does not distinguish between liquid and solid states. Consequently, the sintering process is applied even above the melting temperature of particles – conditions under which two particles would be expected to coalesce immediately upon collision. This liquid-like behaviour is achieved through rapid sintering kinetics arising from the temperature and size dependence of the modelled sintering rate, which is discussed in the next section.

Following Eggersdorfer et al. [63], the rate of change in primary centre to neck distance is

$$\frac{\mathrm{d}x_{ij}}{\mathrm{d}t} = -\frac{d_p^4}{16\tau A_{\mathrm{n},ij}}\left(\frac{1}{r_i - x_{ij}} - \frac{1}{R_{ij}}\right), \tag{4.8}$$

where x_{ij} is the distance from the centre of primary p_i to the neck formed with neighbour p_j, d_p is the primary diameter, taken as the smaller of the two primary diameters, $d_p = \min(d_p(p_i), d_p(p_j))$, τ is the characteristic sintering time, $A_{\mathrm{n},ij}$ is the neck area, R_{ij} is the neck radius and r_i is the radius of the primary p_i. The characteristic time τ (in seconds) is given by

$$\tau = 9.11 \times 10^{17} d_p^4 T A_s \exp\left(\frac{258\,\mathrm{kJ\,mol^{-1}}}{RT}\left(1 - \left(\frac{d_{p,\mathrm{crit}}}{d_p}\right)^{\alpha_{\mathrm{crit}}}\right)\right), \tag{4.9}$$

where d_p is the primary diameter (in nm), R is the ideal gas constant, T is the temperature (in K), A_s, $d_{p,\text{crit}}$, and α_{crit} are sintering model parameters fitted to the characteristic sintering time calculated by Buesser et al. [36]. The values for parameters A_s, $d_{p,\text{crit}}$, and α_{crit} are 0.25, 2.5 nm, and 7, respectively.

Numerical methods

The gas-phase profiles, supplied as input to the population balance simulation, are expressed in terms of the residence time of a Lagrangian particle travelling from the burner to stagnation plate using the combined convective and thermophoretic velocities. To account for the effect of thermophoretic transport near the stagnation surface, a thermophoretic correction is introduced to the post-process through a modified simulation sample volume scaling term. The thermophoretic correction has been discussed by Lindberg et al. [132].

A stochastic numerical method is used in the second step to solve the population balance equations. The method employs a direct simulation algorithm [201] with a majorant kernel and fictitious jumps [82, 177] to improve the computational speed of calculating the coagulation rate, and a linear process deferment algorithm [178] to provide an efficient treatment of sintering and surface growth. Simulation results are averaged over 4 runs, each with 8192 stochastic particles.

4.4 Image analysis

The image analysis procedures for primary particle size distribution and aggregate size distributions were performed on images from the same TEM samples but taken at different magnifications and locations on the grid. The carbon film on the TEM grid contains holes with varying sizes and densities. For primary particle analysis, the images are taken at areas with high density of holes that has the "lacy" appearance. This results in high particle concentration and better contrast. For aggregate analysis, the images are taken at areas with low density of holes such that it is possible to have a complete film coverage, i.e. no holes, on the TEM images. This is to ensure a low particle concentration to minimise overlap and to allow image processing algorithm as described below.

For primary particle size analysis, approximately 20–30 images with 150,000× magnification were used (0.13 nm/pixel resolution) with minimum particle count of approximately 1100 (see Table 4.6). For aggregate size analysis, magnifications of 80,000× (0.24 nm/pixel),

60,000× (0.32 nm/pixel), and 40,000× (0.47 nm/pixel) were used for 4, 12, and 30 ml/h TTIP loading cases, respectively. The different magnifications were chosen to maintain a similar pixel count per particle across the TTIP loadings tested. Approximately 100 images per sample were used with minimum particle count of approximately 1500 (see Table 4.7).

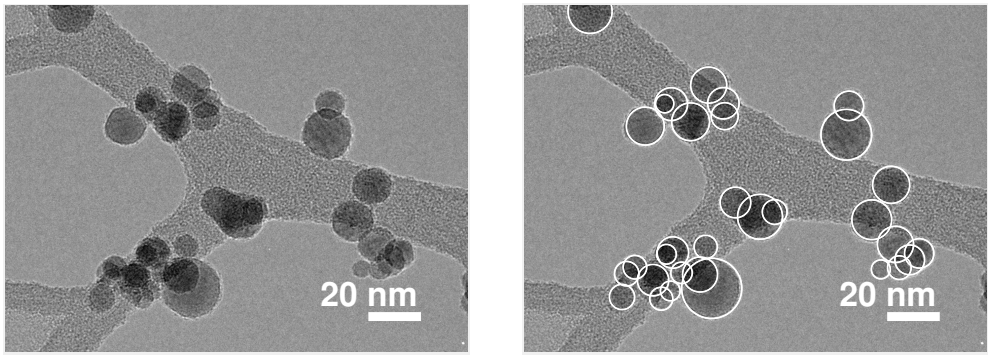

(a) *A TEM image with 150,000× magnification.*

(b) *An annotated image showing spherical primary particles.*

Figure 4.4: *TEM images showing primary particle size measurement procedure employed ($\phi = 1.67$, 30 ml/h TTIP loading rate).*

Primary particle size analysis For primary particle size analysis, the measurement of primary particle diameter, d_p, was performed using a MATLAB user interface by specifying the center of the sphere and a point on the circumference manually. The uncertainty of the measured d_p from manual measurement is estimated to be ± 2 pixel or ± 0.25 nm. Figure 4.4 shows an example of TEM images with the spherical primary particles annotated. Due to the limited resolution of the TEM imaging, only particles larger than 3 nm were clearly distinguishable and measured. The average diameter ($\overline{d}_p$), Sauter mean diameter ($\overline{d}_{32}$), standard deviation (SD), and geometric standard deviation (GSD) were calculated for each case as follows,

$$\overline{d}_p = \frac{1}{N}\sum_{i=1}^{N} d_{p,i} \tag{4.10}$$

$$\overline{d}_{32} = \frac{\sum_{i=1}^{N} d_{p,i}^3}{\sum_{i=1}^{N} d_{p,i}^2} \tag{4.11}$$

$$\mathrm{SD} = \sqrt{\frac{1}{N-1}\sum_{i=1}^{N} |d_{p,i} - \overline{d}_p|^2} \tag{4.12}$$

$$\mathrm{GSD} = \exp\sqrt{\frac{1}{N}\sum_{i=1}^{N}\left(\ln\frac{d_{p,i}}{\mu_g}\right)^2}, \tag{4.13}$$

where $d_{p,i}$ is the spherical equivalent diameter of an individual primary particle, N is the total number of primary particles measured, and μ_g is the geometric mean of the measured data set $\{d_{p,1}, d_{p,2}, ..., d_{p,N}\}$.

Aggregate size analysis The projected area analysis for aggregates is performed for both experimental TEM images and simulated TEM-like images. The image analysis algorithm is described in Appendix B.4.

From the aggregate analysis, a data set $\{\mathbf{P}_1, \mathbf{P}_2, ..., \mathbf{P}_N\}$ was obtained where $\mathbf{P}_i$ contains a list of coordinates of the constituent pixels of aggregate i: $\{(x_{i,1}, y_{i,1}), (x_{i,2}, y_{i,2}), ..., (x_{i,L}, y_{i,L})\}$. The projected spherical equivalent diameter ($d_{\mathrm{sph},i}$) and the projected diameter of gyration ($d_{g,i}$) of aggregate i were calculated as follows,

$$d_{\mathrm{sph},i} = 2s\sqrt{\frac{L}{\pi}} \tag{4.14}$$

$$d_{g,i} = s\sqrt{\frac{1}{L}\sum_{j=1}^{L}\left(|x_{i,j} - \overline{x_i}|^2 + |y_{i,j} - \overline{y_i}|^2\right)} \tag{4.15}$$

$$(\overline{x_i}, \overline{y_i}) = \frac{1}{L}\sum_{j=1}^{L}(x_{i,j}, y_{i,j}), \tag{4.16}$$

where s is the image scale factor (nm per pixel) and L is the total number of pixels for aggregate i. Additionally, a parameter α_i was defined as the ratio of $d_{g,i}$ to $d_{\mathrm{sph},i}$, which is indicative of the degree of aggregation of an analysed particle. A projected sphere, i.e. circle, has a characteristic $\alpha = \sqrt{1/2} \approx 0.71$, while for a projected dimer with no overlap, $\alpha = \sqrt{3/4} \approx 0.87$. However, calculation of radius of gyration according to Eq. 4.15 tends to be an overestimate for a pixelated circle with less than 100 pixels and thus the value of α is expected to be slightly larger than 0.71 for a projected sphere (this is discussed further in Section 4.5.3). The average aggregate projected area, $\overline{d}_{\mathrm{sph}}$, and the average projected aggregate gyration diameter, $\overline{d}_g$, were calculated as follows,

$$\overline{d}_{\mathrm{sph}} = \frac{1}{N}\sum_{i=1}^{N} d_{\mathrm{sph},i} \tag{4.17}$$

$$\overline{d}_g = \frac{1}{N}\sum_{i=1}^{N} d_{g,i}, \tag{4.18}$$

where N is the total number of aggregates identified in the analysis.

The projected diameter gyration, d_g, calculated in Eq. 4.15 is not equivalent to the actual diameter of gyration, d_g^{3D}, typically used in the literature. For fractal aggregates with fractal dimension, $D_f > 2$, the following relationship applies [39]

$$d_g^{3D} = \left(\frac{2D_f}{D_f+2}\right)^{1/2} d_g. \tag{4.19}$$

This equation implies a correction factor of 1.095 for a compact sphere (number of primary particles, $N = 1$, $D_f = 3$). For $N = 2$, assuming no particle screening, both gyration sizes are exact and can be derived analytically ($d_g^{3D} = \sqrt{8/5}d$, $d_g = \sqrt{3/2}d$, d = primary diameter) resulting in a correction factor of 1.033, equivalent to $D_f = 2.3$ according to Eq. 4.19. For mature aggregates with $D_f \leq 2$, typical for soot, Sorensen and Feke [208] calculated a conversion factor of 1.023. In this work, TEM images (as discussed later) show a significant proportion of particles with N ranging from 1 to 4. As shown above, the conversion factor shows dramatic change from $N = 1$ (sphere) to $N = 2$ (dimer) while for larger aggregates, this conversion factor is almost constant [207, 208]. Thus the conversion to the actual gyration diameter would introduce significant additional uncertainty in this work due to the large variance in the particle fractal dimension. In addition, for the purpose of defining the particle morphology, the value of α calculated with the projected diameter of gyration is sufficient (see Section 4.5.3). For these reasons, the conversion of the gyration sizes is not performed here.

4.5 Results and discussion

4.5.1 Sampling line transport efficiency

Due to the diffusive particle loss to the wall, the transport efficiency, η, of the sampling system is less than unity and is particle size-dependent [32]. The transport efficiency with diffusive particle loss in a pipe is given as

$$\eta = \exp\left(-\frac{\pi D L_{\text{pipe}}}{Q}\text{Sh}\right), \tag{4.20}$$

where D is the particle diffusion coefficient, L_{pipe} is the pipe length, Q is the volumetric flow rate through the tube, and Sh is a dimensionless Sherwood number. The diffusion coefficient

D is given as

$$D = \frac{k_B T C_c}{6\pi\mu r}, \tag{4.21}$$

where k_B is the Boltzmann constant, T is the temperature, μ is the gas dynamic viscosity, r is the particle radius. C_c is the Cunningham slip correction factor given by

$$C_c = 1 + \mathrm{Kn}(1.257 + 0.4\exp(-1.1/\mathrm{Kn})), \tag{4.22}$$

where Kn is the Knudsen number defined as λ/r and λ is the mean free path of the gas molecules.

The Sherwood number is given for different flow regimes as a function of Reynolds number ($\mathrm{Re} = U d_{\mathrm{pipe}}/\nu$, U: fluid velocity, d_{pipe}: inner pipe diameter ν: fluid kinematic viscosity) and Schmidt number ($\mathrm{Sc} = \nu/D$) as follows [93, 76]

$$\mathrm{Sh} = \begin{cases} 3.66 + \dfrac{0.0668\frac{d_{\mathrm{pipe}}}{L_{\mathrm{pipe}}}\mathrm{ReSc}}{1 + 0.04\left[\frac{d_{\mathrm{pipe}}}{L_{\mathrm{pipe}}}\mathrm{ReSc}\right]^{2/3}} & \text{for } \mathrm{Re} < 3000 \\ 0.0118\mathrm{Re}^{7/8}\mathrm{Sc}^{1/3} & \text{for } \mathrm{Re} \geq 3000. \end{cases} \tag{4.23}$$

Figure 4.5 shows a simplified schematic of the sampling manifold between the sampling orifice and DMS inlet and TEM sampler. The transport efficiencies for the the DMS and

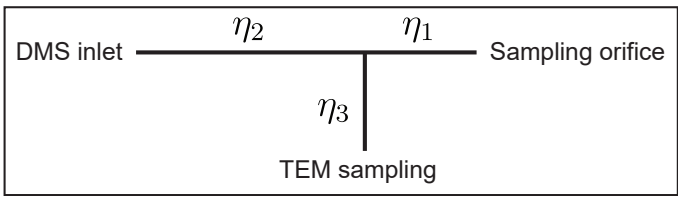

Figure 4.5: *A simplified schematic of the sampling manifold (detailed description of the experimental setup is given in Appendix B.1). The transport efficiencies, η, of different sections are labelled.*

TEM measurements can be calculated as follows

$$\eta_{\mathrm{DMS}} = \eta_1 \eta_2 \tag{4.24}$$

$$\eta_{\mathrm{TEM}} = \eta_1 \eta_3, \tag{4.25}$$

where the subscripts 1, 2, and 3 correspond to the transport efficiencies for different sections of the sampling manifold. These sections are characterised by their length and volumetric flow rates: $L_{\text{pipe},1} = 23$, $L_{\text{pipe},2} = 67$, $L_{\text{pipe},3} = 21$ cm, $Q_1 = 36$, $Q_2 = 9$, $Q_3 = 27$ lpm (STP). The pipe diameter, d_{pipe}, is 6 mm. The gas temperature is 40°C and the kinematic viscosity of N_2 is used, $\nu = 17.16 \times 10^{-6}$ m^2 s^{-1}. The gas mean free path is 70.9 nm (for N_2).

The calculated transport efficiencies η_{DMS} and η_{TEM} are shown in Fig. 4.6. These transport efficiencies are subsequently used to correct for the size-dependent particle diffusion losses of the DMS and TEM-derived size distributions in the following sections.

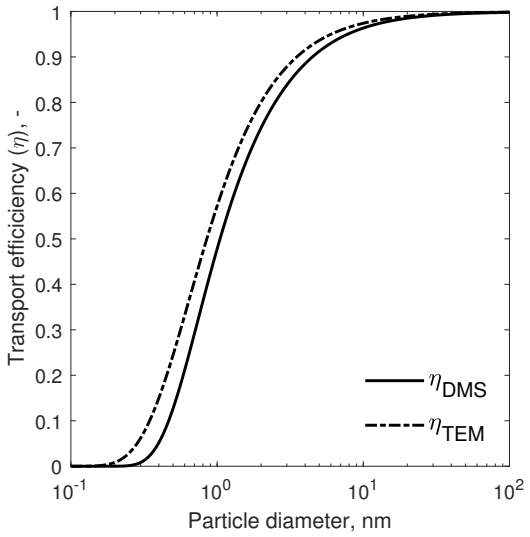

Figure 4.6: *Calculated transport efficiencies (η) for DMS and TEM sampling.*

4.5.2 Validation of TEM sampling methodology

The TEM sampling methodology employed in this work is different from the thermophoretic sampling commonly used for in-situ particle sampling [8, 26, 10]. Instead of thermophoresis, the particle deposition here relies on two main physical mechanisms, namely inertial impaction and Brownian diffusion as the sample flows through the holey TEM grid suspended perpendicular to the flow direction. It is assumed that interception can be ignored here given the size of the holes on the TEM grid is typically much larger than the particles [190].

Due to the size dependency of inertial impaction and Brownian diffusion, it is necessary to perform a correction to the particle size distributions obtained using this methodology. However, as demonstrated below, the narrow size distribution produced with the stagnation flame configuration combined with the high sampling flow velocity results in a minimal

correction. In this section, the overall collection efficiency of the holey TEM is estimated using a similar approach used by Ogura et al. [170]. Subsequently, the corrected particle size is validated by comparison with the electrical mobility diameter measured with the DMS.

Correction for TEM collection efficiency

Taking into account Brownian diffusion and inertial impaction, assuming both mechanisms act independently, the overall collection efficiency, E, can be expressed as

$$E = 1 - (1 - E_{\mathrm{D}})(1 - E_{\mathrm{I}}), \tag{4.26}$$

where E_{D} is the collection efficiency due to Brownian diffusion, and E_{I} is the collection efficiency due to inertial impaction.

Brownian diffusion The collection efficiency due to particle diffusion to the front surface of a filter can be calculated using an expression proposed by Manton [139],

$$E_{\mathrm{D}} = 1 - \exp\left(\frac{-\alpha_1 \mathrm{Pe}^{-2/3}}{1 + (\alpha_1/\alpha_2)\mathrm{Pe}^{-7/15}}\right) \tag{4.27}$$

$$\alpha_1 = 4.57 - 6.46 P_{\mathrm{grid}} + 4.58 P_{\mathrm{grid}}^2 \tag{4.28}$$

$$\alpha_2 = 4.5, \tag{4.29}$$

where Pe is the Peclet's number given by $\mathrm{Pe} = D_0 U_0 / D$, D_0 is the grid hole diameter, D is the diffusion coefficient (given in Eq. 4.21), U_0 is the frontal velocity, P_{grid} is the grid porosity, α_1 and α_2 were determied from a least-squares fitting for $0.05 < P_{\mathrm{grid}} < 0.64$.

Inertial impaction The collection efficiency due to particle impaction is calculated using a formulation proposed by Pich [180] as follows,

$$E_I = \frac{2\varepsilon_I}{1+\xi} - \left(\frac{\varepsilon_I}{1+\xi}\right)^2 \tag{4.30}$$

$$\varepsilon_I = 2\mathrm{Stk}\sqrt{\xi} + 2\mathrm{Stk}^2\xi \exp\left(-\frac{1}{Stk\sqrt{\xi}}\right) - 2\mathrm{Stk}^2\xi \tag{4.31}$$

$$\xi = \frac{\sqrt{P_{\mathrm{grid}}}}{1 - \sqrt{P_{\mathrm{grid}}}}, \tag{4.32}$$

where Stk is the Stokes number given by

$$\mathrm{Stk} = \frac{4\rho_s r^2 U_0 C_c}{9\mu D_0}, \tag{4.33}$$

and ρ_s is the particle density.

Table 4.2: *Parameters used for size-dependent collection efficiency calculation.*

Parameters	Short description	Value	Notes
λ	Mean free path	70.9 nm	N_2 at 313.15 K, 1 atm
μ	Gas dynamic viscosity	1.85×10^{-5} kg/m/s	N_2 at 313.15 K
ρ_s	Anatase density	3780 kg/m^3	For $\phi = 0.35$
	Rutile density	4250 kg/m^3	For $\phi = 1.67$
T	Gas temperature	313.15 K	Experimental condition
U_0	Face velocity	7 and 14 m/s	Experimental condition
D_0	Hole diameter	1.67 μm	[190]
P_{grid}	Grid porosity	0.4	[190]

In this analysis, the particle size is assumed to be equal to the spherical equivalent size from projected area analysis, i.e. $2r = d_{\mathrm{sph}}$. This assumption is a valid approximation given that the particles observed on the TEM are mostly single primaries with some small aggregates (discussed further in Section 4.5.3). The parameters used in the calculation of TEM grid collection efficiency (Eq. 4.26) are given in Table 4.2. The face velocity is approximately 14 m/s, estimated from the total flow rate flowing through the filter (27 lpm) and the tube cross-section area (32 mm^2). However, the actual face velocity is likely to be lower due to flow divergence on the TEM surface. As an estimate, two different face velocities are tested here, 14 and 7 m/s. The hole diameter and grid porosity are taken from Ref. [190] for a typical holey carbon grid. The density of anatase is used for particles prepared in $\phi = 0.35$ flames while density of rutile is used for $\phi = 1.67$ [155].

The calculated collection efficiency, E, is shown in Fig. 4.7(a). The TEM-derived particle size distributions ($\mathrm{PSD}_{\mathrm{TEM}}$) are then calculated as

$$\mathrm{PSD}_{\mathrm{TEM}} = \frac{\mathrm{PSD}_{\mathrm{TEM,expt}}}{\eta_{\mathrm{TEM}} E}, \tag{4.34}$$

where $\mathrm{PSD}_{\mathrm{TEM,expt}}$ is the aggregate size distribution from the TEM image analysis and η_{TEM} is the sampling transport efficiency given in Eq. 4.25.

In order to demonstrate the effect of this correction across the conditions studied in this work, the median spherical-equivalent particle sizes, $\langle d_{\mathrm{sph}} \rangle$, for $\phi = 0.35$ flame, before and

after correction, are plotted in Fig. 4.7(b). It is noted that the correction is relatively small, especially for small TTIP loadings which is due to the narrow particle distributions. In addition, the correction seems to be almost insensitive to the choice of the face velocity. Subsequently, a similar correction with $U_0 = 7$ m/s is applied to all TEM aggregate particle size distributions presented in this work. This correction, however, is not applied for primary particle size distributions as the collection efficiency is a function of the aggregate size.

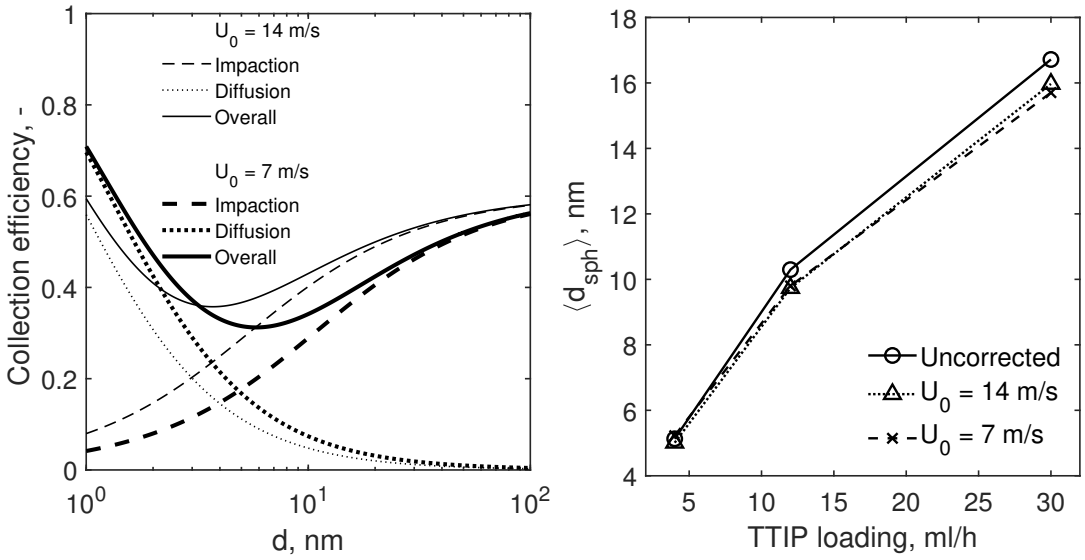

Figure 4.7: *(a) The collection efficiencies calculated based on Eqs. 4.26, 4.27, and 4.30 with face velocities, U_0, of 7 and 14 m/s (thick and thin lines, respectively), using anatase density. (b) The median spherical-equivalent particle sizes, $\langle d_{sph} \rangle$, before and after collection efficiency correction for $\phi = 0.35$ flames. The lines are added as a visual aid.*

Comparison with electrical mobility measurements

The DMS500 used in this study was calibrated at the factory against a differential mobility analyzer (DMA). Here, calibration for spherical particles with a monomodal distribution was used. The Stokes-Cunningham formula for electrical mobility, Z, used with the DMA, is given by

$$Z/q = \frac{C_c}{6\pi\mu r}, \tag{4.35}$$

where q is the charge in the particle. The empirical Stokes-Cunningham formula is typically consistent with Eipstein's formula assuming a diffuse scattering model. However, it has

been shown that in the limit of Kn $\gg 1$, the mobility particle size based on the Stokes-Cunningham formula tends to be over-predicted by 10–20% compared to particle size from electron microscopy due to increasing influence of long-range potential forces on particle scattering [192, 117, 129].

Li and Wang [128] suggests a generalised expression that accounts for gas-particle interactions in Kn $\gg 1$ limit,

$$Z/q = \frac{3}{8}\frac{1}{\sqrt{2\pi m_r k_\mathrm{B} T N_g r^2 \Omega_{\mathrm{avg}}^{(1,1)^*}}} \tag{4.36}$$

$$\Omega_{\mathrm{avg}}^{(1,1)^*} = \varphi\Omega_{\mathrm{d}}^{(1,1)^*} + (1-\varphi)\Omega_{\mathrm{s}}^{(1,1)^*}, \tag{4.37}$$

where m_r is the reduced mass of the gas molecule, m_g, and particle, m_p, such that $m_r = m_g m_p/(m_g + m_p)$, N_g is the gas number density given by ρ_g/m_g, ρ_g is the gas density. φ is the empirical momentum-accommodation function given by

$$\varphi = \frac{1 + 0.9\mathrm{Kn}\{1 - 1/[1 + (r/\beta)^{15}]\}}{1 + \mathrm{Kn}}, \tag{4.38}$$

where $\beta = 2.5$ nm. $\Omega_{\mathrm{d}}^{(1,1)^*}$ and $\Omega_{\mathrm{s}}^{(1,1)^*}$ are reduced collision integrals, parameterised as functions of σ', a non-dimensionalised collision diameter, and T^*, a modified reduced temperature. The parameters σ' and T^* are related to the Lennard-Jones 12-6 parameters, i.e. well depth, ε, and collision diameter, σ, for the interaction between a fluid molecule and a constituent atom or molecule of the particle, as follows,

$$\sigma' = \frac{\sigma}{r} \tag{4.39}$$

$$T^* = \frac{3V k_\mathrm{B} T}{2\pi\varepsilon\sigma^3}, \tag{4.40}$$

where V is the effective volume of the particle per molecule given by $\bar{M}/\rho_\mathrm{s}$, $\bar{M}$ is the mean atomic mass of particle material, and ρ_s is the mass density of the particle. The interaction potential parameters, σ and ε, can be estimated from the combination rules $\sigma = (\sigma_g + \sigma_s)/2$ and $\varepsilon = \sqrt{\varepsilon_g \varepsilon_s}$, where subscripts g and s denote the gas molecule and particle molecule or atom.

The parameters σ_s and ε_s for TiO_2 are estimated using the melting point, T_m, and the mass density at melting point, ρ_{s,T_m}, of TiO_2, such that $\varepsilon_s = 1.92 k_\mathrm{B} T_m$, and $\sigma_s = \sqrt[3]{1.8\bar{M}/\rho_{s,T_m}}$ [192]. Here the melting point of TiO_2 is taken as 2250 K and the density at melting point is 3210 kg/m^3 [7]. The parameters used in this section are summarised in Table 4.3. Similar to

the TEM collection efficiency correction, the density of anatase is used for particles prepared in $\phi = 0.35$ flames while density of rutile is used for $\phi = 1.67$ [155]. The working pressure and temperature of the DMS500 used in this analysis are 250 mbar and 50°C.

Table 4.3: *Parameters used for mobility size correction.*

Parameters	Short description	Value	Notes
μ	Gas viscosity	1.89×10^{-5} kg/m/s	N_2 at 323.15 K
λ	Mean free path	294 nm	N_2 at 323.15 K, 250 mbar
ε_g/k_B	L-J 12-6 parameter	98.4 K	N_2 [129]
σ_g	L-J 12-6 parameter	3.652 Å	N_2 [129]
ε_s/k_B	L-J 12-6 parameter	4320 K	TiO_2
σ_s	L-J 12-6 parameter	4.193 Å	TiO_2
m_g	Gas molecule mass	28.0 g/mol	N_2
ρ_g	Gas density	0.261 kg/m^3	N_2 at 323.15 K, 250 mbar
$\bar{M}$	Particle mass	79.9 g/mol	TiO_2
ρ_s	Anatase density	3780 kg/m^3	For $\phi = 0.35$
	Rutile density	4250 kg/m^3	For $\phi = 1.67$
T	Temperature	323.15 K	Experimental condition

The correction to the mobility diameter is performed by firstly calculating the electrical mobility, Z/q, based on Eqs. 4.22 and 4.35 for each size class of the DMS500 [23]. The calculated Z/q is used to solve for the corrected size classes according to Eq. 4.36. Further, to account for the sampling line transport efficiency, the DMS-derived particle size distribution (PSD_{DMS}) is calculated as

$$PSD_{DMS} = \frac{PSD_{DMS,expt}}{\eta_{DMS}}, \tag{4.41}$$

where $PSD_{DMS,expt}$ is the measured particle size distribution after the mobility correction and η_{DMS} is the sampling transport efficiency given in Eq. 4.24. The resulting size distribution is then fitted with a log-normal distribution to obtain the median particle size, $\langle d_m \rangle$, and the geometric standard deviation (GSD).

The uncertainty of the corrected mobility sizes is evaluated here by considering two parameters used in the correction which have the highest uncertainties, particle density ρ_s, and β from Eq. 4.38. As discussed before, the particle density was chosen based on the major phase identified with powder diffraction for the given equivalence ratio. However, this does not take into account mixtures of phases with different densities or possibility of a size-dependent density which can result in higher or lower effective density. Here a maximum uncertainty

for ρ_s is taken as 20%, approximately representing the difference between the densest and the least dense phases of TiO_2. The parameter β represents the crossover size between specular to diffuse scatterings. Li and Wang [129] determined this empirically to be 2.5 nm using the available experimental data for Ag and Cu while other studies suggested smaller values, i.e. 1–2 nm [216]. Thus the uncertainty for β is estimated to be ± 1 nm. These values are used to calculate the sensitivity of the median particle sizes for all cases in Table 4.4. The results suggest that the median sizes are relatively insensitive to the density (approximately 1% change for all cases). Similar insensitiviy is observed for β except for the 4 ml/h loading cases with larger β (maximum change of 8%). This is expected as the particle sizes for the low loading cases are close to the crossover size. The uncertainties shown in Table 4.4 are comparable to the average error calculated by Li and Wang [129], i.e. 7%.

Table 4.4: *Sensitivity of the median mobility size after correction to particle density ρ_s and momentum accomodation function parameter β. Reference values for ρ_s are given in Table 4.3 while the reference $\beta = 2.5$ nm.*

ϕ	TTIP, ml/h	Change in $\langle d_m \rangle$, %			
		$\rho_s = 0.8\rho_s$	$\rho_s = 1.2\rho_s$	β = 1.5 nm	β = 3.5 nm
0.35	4	1.5	-1.3	-1.6	8.2
0.35	12	1.5	-0.9	-0.1	0.8
0.35	30	1.5	-0.7	-0.0	0.2
1.67	4	1.5	-1.2	-0.6	4.3
1.67	12	1.5	-1.0	-0.0	0.8
1.67	30	1.5	-0.8	-0.0	0.2

Finally, the uncorrected and corrected mobility sizes are compared with the spherical equivalent sizes for all cases in this work, shown in Fig 4.8(a). Here the error bars represent the estimated error of 7% in addition to the measurement uncertainty of ± 0.25 nm (Fig. B.5) for the mobility sizes and the uncertainty due to the resolution of the TEM images (± 0.24 nm, ± 0.32 nm, ± 0.47 nm for the 4, 12, and 30 ml/h TTIP loading cases, respectively) for the spherical equivalent sizes. The comparison is further summarised in Table 4.5. As the DMS500 resolution is limited, a lower cutoff point of 3.8 nm – equivalent to the smallest DMS500 size class of 4.9 nm after correction – is applied to the spherical equivalent size data from the TEM image analysis. The resulting distribution is then fitted with a truncated log-normal distribution to obtain the median particle size, $\langle d_{\text{sph}} \rangle$, and the geometric standard deviation (GSD). The TEM-derived sizes are taken as the reference particle sizes for error calculation as a significant proportion of the particles are spherical (discussed further in the next section). As expected, the discrepancy for uncorrected mobility size is greatest for the

smallest particles. The correction applied reduces the average difference from 19% to 4%, similar to the average difference reported by Li and Wang [129] for previous experimental data.

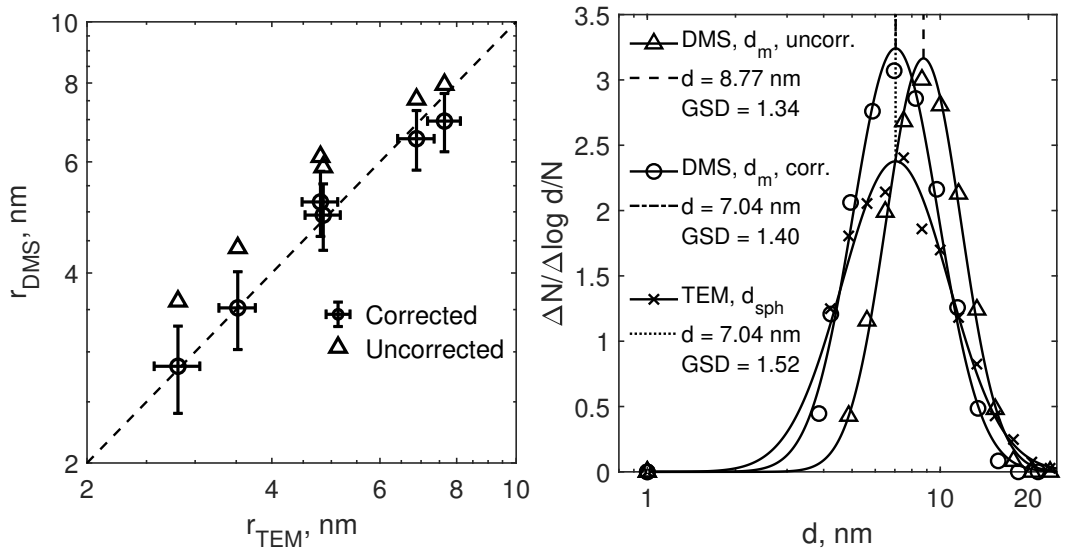

Figure 4.8: *(a) Comparison between TEM-derived radii, r_{TEM}, and the mobility radii, r_{DMS}, corrected and uncorrected. The interpretation of the error bars is discussed in the text. (b) Particle size distributions measured using DMS, d_m, corrected and uncorrected, and from TEM image analysis, d_{sph}, for $\phi = 1.67$ and 4 ml/h TTIP condition. The vertical lines indicate the median values from log-normal fits to the distributions used in the correction. The geometric standard deviations (GSD) are also indicated.*

Table 4.5: *Particle sizes from TEM projected area analysis and mobility measurements, before and after correction, with the DMS.*

ϕ	TTIP, ml/h	TEM		DMS			DMS, corrected		
		$\langle d_{sph} \rangle$, nm	GSD	$\langle d_m \rangle$, nm	Err., %	GSD	$\langle d_m \rangle$, nm	Err., %	GSD
0.35	4	5.63	1.50	7.22	28.3	1.30	5.69	1.2	1.33
0.35	12	9.60	1.63	12.23	27.3	1.39	10.37	8.0	1.44
0.35	30	15.28	1.59	15.91	4.1	1.40	13.93	-8.9	1.45
1.67	4	7.04	1.52	8.77	24.5	1.34	7.04	0.1	1.40
1.67	12	9.70	1.63	11.77	21.4	1.35	9.88	1.9	1.41
1.67	30	13.76	1.61	15.07	9.5	1.38	13.06	-5.1	1.43
		Mean absolute error, %			19.2			4.2	

Figure 4.8(b) shows the corrected and uncorrected mobility size distributions as well as the spherical-equivalent size distribution obtained from the TEM image analysis for $\phi = 1.67$

and 4 ml/h TTIP loading where the mobility measurement overpredicts the particle size by approximately 25%. This is consistent with previous studies comparing mobility and microscopy sizes where an average overprediction of 20% was reported [192, 117]. The applied correction results in a much better agreement between the mobility and spherical equivalent median sizes.

However, some discrepancies are observed for the distribution widths as indicated by the GSD, also tabulated in Table 4.5. The TEM-derived size distributions has an average GSD of 1.58 compared to 1.36 and 1.41 for uncorrected and corrected mobility size distributions, respectively. The broadening of the mobility size distributions after correction is a result of the size-dependent correction (i.e. larger correction for smaller particles). As a comparison, Tolmachoff et al. [221] reported GSD of 1.3-1.5 for similar TTIP loading range. Similar discrepancy between the TEM and DMS distribution widths has been observed in other comparative studies before [47, 117] although the reason is unclear.

Here, two possible reasons for the discrepancies are suggested which will be investigated in further studies. First, the TEM image analysis does not always capture the projected particle shape precisely due to multiple factors including image quality as discussed in Section 4.4. For example, the aggregates can be artificially combined when the projections are too close or fragmented when some parts of the particles are not on the focus plane. These measurement errors result in broadening of the actual distributions.

Second, the mobility size distributions measured by the DMS500, especially the widths, are sensitive to the classifier transfer function used by the DMS500 [23]. This is represented by the internal calibration matrices generated by the supplier (Cambustion Ltd.) with different aerosol standards. For example, the same measurements performed with calibration matrix generated with soot agglomerates tends to produce significantly broader distributions than those with a calibration matrix generated with spherical aerosols although the median sizes are similar (unpublished data). The aggregate particle morphology could also affect the particle charge distribution from the unipolar diffusion charger [84, 121]. However, this is unlikely to be significant as the majority of particles are spherical or have low aspect ratio and are therefore well described by the Fuchs' limiting-sphere theory as employed in the DMS500 charging model [23].

The close agreement between the corrected mobility particle size and TEM-derived particle size confirms that the sampling methodology used in this work can be used to characterise the morphology of small nano-aggregates as discussed in the next section.

4.5.3 Particle morphology

Table 4.6 summarises the measured primary particle sizes from the TEM images with high magnification (150,000×). It is important to point out that due to the resolution limit, poorer contrast, and higher chance of overlap, smaller particles are harder to measure manually (with only particles larger than approximately 3 nm can be confidently identified). This is likely to result in slight bias towards larger particles. As such, the Sauter mean diameter, $\bar{d}_{3/2}$, is reported here in addition to the averaged mean, $\bar{d}_p$, as it tends to represent data closer to the right end of the distribution. The primary particle distributions are relatively narrow as indicated by the geometric standard deviations (GSD).

Table 4.6: *Summary of primary particle analysis.*

ϕ	TTIP, ml/h	Primary particles			
		count	$\bar{d}_p \pm$ SD, nm	GSD	$\bar{d}_{3/2}$, nm
0.35	4	1462	5.9 ± 1.3	1.25	6.5
0.35	12	1427	9.3 ± 2.4	1.29	10.6
0.35	30	1323	11.9 ± 3.7	1.37	14.3
1.67	4	1121	6.2 ± 1.3	1.23	6.8
1.67	12	1637	8.4 ± 2.2	1.30	9.5
1.67	30	1136	12.1 ± 3.3	1.33	13.9

Table 4.6 suggests that the primary sizes are strongly affected by the TTIP loading but are relatively insensitive to the flame temperature. This is surprising as the rich flame ($\phi = 1.67$) is approximately 450 K hotter than the lean flame ($\phi = 0.35$). The insensitivity of particle size to the maximum flame temperature can be explained by the reduced particle residence time in hotter flames due to a higher convective velocity.

Figure 4.9 shows the TEM images used for the aggregate projected area analysis (see Section 4.4). The particle morphology can be described as a mixture of single spherical particles and small aggregates with small degree of sintering. High magnification experimental TEM images, not shown here, reveal highly crystalline primary particles. These observations are in agreement with previous studies [155, 221].

In order to describe the particle morphology, α, the ratio of d_g to d_{sph}, is used to characterise the level of particle aggregation. Spherical particles have α close to 0.7 while aggregates with an open structure have a larger α. As α is affected by the pixel resolution of the particles, the image magnifications were adjusted for different TTIP loading cases such that the average number of pixels per particle is conserved. This ensures that the particle morphology as characterised by α is comparable across all loadings tested.

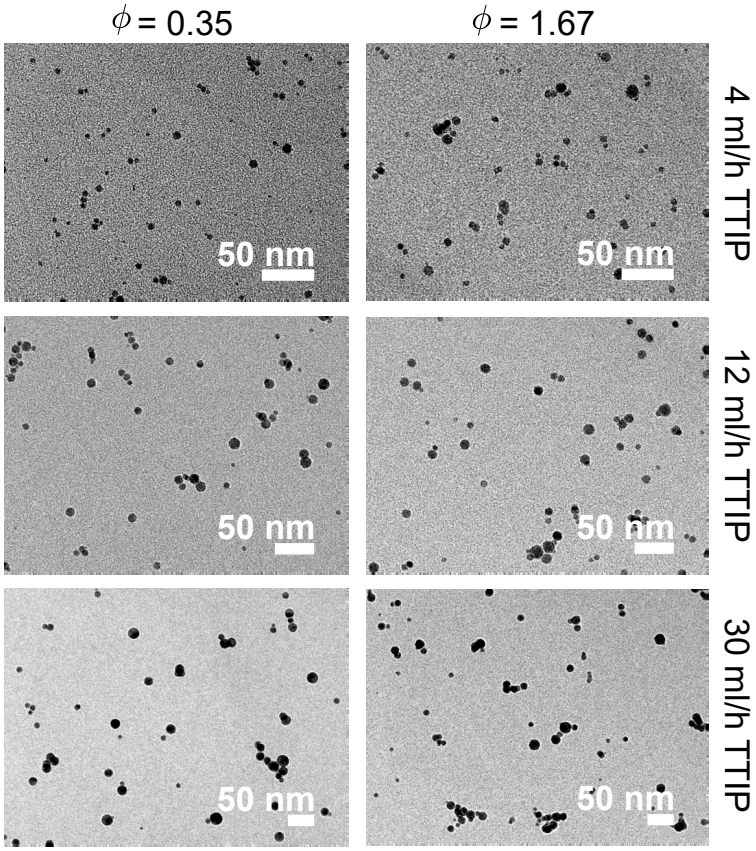

Figure 4.9: *Examples of TEM images used for aggregate size analysis for all conditions tested in this work. In order to minimise bias from particles overlapping, only TEM images with a particle coverage of less than 5% were included in the analysis.*

Figure 4.10 shows examples of typical aggregates observed in the aggregate size analysis with their corresponding α. Spherical particles (Fig. 4.10(a)) are typically characterised by α around 0.7. As the structure becomes more open and non-spherical, α, increases to a maximum of around 1.3.

Figure 4.11 shows the bivariate histograms of all particles analysed in this work characterised by the parameters d_{sph} and α. Two important observations are made here: First, a significant proportion of particles have α close to 0.7 (shown by the color scale). This is consistent with the qualitative observation that most particles have spherical morphology. Second, larger particles tend to have larger α which is expected as larger particles sinter more slowly leading to the formation of more open structures.

In this work, a condition of $\alpha < 0.73$ is assumed to define a spherical particle. This is slightly larger than a perfect circle whose $\alpha = 0.71$ to allow for some degree of roughness from the image analysis algorithm. Table 4.7 summarises the important metrics of the

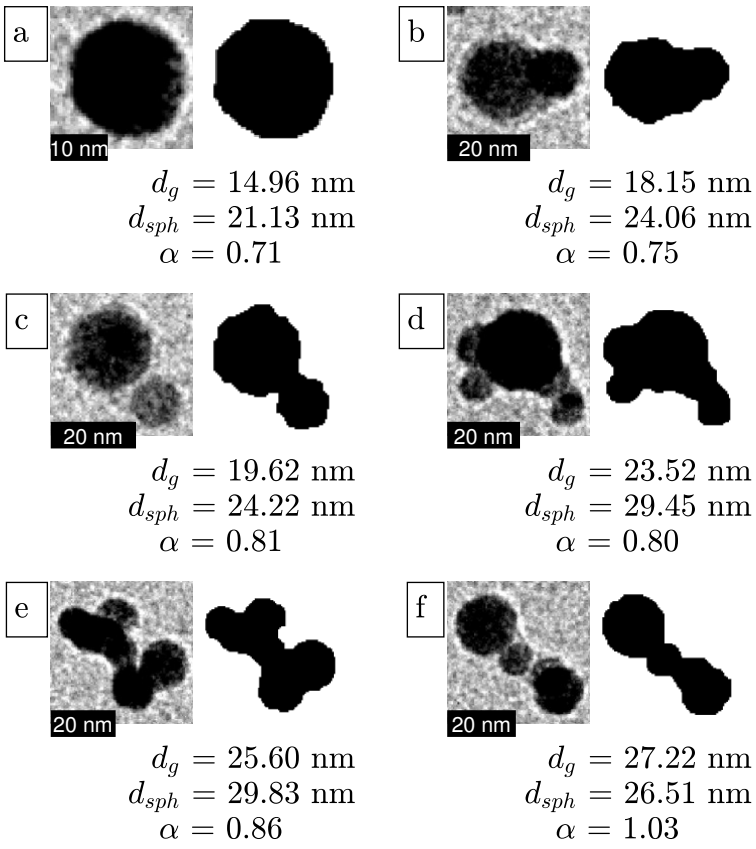

Figure 4.10: *Examples of particles observed in the TEM image analysis and the corresponding pixel mask at varying degree of aggregation (with $\alpha = d_g/d_{\mathrm{sph}}$ ranging from 0.7 to 1). A spherical particle is defined as having $\alpha < 0.73$ in this work.*

particle morphology obtained from the aggregate image analysis. Taking into account the size-dependent collection efficiency, $E(d)$ (Eq. 4.26), and transport efficiency, $\eta_{\mathrm{TEM}}(d)$ (Eq. 4.25), an average property, $\bar{X}$, can be calculated as follows

$$\bar{X} = \frac{\sum_i^N X_i E(d_{\mathrm{sph},i})^{-1} \eta_{\mathrm{TEM}}(d_{\mathrm{sph},i})^{-1}}{\sum_i^N E(d_{\mathrm{sph},i})^{-1} \eta_{\mathrm{TEM}}(d_{\mathrm{sph},i})^{-1}}. \tag{4.42}$$

In all cases, the value of $\bar{\alpha}$, lies within a narrow range of 0.75–0.77 indicating a small degree of particle aggregation which is almost insensitive to the conditions tested. The degree of aggregation can be further quantified by the proportion of particles with spherical morphology ($\alpha < 0.73$), f_α, which ranges from 57–69%. This significant proportion of single spherical particles justifies the choice of using d_{sph} as the particle size for TEM collection efficiency and mobility size corrections discussed in Section 4.5.2.

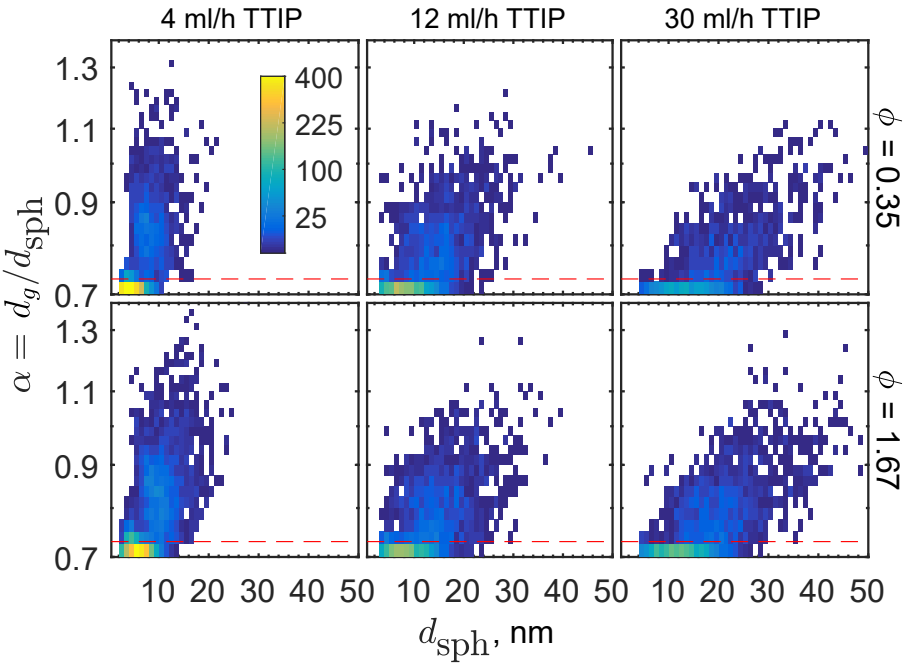

Figure 4.11: *Bivariate histograms of all particles analysed in this work characterised by their geometric parameters d_{sph} and α. The color scale represents particle count. The bin sizes are 1 nm and 0.025 for d_{sph} and α, respectively. The horizontal dashed lines indicate $\alpha = 0.73$.*

Table 4.7: *Summary of aggregate size analysis (after size-dependent collection efficiency correction).*

ϕ	TTIP, ml/h	All aggregates				Aggregates, $\alpha < 0.73$		
		count	$\bar{d}_{sph}$, nm	$\bar{d}_g$, nm	$\bar{\alpha}$	f_α[a], %	$\bar{d}^*_{sph}$, nm	Δ[b], %
0.35	4	3016	5.72	4.46	0.76	69	4.65	-21.2
0.35	12	2601	10.68	8.29	0.75	65	8.31	-10.7
0.35	30	1582	16.94	13.14	0.75	62	13.21	10.3
1.67	4	3823	7.53	6.02	0.77	57	5.92	-6.0
1.67	12	2676	10.86	8.44	0.76	61	8.39	-0.9
1.67	30	2633	15.41	12.00	0.75	63	11.84	-1.8

[a] $f_\alpha = [\sum_{\alpha_i<0.73} E(d_{sph,i})^{-1}\eta(d_{sph,i})^{-1}]/[\sum_{all\ i} E(d_{sph,i})^{-1}\eta(d_{sph,i})^{-1}]$
[b] $\Delta = (\bar{d}^*_{sph} - \bar{d}_p)/\bar{d}_p$ (values of $\bar{d}_p$ from Table 4.6)

Next, the primary size distributions are compared to the aggregate size distributions from the projected area analysis in Fig. 4.12. The distributions are represented as non-parametric continuous functions (kernel distributions) generated using the kernel density estimator

function in MATLAB [29] in order to avoid making any assumptions of the underlying distribution shapes. In general, the aggregate size distributions, d_{sph}, are broader than the primary size distributions, d_p, but the modes of the two distributions are similar due to the high proportion of single primary particles. The size distributions of particles with $\alpha < 0.73$, denoted as d^*_{sph}, are also shown. It is interesting to note that d^*_{sph} and d_p distributions show relatively good agreement. This suggests that the use of $\alpha < 0.73$ to isolate the spherical particles is appropriate.

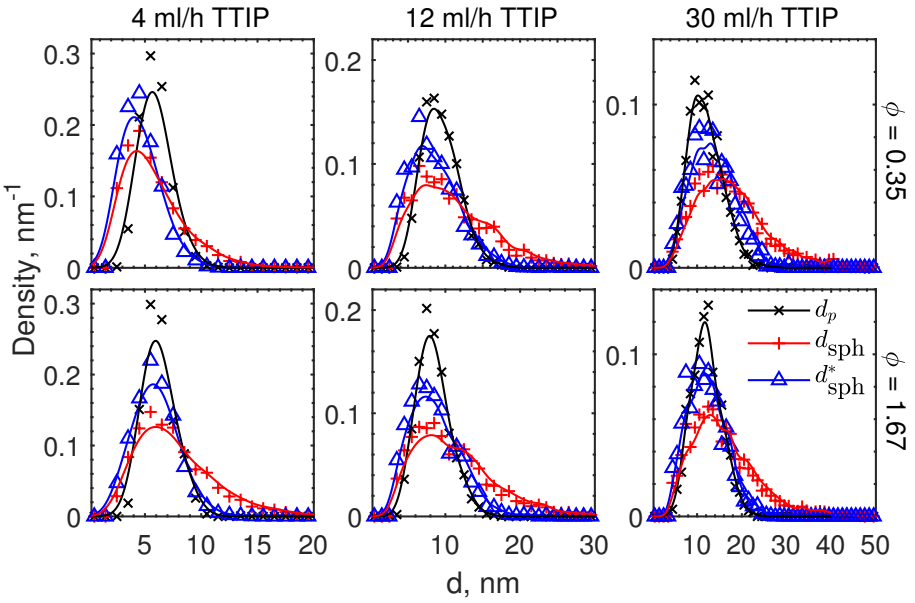

Figure 4.12: *The primary diameter, d_p, and spherical equivalent diameter from aggregate projected area, d_{sph}, distributions for all conditions tested. d^*_{sph} is the spherical equivalent diameter of aggregates with $\alpha < 0.73$ (single primaries). The bin size and the bandwidth for the density estimation are 1 nm.*

A rather significant discrepancy is observed for the 4 ml/h case for $\phi = 0.35$ (20%, Table 4.7). The disagreement between $\bar{d}^*_{\text{sph}}$ from aggregate size analysis and $\bar{d}_p$ from primary particle analysis is likely a result of a bias in the latter towards large particles. This is due to poor contrast and particle overlap especially when the particles are smaller than 4 nm. The comparison of the Sauter mean diameters, $\bar{d}_{3/2}$, for this case shows a smaller difference of 10% suggesting that the discrepancy mainly comes from the left tail of the distribution (small particles).

Lastly, the relatively good agreement between d^*_{sph} and d_p over all conditions, except for the $\phi = 0.35$ flames with low loading cases, tested suggests that no significant growth through sintering occurs after the aggregation. This likely means that the aggregation does not occur in flame but near the stagnation plate, i.e. if the aggregation happens earlier in flame,

further sintering would have resulted in larger primary particles in aggregates compared to non-aggregated spherical particles. This is plausible as the gas temperature only decreases steeply near the stagnation plate [221]. This is supported by the observation that the primary particles in the aggregates are mostly in point contact with a small degree of sintering (see Fig. 4.9).

4.5.4 Comparison with simulation

Temperature and flame distance

The simulation of a stretch stabilised flame such as the one used in this study requires knowledge of the flame standing distance or temperature profiles due to the limitation of the one-dimensional stagnation flow approximation in capturing a non-parabolic flow profile [20]. However, in this study only temperature measurements for the undoped lean flame ($\phi = 0.35$) were available due to the thermocouple service temperature limit. In this work, the temperature measurements were used to estimate the point at which the temperature rises sharply for the lean ($\phi = 0.35$) flame and to adjust the boundary conditions in the simulation (with the energy equation solved) to reproduce this. The comparison between the simulated temperature profile for this flame and the flame image shows that the simulated H peak coincides with the point at which the flame intensity is half of the maximum intensity (see Appendix B.5). An arbitrary assumption is then made to use the same criteria to define the flame standing distance and to adjust the boundary conditions (Table 4.1) for all other cases because no temperature measurements for these cases are available.

Figure 4.13 shows the measured and simulated temperature profiles for the undoped lean flame ($\phi = 0.35$) showing a good agreement in the combustion zone widths. A significant difference is observed in the profile shape and the maximum temperature. The measured temperature profile suggests that the calculated adiabatic flame temperature is reached earlier near the upstream edge of the flame while the simulated profile shows the temperature increases to a maximum point nearer to the stagnation plate. It is likely that the proximity of the peak temperature region to the stagnation plate (cold boundary) in the simulation results in a lower maximum temperature compared to the measured maximum temperature which is close to the adiabatic temperature. The origin of the discrepancy in the temperature profiles is unclear but a possible reason is the deviation from the one-dimensional stagnation flow solution. Another possible source of error in the temperature measurements is the catalytic reaction on the uncoated thermocouple surface. Catalytic heating is expected to affect the region near the flame front where there is more unreacted premixed gas [198]. This will

result in artificially higher temperature estimates at the flame front, which is the case in this work. This can also explain the measured temperature being slightly higher than the calculated adiabatic flame temperature. This will be investigated in a future study.

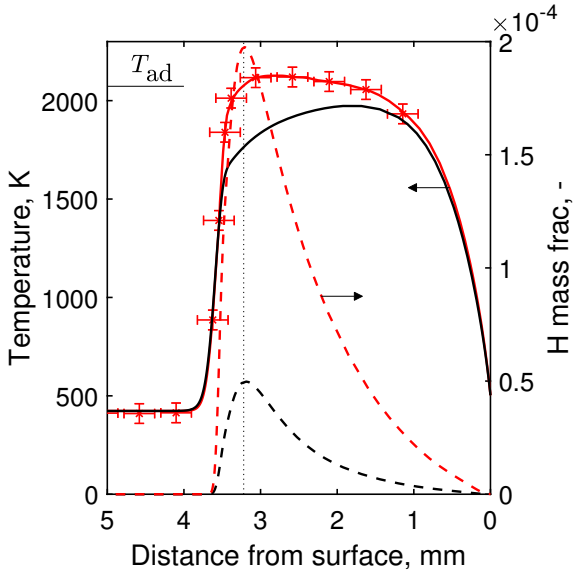

Figure 4.13: *Temperature and H mass fraction profiles for $\phi = 0.35$ flame (no TTIP). The black lines are from the calculated temperature simulation and the red lines are from the imposed temperature simulation corresponding to the experimental measurements (symbols). The adiabatic flame temperature, T_{ad}, is annotated for comparison.*

Figure 4.13 also shows the H concentration profiles of the simulated flames, one with the calculated temperature profile (black line) and another with an imposed temperature profile from the experimental measurement (red line). The higher temperature in the imposed temperature simulation results in a significantly higher H concentration compared to the calculated temperature simulation (by a factor of 4). However, the location of the maximum H concentration remains unchanged. It is found that this location (denoted by the vertical dotted line in Fig. 4.13) coincides with the flame standing distance measured from the flame image analysis (see Appendix B.5). Thus, an assumption is made here to use the peak H concentration from the simulation to define the flame standing distance for the rich flame ($\phi = 1.67$) where temperature profile measurements were not available. Furthermore, it is assumed that the addition of TTIP does not affect the flame standing distance due to the relatively small amount of TTIP used. The flame distances of the simulated flames with varying TTIP loading used in this work are summarised in Table 4.8. This was adjusted to match the measured flame distance (3.22 mm for $\phi = 0.35$ and 3.92 mm for $\phi = 1.67$) within the uncertainty range of ± 0.2 mm.

Table 4.8: *Flame distances of the simulated flames, in mm, taken as the distance of the peak H concentration from the stagnation surface.*

	$\phi = 0.35$			$\phi = 1.67$		
	4 ml/h (194 ppm)	12 ml/h (582 ppm)	30 ml/h (1454 ppm)	4 ml/h (194 ppm)	12 ml/h (582 ppm)	30 ml/h (1454 ppm)
Calculated T	3.21	3.17	3.27	4.00	4.00	3.98
Imposed T	3.21	3.21	3.27	-	-	-

Simulated particle morphology

The simulated particle morphological descriptors are shown in Fig. 4.14. These include the primary particle distribution, aggregate size distribution, and the fraction of spherical particles, f_α, for the 6 flame conditions employed in this study. The aggregate size distribution and f_α are obtained from the image analysis of TEM-like images analogous to the experimental TEM analysis.

Figure 4.14 also shows the experimentally measured primary (d_p) and aggregate (d_{sph}). The simulated primary sizes are in general slightly smaller than the measurements for all cases. This suggests that either surface growth or sintering rates are underestimated. The aggregate sizes show good agreement for larger TTIP loading (12 and 30 ml/h) but reveal some discrepancies for the 4 ml/h loading case. This could be attributed to the large uncertainty with identifying small particles through the TEM image analysis as discussed above. The comparison of f_α reveals a consistent underprediction of approximately 10% for the $\phi = 0.35$ flames while the discrepancies for the $\phi = 1.67$ flames are loading-dependent (maximum discrepancy is also about 10%). One possible explanation of this is the free molecular coagulation enhancement factor which is assumed as a constant. However, some studies have suggested that this may be strongly temperature and size dependent [200].

4.5.5 Sensitivity analysis

It is noted that the simulations are subjected to the uncertainties related to the experimental temperature measurement and flame distance estimation as discussed above. In order to understand the effect of the temperature profile uncertainties on the simulated particle properties, three parameters related to the experimental measurements are investigated in this work. These are the profile shape, flame standing distance, and surface temperature.

First, the effect of the temperature profile shape is assessed by comparing simulations with the calculated and the imposed temperature profiles. Figure 4.15 shows the temperature

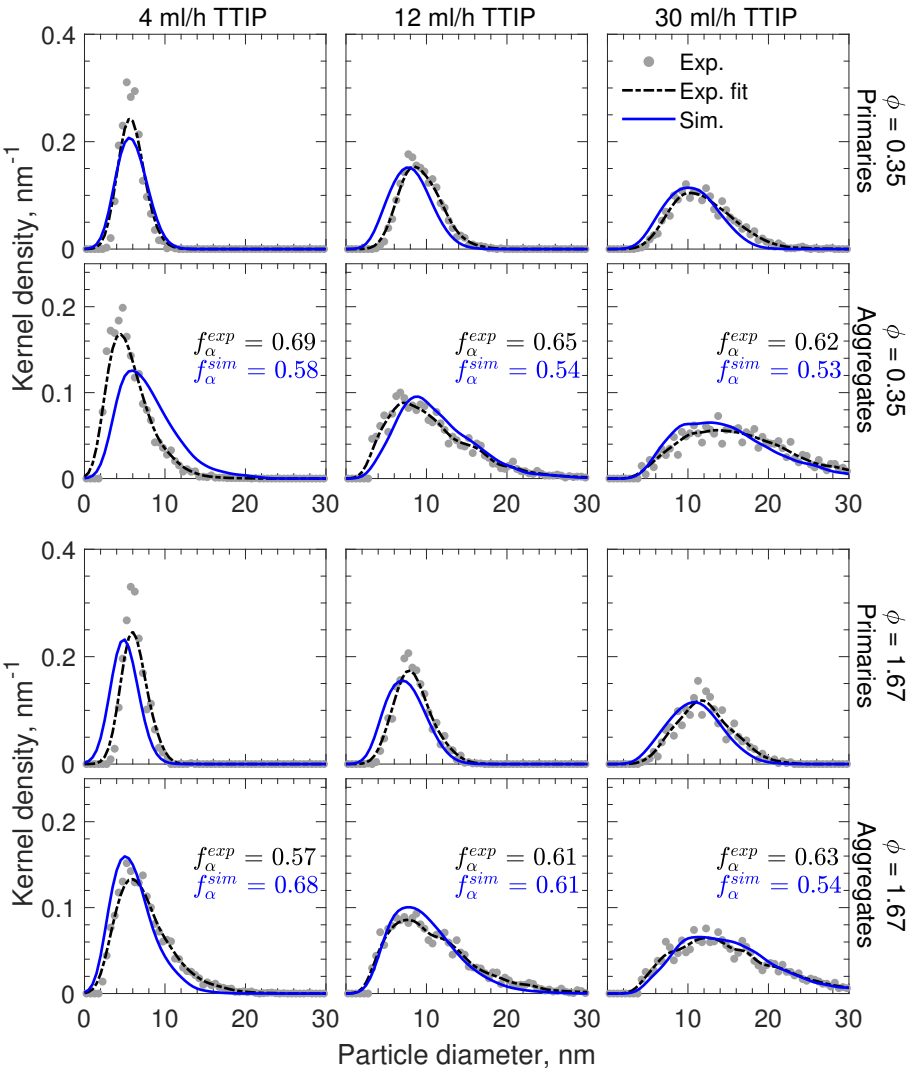

Figure 4.14: *Simulated and measured primary and aggregate size distributions. The experimental data points are normalised particle counts with a binwidth of 0.5 nm. The lines are from kernel distribution fits using 1 nm bandwidth. f_α denotes the fraction of spherical particles from image analysis.*

profiles for the lean flames with varying TTIP loading rate. For the 4 ml/h TTIP loading rate case, the imposed temperature profile is assumed to be the same as the measured profile for the undoped flame (symbols in Fig. 4.15). For the 12 and 30 ml/h cases, the temperature profiles are shifted upwards by 70 and 200 K, respectively, to account for the effect of TTIP combustion. These shifts are approximately consistent with the shifts in the corresponding calculated temperature cases. Similar to the undoped flame case, the temperature profile shape does not seem to affect the flame standing distance (Table 4.8). The imposed temperature

simulations are only attempted for the lean flames ($\phi = 0.35$) as no temperature measurement is available for the rich flame.

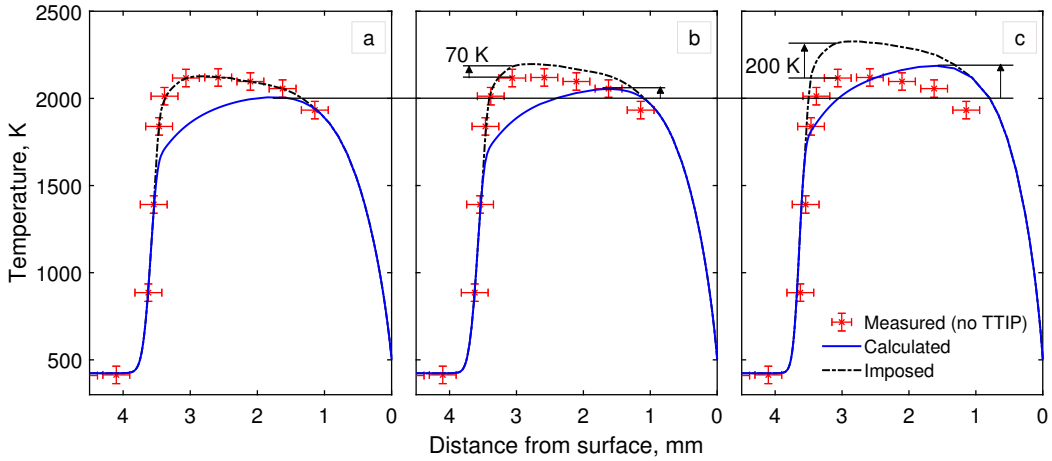

Figure 4.15: *Calculated and imposed temperature profiles for $\phi = 0.35$ flames (a: 4 ml/h, b: 12 ml/h, c: 30 ml/h TTIP loading). The imposed temperature profile for 4 ml/h case is taken from experimental measurement (with no TTIP) while those for 12 ml/h and 30 ml/h cases are shifted by 70 and 200 K, respectively, similar to the shifts in the calculated maximum temperature profiles (arrows) to account for the additional heat release from TTIP combustion.*

Second, the effect of the flame distance is assessed by comparing simulations with varying flame distance (i.e. peak H concentration) by ± 0.2 mm with reference values in Table 4.8. This is approximately the same as the experimentally observed fluctuation in the flame front.

Finally, the effect of the surface temperature is assessed by comparing simulations with varying stagnation temperature by ± 50 K ($T_s = 503$ K for $\phi = 0.35$ and $T_s = 580$ K for $\phi = 1.67$). This uncertainty in the stagnation plate temperature comes from the fluctuation during experiment as well as a typical uncertainty for a K-type thermocouple.

Figure 4.16 presents the changes in primary particle and aggregate properties for all conditions tested in this work with respect to the uncertainties in the three temperature profile parameters discussed above. Here the widths of the size distributions are quantified using the coefficient of variation (CV) which is the ratio of mean to the standard deviation, i.e. CV = $\bar{d}$/SD.

First, all of the particle properties are insensitive to the shape of the temperature profile (imposed T vs. calculated T). Second, the mean primary and aggregate diameters are only sensitive to the flame distance – primarily the lean flame with high TTIP loading. Meanwhile, the coefficients of variation show very little sensitivity in all cases. f_α shows the greatest degree of sensitivity across the temperature profile parameters F_d and T_s.

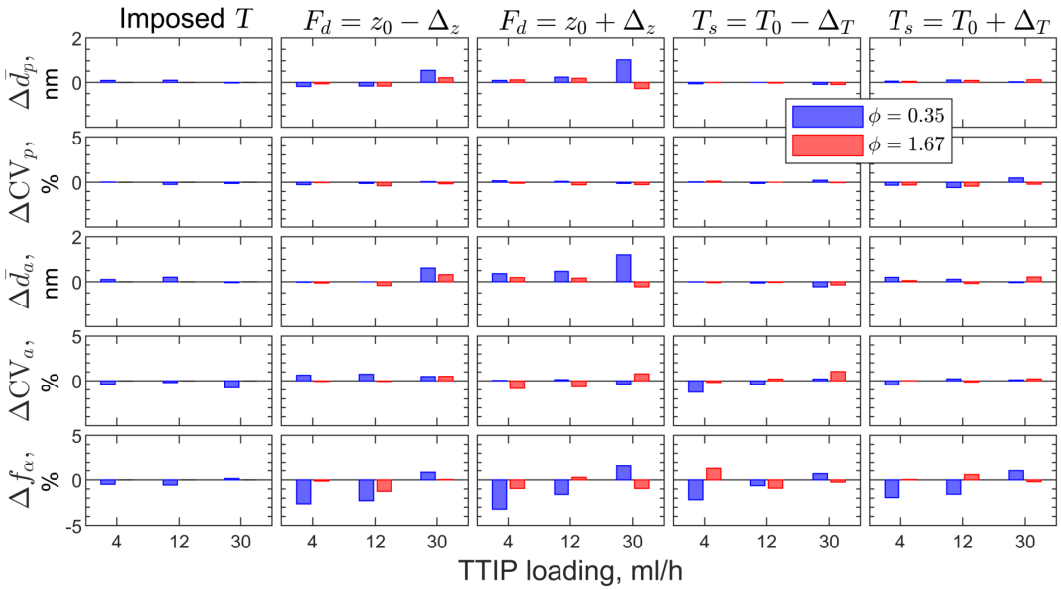

Figure 4.16: *The changes in particle descriptors as the temperature profile shape (refer to text), flame distance, F_d, and surface temperature, T_s, are varied against the base case (calculated temperature, flame distance z_0, and surface temperature T_0) for all cases studied here. The particle descriptors are: (1) primary mean diameter, $\Delta\bar{d}_p$, (2) primary coefficient of variation, ΔCV_p, (3) aggregate mean diameter $\Delta\bar{d}_a$, (4) aggregate coefficient of variation, ΔCV_a, and (5) fraction of particles with circular projection, Δf_α. The perturbations Δ_z and Δ_T are 0.2 mm and 50 K, respectively.*

Overall, the changes in particle sizes are less than 1 nm, except for the lean flame with 30 ml/h TTIP loading (less than 2 nm). The maximum changes for CV and f_α are 1% and 3%, respectively. This suggests that the particle properties are relatively insensitive to the temperature profile parameters. More importantly, the changes in Fig. 4.16 give an indication of the degree of model prediction uncertainties carried forward from the uncertainties in experimental measurements feeding into the simulation, i.e. temperature and flame distance.

4.6 Chapter summary

In this work, the use of a TEM sampling method that relies on impaction and diffusion to characterise the morphology of titania nano-aggregates prepared in a stagnation flame reactor is demonstrated. TEM images were taken and semi-automated image analysis procedures were performed. The method is validated against electrical mobility measurements taking into account size-dependent collection efficiency of the TEM sampling and mobility size correction. The excellent agreement between TEM-derived and mobility sizes suggests that

the TEM sampling combined with image analysis can be used to characterise the particle morphology for the conditions presented here.

The analysis reveals that the primary particle and aggregate sizes are mostly affected by the precursor loading but not the flame temperature. In contrast, the degree of aggregation is found to be insensitive to the precursor loading or the flame temperature. The degree of aggregation is described by α, the ratio of gyration to spherical-equivalent diameters, where spherical particles are defined as having $\alpha < 0.73$. Approximately 60–70% particles analysed have spherical morphology (single spherical particles) while the rest form small aggregated structure with $\alpha = 0.73$–1.3. The aggregation explains the previously observed discrepancy between TEM and mobility sizes. The primary particle size distributions are similar to the spherical particle size distributions which suggests that the aggregation only occurs very late in the particle growth stage (i.e. near the stagnation plate). This is consistent with the qualitative observation of minimal sintering level in the aggregates.

Furthermore, the simulated particle properties show a good agreement with the experimental measurements in general. Interestingly, the simulated particle properties show little sensitivity to the temperature profile shape, flame standing distance, and surface temperature – all of which present relatively large experimental uncertainties. This suggests that the present approach for estimating the flame standing distance to constrain the simulations is acceptable in this case.

Chapter 5

Polymorphism of TiO_2 nanoparticles prepared in a stagnation flame

This chapter presents an experimental characterisation of TiO_2 polymorphs prepared in a stagnation flame as a function of mixture equivalence ratio. A metastable "high-pressure" phase known as the α-PbO_2-type TiO_2 or TiO_2-II is identified. This is the first time this phase has been identified in flame-synthesised TiO_2. Three other TiO_2 polymorphs, namely anatase, rutile and TiO_2-B phases, can also be obtained by tuning the mixture equivalence ratio. The TiO_2-II is observed as a mixture with rutile in oxygen-lean flame conditions. The formation of TiO_2-II in an atmospheric pressure flame cannot be explained thermodynamically and is hypothesised to be kinetically driven through the oxidation and solid-state transformation of a sub-oxide TiO_{2-x} intermediate. Rutile is subsequently nucleated from the metastable TiO_2-II phase instead of from anatase or a molten/amorphous state.

5.1 Background

The ability to control the phase composition of crystalline TiO_2 by controlling process variables in flame synthesis has been demonstrated by many authors previously. In particular, anatase-rutile stability is shown to be highly sensitive to the mixture equivalence ratio [108, 155]. Some authors have proposed that anatase is the initially formed phase in flame synthesis due to the higher thermodynamic stability of anatase compared to rutile for small particles [255, 258]. The phase transformation from anatase to rutile subsequently occurs

as particles further grow through surface growth and coalescence. It was argued that this transformation is enhanced by the oxygen lean environment which explains the sensitivity to the equivalence ratio.

Recently, Riad et al. [189] demonstrated the formation of another metastable phase TiO_2-B in flame spray pyrolysis experiments as a mixture with anatase. Given the structural relationship between TiO_2-B and anatase [33], it is possible that the TiO_2-B acts as a precursor phase of anatase. The presence and identification of metastable phases thus provide important insights into the phase formation mechanism of TiO_2 in flame synthesis.

Another lesser-studied metastable structure of TiO_2 is TiO_2-II or Columbite. TiO_2-II is an orthorhombic high-pressure phase of TiO_2 isostructural with α-PbO_2. Although pure TiO_2-II is only thermodynamically stable at high pressure conditions, experiments and first-principles studies have shown that it can be retained at ambient pressure as a metastable phase [154]. Zhao et al. [269] suggested that small domains of TiO_2-II could be stabilised at a three-phase anatase/TiO_2-II/rutile junction. They predicted that such a three-phase junction will lead to a synergistic effect in mixed-phase TiO_2 catalysts to enhance the electron-hole separation in photocatalysis. However, the role of TiO_2-II as photocatalyst is still inconclusive as the properties are strongly dependent on the synthesis routes used [17, 61, 164].

The purpose of this chapter is to demonstrate, for the first time, the formation of the TiO_2-II phase (a high pressure phase) at atmospheric pressure via stagnation flame synthesis in addition to the commonly observed phases anatase and rutile, as well as the previously reported metastable phase TiO_2-B. The relative composition of these phases is strongly dependent on the oxygen/fuel ratio in the synthesis. The phase formation and transformation mechanisms of TiO_2 nanoparticles in flames are discussed based on these observations.

5.2 Experimental details

5.2.1 Sample preparation

TiO_2 nanoparticles in this study were prepared with a premixed flame stabilised on a stagnation surface. The setup here is similar to the configuration used in Chapter 4. Briefly, a mixture of ethylene, oxygen, and argon was issued from a central aerodynamic nozzle with a total volumetric flow rate of 28 slpm. The nozzle had an exit diameter of 1.4 cm, resulting in an exit velocity of 436 cm/s at 150°C. The nozzle shape induced a flat plug flow of premixed gas that impinged on a stagnation surface. Titanium tetraisopropoxide (TTIP,

$\geq$ 97%, Sigma-Aldrich) was injected into the unburned gas mixture with a syringe pump at 8 ml/h, corresponding to 365 ppm TTIP mole fraction. The gas line, precursor line, and burner surface were heated to 150°C to prevent TTIP condensation. During the experiment, the undoped flame was first stabilised for 15 minutes before TTIP was injected for 4 minutes. A shroud flow of 20 slpm N_2 gas was used to stabilise the jet flow.

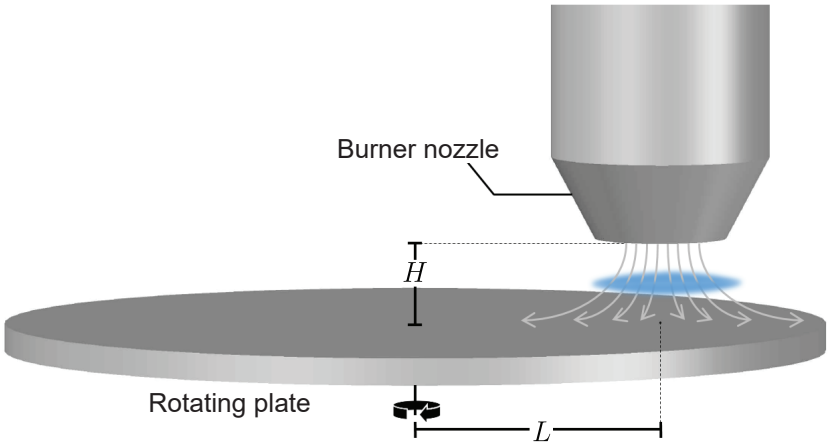

Figure 5.1: *Schematic of the stagnation flame stabilised on a rotating plate (not drawn to scale). A burner nozzle is fixed at $H = 1$ cm above the rotating plate and at $L = 10$ cm from the rotational axis.*

Two types of stagnation surfaces were located 1 cm under the nozzle to stabilise the flame by flow stretch and to accommodate a substrate for collecting the TiO_2 sample. The first one was a rotating (300 rpm), circular stainless steel plate with its rotational axis located at 10 cm from the burner centerline (Fig. 5.1). Slots in the stagnation surface enabled the positioning of glass substrates while the plate rotation convectively cooled the substrate and the deposited particles. In the second configuration, a water-cooled non-rotating plate was used as the stagnation surface. In both cases, a flat flame was stabilised at 3–3.5 mm above the stagnation plate depending on the flame equivalence ratio. The equivalence ratio, ϕ, defined as the ratio of O_2 required for the complete oxidation of introduced C_2H_4 divided by the actual amount of available O_2, was varied as summarised in Table 5.1. After 4 minutes of TiO_2 deposition, the sample was carefully scraped off from the glass substrate and used as prepared for further analyses.

5.2.2 Material characterisation

Powder X-ray diffraction (XRD) patterns were recorded with a D8 Advance diffractometer (Bruker) with Cu K_α radiation (40 kV, 30 mA). The 2θ scan range was 20–90° with a step

Table 5.1: *Flame mixture composition and the calculated flame adiabatic temperatures.*

ϕ	Mixture mole fractions			T_{ad},
	C_2H_4	O_2	Ar	K
0.35	0.035	0.300	0.665	2073
0.50	0.035	0.210	0.755	2141
0.70	0.040	0.172	0.788	2327
0.80	0.040	0.150	0.810	2336
0.90	0.045	0.150	0.805	2437
1.00	0.050	0.150	0.800	2500
1.10	0.054	0.147	0.799	2518
1.30	0.061	0.141	0.798	2454
1.50	0.075	0.150	0.775	2422
1.67	0.103	0.185	0.712	2542
2.00	0.130	0.195	0.675	2402
2.30	0.172	0.224	0.604	2340
2.50	0.209	0.251	0.540	2309

size of 0.02° and 3 s acquisition time per step. Zero-background silicon sample holders were used with powder samples pressed to create a dense film.

X-ray photoelectron spectra (XPS) were recorded using a Kratos AXIS Ultra photoelectron spectrometer (Kratos Analytical Ltd.) fitted with a monochromatic Al K_α source (1486.71 eV, 5 mA, 15 kV). The photoelectrons were collected at an electron take-off angle of 90°. The binding energy shift is corrected by setting the C–C binding energy to 284.8 eV.

Transmission electron microscopy (TEM) images and selected area electron diffraction (SAED) patterns were taken with a JEM-2100F FETEM (JEOL Ltd.) with 200 kV accelerating voltage. The TEM samples were prepared by applying a few drops of TiO_2 suspension in ethanol on TEM grids followed by air-drying.

5.3 Computational details

The XRD patterns were simulated with BRASS [22] using a simple isotropic size broadening model (Lorentzian) and experimental instrumental broadening parameters, assuming a zero background and 9 nm crystallite size. Instrumental broadening parameters were obtained experimentally with standard reference material 640e from NIST.

The undoped flames were simulated using *k*inetics®[49] as one-dimensional stagnation flows coupled with detailed hydrocarbon chemistry described by the USC-Mech II model [234] according to the methodology outlined in Chapter 3. The stagnation surface temperature was taken as 420 K [221]. The flame standing location was estimated to be approximately 3.5 mm from the stagnation surface. The boundary conditions of the stagnation flow simulations were imposed to recover this flame standing distance, similar to the approach used in Chapter 4. These boundary conditions are summarised in Table 5.2.

Table 5.2: *Boundary conditions imposed at nozzle exit (1 cm) and stagnation surface: burner exit temperature, T_0, velocity, u_0, and velocity gradient, a_0, and stagnation surface temperature, T_s.*

Case	T_0, K	u_0, cm/s	a_0, s^{-1}	T_s, K
$\phi = 0.50$, undoped	423.15	436	-220	420
$\phi = 1.00$, undoped	423.15	436	-30	420
$\phi = 1.67$, undoped	423.15	450	0	420

Constant-volume equilibrium simulations at 1 atm and 150°C were performed using *k*inetics® to estimate the adiabatic flame temperature (summarised in Table 5.1). It is noted that the adiabatic flame temperature is usually slightly higher than the actual flame temperature as there is convective heat loss to the colder stagnation plate.

5.4 Results and discussion

5.4.1 Particle morphology

Figure 5.2 shows the TEM images of the particles and the measured particle sizes. The particles form agglomerates consisting of nearly spherical primary particles. Similar particle shapes and sizes were observed in previous studies [221, 155] and in Chapter 4. Given the particles sampled from the flame are mostly spherical with a small degree of aggregation (as discussed in Chapter 4), the agglomerates are likely formed during the particle deposition and TEM sample preparation.

The volume-averaged primary particles diameter, $\bar{d}_V$, is approximately 9 nm which is slightly larger than expected based on the findings from the previous chapter. This is due to the fact that a volume averaging is used here compared to the number averaging used in Chapter 4. The volume averaging is used here as the intensity of XRD peaks scale with the material

volume. In addition, in this chapter, bias towards larger particles is likely as small particles are difficult to identify from the TEM images of the agglomerates. This suggests that the no significant particle growth occurs on the substrated during sample collection. In addition, no significant difference in $\bar{d}_V$ is observed with varying equivalence ratio despite approximately 500 K maximum variation in the adiabatic flame temperature (Table 5.1).

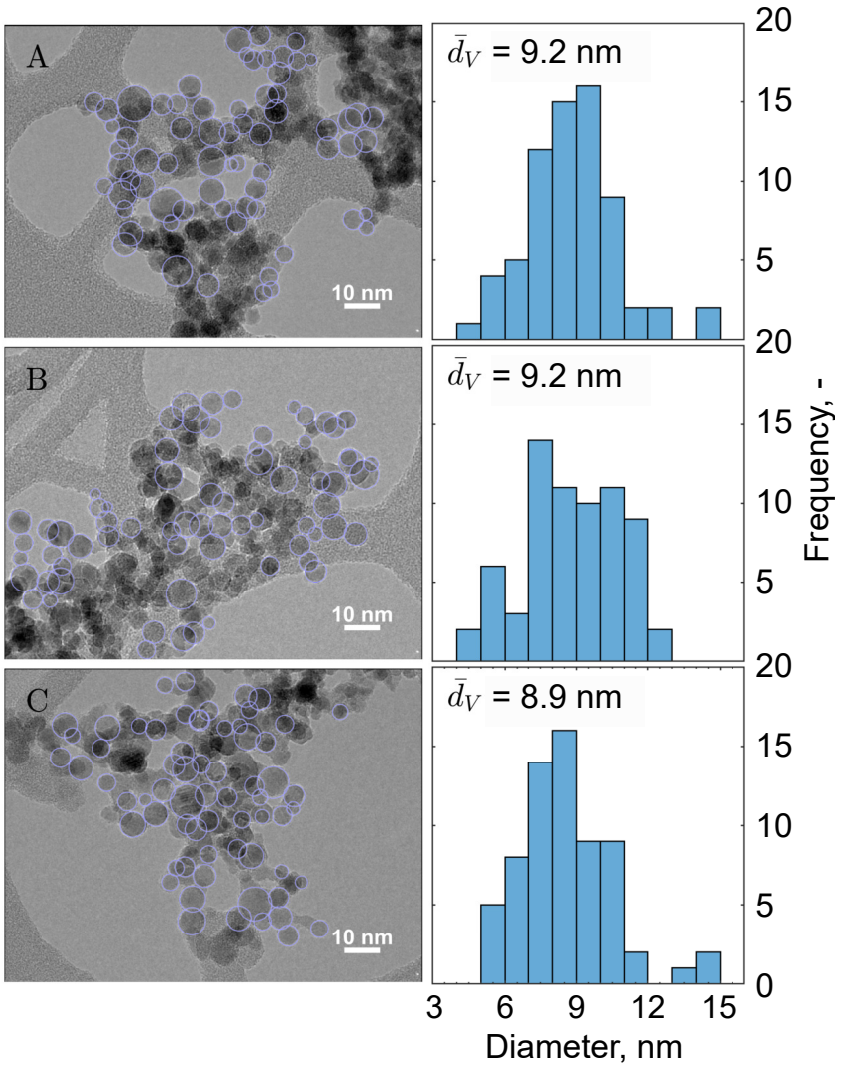

Figure 5.2: *Annotated TEM images (left panel) of particles prepared in lean (A, $\phi = 0.50$), stoichiometric (B, $\phi = 1.00$), and rich (C, $\phi = 1.67$) flames. Particles size histograms (right panel) and the volume averaged particle size, $\bar{d}_V$, are from manual measurements of approximately 70 spherical primary particles on each TEM image; standard deviation, SD = 2.0 nm (A), 2.0 nm (B), 2.2 nm (C).*

The insensitivity of particle size to maximum flame temperature could be explained by the reduced particle residence time in hotter flames due to an increased convective velocity.

Figure 5.3 shows the simulated temperature profiles and particle residence times for all three flames. The residence time is calculated from the convective and thermophoretic velocities experienced by the particles. The profiles demonstrate that the particle residence time decreases as the flame temperature increases. This is expected as higher temperature leads to more gas expansion and subsequently higher convective velocity. This compensating effect results in the close particle sizes observed in Fig. 5.2.

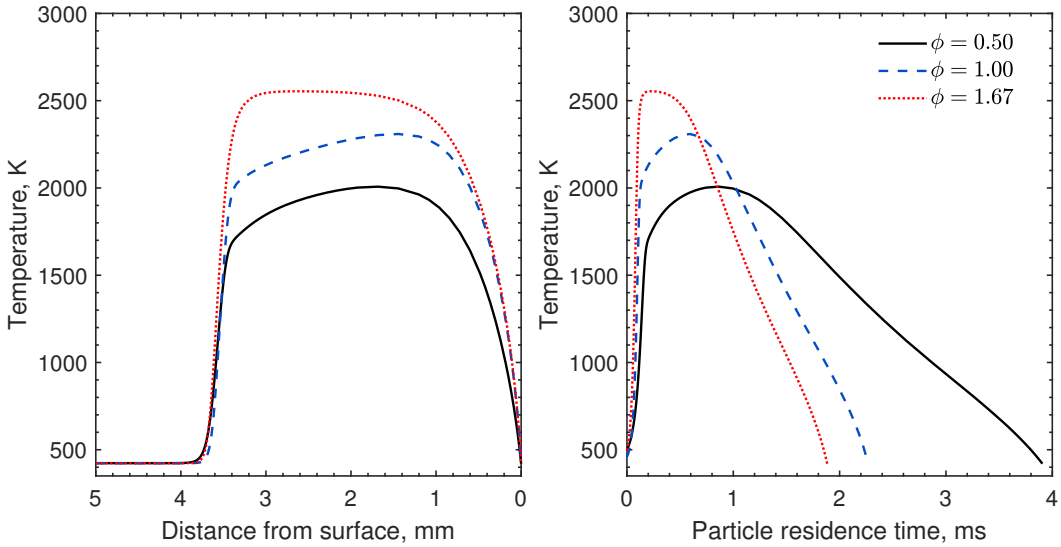

Figure 5.3: *Simulated (a) temperature and (b) particle residence time profiles in undoped lean ($\phi = 0.50$), stoichiometric ($\phi = 1.00$), and rich ($\phi = 1.67$) flames. Particles are assumed to be formed at $T \approx 500$ K ($t_{res} = 0$).*

5.4.2 Qualitative phase identification

Powder XRD and electron diffraction analysis

The TiO_2 phases that can be produced with the investigated flames were identified for three representative synthesis conditions of fuel lean ($\phi = 0.50$), stoichiometric ($\phi = 1.00$), and fuel rich ($\phi = 1.67$). Figures 5.4(b), (e), and (h) show the XRD patterns for these conditions. For the purposes of qualitative comparison, simulated XRD patterns were produced with a simple isotropic size broadening model (Lorentzian) and experimental instrumental broadening parameters, assuming a zero background and 9 nm crystallites based on the observed primary particle size (Fig. 5.2). A complete Rietveld refinement of the XRD

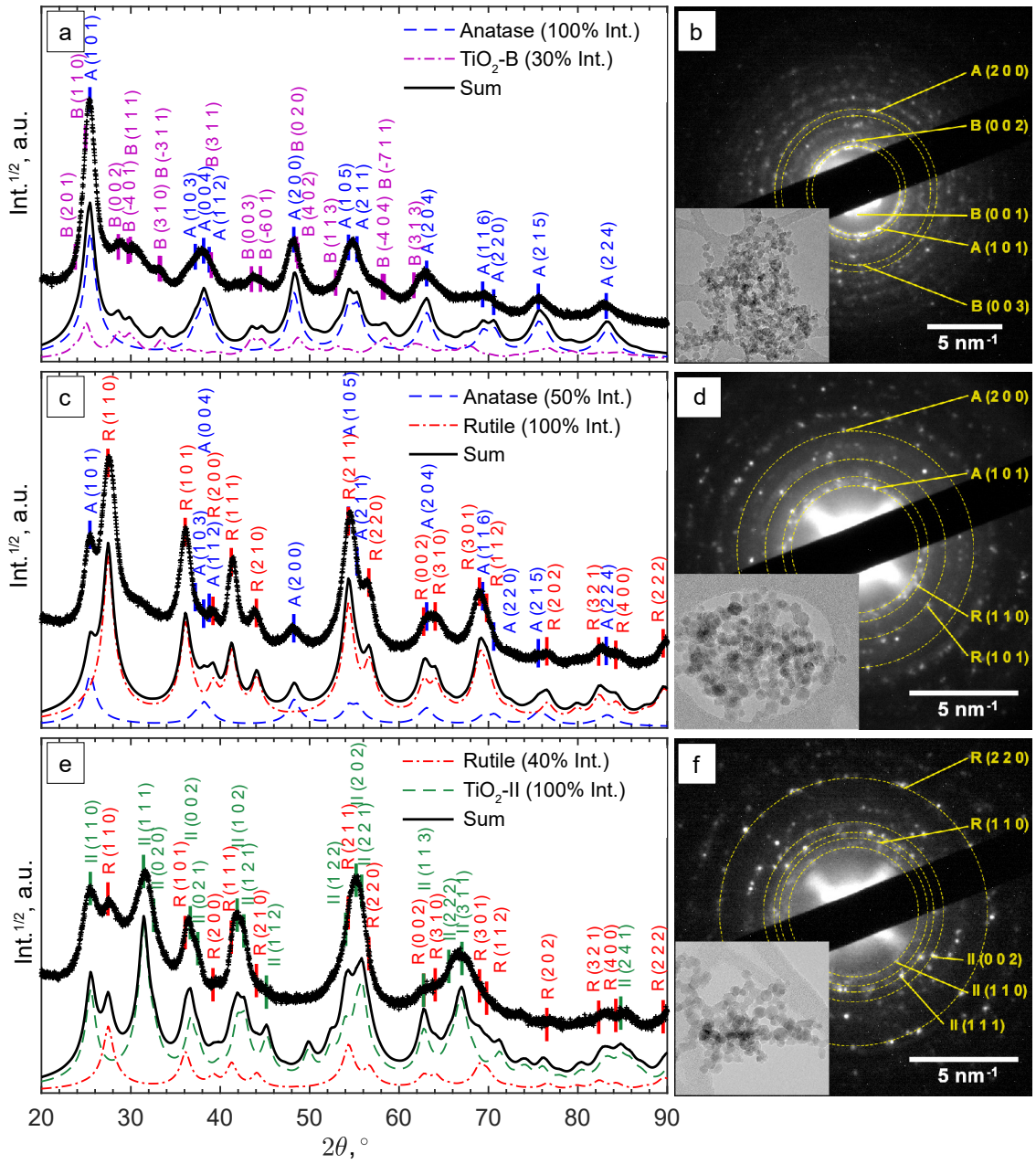

Figure 5.4: *Characterisation of particles prepared in fuel lean (**top row, a-b**), stoichiometric (**middle row, c-d**), and rich (**bottom row, e-f**) flame conditions. **Left column**: experimental (+) and simulated (lines, see text for details) XRD patterns for qualitative comparison. The locations of the main diffraction peaks for different TiO_2 polymorphs (ICSD catalogue) are annotated and marked with vertical ticks. **Right column**: Selected area electron diffraction (SAED) patterns with labels for the main diffraction spots and the corresponding TEM images as inset.*

patterns was not possible due to the complex mixtures of nano-sized crystals. It is suspected that the rapid sample quenching introduced additional peak broadening through microstrain (see below) and possibly some degree of anisotropy in the strain and size induced broadening. In the following discussion, prefixes A, R, B and II denote anatase, rutile, TiO_2-B and TiO_2-II crystal phases, respectively.

In the lean flame ($\phi = 0.50$, Fig. 5.4(a) and (b)), the major diffraction peaks can be ascribed to anatase (ICSD No. 92363), e.g., A(1 0 1) at 25.3° and A(2 0 0) at 48.1°. The presence of TiO_2-B (ICSD No. 41056) can be identified from the smaller peaks at $2\theta = 27$–34°, i.e. B(0 0 2), B(1 1 1), B(3 1 0). The simulated XRD pattern with a 100:30 intensity ratio of anatase to TiO_2-B correctly predicts all the main peaks observed in the experimental pattern. The simulated 2θ-dependent peak broadening due to crystal size is insufficient to reproduce the broad peaks observed at high angles, e.g., A(2 1 5) and A(2 2 4), suggesting additional peak broadening due to micro strain.

In the stoichiometric flame ($\phi = 1.00$, Fig. 5.4(c) and (d)), rutile (ICSD No. 16636) formed in addition to anatase, as is evident from the R(1 1 0), R(1 0 1), R(1 1 1), and R(2 1 1) reflections. The presence of a broad shoulder at $2\theta = 31°$ potentially originates from a third phase, such as a small amount of TiO_2-B or TiO_2-II. The qualitative agreement observed between the experimental and simulated XRD patterns confirms that rutile and anatase are the main polymorphs formed in the stoichiometric flame (at approximately 2:1 intensity ratio).

In the rich flame ($\phi = 1.67$, Fig. 5.4(e) and (f)), a significant reflection at $2\theta = 31.5°$ is observed which is consistent with a II(1 1 1) reflection of TiO_2-II polymorph (ICSD No. 158778). It is noted that the peak at 25.5° can either be ascribed to A(1 0 1) or II(1 1 0) but the lack of the A(2 0 0) reflection at 48° suggests that the latter is the case. In addition, rutile can be identified from the R(1 1 0) peak at 27.5°. Comparison between the simulated and measured XRD pattern indicates slightly broader experimental peaks at low 2θ, indicating that the measured crystals are smaller than the 9 nm assumed for the simulated XRD. The difference in peak broadening increases with 2θ, suggesting the presence of additional micro strain. Furthermore, it can be observed that some peaks such as II(1 1 2) at 44.5° and II(1 1 3) at 62.5° are significantly smaller and/or broader than expected, most likely due to anisotropy in the crystals. It is interesting to note that similar XRD patterns with strong anisotropy in size and strain-induced broadening were observed in rutile and TiO_2-II formed through high-energy milling experiments [61, 17].

For all three flames, the selected area electron diffraction patterns (SAED) of agglomerated particles (Figs. 5.4(b), (d), and (f)) are consistent with the powder XRD patterns. The

presence of TiO_2 phase mixtures on an aggregate scale suggests intimately mixed crystals at particle level. For samples prepared in lean flames, the presence of diffraction spots with approximately 0.63 nm lattice spacing corresponding to B(0 0 1) reflection confirms the presence of TiO_2-B phase (Fig. 5.4(b)).

HRTEM image analysis

The four phases discussed above can be further verified using HRTEM images where the crystal lattices are directly imaged. In most cases, images showing multiple planes are used to allow identification of these phases by their lattice spacings and the interplanar angles. The interplanar angles are very useful for phase identification as they are less affected by the accuracy of the TEM magnification. These HRTEM images are shown in Fig. 5.5. The lattice spacings are analysed using the fast Fourier transform (FFT) analysis of selected areas on the images as shown. The spots from the FFT analysis reflect the periodicity of the crystal lattices. The spots used for measurements are circled and annotated. The results of the FFT analysis are summarised in Table 5.3. The corresponding lattice spacings and the interplanar angles for each phase from the ICSD catalogues are shown for comparison.

The lattice spacings measured from the HRTEM images (Table 5.3) agree with those from the ICSD data to within 5% accuracy (a reasonable uncertainty expected from TEM [244]). It is also noted lattice spacings of nanocrystals may differ slightly to those from the ICSD reference data due to the size effects.

Figure 5.6 presents the same HRTEM images as shown in Fig. 5.5 but with the areas of interest enlarged. In some cases, the particles are slightly faceted, e.g., Figs. 5.6(a) and (b) while some surface amorphous layers are observed in other cases, e.g., Figs. 5.6(c) and (d).

These images are of samples collected from flames with different equivalence ratios. Anatase and TiO_2-B particles are identified in samples prepared in $\phi = 0.5$ flame. Rutile and TiO_2-II particles are identified in samples prepared in $\phi = 1.0$ and $\phi = 1.67$ flames, respectively. The corresponding structural models for these phases are also shown in Fig. 5.6. This directly confirms the presence of the anatase, rutile, TiO_2-B and TiO_2-II phases identified through the powder XRD and SAED pattern analyses as discussed previously. In particular, TiO_2-B can be readily identified by the large spacing of B(0 0 1) planes in Fig. 5.6(b) ($d = 6.32$ Å, ref. $d_{\mathrm{B}(0\,0\,1)} = 6.24$ Å). In Fig. 5.6(d), lattice planes corresponding to II(1 1 $\bar{1}$) ($d = 2.86$ Å, ref. $d_{\mathrm{II}(1\,1\,\bar{1})} = 2.85$ Å) and II(0 1 0) ($d = 5.63$ Å, ref. $d_{\mathrm{II}(0\,1\,0)} = 5.50$ Å) are marked. The measured interplanar angle is 60.5° (ref. $\alpha_{\mathrm{II}(1\,1\,\bar{1})/(0\,1\,0)} = 58.8°$). It is noted that the phases

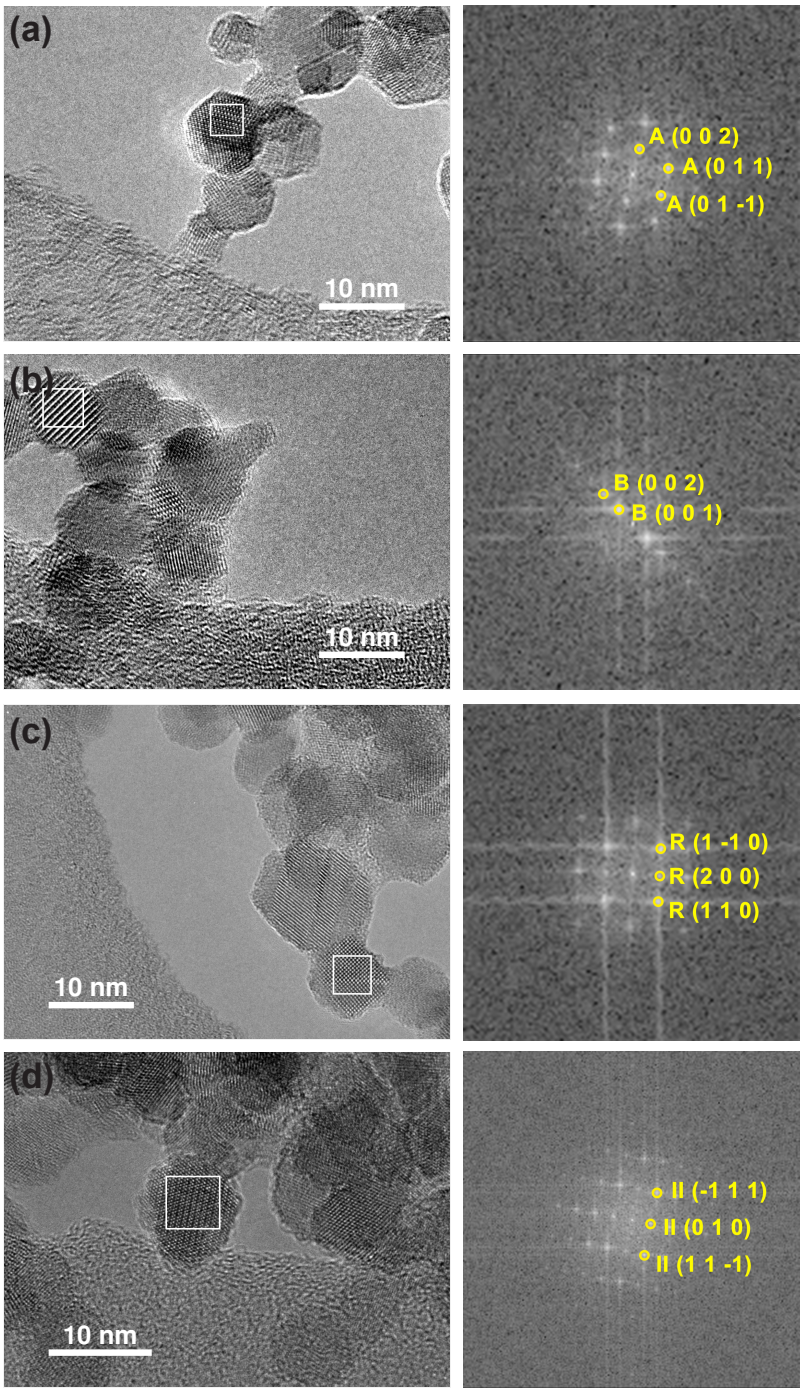

Figure 5.5: *HRTEM images and the corresponding annotated FFT spectra (right): (a) Anatase, $\phi = 0.50$, (b) Brookite, $\phi = 0.50$ (c) Rutile, $\phi = 1.00$, and (d) TiO_2-II, $\phi = 1.67$. The summary of FFT analysis is given in Table 5.3.*

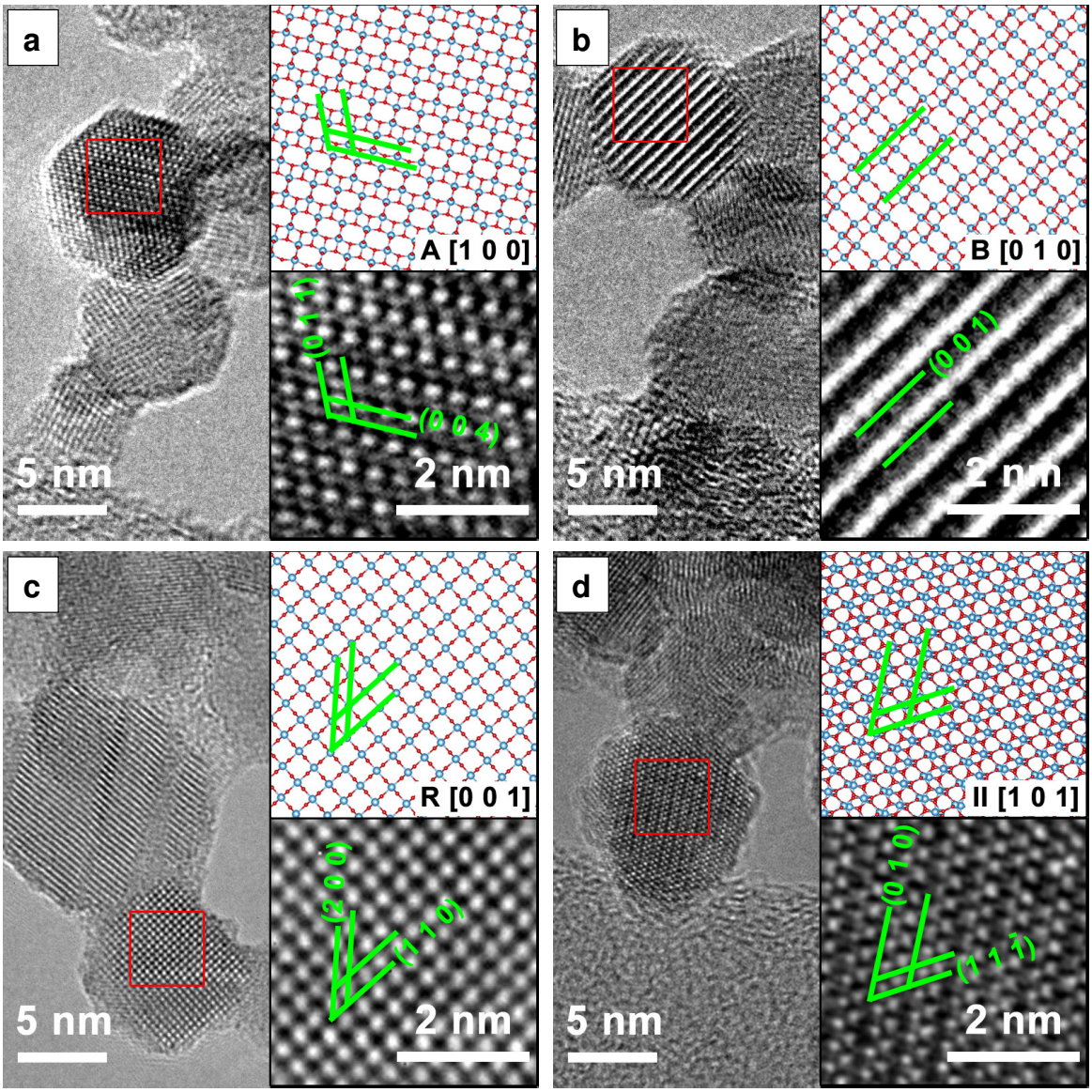

Figure 5.6: *HRTEM images of the four TiO_2 polymorphs identified at different flame equivalence ratios ϕ: (a) Anatase, $\phi = 0.50$, (b) TiO_2-B, $\phi = 0.50$, (c) Rutile, $\phi = 1.00$, (d) TiO_2-II, $\phi = 1.67$. The bottom inset is an enlarged view of the area in the red square. The top inset is a ball-and-stick representation of the particular polymorph with the same orientation as in the HRTEM image (Ti: blue, O: red). The relevant crystal planes are annotated in green.*

Table 5.3: *Lattice spacing, d, and the interplanar angles (relative to the first plane), α, obtained from FFT analysis of HRTEM images shown in Fig. 5.5. The reference data are taken from ICSD catalogue (see text for details on catalogue number for each phase).*

Image	Measured (FFT)		Reference (ICSD)		
	d, Å	Relative α, °	Lattice plane	d, Å	Relative α, °
5.5(a)	3.67	0	A (0 1 $\bar{1}$)	3.50	0
	3.56	44.5	A (0 1 1)	3.50	43.6
	4.82	113.6	A (0 0 2)	4.72	111.8
5.5(b)	6.32	0	B (0 0 1)	6.24	0
	3.15	0.4	B (0 0 2)	3.12	0
5.5(c)	3.38	0	R (1 1 0)	3.25	0
	2.35	43.5	R (2 0 0)	2.30	45
	3.34	92.4	R (1 $\bar{1}$ 0)	3.25	90
5.5(d)	2.86	0	II (1 1 $\bar{1}$)	2.85	0
	5.63	60.5	II (0 1 0)	5.50	58.8
	2.87	117.9	II ($\bar{1}$ 1 1)	2.85	117.7

identified through HRTEM images are not necessarily representative of the whole samples as the analysis is focused on only a few particles with clear lattices.

Presence of crystal defects

While Fig. 5.6 indicates the presence of single crystal primary particles, other TEM images showed stacking faults and possibly even multiple crystals within single primary particles. The examples of these TEM images are show in Fig. 5.7. These different crystal domains are especially evident in particles prepared in the fuel rich flame ($\phi = 1.67$), explaining the anisotropy observed in the powder XRD patterns (Fig. 5.4(h)). In addition, some shear structures are observed, e.g., Figs. 5.7(a) and (b), which are common in reduced rutile. Unfortunately, it was not possible to confidently determine the actual crystal phases, orientations and boundaries or their epitaxial relationships, if any, in a single primary particle.

5.4.3 Effects of flame equivalence ratio

Additional XRD patterns of samples prepared in fuel lean ($\phi = 0.35$–1.00) and rich ($\phi = 1.00$–2.50) flames were measured to elucidate the effect of fuel/oxygen equivalence ratio ϕ on the formed TiO_2 polymorphs (Fig. 5.8). In the range of $\phi = 0.35$–0.90, no substantial

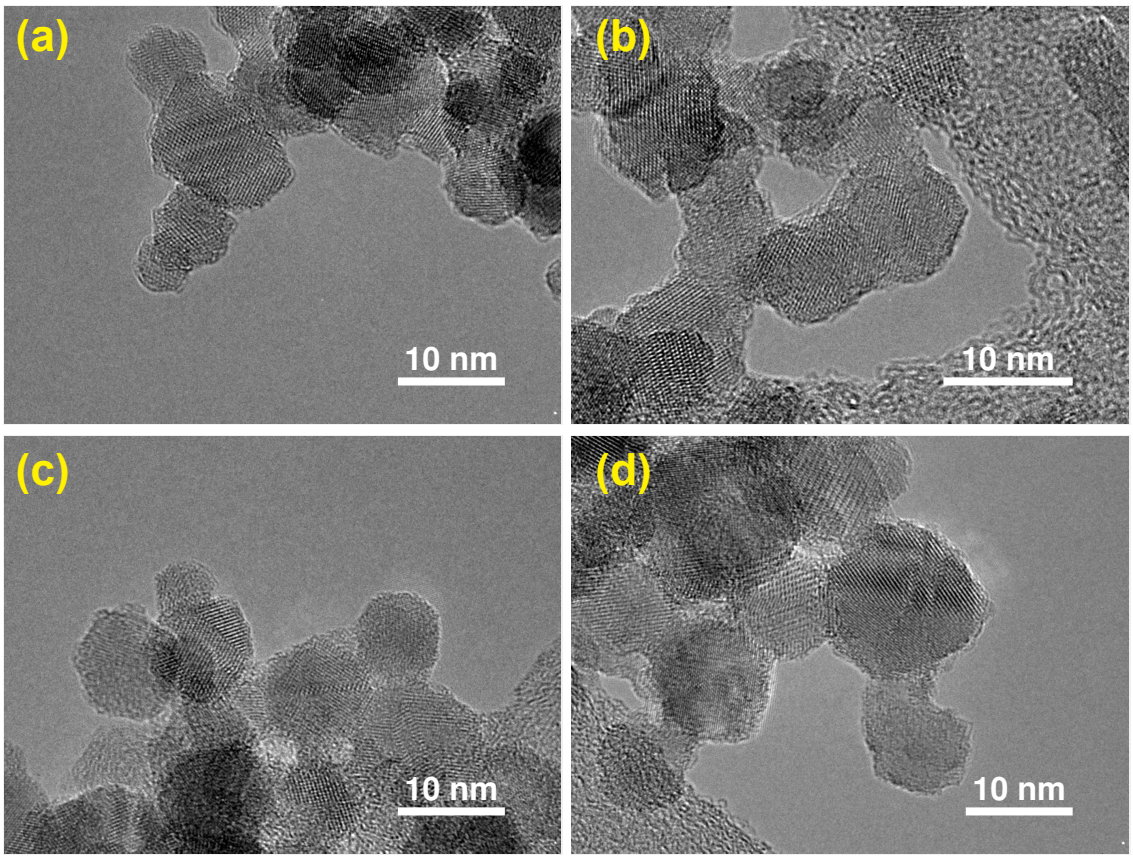

Figure 5.7: *HRTEM images showing primary particles with possibly multiple crystal domains (not indexed) prepared in flames with equivalence ratio, ϕ, of 1.67 (a, b) and 1.00 (c, d).*

change is observed despite the significant variations in adiabatic flame temperatures of up to 400 K (Table 5.1). The particles are predominantly anatase with some amount of TiO_2-B as discussed in Section 5.4.2. Using a rotating stagnation plate, very similar to the one used in this study, Memarzadeh et al. [155] and Liu et al. [135] observed only anatase in lean flames ($\phi = 0.45$–0.9) with a small amount of rutile. McCormick et al. [146] reported the formation of anatase with a minor amount of a metastable phase identified as brookite prepared in a $\phi = 0.36$ flame followed by annealing at 773 K. This discrepancy likely arises from varying stagnation surface temperatures in these studies, leading to different quenching rates compared to this work. For example, Riad et al. [189] recently reported, for the first time, the formation of the metastable TiO_2-B phase (27% as mixture with anatase and amorphous phases) in samples prepared through flame spray pyrolysis (FSP) synthesis. In their study, TiO_2-B was preferentially formed in oxygen rich conditions, consistent with the observations made in this work. As increasing oxygen content leads to shorter residence time

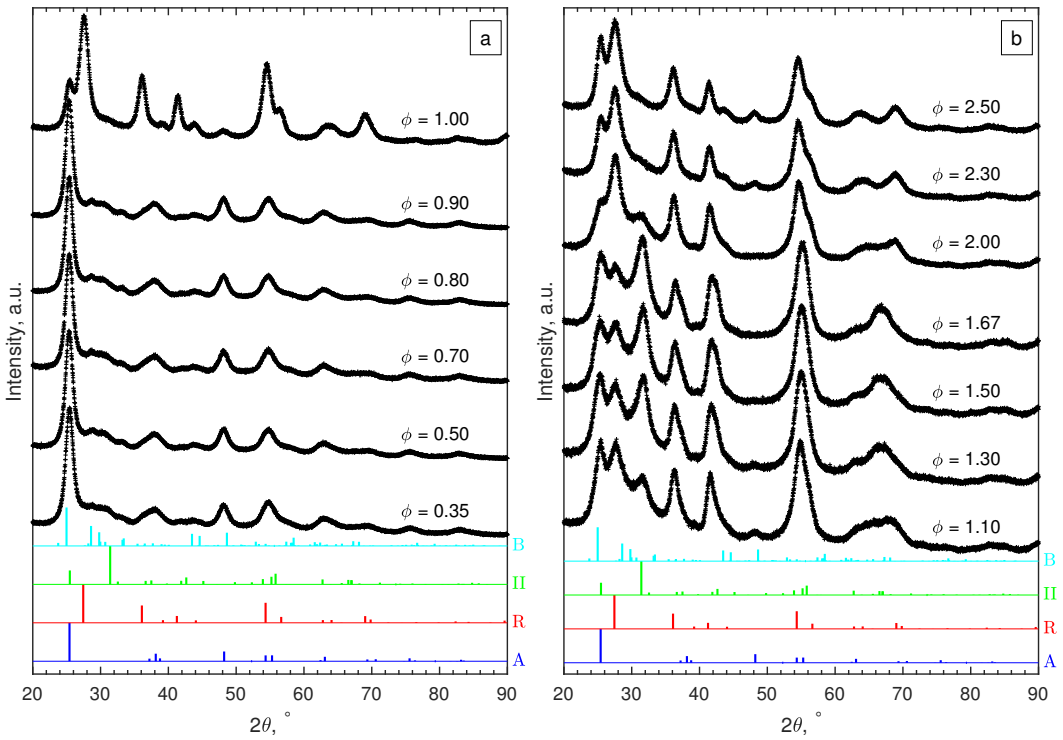

Figure 5.8: *Powder XRD patterns of particles prepared at varying flame mixture equivalence ratios, ϕ: (a) fuel-lean and (b) fuel-rich flames. Reference XRD patterns for different polymorphs from the ICSD catalogue are given at the bottom (A: Anatase, B: TiO_2-B, R: Rutile, II: TiO_2-II).*

in the FSP, it is suggested that the short residence time is responsible for the formation of TiO_2-B.

Near the stoichiometric point ($\phi = 0.90$–1.00), anatase and rutile are the two main phases observed. The rutile content increases with increasing equivalence ratio as is evident from the R(1 1 0) peak at 27.5°. An anatase/rutile transition near the stoichiometric point was also observed by Liu et al. [135]. The strong sensitivity of the anatase/rutile ratio to the equivalence ratio is in further agreement with the study by Kho et al. [108].

As the equivalence ratio is increased further ($\phi = 1.00$–1.30), the XRD results indicate that the anatase content decreases (i.e. A(2 0 0) peak at 48.1°) while TiO_2-II starts to form. It is noted that the XRD results obtained by Liu et al. [135] at $\phi = 1.15$ and 1.33 also showed a peak at $2\theta = 31.5°$ but it was attributed to the presence of impurity (Ti_3O_5). As discussed previously, it is suggested that this peak originates from the II(1 1 1) reflection instead. It should also be noted that Liu et al. [135] assigned the reflection at 25.3° to A(1 0 1) but that it might also be caused by II(1 1 0), which would explain the absence of the A(2 0 0) reflection in their pattern. The higher intensity of the $2\theta = 31.5°$ peak in the present study is

likely caused by differences in the synthesis conditions such as the deposition time, actual gas flow rates, stagnation surface temperature, or burner nozzle diameter.

In the ϕ range of 1.50–1.67, the two main phases identified are rutile and TiO_2-II with significant amount of the latter. The as-synthesised powders appeared slightly blue suggesting the presence of lattice oxygen deficiencies [31, 217]. To the best of our knowledge, our work is the first to report a substantial amount of TiO_2-II prepared through flame synthesis. A detailed discussion on the possible formation routes is given below.

For the very fuel rich flame condition (ϕ = 2.00–2.50), soot is formed together with TiO_2 causing the obtained powder to be coloured grey-black. Based on the XRD pattern (Fig. 5.8(b)), rutile and TiO_2-II are still present but with higher content of rutile. Additionally, anatase is formed as the equivalence ratio increases above 2.0 as evidenced by the A(2 0 0) peak at 48.1°.

XPS analysis

The Ti 2p XPS spectra of samples from the lean, stoichiometric, and rich flames (Fig. 5.9(a)) show very similar binding energies and intensities for Ti^{4+} $2p_{3/2}$ and Ti^{4+} $2p_{1/2}$ peaks with a $2p_{3/2}$-$2p_{1/2}$ splitting value of 5.8 eV, consistent with reported values for TiO_2 [21]. No detectable Ti^{3+} presence is observed suggesting that the particle surface is completely oxidised regardless of the difference in the oxygen environment (positions of Ti^{3+} binding energies are marked for reference in Fig. 5.9(a)) [45]. The main O 1s peak around 530.1 eV can be assigned to bulk oxygen in TiO_2 (Fig. 5.9(b)). The smaller peaks at higher binding energies likely belong to surface oxygens, the acidic OH(s) and the basic TiOH, formed from H_2O chemisorption on the surface [199].

5.4.4 Formation of TiO_2-II polymorph

In the rich flames where TiO_2-II is formed (ϕ = 1.10–2.00), the calculated adiabatic flame temperature is 2400–2500 K (Table 5.1). At this temperature, incipient particles in the flame are likely to be melt or liquid-like without any long range order [7] (melting point of bulk TiO_2 is approximately 2100 K). The particles grow in size through surface growth and coalescence until they approach the stagnation surface where they are rapidly cooled and solidify (Fig. 5.3). The presence of both TiO_2-II and rutile in these samples most likely indicates that one of them formed first and that the other developed through a phase transformation. One possibility is the formation of solid rutile particles followed by a solid-

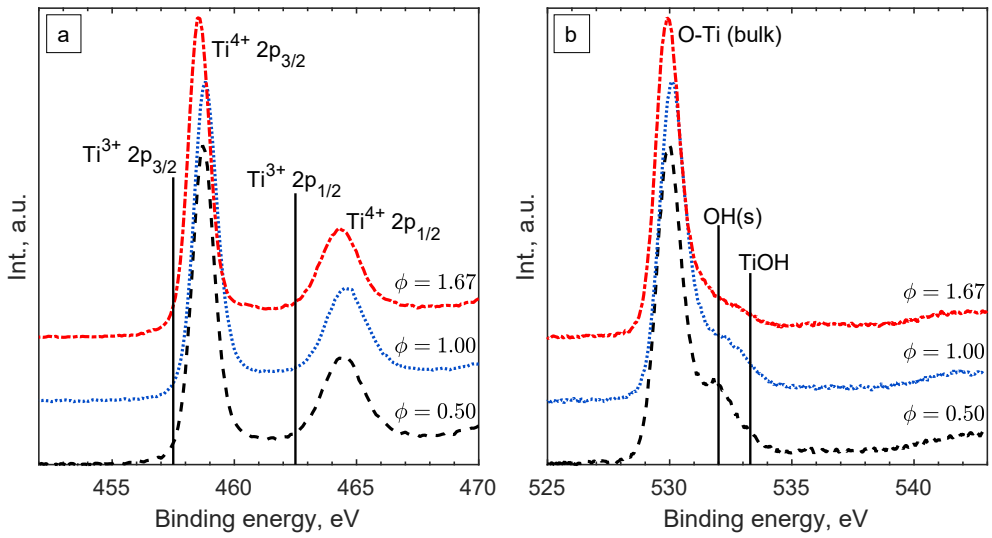

Figure 5.9: *Ti 2p (a) and O 1s (b) XPS spectra of TiO_2 particles synthesised at lean, stoichiometric, and rich flame conditions with normalised intensities.*

state transformation to TiO_2-II. Another option would be the direct formation of TiO_2-II (or a pre-TiO_2-II intermediate phase) and a subsequent solid-state transformation to rutile. Both scenarios are considered here and will be discussed below.

Numerous works have documented solid-state transformations of rutile, anatase, or brookite to TiO_2-II but this typically requires high-pressure conditions of up to 5-9 GPa [246, 209]. Such high pressure can be achieved through static pressing, shock wave, or high-energy milling experiments. As the TiO_2-II in the present study was prepared in an atmospheric pressure flame, a solid-state transformation of rutile to TiO_2-II is considered unlikely.

In order to elucidate the possibility of direct TiO_2-II formation with subsequent phase transformation to rutile, additional XRD patterns (Fig. 5.10) were recorded of samples collected for different durations on a water-cooled plate (instead of a rotating stagnation plate). Note that the surface temperature of the stationary plate is likely to be higher than of the rotating plate, thus the results in Figs. 5.8 and 5.10 are not directly comparable. Nevertheless, the change of phase composition with prolonged deposition time can give valuable information into the origin of the TiO_2 polymorphs. It can be observed in Fig. 5.10 that the rutile content increases with increasing deposition time and thus prolonged exposure to elevated temperatures. This suggests that TiO_2-II is formed first and that rutile originates from a solid-state phase transformation of the already deposited TiO_2-II particles. Furthermore, the solid-state transformation is consistent with the observed crystal domains within a single primary particle (Fig. 5.7) and the accompanied crystal anisotropy.

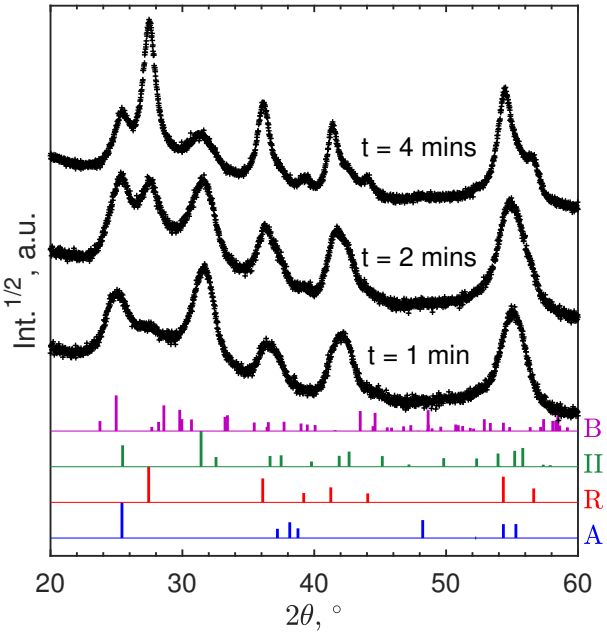

Figure 5.10: *Powder XRD patterns of particles prepared at equivalence ratio, ϕ, of 1.67 with non-rotating stagnation plate at varying deposition time, t. The XRD results are plotted as* $Int^{1/2}$ *to highlight the small features/peaks. Reference XRD patterns for different polymorphs from the ICSD catalogue are given at the bottom (A: Anatase, B: TiO_2-B, R: Rutile, II: TiO_2-II).*

A comparison to other ambient pressure TiO_2-II synthesis routes might help explain the role of the oxygen/fuel equivalence ratio on the TiO_2-II formation and the possible involvement of a pre-TiO_2-II intermediates. Aarik et al. [2] used atomic layer deposition (ALD) to grow TiO_2-II solid films from a $TiCl_4$ gas-phase precursor and water as the sole oxygen source. It was observed that TiO_2-II grows with some preferred orientation in the pure crystalline phase or in a mixture with rutile at low water doses (i.e. oxygen lean environments) [2], in agreement with our findings for fuel rich (i.e. oxygen lean) flames. A preferred growth orientation for TiO_2-II was also observed by Grey et al. [87] who reacted TiO_2 sub-oxide (with composition close to Ti_3O_5) with boiling sulphuric acid. They proposed that TiO_2-II was formed through a solid state transformation of an α-Ti_3O_5 due to a small long-range misfit between the atomic arrangements of α(1 1 0) and II(1 0 1) layers. Therefore, the results from Aarik et al. [2] and Grey et al. [87] demonstrate the importance of a non-stoichiometric surface layer [2] or solid state transformation from α-Ti_3O_5 sub-oxide in the formation of TiO_2-II crystals. Such sub-oxide species can potentially be formed in the gas phase through clustering of species such as Ti and TiO which have recently been identified as important products in TTIP decomposition [67]. Similarly, sub-oxide structures such as Ti_3O_5 and Ti_5O_7 have been reported to form during plasma synthesis of TiO_2 from TiC oxidation [98].

Therefore, it is possible that during flame synthesis, sub-oxide species form directly from Ti and TiO clustering in the fuel rich flames. In the high temperature flame environment, these sub-oxide clusters would continue to grow in a liquid-like state and at the same time be oxidised to form stoichiometric TiO_2. With high cooling rates, it is possible that the sub-oxide clusters solidify prior to complete oxidation. In this case, diffusion of lattice oxygen can occur to further oxidise the TiO_2 bulk, kinetically favouring the formation of TiO_2-II over rutile through a similar mechanism to that described by Grey et al. [87], i.e. solid-state transformation driven by the close structural match between (1 1 0) α-Ti_3O_5 and (1 0 1) TiO_2-II planes.

If sub-oxide species indeed solidified and later oxidised to TiO_2-II through the diffusion of lattice oxygen, some residue of Ti^{3+} could be expected. Such oxygen deficient titania was reported to be blue in colour [217], similar to the colour of the particles synthesised here with the fuel rich flames. Notably, the presence of some Ti^{3+} or oxygen vacancies in the particle core does not contradict the absence of a Ti^{3+} peak in the surface sensitive XPS spectra (Fig. 5.9). Rather, it is assumed that the particles have a completely oxidised surface as confirmed by XPS but some oxygen vacancies or Ti^{3+} exist in the core resulting in the blue coloration of the powder.

Surface modifications can also explain the TiO_2-II formation as they can strongly affect the energetics of nanocrystals [14, 135]. For example, Barnard and Zapol [15] show that anatase-to-rutile phase transition size is significantly affected by surface passivation. The effect of surface hydration has been demonstrated for Y_2O_3 polymorphic stability where nano-sized particles with a metastable high-pressure polymporh have been prepared in ambient pressure [260, 124]. The XPS data in Fig. 5.9(b) suggests that there are some qualitative differences in the shape and intensity of the surface oxygen peaks. However, the interpretation of these peaks is beyond the scope of the present work and will be investigated in future work.

Lastly, the decrease in the relative ratio of TiO_2-II to rutile and the onset of anatase formation in very rich flames ($\phi = 2.00 - 2.50$, Fig. 5.8(b)) is likely connected to the soot formation at these conditions. The formation of soot is evident from the gray-black coloration of the collected powder and is expected to decrease the flame temperature due to radiative heat loss and might further affect the gas-phase chemistry.

5.5 Chapter summary

Four different TiO_2 polymorphs and their mixtures were prepared with a single synthesis step using a premixed laminar stagnation flame. Metastable phases TiO_2-B and TiO_2-II were identified from diffraction and microscopy analysis. The obtained crystal structure was controlled by varying the fuel/oxygen equivalence ratio, ϕ, where mixtures of anatase/TiO_2-B, anatase/rutile, and rutile/TiO_2-II were formed in fuel-lean, stoichiometric, and fuel-rich conditions, respectively.

Notably, this is the first time that TiO_2-II is reported to form in atmospheric pressure flames even though similar XRD patterns were observed in previous flame studies. The mechanism leading to the formation of rutile/TiO_2-II mixtures in fuel rich (i.e. oxygen lean) flames was elucidated based on the phase composition as function of collection time and previous reports of TiO_2-II formation. It is proposed that rutile is formed through a solid-state transformation of TiO_2-II. The TiO_2-II formation hereby likely involves some titania sub-oxide intermediates that are subsequently oxidised to stoichiometric TiO_2-II. The formation of and transformation between four different TiO_2 polymorphs cannot be explained by the current understanding of TiO_2 phase formation and transformation mechanism, and thus requires re-evaluation of the current working hypotheses.

Chapter 6

Understanding the formation of TiO_2 polymorphs

This chapter presents experimental and computational studies of the relative stability of anatase and rutile in stagnation flame synthesis with stoichiometric $C_2H_4/O_2/Ar$ flames. The experimental measurements reveal a high sensitivity of anatase-rutile composition to the flame dilution. It is demonstrated that anatase formation is favoured in more dilute (colder) flames while rutile is favoured in less dilute (hotter) flames. A particle model with a detailed description of aggregate morphology and crystal phase composition is applied to investigate the anatase-rutile stability. A size-dependent phase transformation model is implemented in which rutile is formed for particles larger than a "crossover" size while anatase is formed for those smaller than the crossover size. Following the assumption commonly used in the literature, the nascent particles are assumed to be stoichiometric TiO_2 and thus the crossover size is given by some intrinsic thermodynamic quantities. This hypothesis captures the general trend in the measured anatase-rutile composition but fails to explain the sensitivity to the flame dilution. It is proposed that non-stoichiometric TiO_{2-x} oxide particles are formed during the early stages of particle formation. This likely affects the anatase-rutile relative stability through defect stabilisation and kinetic effects. Using the gas-phase reaction model, the particle composition is approximated from the relative concentration of $Ti(OH)_3$ and $Ti(OH)_4$. The particle composition is found to be strongly influenced by various assumptions about the growth mechanisms and rates which are still poorly understood.

6.1 Background

Thermodynamically, the relative stability of anatase and rutile is mainly governed by the competing contributions of bulk and surface energies. Below a certain particle size, surface energy dominates, leading to anatase nanoparticles being energetically more stable even though rutile is the thermodynamically more stable phase for bulk TiO_2. The appearance of a "crossover" size has been supported by experimental observations [255, 258]. In addition, the size-dependent stability can also be captured by a simple thermodynamic model of melting point depression of nano-sized particles [90] in which the melting point of nanoparticles depends on the solid/liquid interfacial energy.

While the size-dependent model has been proved satisfactory in some cases, it falls short of explaining the effect of other factors which are often observed in bottom-up syntheses, including flame-assisted synthesis. Studies have shown that the phase composition depends on factors such as temperature, oxygen environment, precursor, residence time, etc. It is generally accepted that oxygen-lean environments favour rutile formation over anatase. For flame synthesis, the anatase-rutile stability is especially sensitive when the mixture equivalence ratio (defined as the ratio of the actual fuel/oxygen ratio to the stoichiometric fuel/oxygen ratio) is near 1, i.e. a stochiometric mixture [155, 135, 108]. While the link between the oxygen environment and anatase-rutile relative stability is well established, the physical mechanisms behind it are not yet fully understood. In addition, the oxygen environment inevitably affects other synthesis conditions such as temperature and particle residence time. This is further complicated by the presence of other metastable phases such as TiO_2-B and TiO_2-II as discussed in the previous chapter.

The formation of the metastable TiO_2-II can be explained by sub-oxide intermediates. The formation of sub-oxides may explain the preferential formation of rutile over anatase in oxygen-lean environments [99]. Rutile is known to better accommodate a high concentration of oxygen defects compared to anatase [56, 28]. For example, rutile can be easily reduced to form TiO_{2-x} crystals through formation of defect structures such as double charged oxygen vacancies, Ti interstitial, or planar defects [56, 169, 131]. At higher oxygen vacancy concentration, a homologous series of Magnéli phase is formed which can be expressed as Ti_nO_{2n-1} with $n = 3,4,5,...$ [9, 172]. The Magnéli phase structures are related to rutile structure through the planar defect structure or so-called crystallographic shear structure. In rutile reduction experiments, a weight loss of more than 2% is shown to result in formation of lower oxides, Ti_3O_5 or Ti_2O_3 depending on the temperature [85].

The purpose of this chapter is to investigate the origin of the sensitivity of anatase-rutile stability in stoichiometric flames when the flame dilution is varied. This is done by comparing the model prediction to the experimental data. A size-dependent stability model commonly used in the literature which takes into account the contributions from bulk and surface energies is considered. The discrepancy between the model prediction and experimental observations is discussed. Non-stoichiometric metal oxides are proposed to form in the initial stages of particle formation which are likely to affect the anatase-rutile stability.

6.2 Experimental details

The setup used to prepare the TiO_2 nanoparticles in this study has been described in Chapter 5. Stoichiometric mixtures of premixed gas were used in this study with varying Ar dilution. This is summarised in Table 6.1. Titanium tetraisopropoxide (TTIP, $\geq 97\%$, Sigma-Aldrich) was injected into the unburned gas mixture with a syringe pump at 8 ml/h, corresponding to 365 ppm mole fraction.

Table 6.1: *The mixture fractions and equivalence ratio (ϕ) for all flames used in this study. T_{ad} and $X_{O_2,ad}$ are the adiabatic flame temperature and the equilibrium mole fraction of O_2 from the adiabatic simulations.*

Case	C_2H_4, %	O_2, %	Ar, %	ϕ	T_{ad}, K	$X_{O_2,\,ad}$
Flame 1	4.5	13.5	82.0	1.0	2419	0.91×10^{-2}
Flame 2	4.7	14.1	81.2	1.0	2453	1.04×10^{-2}
Flame 3	4.7	14.2	81.1	1.0	2457	1.05×10^{-2}
Flame 4	4.8	14.3	80.9	1.0	2466	1.09×10^{-2}
Flame 5	5.0	15.0	80.0	1.0	2500	1.24×10^{-2}
Flame 6	5.8	17.4	76.8	1.0	2603	1.78×10^{-2}

The rotating stagnation surface is used for sample deposition as described in Chapter 5. The deposition time for sample collection was 4 minutes. The water-cooled non-rotating plate was used as the stagnation surface with a pinhole orifice for size measurements with a DMS500 fast particulate analyser as described in Chapter 4. In both cases, a flat flame was stabilised at 3–4 mm above the stagnation plate depending on the flame mixture.

Powder X-ray diffraction (XRD) patterns of the collected samples were recorded with a D8 Advance diffractometer (Bruker) with Cu K_α radiation (40 kV, 30 mA). The 2θ scan range was 20–90° with a step size of 0.02° and 3 s per step. Zero-background silicon sample holders were used with powder samples pressed to create a dense and smooth film. The Rietveld

refinement was performed with BRASS [22] using a simple size-strain broadening model, a spline-interpolated background, and experimental instrumental broadening parameters. Instrumental broadening parameters were obtained experimentally with standard reference material 640e from NIST. The structural parameters from the inorganic crystal structure database (ICSD) were used for anatase (no. 92363), rutile (no. 16636), TiO_2-B (no. 41056), and TiO_2-II (no. 158778).

6.3 Computational details

The adiabatic flame temperature is obtained from equilibrium simulations with constant pressure and enthalpy performed with the *k*inetics® software package [49]. The initial conditions are taken as the conditions of the premixed gas mixtures without TTIP in Table 6.1.

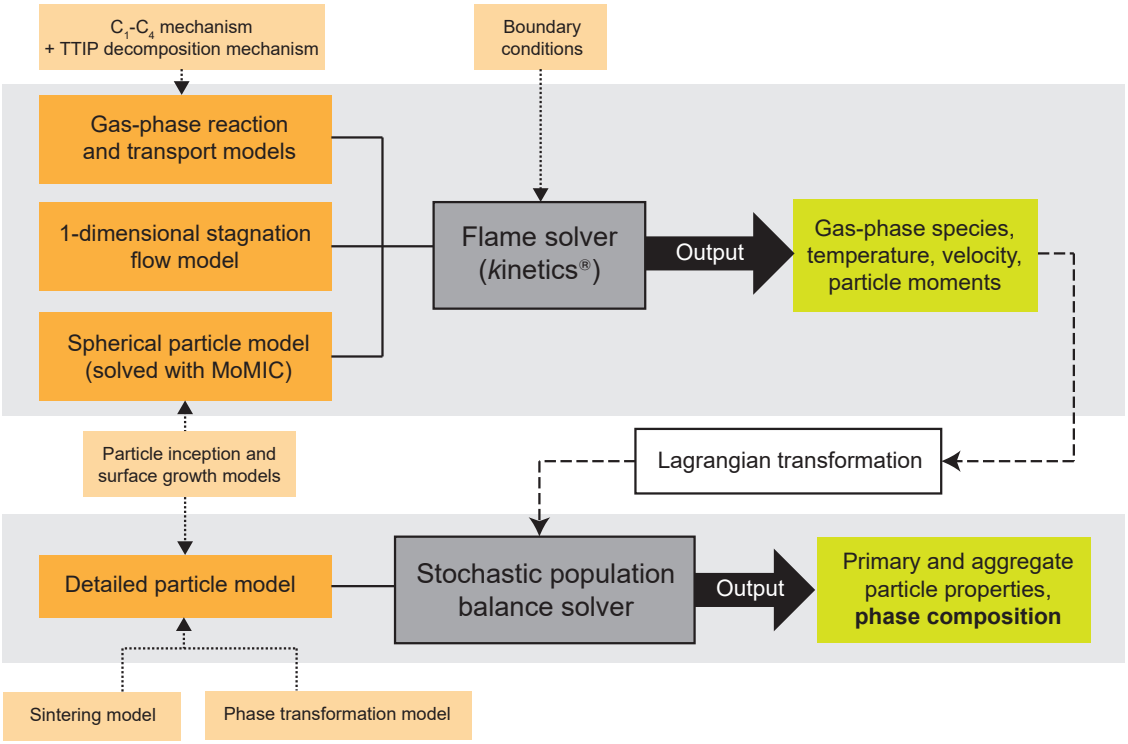

Figure 6.1: *A schematic of the modelling method used in this chapter. The grey boxes denote the general model frameworks.*

Particle formation in the stagnation flame is simulated using a two-step methodology [132] as shown in Fig. 6.1. Briefly, the flame structure, e.g., temperature profile and species composition, is modelled using a one-dimensional stagnation flow approximation with a

MoMIC-based particle model (Chapter 3). Subsequently, the resulting gas-phase profile is post-processed with the detailed particle model.

The modelling methodology is similar to that described in Chapter 4 except for the extension to the detailed particle model. The extended type space in the detailed particle model captures the atomic and crystal phase composition. The phase composition is determined by the phase transformation model which is described below.

6.3.1 Flame simulation

Gas-phase chemistry

The chemical reaction model consists of a TTIP decomposition mechanism combined with hydrocarbon combustion chemistry described by the USC-Mech II model [234]. The TTIP mechanism contains 25 Ti species and 61 reactions, and describes the decomposition of TTIP to titanium (IV) hydroxide ($Ti(OH)_4$) through the C_3H_6 and CH_3 abstraction pathways calculated by Buerger et al. [34] as well as dissociation reactions of $Ti(OH)_4$ to form small TiO_xH_y identified by Shmakov et al. [203] which are assumed to be barrierless due to the lack of available kinetics data. These are summarised below.

$$\begin{aligned} \mathrm{TTIP} \longleftrightarrow \ldots \longleftrightarrow \mathrm{Ti(OH)_4} \\ \mathrm{Ti(OH)_4} \longleftrightarrow \mathrm{TiO_xH_y} \end{aligned}$$

Particle inception and surface growth

In this work, $Ti(OH)_4$ and/or $Ti(OH)_3$ are treated as the collision species for the particle inception and surface growth reactions in the particle model. The inception (in) and surface growth (sg) reactions can be written generally as

$$\mathrm{Ti(OH)}_a + \mathrm{Ti(OH)}_b \xrightarrow{k_{\mathrm{in}}} \left[\mathrm{Ti_2O_{\frac{1}{2}(a+b)}}\right]_s + \frac{1}{2}(a+b)\mathrm{H_2O} \tag{6.1}$$

$$\mathrm{Ti(OH)}_a + \left[\mathrm{Ti_xO_y}\right]_s \xrightarrow{k_{\mathrm{sg}}} \left[\mathrm{Ti_{x+1}O_{y+\frac{1}{2}a}}\right]_s + \frac{1}{2}a\mathrm{H_2O}, \tag{6.2}$$

where a and b can be 3 or 4, the subscript s denotes the particle space. The rates k_{in} and k_{sg} are assumed to be collision limited and calculated according to Eqs 4.3 and 4.5. The collision diameters of $Ti(OH)_4$ and $Ti(OH)_3$ are assumed to be equal, $d_{\mathrm{Ti(OH)_3}} = d_{\mathrm{Ti(OH)_4}} = 0.5128$ nm.

Collision efficiency factors, γ_{IN} and γ_{SG}, are applied as multipliers to Eqs 4.3 and 4.5 for inception and surface growth, respectively.

The MoMIC-based particle model is a univariate model that only tracks the number of monomers (e.g., TiO_2 or Ti units) and thus is not able to track the Ti and O composition separately. The oxygen content of the particles is resolved during the post-processing step with the detailed particle model.

In this work the collision species and the growth rate parameters γ_{IN} and γ_{SG} are varied to investigate their influence on the predicted phase composition. These growth parameter sets are referred to in the rest of this work as $z^{(m)}$ with $m = 1,2,3$. These parameters are summarised in Table 6.2. The first set ($m = 1$) represents the parameters originally used in Chapter 4 with $Ti(OH)_4$ as the particle precursor. This model has been shown to compare reasonably well against the experimentally measured particle morphology (aggregate and primary particle sizes) for varying TTIP loadings and flame equivalence ratios. In the second set ($m = 2$), the same set of parameters were applied except both $Ti(OH)_4$ and $Ti(OH)_3$ species are used as precursor species. Lastly, to investigate the effect of the gas-phase chemistry on the phase formation, slower inception and surface growth are used in the third set ($m = 3$).

Table 6.2: *The growth parameters varied in this work ($z^{(m)}$, $m = 1,2,3$). Particle precursor is the species involved in inception and surface growth, γ_{IN} and γ_{SG} are the collision efficiencies for inception and surface growth processes.*

m	Particle precursor	γ_{IN}	γ_{SG}
1	$Ti(OH)_4$	1.0	1.0
2	$Ti(OH)_4$ and $Ti(OH)_3$	1.0	1.0
3	$Ti(OH)_4$ and $Ti(OH)_3$	1×10^{-3}	0.2

Boundary conditions

The flame distance is estimated using the same approach used in Chapter 4. Briefly, the experimental flame distance is taken as the location of the point at which the flame intensity is half of the maximum intensity (at the flame front). The simulation boundary conditions are then adjusted to recover the same flame distance as defined by the peak of H concentration.

The flame distances and the boundary conditions including burner exit temperature (T_0), velocity (u_0), velocity gradient (a_0), and the plate temperature (T_s) for all flames studied in this chapter are summarised in Table 6.3.

Table 6.3: *Flame distance (from the stagnation surface) and boundary conditions imposed at nozzle exit (1 cm) and stagnation surface.*

Case	Flame dist., mm	T_0, K	u_0, cm/s	a_0, 1/s	T_s, K
Flame 1, Ar = 82.0%	3.58	423.15	436	-290	600
Flame 2, Ar = 81.2%	3.78	423.15	436	-280	600
Flame 3, Ar = 81.1%	3.87	423.15	436	-290	600
Flame 4, Ar = 80.9%	3.94	423.15	436	-294	600
Flame 5, Ar = 80.0%	4.28	423.15	436	-307	600
Flame 6, Ar = 76.8%	5.88	423.15	436	-465	600

6.3.2 Stochastic population balance simulation

Particle type space

The detailed particle model has been described elsewhere by Lindberg et al. [134], so only a brief description is given here.

An aggregate particle P_q containing $n_\mathrm{p}(P_q)$ primary particles is represented as

$$P_q = P_q\left(p_1, \ldots, p_{n_\mathrm{p}(P_q)}, \mathbf{C}\right), \tag{6.3}$$

where a primary particle p_i, with $i \in \{1, \ldots, n_\mathrm{p}(P_q)\}$, is represented by its internal coordinates

$$p_i = p_i\left(\eta, r, \mathbf{x}\right), \tag{6.4}$$

and the matrix $\mathbf{C}$ represents the primary particle connectivity. r is the radius of the primary, $\mathbf{x}$ is the position of the primary centre relative to the centre of mass of the aggregate and η is the primary composition.

In the model used previously in Chapter 4 (based on the work by Lindberg et al. [134]), η describes the number of TiO_2 monomer. In this chapter, η is extended to describe the number of Ti and O atoms in each tracked phase. Three phases are considered here: anatase (An),

rutile (Ru), and non-crystalline (NC), which encompasses melt or amorphous phase,

$$\eta = (\eta_{\mathrm{Ti,NC}}, \eta_{\mathrm{O,NC}}, \eta_{\mathrm{Ti,An}}, \eta_{\mathrm{O,An}}, \eta_{\mathrm{Ti,Ru}}, \eta_{\mathrm{O,Ru}}). \tag{6.5}$$

The oxygen to titanium ratio, $\sigma_{\mathrm{O},i}$, and the rutile fraction, $\mathrm{f}_{\mathrm{R},i}$, of particle i are calculated as follows,

$$\sigma_{\mathrm{O},i} = \frac{(\eta_{\mathrm{O}})_i}{(\eta_{\mathrm{Ti}})_i} = \frac{(\eta_{\mathrm{O,NC}})_i + (\eta_{\mathrm{O,An}})_i + (\eta_{\mathrm{O,Ru}})_i}{(\eta_{\mathrm{Ti,NC}})_i + (\eta_{\mathrm{Ti,An}})_i + (\eta_{\mathrm{Ti,Ru}})_i} \tag{6.6}$$

$$\mathrm{f}_{\mathrm{R},i} = \frac{(\eta_{\mathrm{Ti,Ru}})_i}{(\eta_{\mathrm{Ti}})_i} = \frac{(\eta_{\mathrm{Ti,Ru}})_i}{(\eta_{\mathrm{Ti,NC}})_i + (\eta_{\mathrm{Ti,An}})_i + (\eta_{\mathrm{Ti,Ru}})_i}. \tag{6.7}$$

Particle processes

Similar to the models implemented in the flame solver, inception and surface growth are assumed to be collision limited. The rates of inception and surface growth are given by the free-molecular kernel with collision efficiencies γ_{IN} and γ_{SG} respectively.

A particle containing a single primary, assumed to be in the non-crystalline (NC) phase, is incepted from a bimolecular collision of gas-phase species, which can be either $Ti(OH)_3$ or $Ti(OH)_4$. The inception reaction (Eq. 6.1) can be written as

$$\begin{aligned} &\mathrm{Ti(OH)}_a + \mathrm{Ti(OH)}_b \rightarrow \frac{1}{2}(a+b)\mathrm{H_2O} + \\ &P_q\left(p_1\left(\eta_{\mathrm{Ti,NC}} = 2, \eta_{\mathrm{O,NC}} = \frac{1}{2}(a+b), \eta_{\mathrm{Ti,An}} = 0, \eta_{\mathrm{O,An}} = 0, \eta_{\mathrm{Ti,Ru}} = 0, \eta_{\mathrm{O,Ru}} = 0, r, \mathbf{x}\right), \mathbf{C}\right). \end{aligned} \tag{6.8}$$

Surface growth is described by collision events between a gas-phase species and a particle. As per Lindberg et al. [134], the mass is added to a primary p_i selected with probability proportional to its surface area relative to that of the entire aggregate particle. The number of Ti and O atoms of phase α in the selected primary is increased. The phase α is chosen with probability proportional to the relative phase composition of the primary. The surface growth reaction (Eq. 6.2) can be written as

$$P_q + \mathrm{Ti(OH)}_a \rightarrow P_q\left(..., p_i\left(\eta_{\mathrm{Ti},\alpha} + 1, \eta_{\mathrm{O},\alpha} + \frac{1}{2}a, ..., r + \Delta r, \mathbf{x}\right), ..., \mathbf{C}\right) + \frac{1}{2}a\mathrm{H_2O}. \tag{6.9}$$

The rest of the particle model parameters used in this work are given in Table 6.4. The rate of coagulation is given by the transition kernel [177] and the orientation and point of contact between the colliding particles is determined by ballistic cluster-cluster aggregation [101]. A molecular enhancement factor ε is applied to the free-molecular kernel for all collision processes. Sintering is described by a grain boundary diffusion model with optimised parameters A_s, $d_{p,\mathrm{crit}}$, and α_{crit}.

Table 6.4: *Summary of detailed particle model parameters used in this work.*

Parameter	Value
Collision limited processes:	
Enhancement factor, ε	2.64
Inception efficiency, γ_{IN}	see Table 6.2
Surface growth efficiency, γ_{SG}	see Table 6.2
Sintering:	
Prefactor, A_s	0.25
Critical diameter, $d_{p,\mathrm{crit}}$	4 nm
Critical exponent, α_{crit}	3
Other:	
Density, ρ_s	3.84 g/cm^3

In addition to the aforementioned particle processes, primary particles can also undergo a phase transformation, which is outlined below.

Phase transformation

A primary particle is able to undergo a temperature and size dependent phase transformation. This is treated as a discrete event that transforms the entire primary composition from one phase to another. The transformation event is independent from the processes described above, e.g., surface growth, sintering, coalescence, and therefore does not affect the particle morphology such as primary and aggregate sizes. The transformation event for particle i is controlled by two parameters: $T_{\mathrm{trans},i}$ and $d_{\mathrm{cross},i}$.

The transformation temperature $T_{\mathrm{trans},i}$ determines the temperature at which a transformation occurs between the non-crystalline and crystalline phases. Meanwhile, a crossover diameter $d_{\mathrm{cross},i}$ determines which crystal phase is formed (anatase or rutile). The dependencies of parameters $T_{\mathrm{trans},i}$ and $d_{\mathrm{cross},i}$ vary depending on the submodel assumptions discussed later in Section 6.5.4.

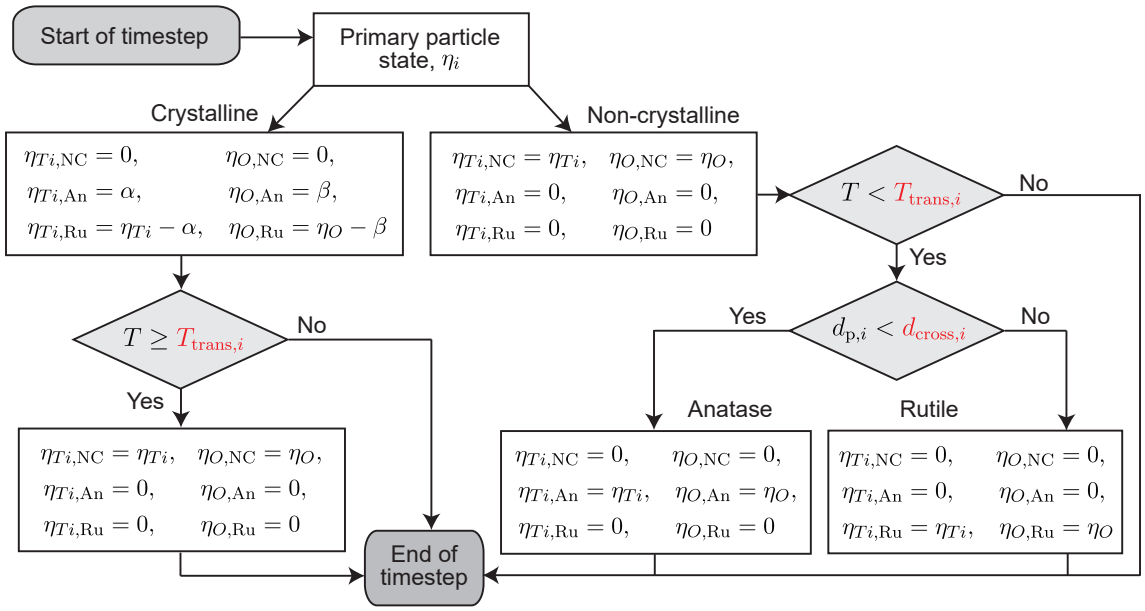

Figure 6.2: *Phase transformation algorithm. $T_{\mathrm{trans},i}$ and $d_{\mathrm{cross},i}$ (shown in red) are a function of the model parameter vector $\boldsymbol{\theta}$ which is defined in the submodel description.*

Figure 6.2 shows the schematic for the phase transformation algorithm. Above the transformation temperature $T \geq T_{\mathrm{trans},i}$, the primary, containing η_{Ti} titanium and η_{O} oxygen atoms, is in a non-crystalline state. The composition vector of particle i is written as

$$\begin{aligned}\eta_i = (\eta_{\mathrm{Ti,NC}} = \eta_{\mathrm{Ti}}, \quad & \eta_{\mathrm{O,NC}} = \eta_{\mathrm{O}},\\ \eta_{\mathrm{Ti,An}} = 0, \quad & \eta_{\mathrm{O,An}} =,\\ \eta_{\mathrm{Ti,Ru}} = 0, \quad & \eta_{\mathrm{O,Ru}} = 0).\end{aligned}$$

Below the transformation temperature $T < T_{\mathrm{trans},i}$ the non-crystalline primary transforms into a crystal phase (anatase or rutile) determined by the primary size $d_{\mathrm{p},i}$. The primary size $d_{\mathrm{p},i}$ is assumed to be the spherical equivalent diameter. Below the crossover diameter $d_{\mathrm{p},i} < d_{\mathrm{cross},i}$, the primary is assumed to transform into anatase, so that the primary composition is now

$$\begin{aligned}\eta_i = (\eta_{\mathrm{Ti,NC}} = 0, \quad & \eta_{\mathrm{O,NC}} = 0,\\ \eta_{\mathrm{Ti,An}} = \eta_{\mathrm{Ti}}, \quad & \eta_{\mathrm{O,An}} = \eta_{\mathrm{O}},\\ \eta_{\mathrm{Ti,Ru}} = 0, \quad & \eta_{\mathrm{O,Ru}} = 0),\end{aligned}$$

while above the crossover diameter $d_{\mathrm{p},i} \geq d_{\mathrm{cross},i}$, the primary transforms into rutile:

$$\begin{aligned}\eta_i = (&\eta_{\mathrm{Ti,NC}} = 0, \quad \eta_{\mathrm{O,NC}} = 0,\\ &\eta_{\mathrm{Ti,An}} = 0, \quad \eta_{\mathrm{O,An}} = 0,\\ &\eta_{\mathrm{Ti,Ru}} = \eta_{\mathrm{Ti}}, \quad \eta_{\mathrm{O,Ru}} = \eta_{\mathrm{O}}).\end{aligned}$$

A simplifying assumption is made here that the phase transformation between anatase and rutile is negligible due to the fast cooling rate of the particles near the stagnation plate. In addition, the sintering and coalescence of primary particles are assumed to conserve the phase composition of the constituent particles. Thus, the crystallite growth after solidification is only determined by surface growth.

6.4 Parameter estimation

The amount of each phase in particle i is determined by y (a vector of flame conditions), z (a vector of growth parameters in Table 6.2, not optimised in this study), $d_{\mathrm{cross},i}$, and $T_{\mathrm{trans},i}$. The total amount of each phase at the end of the simulations, n_{NC}, n_{A}, n_{R} can be represented by functions g_{NC}, g_{A}, and g_{R} as follows,

$$n_{\mathrm{NC}} = \sum_{i=i}^{N} (\eta_{\mathrm{Ti,NC}})_i = \sum_{i=i}^{N} g_{\mathrm{NC}}(y; z, d_{\mathrm{cross},i}, T_{\mathrm{trans},i}) \tag{6.10}$$

$$n_{\mathrm{A}} = \sum_{i=i}^{N} (\eta_{\mathrm{Ti,An}})_i = \sum_{i=i}^{N} g_{\mathrm{A}}(y; z, d_{\mathrm{cross},i}, T_{\mathrm{trans},i}) \tag{6.11}$$

$$n_{\mathrm{R}} = \sum_{i=i}^{N} (\eta_{\mathrm{Ti,Ru}})_i = \sum_{i=i}^{N} g_{\mathrm{R}}(y; z, d_{\mathrm{cross},i}, T_{\mathrm{trans},i}), \tag{6.12}$$

where N is the number of particles in the simulation. The rutile fraction relative to anatase and rutile, $\mathrm{f_R}$, at the end of the simulation (Fig. 6.1) is represented by a function f,

$$\mathrm{f_R} = \frac{n_{\mathrm{R}}}{n_{\mathrm{A}} + n_{\mathrm{R}}} = f(y; z, \theta). \tag{6.13}$$

where θ is a vector containing the dependencies of $d_{\mathrm{cross},i}$, and $T_{\mathrm{trans},i}$ which are optimised in this study.

The best parameter set $\hat{\theta}_m$ for the growth parameter set m (see Table 6.2) is evaluated as follows

$$\hat{\theta}_m = \arg\min_{\theta} \sum_{j=1}^{N_{\text{exp}}} (f(y^{(j)}; z^{(m)}, \theta) - \mathrm{f}_{\mathrm{R}}^{\text{exp},(j)})^2, \tag{6.14}$$

where the $y^{(i)}$ is a vector of process conditions for flame i, $z^{(m)}$ is a vector of growth parameters in case m (see Table 6.2), $\mathrm{f}_{\mathrm{R}}^{\text{exp}}$ is the experimentally measured rutile fraction from flame i, and N_{exp} is the number of flame conditions tested which is 6 in this study.

6.5 Results and discussion

6.5.1 Phase composition

Figure 6.3 summarises the results of the experimental phase quantification. The XRD patterns for samples prepared in flames 1–6 are shown in Fig. 6.3(a). The patterns are deconvoluted with the Rietveld refinement (full profile fitting) using four TiO_2 phases: Rutile (R), anatase (A), TiO_2-B (B) and TiO_2-II (II). These four phases have previously been identified in similar flames through XRD pattern analysis as well as high-resolution TEM images and electron diffraction patterns (Chapter 5). The broad peaks of all four phases suggest that the crystallites are nano-sized with possible microstrain present although no size/strain analysis is attempted here due to the high degree of peak overlap and the resulting uncertainty in the fitting.

Figure 6.3(b) shows the phase composition of all samples obtained from the refinement. While the content of metastable TiO_2-B and TiO_2-II phases are nearly constant, the anatase content gradually decreases while rutile increases from flames 1 to 6, i.e. decreasing flame dilution. This trend demonstrates a strong sensitivity of anatase-rutile stability to the mixture dilution. This agrees well with previous experimental observations where anatase-rutile stability was observed to change dramatically near the stoichiometric point [108, 138].

As the aim of this work is to investigate the origin of anatase-rutile stability, the metastable phases TiO_2-B and TiO_2-II are excluded from the rutile fraction calculation. Nevertheless, the fractions of these phases are not negligible (up to 30% in total). In addition, the presence of broad peak around $2\theta = 22 - 35^\circ$ in the background indicates the presence of amorphous TiO_2. Due to the difficulty in fitting the XRD results, no quantification of amorphous phase is performed in this study. Fujiwara and Pratsinis [78] quantified the amorphous phase using

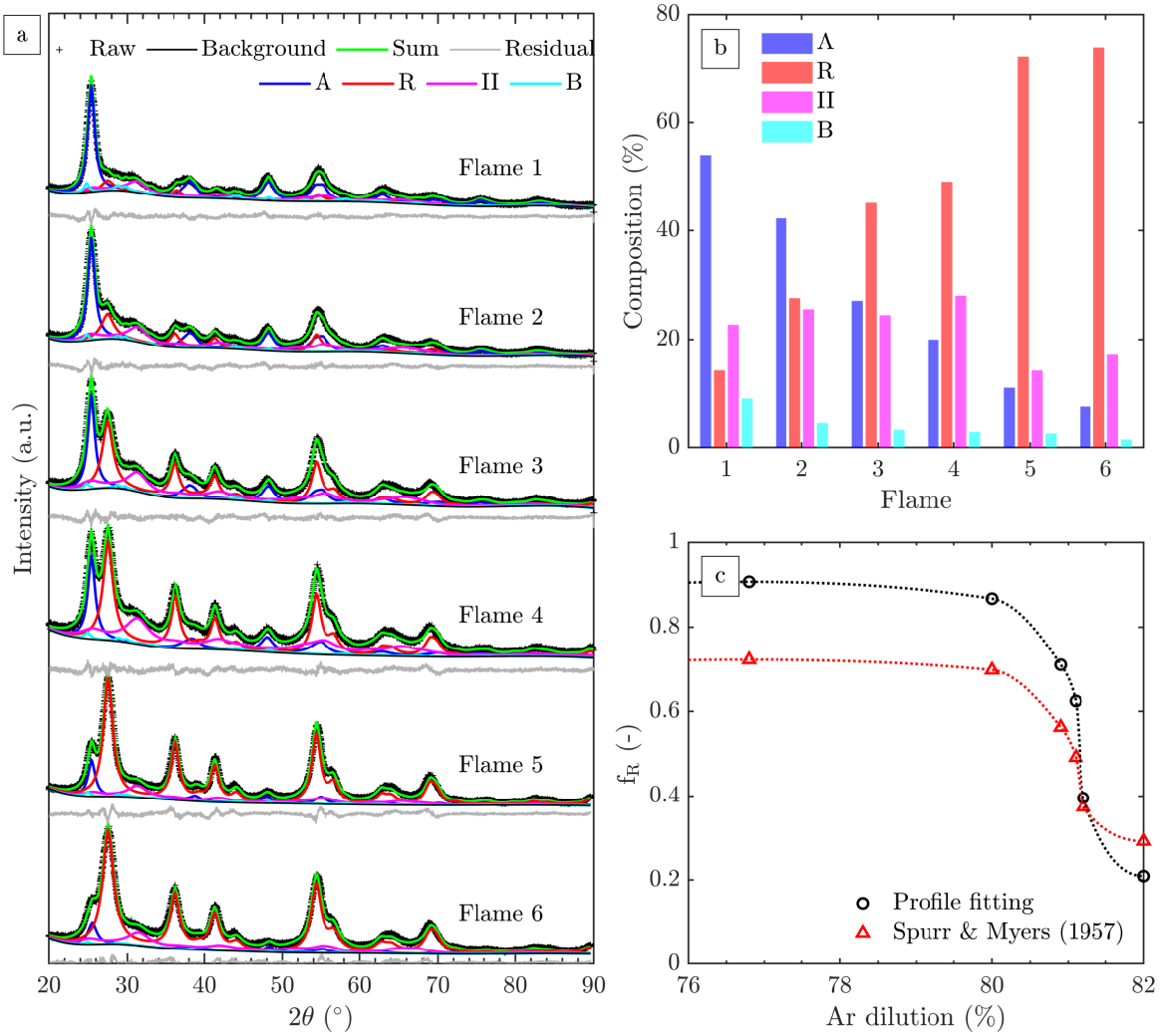

Figure 6.3: *(a) Powder XRD patterns of samples prepared in flames 1–6 and the individual phase profiles obtained from the Rietveld refinement, (b) Phase composition of samples prepared in flames 1–6, (c) Rietveld-determined rutile fraction (relative to anatase and rutile total),* f_R*, compared to the empirical relationship of Spurr and Myers [210] as a function of Ar dilution. The lines are added as a visual aid.*

the internal standard method and found the amorphous fraction ranges from 5–40% for flame spray-made TiO_2. This significant amount of amorphous fraction is likely due to the surface amorphization typical for TiO_2 nanoparticles [258]. For example, a 0.5 nm thick amorphous layer on the surface of a 9 nm spherical particle corresponds to approximately 30% amorphous fraction. The implications of the presence of metastable and amorphous phases is discussed briefly in Section 6.5.4 and will be investigated in the future work.

Figure 6.3(c) shows the relative rutile content, f_R = R/(A+R), where R and A denote the rutile and anatase fractions from the refinement as a function of the Ar dilution. The result

shows a high sensitivity of anatase-rutile stability at Ar dilution of $\approx 81\%$. In addition, an estimation of f_R using the empirical relationship given by Spurr and Myers [210] is shown. The comparison shows a difference of up to 20% between the two methods. This is not surprising as the formula proposed by Spurr and Myers [210] was determined using XRD patterns for powder samples with crystallite size of approximately 50-500 nm with much less broadening compared to the present results. In addition, only anatase and rutile were present in their powder sample compared to the four phases in the this work.

The presence of the metastable polymorphs indicates a limited phase transformation of the deposited particles on the rotating surface. This is due to the rapid quenching of the formed particles near the stagnation plate. For example, the results from Chapter 5 suggest that the TiO_2-II phase eventually transforms to rutile upon prolonged exposure to the flame (when a non-rotating stagnation plate was used).

Ma and Yang [138] previously demonstrated the effect of the premixed gas dilution (with N_2) on the anatase-rutile stability of TiO_2 prepared in a bunsen burner and showed a trend that is the opposite of the data in Fig. 6.3(c). In their study, increasing Ar dilution results in a higher rutile fraction. They suggest that this trend is due to a faster anatase-rutile transformation in oxygen lean environments as the initial oxygen content is lower in more diluted flames. It should be noted that the samples in their study were collected from 3 cm and 5 cm above the burner (Figs. 6 and 7 in [138]), corresponding to an estimated residence time of 25–60 ms (estimated based on the process conditions reported as no residence time calculation was given). This is in contrast with the residence time of 3–5 ms estimated for the flames used in this study. The longer residence time in Ref. [138] compared to this study is consistent with the particle size (20-500 nm) that is much larger than reported here (7–8 nm, discussed in the next section). Thus, it is suggested that the sensitivity shown in Fig. 6.3(c) is pertinent to the very early stages of particle formation and does not necessarily contradict the results reported by Ma and Yang [138].

6.5.2 Particle size

Figure 6.4(a) shows the measured aggregate mobility sizes for all flames. The aggregate sizes are similar for the different flame conditions (flames 1–6). This is consistent with the results from Chapter 5 where it was demonstrated that the particle sizes are not sensitive to the flame distance/equivalence ratio due to the compensating effect between temperature and particle residence time.

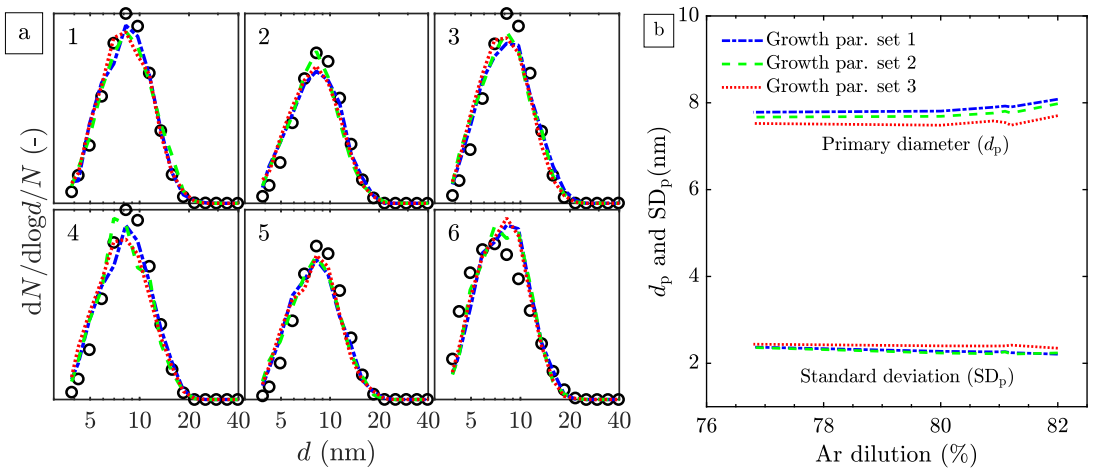

Figure 6.4: *Particle sizes at the stagnation point: (a) Measured and simulated aggregate size distributions, (b) simulated mean primary particle size, d_p, and the standard deviations, SD_p, as a function of Ar dilution. The measured data is shown in symbols, simulated data is shown with lines. For description of growth parameter sets 1–3, see Table 6.2.*

The simulated aggregate size (spherical equivalent size from projected area analysis) for three cases considered in this work (see Table 6.2) are also presented in shown Fig. 6.4(a). The validity of comparing the experimentally measured mobility aggregate size with the simulated spherical equivalent size has been discussed in Chapter 4. The predicted aggregate sizes compare well with the measured aggregate size. In addition, the results for the three different growth parameter sets considered (Table 6.2) are very similar, suggesting that the particle morphology is insensitive to the choice of precursor species and the gas-phase chemistry.

The predicted mean primary particle size is shown in Fig. 6.4(b). The primary particle size increases slightly with increasing Ar dilution, at around ~ 8 nm, which is in good agreement with previous primary particle size measurements with TEM in Chapter 4 (the primary particle sizes for 4 and 12 ml/h TTIP loading were 6 and 9 nm, respectively).

6.5.3 Flame structure

The one-dimensional stagnation flow approximation was used to estimate the temperature and other flame structure information. Figures 6.5(a) and 6.5(b) show the simulated temperature and oxygen mole fraction profiles for flames 1–6. It shows that flames 1–6 differ mainly in the location of their flame front, which is consistent with the experimentally observed

luminous flame location. In addition, the flames differ in their maximum temperature (and consequently particle time-temperature history).

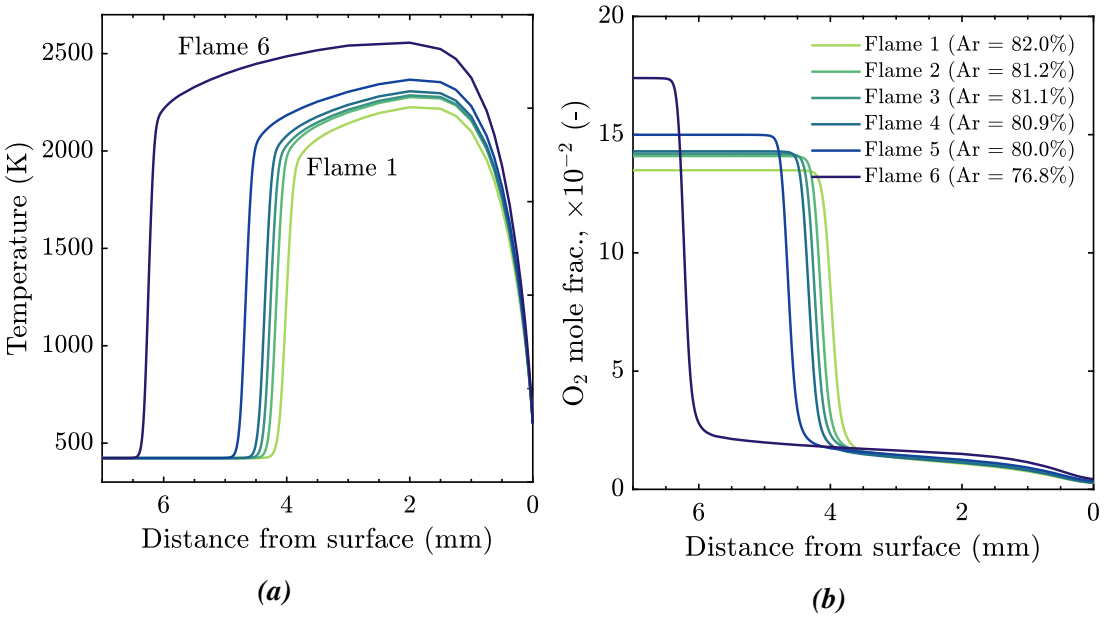

Figure 6.5: *The simulated flame structure for flames 1–6: (a) temperature and (b) O_2 mole fraction profiles.*

The maximum flame temperature varies by approximately 300°C between flames 1 and 6, similar to the difference of the calculated adiabatic flame temperature as summarised in Table 6.1. The oxygen mole fraction initially varies between flames 1–6 as a consequence of the difference in the diluent gas (Ar) fraction. In the post-flame region, however, the O_2 mole fractions show little variation across the flames at approximately 1×10^{-2}. This value is comparable to the adiabatic O_2 mole fraction obtained from the equilibrium simulation (Table 6.1).

6.5.4 Origin of anatase-rutile stability

The origin of the dramatic shift in the anatase-rutile composition as a function of flame dilution (Fig. 6.3(c)) is examined by considering two main formation pathways as illustrated in a simplified phase diagram in Fig. 6.6.

The **first pathway** assumes that the incipient particles reach a stoichiometric composition of TiO_2 at the point of crystallisation. As such, the free Gibbs energy of a spherical nanoparticle can be calculated from the bulk and suface energies of TiO_2 [255, 258]. This results in

a crossover particle size below which anatase is found to be thermodynamically more stable while rutile is more stable for larger particles. This pathway is referred to as the size-dependent stability hypothesis.

In the **second pathway**, rapid clustering and cooling result in a non-stoichiometric melt which solidifies to form sub-oxides. The sub-oxide intermediates are likely to affect the anatase-rutile stability. For example, the more oxygen deficient particles are hypothesised to preferentially transform to rutile due to the defect stabilisation in rutile lattice and structure similarity between rutile and some sub-oxides. Thus, the composition of the nascent particles is key in determining the anatase-rutile stability, i.e. composition-dependent stability hypothesis.

It is important to note that the analysis given here only takes into account anatase and rutile while ignoring the other metastable phases and is therefore only qualitative in nature. More importantly, the question this analysis seeks to answer is: *given the variation in the flame temperature/dilution, is the trend in anatase-to-rutile ratio consistent with the formation pathways outlined above*?

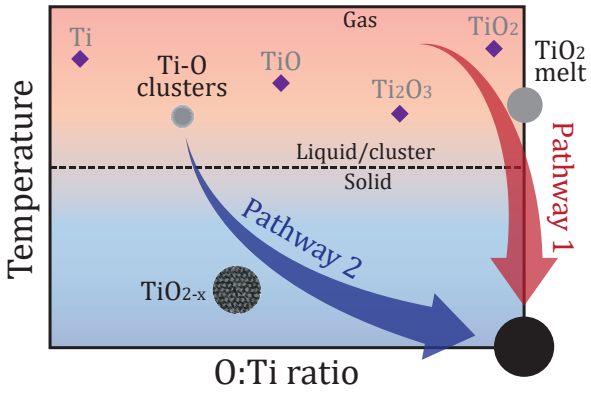

Figure 6.6: *A schematic illustrating two TiO_2 formation pathways.*

Pathway 1: Size-dependent stability

The surface energy-dependency of the anatase-rutile crossover size can be captured by two models. The first model is motivated by the thermodynamic analysis of Zhang and Banfield [255, 258]. This approach is termed the **Gibbs free energy model** as the crossover size arises from the formulation of anatase-rutile transformation Gibbs free energy by taking into account contributions from the surface free energy and surface stress of crystalline nanoparticles. In the second model, the crossover size arises when cooling of melt is

considered following the approach of Guisbiers et al. [90]. In this case, the phase with the higher melting point, which is a function of particle size, solidifies first and is stabilised. This is subsequently termed the **melting model**.

Gibbs free energy model

Following the thermodynamic analysis of Zhang and Banfield [255, 258], the anatase-rutile transformation Gibbs free energy, $\Delta G^{\circ}_{\mathrm{A}\to\mathrm{R}}$, is determined by a few thermodynamic quantities including the bulk Gibbs energies and surface free energy (derivation in Appendix C.1),

$$\Delta G^{\circ}_{\mathrm{A}\to\mathrm{R}} = \Delta G^{\circ}_{f,\mathrm{R}} - \Delta G^{\circ}_{f,\mathrm{A}} + 2(2t+3)\frac{M}{d}\left(\frac{\gamma_{\mathrm{R}}}{\rho_{\mathrm{R}}} - \frac{\gamma_{\mathrm{A}}}{\rho_{\mathrm{A}}}\right), \tag{6.15}$$

where $\Delta G^{\circ}_{f,\mathrm{R}}$ and $\Delta G^{\circ}_{f,\mathrm{A}}$ are the Gibbs free energies of formation of rutile and anatase, t is the ratio of surface stress to surface free energy, M is the molar mass of TiO_2, $d = 2r$ is the crystalite size, ρ_{R} and ρ_{A} are the mass densities of rutile and anatase, γ_{R} and γ_{A} are the surface free energies of rutile and anatase. In general, the term $\Delta G^{\circ}_{f,\mathrm{R}} - \Delta G^{\circ}_{f,\mathrm{A}}$ is negative (rutile is thermodynamically more stable for bulk) while the second term $\gamma_{\mathrm{R}}/\rho_{\mathrm{R}} - \gamma_{\mathrm{A}}/\rho_{\mathrm{A}}$ is positive (anatase has lower surface energy). Thus,

$$\Delta G^{\circ}_{\mathrm{A}\to\mathrm{R}} \begin{cases} > 0 \text{ (anatase is more stable)}, & \text{for } d < d_0 \\ = 0 \text{ (equilibrium)}, & \text{for } d = d_0 \\ < 0 \text{ (rutile is more stable)}, & \text{for } d > d_0 \end{cases}, \tag{6.16}$$

where d_0 is the size at which anatase and rutile are thermodynamically in equilibrium. d_0 is thus determined by the thermodynamic quantities in Eq. 6.15, i.e.

$$d_0 = d_0(\Delta G^{\circ}_{f,\mathrm{A}}, \Delta G^{\circ}_{f,\mathrm{A}}, t, M, \gamma_{\mathrm{A}}, \gamma_{\mathrm{R}}, \rho_{\mathrm{A}}, \rho_{\mathrm{R}}). \tag{6.17}$$

Precise determination of the surface free energy is challenging for a few reasons. First, nanoparticles may undergo significant surface reconstructions resulting in a lower surface free energy compared to that of clean-cut surface. The surface reconstruction itself is expected to vary with particle size which results in size-dependent surface free energies [165]. Second, the surface energetics are heavily affected by the chemical environments, e.g., degree of hydrogenation and adsorbed species [15, 14]. The uncertainty of the surface energies leads to a massive uncertainty in calculation of d_0 as the nominal values of $\gamma_{\mathrm{R}}/\rho_{\mathrm{R}}$ and $\gamma_{\mathrm{A}}/\rho_{\mathrm{A}}$ are

close (see the last term in Eq. 6.15). This explains the large uncertainty of surface energies found in the literature both calculated and experimentally measured [187]. For example, with the surface energies found in the literature, a critical size of anywhere between 2 to 50 nm can be justified using Eq. 6.15.

The uncertainties in the thermodynamic quantities motivate the choice of imposing d_0 directly as a free parameter in this model. It is also noted that the quantities in Eq. 6.15, e.g., $\Delta G^{\circ}_{f,\mathrm{A}}$, $\Delta G^{\circ}_{f,\mathrm{A}}$, t, γ_{A}, γ_{R}, ρ_{A}, ρ_{R} are temperature dependent but the overall temperature dependence of $\Delta G^{\circ}_{\mathrm{A}\to\mathrm{R}}$ is often assumed to be negligible due to the difference terms. Therefore, $d_{\mathrm{cross},i}$ can now be written as

$$d_{\mathrm{cross},i} = d_0 = \alpha_1, \tag{6.18}$$

where α_1 is a constant and a free model parameter.

The anatase-rutile stability given by $\Delta G^{\circ}_{\mathrm{A}\to\mathrm{R}}$ only considers the thermodynamic stability. In order to account for the kinetic effect, another model parameter α_2 is introduced such that the transformation as dictated by the thermodynamic stability only occurs (simultaneously) when $T \geq \alpha_2$ and completely arrested when $T < \alpha_2$. Therefore,

$$T_{\mathrm{trans},i} = \alpha_2. \tag{6.19}$$

The rutile fraction function in Eq. 6.13 is now written as

$$\mathrm{f_R} = f_{\mathrm{Gibbs}}(y; z, \theta) \quad \text{where } \theta = [\alpha_1, \alpha_2]. \tag{6.20}$$

Figure 6.7(a) shows the predicted rutile fraction as a function of the parameters α_1 and α_2 according to Eq. 6.20 for flame 1 and growth parameter set 1 (see Table 6.2). Qualitatively, the model responses are very similar for all flames and growth parameter sets tested. This is a consequence of the similarity in the simulated size-temperature trajectories of the particles. As the crossover size (α_1) increases the rutile fraction decreases as expected. The rutile fraction is less sensitive to the transformation temperature (α_2). This is due to the high cooling rates near the stagnation plate where the particle growth is limited.

The best fit parameters for the Gibbs free energy model are calculated according to Eq. 6.14 for $\alpha_1 = [4 \;\; 12]$ nm and $\alpha_1 = [1500 \;\; 2000]$ K. An upper limit of 2000 K for α_1 is used considering the melting point of bulk anatase is 2075 K. Figure 6.7(b) shows the measured and predicted rutile fractions with these fitted parameters for the three growth parameter sets in Table 6.2. The fitted parameters $\hat{\theta}_m$ are very similar for all growth parameters

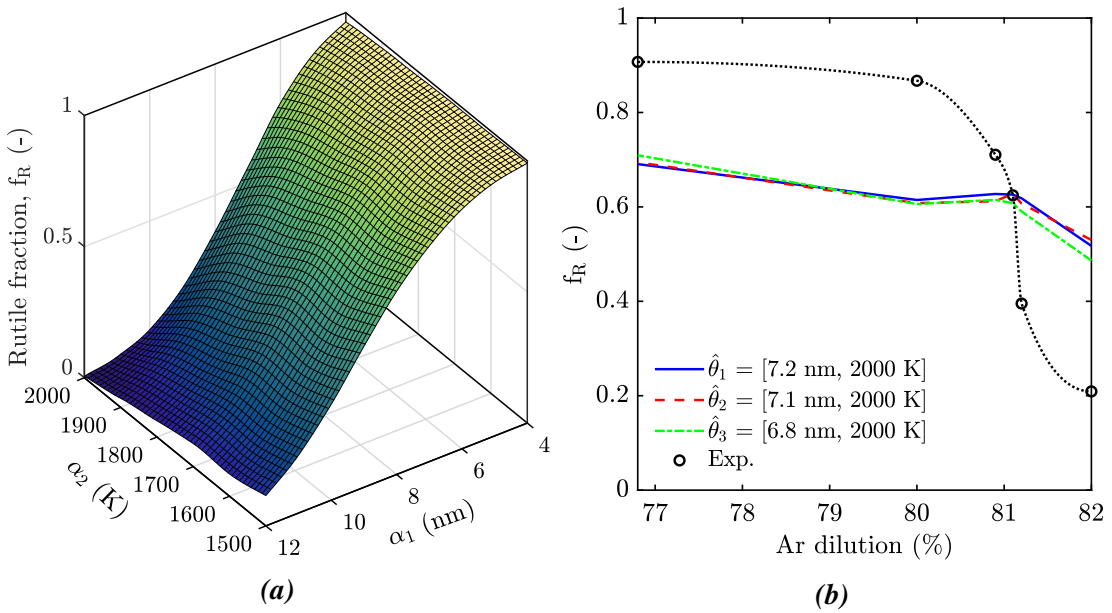

Figure 6.7: *(a) The predicted rutile fraction,* $f_R = f_{Gibbs}(y^{(1)}; z^{(1)}, \theta)$ *with* $\theta = [\alpha_1, \alpha_2]$*, for flame 1 (Ar = 82.0%) and growth parameter set 1 (see Table 6.2), according to the Gibbs free energy model. (b) The measured and predicted rutile fractions as a function of Ar dilution with the best fit parameters* $\hat{\theta}_1$*,* $\hat{\theta}_2$*, and* $\hat{\theta}_3$ *according to Eq. 6.14. The line is added to the experimental data as a visual aid.*

used ($m = 1, 2, 3$). This is not surprising as the particles sizes are insensitive to the growth parameters as shown in Fig. 6.4. The fitted crossover size is ~7 nm which is smaller than the crossover size calculated by Zhang and Banfield [255] (14 nm). The Gibbs free energy model correctly predicts a decreasing rutile fraction trend with increasing Ar dilution albeit with a much weaker sensitivity compared to the measurements.

Melting model

In the Gibbs model, the effect of particle polydispersity on the transformation temperature is neglected (Eq. 6.19). The particle polydispersity can be accounted for in the melting model by assuming that the transformation temperature is equal to the melting point. Following the approach by Guisbiers et al. [90], the melting point of a particle with size d, T_d^m, can be expressed as

$$\frac{T_d^m}{T_\infty^m} = 1 - \frac{\gamma_s - \gamma_l}{\Delta H_{m,\infty}} \frac{A}{V} = 1 - \frac{\beta}{d}, \tag{6.21}$$

T_∞^{melt} is the bulk melting point, γ_s and γ_l are the solid and liquid surface energies, and $\Delta H_{\text{m},\infty}$ is the bulk melting enthalpy. Similar to the Gibbs free energy model, the thermodynamic quantities are subject to massive uncertainties and thus are treated as a model parameter β (β_1 for anatase and β_2 for rutile).

Rutile has a higher melting point than anatase ($T^{\text{m}}_{\infty,\text{An}} = 2075$ K for anatase, $T^{\text{m}}_{\infty,\text{Ru}} = 2143$ K for rutile [90]). Therefore, for $\beta_1 < \beta_2$ the melting points of anatase and rutile intersect at $T^{\text{m}}_{d,\text{Ru}} = T^{\text{m}}_{d,\text{An}} = T^*$ and $d = d^*$. For example, Fig. 6.8 shows the melting points of anatase and rutile as a function of $1/d$ for $\beta_1 = 2.0$ nm and $\beta_2 = 2.5$ nm.

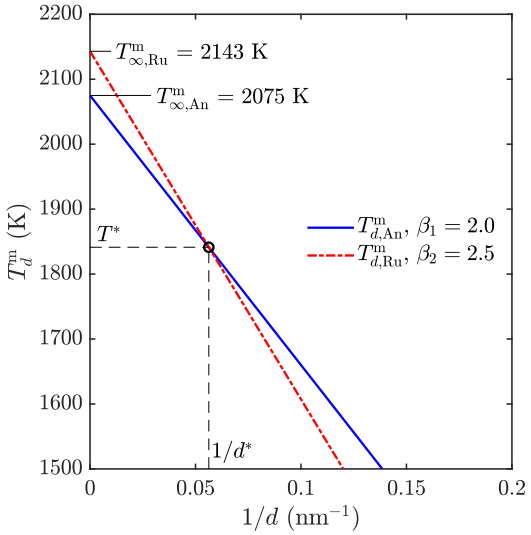

Figure 6.8: *The melting points of anatase and rutile as a function of reciprocal particle size. When $\beta_1 < \beta_2$, the two melting points intersect at $T^{\text{m}}_{d,\text{Ru}} = T^{\text{m}}_{d,\text{An}} = T^*$ and $d = d^*$.*

For a melt with size d, the solidification will occur at $T = T^{\text{m}}_d$ given by

$$T^{\text{m}}_d = \max\left(T^{\text{m}}_{d,\text{An}}, T^{\text{m}}_{d,\text{Ru}}\right). \tag{6.22}$$

Assuming phase transformation only occurs at the solidification point, the transformation temperature for particle i, $T_{\text{trans},i}$, is equal to $T^{\text{m}}_{d_i}$ and is defined by a function h_1,

$$T_{\text{trans},i} = T^{\text{m}}_{d_i} = h_1(\beta_1, \beta_2, d_i), \tag{6.23}$$

where

$$h_1(\beta_1, \beta_2, d_i) = \max\left(\left[T^{\text{m}}_{\infty,\text{An}}\left(1 - \frac{\beta_1}{d_i}\right)\right], \left[T^{\text{m}}_{\infty,\text{Ru}}\left(1 - \frac{\beta_2}{d_i}\right)\right]\right) \tag{6.24}$$

Meanwhile, the crossover size for particle i, $d_{\text{cross},i}$, is equal to d^*,

$$d_{\text{cross},i} = d^* = h_2(\beta_1, \beta_2), \tag{6.25}$$

where

$$h_2(\beta_1, \beta_2) = \frac{T^{\text{m}}_{\infty,\text{Ru}}\beta_2 - T^{\text{m}}_{\infty,\text{An}}\beta_1}{T^{\text{m}}_{\infty,\text{Ru}} - T^{\text{m}}_{\infty,\text{An}}}. \tag{6.26}$$

Finally, the rutile fraction function in Eq. 6.13 is now written as

$$\text{f}_\text{R} = f_{\text{melt}}(y; z, \theta) \quad \text{where } \theta = [\beta_1, \beta_2], \tag{6.27}$$

where β_1 and β_2 are the free model parameters.

For easier comparison to the Gibbs free energy model, the function $f_{\text{melt}}(x;\theta)$ can be transformed to $f^*_{\text{melt}}(x;\theta^*)$ as follows

$$f_{\text{melt}}(y; z, \theta) = f^*_{\text{melt}}(y; z, \theta^*) \quad \text{where } \theta^* = [d^*, T^*], \tag{6.28}$$

where d^* is the crossover diameter, given by $h_2(\beta_1, \beta_2)$ in Eq. 6.26, and T^* is the melting point of particle with size d^*, given by $h_3(\beta_1, \beta_2)$ below,

$$T^* = h_3(\beta_1, \beta_2) = \frac{\beta_2 - \beta_1}{\beta_2/T^{\text{m}}_{\infty,\text{An}} - \beta_1/T^{\text{m}}_{\infty,\text{Ru}}}, \tag{6.29}$$

Figure 6.9(a) shows the predicted rutile fraction as a function of the parameters d^* and T^* according to Eq. 6.28 for flame 1 and growth parameter set 1 (see Table 6.2). Interestingly the model response is very similar to the Gibbs free energy model. This suggests that the effect of particle polydispersity is insignificant for the cases considered here. This is a result of the narrow particle size distribution as shown by the small standard deviations in Fig. 6.4(b).

The similarity between the melting and the Gibbs free energy models are further shown by the predicted rutile fractions in Fig. 6.9(b) (compared to Fig. 6.7(b)). The best fit parameters for the melting model are calculated according to Eq. 6.14 for $d^* = [4\ \ 12]$ nm and $T^* = [1500\ \ 2000]$ K. The fitted parameters $d^* = 7$ nm and $T^* = 2000$ K are equivalent to $\beta_1 = 0.253$ nm and $\beta_2 = 0.467$ nm asccording to Eqs. 6.25, 6.26, and 6.29. These are much smaller than the values calculated by Guisbiers et al. [90] ($\beta_1 = 1.27$ nm and $\beta_2 = 2.58$ nm) using the surface energies obtained from molecular dynamics simulations for anatase and rutile with clean cut surfaces [175]. Using their reported values for β_1 and β_2, the predicted

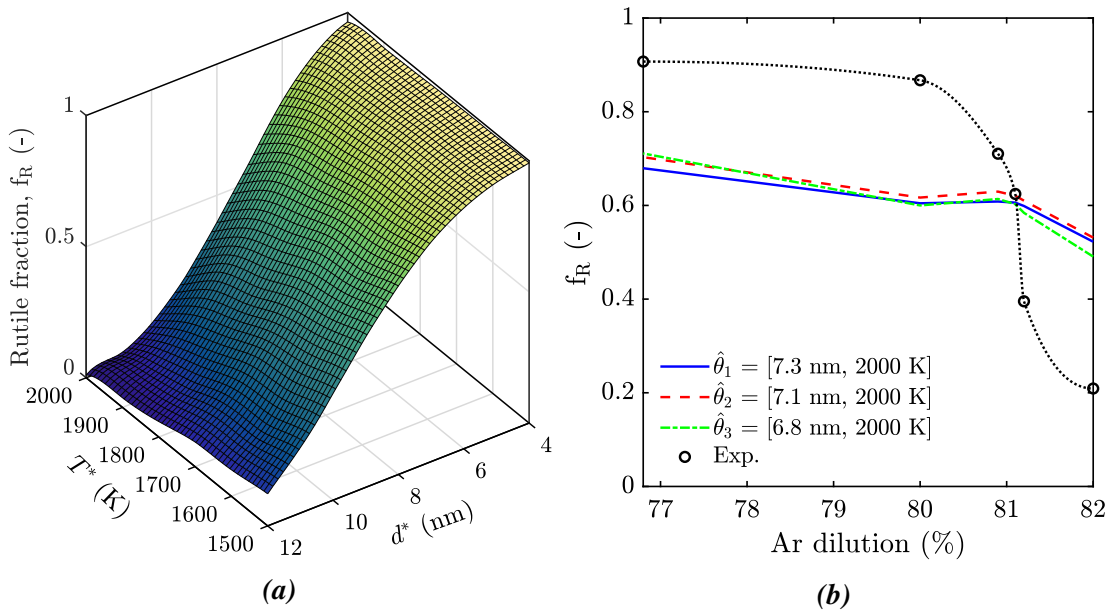

Figure 6.9: *(a) The predicted rutile fraction,* $f_R = f^*_{melt}(y^{(1)}; z^{(1)}, \theta^*)$ *with* $\theta^* = [d^*, T^*]$*, for flame 1 (Ar = 82.0%) and case 1 (see Table 6.2), according to the melting model. (b) The measured and predicted rutile fractions as a function of Ar dilution with the best fit parameters* $\hat{\theta}_1$*,* $\hat{\theta}_2$*, and* $\hat{\theta}_3$ *according to Eq. 6.14. The line is added to the experimental data as a visual aid.*

crossover size is ~ 40 nm. This suggests that the surface energies of the particles formed in flames are much smaller than those calculated for the cut surfaces. Nevertheless, similar to the Gibbs free energy model, the sensitivity of the rutile fraction as a function of Ar dilution predicted by the melting model is much weaker than the trend from the measurements.

Pathway 2: Composition-dependent stability

In the second pathway, the sensitivity of the anatase-rutile ratio as a function of the dilution ratio is explained by considering the effect of flame temperature (Fig. 6.5(a)) on the particle composition. It is proposed that the flame temperature affects the gas-phase chemistry of the particle precursor species and subsequently the particle composition.

The hypothesis is that the nascent particles are oxygen deficient, i.e. TiO_{2-x}, and the anatase or rutile formation is controlled by the oxygen-to-titanium ratio. This is motivated by the experimental observations where rutile is formed in oxygen-lean and anatase in oxygen-rich environments [108, 135]. In a similar way, doping of trivalent ions such as Al, Cr, Fe that create oxygen defects have long been used to promote the formation of rutile over anatase in gas-phase synthesis [5, 251].

The implied assumption is that particle solidification/crystal structure formation occurs at a faster rate than the oxidation of TiO_{2-x} clusters as shown in pathway 2 in Fig. 6.6. These nascent clusters are likely to be amorphous as demonstrated by molecular dynamic studies for TiO_2 particles smaller than 2 nm [258]. Formation of oxygen vacancies in amorphous TiO_2 is expected to be easier than in crystalline titania [55]. Teleki and Pratsinis [217] also show that highly oxygen deficient TiO_2 particles, possibly even suboxides, are formed in flame synthesis conditions. The oxygen vacancies explain the blue appearance of powders prepared in oxygen lean environments (which usually has high rutile content) [31].

In reality, the initial clusters are likely to be very complex and possibly contain unreacted hydrocarbon fragments (also nitrogen when present) such as those detected in time-of-flight mass spectrometer measurements [69, 236]. Here we only consider TiO_xH_y (1 Ti centre) species which are assumed to undergo a complete dehydration during inception and condensation reactions (Section 6.3.2). Thus, the oxygen content in the particle can be inferred from the implied oxidation state of the gas-phase particle precursor.

Gas-phase precursors

Figure 6.10 shows the simulated mole fractions of TTIP and small Ti-containing species TiO_xH_y considered in the gas-phase mechanism used here for the growth parameter sets considered (Table 6.2). Among all species, only $Ti(OH)_4$ and $Ti(OH)_3$ are present in significant concentration. This is not surprising as $Ti(OH)_4$ is the final product of the TTIP decomposition mechanism and $Ti(OH)_3$ is formed from direct reactions of $Ti(OH)_4$. These two species have also been detected by Fang et al. [69] in TTIP-doped $CH_4/O_2/N_2$ flames. The importance of $Ti(OH)_4$ and $Ti(OH)_3$ motivates the choice of these species as the precursor species in the particle model (see Section 6.3.2).

Figure 6.11(a) shows the difference in the ratio of $Ti(OH)_3$ to $Ti(OH)_4$ for flames 1–6. The variation in Fig. 6.11(a) is most pronounced in the post flame region around 2 mm from the stagnation plate. The difference in this maximum ratio represents an equilibrium shift in the gas phase due to the increasing maximum temperature from flames 1 to 6. This is demonstrated in Fig. 6.11(b) where the ratio of $Ti(OH)_3$ to $Ti(OH)_4$ at the maximum temperature for each flame (approximately 1.5–2 mm based on Fig. 6.5(a)) is plotted for the different growth parameter sets (Table 6.2). This shows that the trend of the relative ratio of $Ti(OH)_3$ to $Ti(OH)_4$ is insensitive to the growth parameters used and is consistent with the trend from the equilibrium simulations. A similar observation was reported by Buerger et al. [35] where increasing temperature shifts the equilibrium from $Ti(OH)_4$ to $Ti(OH)_3$. The

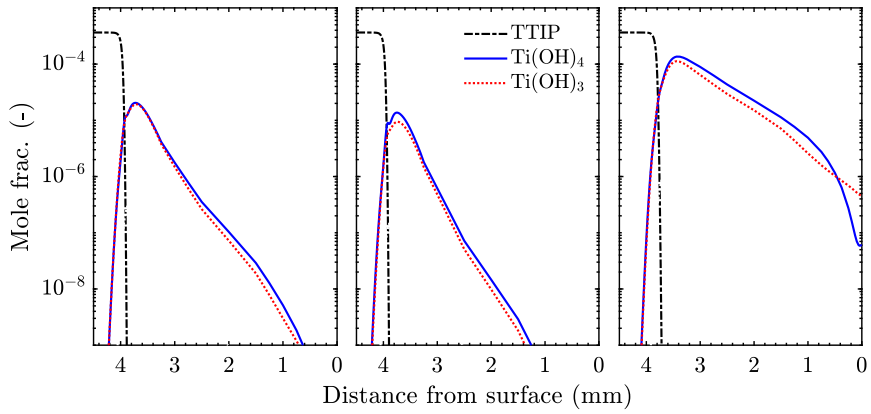

Figure 6.10: *The simulated mole fractions of TTIP and small Ti-containing species TiO_xH_y (post-$Ti(OH)_4$) for flame 1 using different growth parameter sets: set 1 (left), 2 (middle), 3 (right). For description of growth parameter sets 1–3, see Table 6.2.*

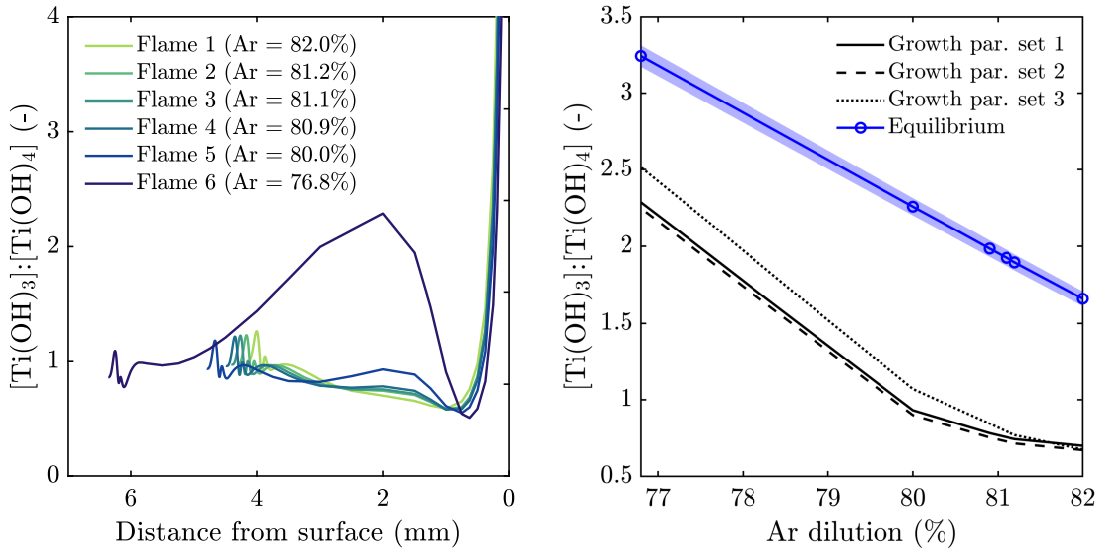

Figure 6.11: *(a) The ratio of $Ti(OH)_3$ to $Ti(OH)_4$ simulated mole fractions for flames 1–6 with growth parameter set 1. The start of the lines correspond to the flame fronts (defined as $T = 500$ K). The small oscillations near the flame front are caused by the particle inception. (b) The ratio of $Ti(OH)_3$ to $Ti(OH)_4$ mole fractions at the maximum flame temperature as a function of Ar dilution (lines) for the different growth parameter sets. The symbols are from the equilibrium simulations. The shaded area represents the equilibrium ratio for mixtures with equivalence ratio of* 1.00 ± 0.01. *For description of growth parameter sets 1–3, see Table 6.2.*

difference between the flames and the equilibrium simulations is attributed to the difference between the maximum flame temperature (shown in Fig. 6.5(a)) and the adiabatic flame

temperature (shown in Table 6.1). The sensitivity of the $Ti(OH)_3$ to $Ti(OH)_4$ equilibrium ratio to the mixture equivalence ratio is shown by the shaded region. A minimum uncertainty of 1.00 ± 0.01 is estimated due to the uncertainty in the experimental flowrates.

Particle composition

$Ti(OH)_4$ and $Ti(OH)_3$ have different implied oxidation states of Ti, i.e. +4 and +3 respectively. Assuming the inception and surface growth preserve the oxidation state of Ti of the precursor by the release of water, the particle formation can be written as

$$\begin{aligned} Ti(OH)_{4(gas)} &\longrightarrow TiO_{2(particle)} + 2\,H_2O_{(gas)} \\ Ti(OH)_{3(gas)} &\longrightarrow TiO_{1.5(particle)} + 1.5\,H_2O_{(gas)}. \end{aligned}$$

Therefore, the relative amount of $Ti(OH)_4$ and $Ti(OH)_3$ strongly affects the oxygen to titanium ratio in the particles, denoted as σ_O. The oxygen to titanium ratio for each particle is calculated according to Eq. 6.6. The solid state oxidation of particles is assumed here to be insignificant due to the low concentration of O_2 (see Fig. 6.5(b)).

In the gas-phase mechanism used in this study, $Ti(OH)_4$ decomposes to form $Ti(OH)_3$ through a OH-abstraction. This reaction competes with the inception and surface growth processes. Therefore, the particle formation rate will also impact the particle composition (σ_O). The growth parameter set 3 (see Table 6.2) is included here to investigate the effect of the particle formation rate, i.e. set 3 assumes slower inception and surface growth compared to set 2.

Figure 6.12 shows the particle frequency map with respect to σ_O and primary particle size for growth parameter set 2. For all flames, σ_O is within 1.75–1.85. In each flame, small particles are shown to have a broader distribution of oxygen deficiency compared to the larger particles. The convergence of σ_O for large particles is due to the averaging effect as particles grow through coalescence. This suggests that σ_O is very sensitive to the very early stages of particle formation.

The average oxygen to titanium ratio in the particle population as a function of the flame dilution is shown in Fig. 6.13. The average σ_O is insensitive to the temperature which corresponds to the particle residence time. This suggests that particle composition is determined very early in the formation stages (near the flame front) and no significant changes occur in the cooling region. However, the average σ_O is strongly influenced by the choice of the growth parameters (see Table 6.2).

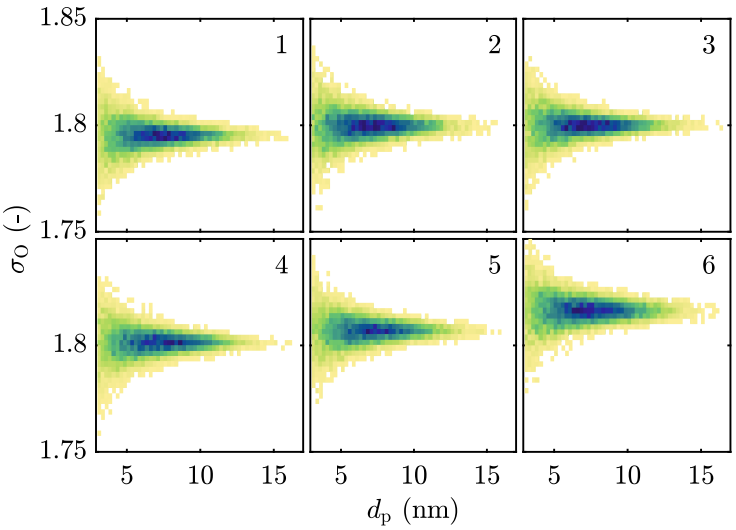

Figure 6.12: *The 2D frequency map with respect to particle size (d_p) and oxygen to titanium ratio (σ_O) for particles at stagnation point using growth parameter set 2 (Table 6.2) for flames 1–6. The color represents the frequency (blue: highest, yellow: lowest).*

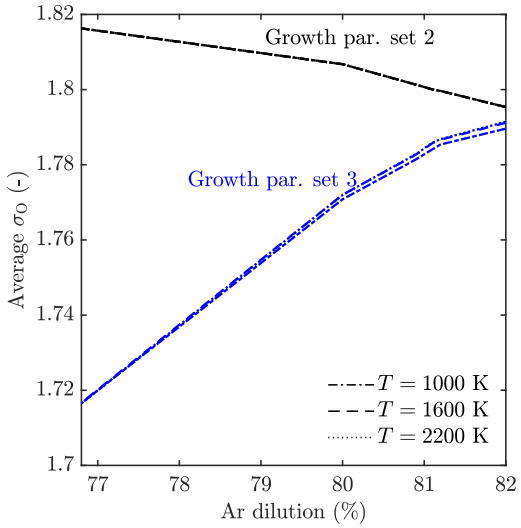

Figure 6.13: *The average particle oxygen to titanium ratio, σ_O, as a function of flame dilution at different temperature for growth parameter sets 2 and 3. The temperature here refers to the flame temperature in the cooling region (between the maximum temperature and the stagnation plate). For description of growth parameter sets, see Table 6.2.*

The contrasting predictions of models with growth parameter sets 2 and 3 can be explained as follows. As shown in Fig. 6.11, the shift of relative abundance of $Ti(OH)_3$ compared to $Ti(OH)_4$ occurs only in the post-flame region. This is a consequence of $Ti(OH)_4$ being formed first although $Ti(OH)_3$ is more stable than $Ti(OH)_4$. As the particle formation rate increases with temperature (due to the increase in collision rate), particle formation in hotter

flames (lower Ar dilution) occurs earlier compared to the colder flames (higher Ar dilution). When the particle formation occurs earlier, less oxygen deficient particles form (due to the higher amount of $Ti(OH)_4$ than $Ti(OH)_3$). As a result, σ_O decreases with increasing flame dilution for the growth parameter set 2 (fast inception and surface growth).

On the other hand, the opposite trend is expected when slower particle formation rates are applied (growth parameter set 3). This results in particle formation occurring later where $Ti(OH)_3$ has had time to form. As the $Ti(OH)_3$ stability over $Ti(OH)_4$ increases with temperature, this leads to more $Ti(OH)_3$ formed in hotter flames (lower Ar dilution), leading to more oxygen deficient particles (smaller σ_O). Therefore, σ_O increases with flame dilution as shown in Fig. 6.13. Thus the growth parameter set 3 represents a case where the particle composition is controlled mainly by thermodynamics (closer to equilibrium) while the kinetic effect is more dominant in the case of growth parameter set 2.

It is important to note that σ_O is strongly influenced by the actual rates of inception and surface growth which are unknown. Thus the absolute values σ_O in Fig. 6.11 are unlikely to represent the actual particle composition. However, the trends in Fig. 6.11 are important because they reflect the impact of the temperature on the stability of small Ti-species, in particular $Ti(OH)_3$ and $Ti(OH)_4$ and their subsequent interaction with incipient Ti-O clusters.

Influence of particle composition on phase stability

Comparison of the the aggregate and primary sizes in Section 6.5.2 reveals the insensitivity of particle morphology on the growth mechanism and rate parameters. However, the results from Fig. 6.13 demonstrate that the assumptions on growth mechanism and rate parameters significantly affect the inferred nascent particle composition. In the absence of a significant particle size effect, as shown by the discrepancies between the predicted and observed rutile fractions (Figs. 6.7(b) and 6.9(b)), it is proposed that the phase stability is mainly influenced by the nascent particle composition. Unfortunately no definitive conclusions can be made given the initial stages of particle growth and formation are still poorly understood.

The effect of the particle composition can be captured in the model implemented in this work by introducing a composition-dependency on the parameters d_{cross} and T_{trans} (see Fig. 6.2). A numerical experiment is included in the Appendix C.3 assuming the growth parameter 3 from Table 6.2. The result suggests that the experimental data can be successfully reproduced if an error function is used to describe the dependency of parameter d_{cross} on σ_O. However, further work is required to infer any physical insights from such empirical model.

Finally, the composition of the nascent particles can also potentially explain the formation of the metastable phases reported in Chapter 5 and in other studies [189]. It was suggested that oxygen deficient cluster intermediates are responsibe for the formation of TiO_2-II which is not predicted by the thermodynamic stability analysis. In particular, Ti_3O_5 has been shown to be a potential intermediate for TiO_2-II due to the small mismatch between the α-Ti_3O_5 and TiO_2-II structures [87]. TiO_2-B phase was shown to form during the dehydration of titanic acids $Ti_4O_7(OH)_2(H_2O)_n$ [223]. These titanic acids can be seen as hydroxylated TiO_2 chains which are likely to form in oxygen rich conditions. In addition TiO_2-B eventually transforms into anatase due to the topotactic relationship between their structures [33] which explains the formation of TiO_2-B/anatase mixure in oxygen rich conditions (Chapter 5).

6.6 Chapter summary

In this chapter, new experimental measurements of TiO_2 phase composition as a function of the flame dilution for stoichiometric mixtures are reported. The measurements demonstrated a high sensitivity of the anatase-rutile stability as a function of the flame dilution. Anatase is shown to form at higher flame dilution while rutile is favoured at lower flame dilution. The results are surprising as the oxygen content of the initial mixture decreases with increasing flame dilution which is expected to favour rutile formation.

The effect of the flame dilution on the relative anatase-rutile composition is investigated by comparing the experimental data and model predictions based on different assumptions on the particle formation pathways/mechanisms. Following a widely used analysis in the literature, the phase stability of anatase and rutile is assumed to be controlled by the particle size. In this scenario, a stoichiometric TiO_2 intermediate is formed and the anatase-rutile crossover size is controlled mainly by the surface energy. The dependency of the crossover size on surface energy can be represented by two different models (Gibbs free energy and melting models) that treat the particle polydispersity differently. These models predict a correct trend of anatase-rutile stability as a function of the flame dilution. However, they fail to reproduce the sensitivity observed in the experiments.

Another possible growth scenario takes into account the possible formation of oxygen-deficient clusters that act as particle precursors. It is demonstrated that the particle composition strongly depends on the assumptions made about the initial stages of particle formation, which are still poorly understood. It is proposed that the level of oxygen deficiency of the nascent particles is a possible explanation for the sensitivity of anatase-rutile stability as a

function of the flame dilution. This highlights the importance of developing a better chemical mechanism in order to understand the phase formation mechanism.

Chapter 7

Conclusions

7.1 Overall conclusions

This thesis investigates the morphology and polymorphism (or crystal phase) of TiO_2 nanoparticles prepared in stagnation flame reactors. The main objective is to gain a better understanding of the early stages of particle formation and how they impact the particle morphology and phase composition. The stagnation flame reactor is an ideal test case for studying the early growth mechanism of flame-made particles due to the short and uniform particle residence times. In addition, control of particle properties can be easily achieved by tuning various process variables including precursor concentration and flame mixture composition. The stagnation flame configuration is also amenable to modelling studies due to the simple geometry and well-defined boundary conditions. Combined with experimental measurements, the computational model allows for investigations of complex particle processes in the early stages of particle formation which are often inaccessible to experiments due to their short time scales.

A univariate moment-based particle model is implemented in a flame solver to simulate the TiO_2 particle formation from TTIP in a stagnation flame reactor. The particle model is solved with a method of moments with interpolative closure (MoMIC) and is fully coupled with the gas-phase chemistry and flow models. A one-step decomposition reaction model for particle inception and surface growth is assumed with rates taken from the literature. The method is used to model flames with varying TTIP loading rate from the literature where experimental size measurements are available. The comparison to the experimental data demonstrates a good agreement between the measured and predicted particle sizes but showed some discrepancy for the particle GSDs. This suggests that some degree of

aggregation is present which is not captured by the assumption of spherical particles inherent in the moment based model. The presence of aggregation also explains the discrepancy between mobility and TEM-derived particle sizes reported in the literature. In addition, the model is used to understand the roles of various particle processes during the particle growth in a stagnation flame. The initial particle growth is shown to be surface growth-controlled as opposed to coagulation-controlled. However, the coagulation is important near the stagnation plate where there is a steep temperature gradient.

In order to better characterise the particle morphology, particle size measurements were performed experimentally using simultaneous TEM sampling and mobility measurements. The results from the TEM image projected area analysis are compared to the corrected mobility sizes which reveals a good agreement within the experimental uncertainty. From the TEM image analysis, the particles are shown to be mostly spherical ($\sim 60\%$) and some form small aggregates ($\sim 40\%$) with small numbers of primary particles (< 10). As a result, the aggregate size distributions are broader than those of primary sizes which confirms the limitation of the spherical particle model. The primary particle size increases with increasing TTIP loading rate. On the other hand, the degree of aggregation is largely independent of the precursor loading which supports the previous conclusion that the aggregation only occurs very near to the stagnation plate due to coagulation. Interestingly, the particle sizes, both primary and aggregate, are insensitive to the flame equivalence ratio or temperature. It is suggested that the effect of flame temperature is compensated by the opposing effect of particle residence time. In order to resolve the particle morphology, the solution from the flame simulation is postprocessed with a stochastic population balance solver. The results show an excellent agreement with the experimentally measured particle morphology descriptors. This demonstrates the suitability of the modelling methodology to study the particle formation in a stagnation flame reactor. The simulation of the flames, however, requires the estimation of the flame standing distance and temperature profiles which are difficult to determine and thus subject to significant uncertainties. Using the model, the effects of these uncertainties are investigated. The results suggest that the predicted particle morphology is insensitive to these parameters within the estimated experimental uncertainties.

Experimental characterisations of the TiO_2 polymorphism are performed as a function of flame mixture equivalence ratio. In order to confidently identify the TiO_2 phases present in the samples, the powder XRD results are complemented with selected area electron diffraction (SAED) and HRTEM image analysis. The finding confirms the previously reported sensitivity of TiO_2 phase composition to the oxygen environments, especially around the stoichiometric point. Anatase is shown to form in oxygen rich conditions while rutile forms in oxygen lean conditions. More importantly, two metastable phases TiO_2-B and TiO_2-II are also

identified. Formation of TiO_2-II is especially interesting as it is a "high-pressure" phase and has never been identified in flame synthesis at atmospheric conditions. These metastable phases are formed as mixtures with anatase and rutile, respectively, i.e. TiO_2-B/anatase or TiO_2-II/rutile. It is suggested that these phases are retained in the prepared samples due to the high cooling rate when the rotating stagnation surface is used. These metastable phases provide new insights into the mechanism of TiO_2 polymorphism in flame which is not well understood. For example, the TiO_2-II is shown to convert to rutile upon prolonged exposure to the flame. It is possible therefore that TiO_2-II is a precursor phase for rutile. This contradicts the assumption often made in the literature in which rutile is formed from anatase, i.e. anatase-rutile transformation. Formation of TiO_2-II is hypothesised to occur through a solid-state transformation of sub-oxides intermediates at the early stages of particle formation.

The effect of flame dilution on TiO_2 polymorphism is investigated experimentally. Flames with stoichiometric mixture and varying dilution are used based on the previous observation that TiO_2 phase composition is highly sensitive at the stoichiometric point. The phase composition is quantified using a full profile fitting of the XRD patterns. The results suggest that all four phases previously identified are present. However, anatase-rutile relative composition is highly sensitive to the flame dilution. Interestingly, anatase is formed in flames with higher dilution (or lower oxygen fraction) while rutile is formed in less diluted flames (higher oxygen fraction). This is surprising as a more oxygenated environment is usually thought to inhibit rutile formation (from anatase). One of the possible explanations is the difference in flame temperature as a function of the flame dilution, i.e. flame temperature decreases with increasing flame dilution.

Subsequently, the origin of the sensitivitiy of the anatase-rutile composition is investigated by comparing the experimental data with detailed model predictions. A phase transformation model with an anatase-rutile "crossover" size parameter is implemented within the population balance solver to test different hypotheses on the phase formation. The first hypothesis assumes the formation of stoichiometric incipient particles in which the crossover size is a function of various thermodynamic quantities which are assumed to be constant within the conditions considered. The results suggest that this hypothesis is not sufficient to explain the experimentally observed sensitivity. The second hypothesis attempts to understand the possible roles of non-stoichiometric intermediates on phase formation. The non-stoichiometric intermediates can promote rutile formation, for example, through the formation of Magnéli phases which have a close structural relationship with rutile. The non-stoichiometric intermediates are assumed to form from the precursor species $Ti(OH)_4$ and $Ti(OH)_3$. The relative thermodynamic stability of $Ti(OH)_4$ and $Ti(OH)_3$ is shown to

be temperature-dependent which may explain the experimental observation. The inicipient particle composition is strongly influenced by the rates of reactions involving these two species. Unfortunately, the kinetic data of reactions involving these species are not available. This analysis demonstrates the importance of a better understanding of the early stages of particle formation, especially the detailed gas-chemistry model of small TiO_xH_y species, in order to explain the polymorphism of TiO_2 nanoparticles prepared in a flame synthesis.

7.2 Suggestions for future work

Based on the findings of this thesis, four important areas are suggested for future work. These areas cover the flame structure characterisation, optical based diagnostics for particle characterisation, structural information from diffraction data, and mechanistic studies of TTIP and $Ti_xO_yH_z$ species at high temperature.

Flame structure characterisation

More extensive flame structure characterisation is needed, including *flame temperature and velocity field* measurements. This will allow comparison with the simulation to evaluate the limitation of model assumptions, such as the one-dimensional flow approximations. The measurements of the temperature and velocity fields at the flame front are especially important as this is where the early stages of particle formation occurs. Unfortunately, due to the flame stability and the steep temperature gradient at the flame front, typical temperature measurement techniques are often not suitable or suffer from massive uncertainties, e.g., thermocouple, CARS spectroscopy.

Optical based diagnostics

While the stagnation flame configuration as used in this thesis is ideal for studying the early stages of particle formation, the short residence time presents another challenge on the experimental studies. The experimental characterisations of particle morphology and polymorphism in this thesis are limited to the *in situ* sampling method at the stagnation surface. This is mainly due to the fact that other types of intrusive sampling techniques can significantly alter the flames as well as the particle dynamics being investigated. Thus, optical based diagnostics would be advantageous as they allow for characterisation with minimal disturbances to the flame. Various optical based diagnostics have been developed

in the past few decades for particle characterisations. The main challenges have been the interpretation of the results which is non-trivial. With recent advances, however, these optical based diagnostics are expected to provide more insights than previously possible.

Another important characterisation target is the *particle composition*. As suggested in the conclusions of this thesis, the particle composition is likely to play a very important role in the crystal phase formation. The ability to probe the particle composition with optical based diagnostics will shed light to the very complex processes of which the understanding is currently lacking. One possible technique is the *in situ* Raman characterisation of the incipient particles. The Raman signal can provide information about the chemical environments of the atoms within the incipient particles. The *in situ* Raman technique, however, is extremely difficult due to the weak scattering signal.

Structural information from the diffraction data

In this thesis, the interpretation of the powder XRD results is limited to the qualitative phase identification and simple phase composition calculation. In principle, the diffraction data is able to provide a wealth of structural information including size anisotropy, micro strain (defects), crystal texture, lattice expansion, etc. This structural information, for example the defect concentration, will provide valuable insights into the formation mechanism of the crystal phases. This type of analysis is notoriously difficult for nanoparticles due to the poor crystallinity which results in peak overlap. However, this can be improved through various means. For example, the peaks can be better resolved with longer scan time or by careful calibration of the background contribution.

Mechanistic studies of TTIP and $Ti_xO_yH_z$

Significant advances have been made in the past decade to better describe the decomposition of TTIP at high temperature conditions. An extensive TTIP decomposition model [35, 34] is now available which offers a significantly more detailed description than the one-step decomposition model often used before. However, a recent experimental study by Ershov et al. [67] suggests that the TTIP decomposition model proposed by Buerger et al. [34] is incomplete as it does not consider an important pathway of acetone elimination. This shows that further investigations, both experimentally and theoretically, are warranted.

In addition, the kinetic data of small $Ti_xO_yH_z$ species are currently lacking. As demonstrated in this thesis, while this has little to no consequence on particle morphology, the small

$Ti_xO_yH_z$ species are potentially the key to better understanding the composition of the nascent particles. This will in turn provide deeper insights into the phase formation mechanism including what roles, if any, are played by the metastable phases.

References

[1] Aarik, J. (1996). Atomic-layer growth of TiO_2-II thin films. *Philos. Mag. Lett.*, 73(3):115–119.

[2] Aarik, J., Aidla, A., Sammelselg, V., Siimon, H., and Uustare, T. (1996). Control of thin film structure by reactant pressure in atomic layer deposition of TiO_2. *J. Cryst. Growth*, 169(3):496–502.

[3] Abdali, A., Fikri, M., Orthner, H., Wiggers, H., and Schulz, C. (2014). Ignition delay times of shock-heated tetraethoxysilane, hexamethyldisiloxane, and titanium tetraisopropoxide. *Chem. Phys. Lett.*, 601:54–58.

[4] Abraham, F. F. (1974). *Homogeneous nucleation theory: The pretransition theory of vapor condensation*. Academic Press, New York.

[5] Akhtar, K. M., Pratsinis, S. E., and Mastrangelo, S. V. R. (1994). Vapor phase synthesis of Al-doped titania powders. *J. Mater. Res.*, 9(5):1241–1249.

[6] Akroyd, J., Smith, A. J., Shirley, R. A., McGlashan, L. R., and Kraft, M. (2011). A coupled CFD-population balance approach for nanoparticle synthesis in turbulent reacting flows. *Chem. Eng. Sci.*, 66(17):3792–3805.

[7] Alderman, O. L. G., Skinner, L. B., Benmore, C. J., Tamalonis, A., and Weber, J. K. R. (2014). Structure of molten titanium dioxide. *Phys. Rev. B*, 90(9):1–13.

[8] Amin, H. M., Bennett, A., and Roberts, W. L. (2019). Determining fractal properties of soot aggregates and primary particle size distribution in counterflow flames up to 10 atm. *Proc. Combust. Inst.*, 37(1):1161–1168.

[9] Andersson, S., Collén, B., Kuylenstierna, U., and Magnéli, A. (1957). Phase analysis studies on the titanium-oxygen system. *Acta Chem. Scand.*, 11:1641–1652.

[10] Arabi-Katbi, O. I., Pratsinis, S. E., Morrison, P. W., and Megaridis, C. M. (2001). Monitoring the flame synthesis of TiO_2 particles by in-situ FTIR spectroscopy and thermophoretic sampling. *Combust. Flame*, 124(4):560–572.

[11] Aravindan, V., Lee, Y. S., Yazami, R., and Madhavi, S. (2015). TiO_2 polymorphs in 'rocking-chair' Li-ion batteries. *Mater. Today*, 18(6):345–351.

[12] Banfield, J. F., Veblen, D. R., and Smith, D. J. (1991). The identification of naturally occurring TiO_2(B) by structure determination using high-resolution electron microscopy, image simulation, and refinement. *Am. Mineral.*, 76:343–353.

[13] Barlow, R. S., Karpetis, A. N., Frank, J. H., and Chen, J. Y. (2001). Scalar profiles and NO formation in laminar opposed-flow partially premixed methane/air flames. *Combust. Flame*, 127(3):2102–2118.

[14] Barnard, A. S. and Xu, H. (2008). An environmentally sensitive phase map of titania nanocrystals. *ACS Nano*, 2(11):2237–2242.

[15] Barnard, A. S. and Zapol, P. (2004). Effects of particle morphology and surface hydrogenation on the phase stability of TiO_2. *Phys. Rev. B*, 70(23):1–13.

[16] Battiston, G. A., Gerbasi, R., Porchia, M., and Gasparotto, A. (1999). Metal organic CVD of nanostructured composite TiO_2-Pt thin films : A kinetic approach. *Chem. Vap. Depos.*, 5(1):13–20.

[17] Begin-Colin, S., Le Caër, G., Mocellin, A., and Zandona, M. (1994). Polymorphic transformations of titania induced by ball milling. *Philos. Mag. Lett.*, 69(1):1–7.

[18] Bergthorson, J. M. and Dimotakis, P. E. (2007). Premixed laminar C_1-C_2 stagnation flames: Experiments and simulations with detailed thermochemistry models. *Proc. Combust. Inst.*, 31 I:1139–1147.

[19] Bergthorson, J. M., Salusbury, S. D., and Dimotakis, P. E. (2011). Experiments and modelling of premixed laminar stagnation flame hydrodynamics. *J. Fluid Mech.*, 681:340–369.

[20] Bergthorson, J. M., Sone, K., Mattner, T. W., Dimotakis, P. E., Goodwin, D. G., and Meiron, D. I. (2005). Impinging laminar jets at moderate Reynolds numbers and separation distances. *Phys. Rev. E*, 72(6):066307.

[21] Biesinger, M. C., Lau, L. W. M., Gerson, A. R., and Smart, R. S. C. (2010). Resolving surface chemical states in XPS analysis of first row transition metals, oxides and hydroxides: Sc, Ti, V, Cu and Zn. *Appl. Surf. Sci.*, 257(3):887–898.

[22] Birkenstock, J., Fischer, R. X., and Messner, T. (2006). BRASS, the Bremen Rietveld analysis and structure suite. *Zeitschrift für Krist.*, 23:237–242.

[23] Biskos, G., Reavell, K., and Collings, N. (2005). Description and theoretical analysis of a differential mobility spectrometer. *Aerosol Sci. Technol.*, 39(6):527–541.

[24] Biswas, P. and Thimsen, E. (2011). High temperature aerosols: Measurement and deposition of nanoparticle films. In Kulkarni, P., Baron, P. A., and Willeke, K., editors, *Aerosol Meas. Princ. Tech. Appl.*, pages 723–738. Wiley, 3rd edition.

[25] Biswas, P., Wang, Y., and Attoui, M. (2018). Sub-2 nm particle measurement in high-temperature aerosol reactors: a review. *Curr. Opin. Chem. Eng.*, 21:60–66.

[26] Botero, M. L., Eaves, N., Dreyer, J. A., Sheng, Y., Akroyd, J., Yang, W., and Kraft, M. (2018). Experimental and numerical study of the evolution of soot primary particles in a diffusion flame. *Proc. Combust. Inst.*, 37(2):2047–2055.

[27] Bouvet, N., Davidenko, D., Chauveau, C., Pillier, L., and Yoon, Y. (2014). On the simulation of laminar strained flames in stagnation flows: 1D and 2D approaches versus experiments. *Combust. Flame*, 161(2):438–452.

[28] Bouzoubaa, A., Markovits, A., Calatayud, M., and Minot, C. (2005). Comparison of the reduction of metal oxide surfaces: TiO_2-anatase, TiO_2-rutile and SnO_2-rutile. *Surf. Sci.*, 583(1):107–117.

[29] Bowman, A. W. and Azzalini, A. (1997). *Applied smoothing techniques for data analysis: The kernel approach with S-Plus illustrations*. OUP Oxford.

[30] Brasil, A. M., Farias, T. L., and Carvalho, M. G. (1999). A recipe for image characterization of fractal-like aggregates. *J. Aerosol Sci.*, 30(10):1379–1389.

[31] Breckenridge, R. G. and Hosler, W. R. (1953). Electrical properties of titanium dioxide semiconductors. *Phys. Rev.*, 91(4):793–802.

[32] Brockmann, J. E. (2011). Aerosol transport in sampling lines and inlets. In Kulkarni, P., Baron, P., and Willeke, K., editors, *Aerosol Meas. Princ. Tech. Appl.*, pages 69–106. Wiley, 3rd edition.

[33] Brohan, L., Verbaere, A., Tournoux, M., and Demazeau, G. (1982). La transformation TiO_2(B) $\rightarrow$ anatase. *Mater. Res. Bull.*, 17(3):355–361.

[34] Buerger, P., Nurkowski, D., Akroyd, J., and Kraft, M. (2017). A kinetic mechanism for the thermal decomposition of titanium tetraisopropoxide. *Proc. Combust. Inst.*, 36(1):1019–1027.

[35] Buerger, P., Nurkowski, D., Akroyd, J., Mosbach, S., and Kraft, M. (2015). First-principles thermochemistry for the thermal decomposition of titanium tetraisopropoxide. *J. Phys. Chem. A*, 119(30):8376–8387.

[36] Buesser, B., Gröhn, A. J., and Pratsinis, S. E. (2013). Sintering rate and mechanism of TiO_2 nanoparticles by molecular dynamics. *J. Phys. Chem. C*, 115(22):11030–11035.

[37] Bursill, L. A. and Hyde, B. G. (1972). Crystallographic shear in the higher titanium oxides: structure, texture, mechanism and thermodynamics. *Prog. Solid State Chem.*, pages 177–253.

[38] Cahn, J. W. (1980). Surface stress and the chemical equilibrium of small crystals–I. The case of the isotropic surface. *Acta Metall.*, 28(10):1333–1338.

[39] Cai, J., Lu, N., and Sorensen, C. M. (1993). Comparison of size and morphology of soot aggregates as determined by light scattering and electron microscope analysis. *Langmuir*, 9(11):2861–2867.

[40] Calvo, M. E., Colodrero, S., Rojas, T. C., Anta, J. A., Ocaña, M., and Míguez, H. (2008). Photoconducting bragg mirrors based on TiO_2 nanoparticle multilayers. *Adv. Funct. Mater.*, 18(18):2708–2715.

[41] Camacho, J., Liu, C., Gu, C., Lin, H., Huang, Z., Tang, Q., You, X., Saggese, C., Li, Y., Jung, H., Deng, L., Wlokas, I., and Wang, H. (2015). Mobility size and mass of nascent soot particles in a benchmark premixed ethylene flame. *Combust. Flame*, 162(10):3810–3822.

[42] Camacho, J., Singh, A. V., Wang, W., Shan, R., Yapp, E. K. Y., Chen, D., Kraft, M., and Wang, H. (2017). Soot particle size distributions in premixed stretch-stabilized flat ethylene-oxygen-argon flames. *Proc. Combust. Inst.*, 36(1):1–9.

[43] Cammarata, R. C. and Sieradzki, K. (1994). Surface and interface stresses. *Annu. Rev. Mater. Sci.*, 24:215–234.

[44] Cancarevic, M., Zinkevich, M., and Aldinger, F. (2007). Thermodynamic description of the Ti-O system using the associate model for the liquid phase. *Calphad*, 31(3):330–342.

[45] Carley, A. F., Chalker, P. R., Riviere, J. C., and Roberts, M. W. (1987). The identification and characterisation of mixed oxidation states at oxidised titanium surfaces by analysis of x-ray photoelectron spectra. *J. Chem. Soc. Faraday Trans. 1*, 83(2):351–370.

[46] Chan, P. and Dahneke, B. (1981). Free-molecule drag on straight chains of uniform spheres. *J. Appl. Phys.*, 52(5):3106–3110.

[47] Chandler, M. F., Yingwu, T., and Köylü, Ü. Ö. (2007). Diesel engine particulate emissions: A comparison of mobility and microscopy size measurements. *Proc. Combust. Inst.*, 31(2):2971–2979.

[48] Chase, M. W. Jr., Davies, C. A., Downey, J. R. J., Frurip, D. J., McDonald, R. A., and Syverud, A. N. (1985). NIST-JANAF Thermochemical Tables.

[49] CMCL Innovations (2019). *k*inetics®.

[50] Cunningham, E. (1910). On the velocity of steady fall of spherical particles through fluid medium. *Proc. R. Soc. A*, 83(563):357–365.

[51] da Silva, A. L., Hotza, D., and Castro, R. H. (2017). Surface energy effects on the stability of anatase and rutile nanocrystals: A predictive diagram for Nb_2O_5-doped-TiO_2. *Appl. Surf. Sci.*, 393:103–109.

[52] Dahneke, B. E. (1973). Slip correction factors for nonspherical bodies–III the form of the general law. *J. Aerosol Sci.*, 4(2):163–170.

[53] Dastanpour, R., Rogak, S. N., Graves, B., Olfert, J., Eggersdorfer, M. L., and Boies, A. M. (2016). Improved sizing of soot primary particles using mass-mobility measurements. *Aerosol Sci. Technol.*, 50(2):101–109.

[54] Debye, P. (1912). Zur theorie der spezifischen wärmen. *Ann. Phys.*, 39:789.

[55] Deskins, N. A., Du, J., and Rao, P. (2017). The structural and electronic properties of reduced amorphous titania. *Phys. Chem. Chem. Phys.*, 19(28):18671–18684.

[56] Diebold, U. (2003). The surface science of titanium dioxide. *Surf. Sci. Rep.*, 48:53–229.

[57] Djenadic, R. and Winterer, M. (2017). Control of nanoparticle agglomeration through variation of the time-temperature profile in chemical vapor synthesis. *J. Nanoparticle Res.*, 19(28).

[58] Dobbins, R. A. and Mulholland, G. W. (1984). Interpretation of optical measurements of flame generated particles. *Combust. Sci. Technol.*, 40(5-6):175–191.

[59] Dreier, T. and Schulz, C. (2016). Laser-based diagnostics in the gas-phase synthesis of inorganic nanoparticles. *Powder Technol.*, 287:226–238.

[60] Dugdale, J. S., Morrison, J. A., and Patterson, D. (1954). The effect of particle size on the heat capacity of titanium dioxide. *Proc. R. Soc. London Ser. A*, 224(1157):228–235.

[61] Dutta, H., Sahu, P., Pradhan, S. K., and De, M. (2003). Microstructure characterization of polymorphic transformed ball-milled anatase TiO_2 by Rietveld method. *Mater. Chem. Phys.*, 77(1):153–164.

[62] Eggersdorfer, M. L., Kadau, D., Herrmann, H. J., and Pratsinis, S. E. (2011). Multiparticle sintering dynamics: From fractal-like aggregates to compact structures. *Langmuir*, 27(10):6358–6367.

[63] Eggersdorfer, M. L., Kadau, D., Herrmann, H. J., and Pratsinis, S. E. (2012). Aggregate morphology evolution by sintering: Number and diameter of primary particles. *J. Aerosol Sci.*, 46(0):7–19.

[64] Eggersdorfer, M. L. and Pratsinis, S. E. (2014). Agglomerates and aggregates of nanoparticles made in the gas phase. *Adv. Powder Technol.*, 25:71–90.

[65] Eibeck, A. and Wagner, W. (2001). Stochastic particle approximations for Smoluchoski's coagulation equation. *Ann. Appl. Probab.*, 11(4):1137–1165.

[66] Epstein, P. S. (1924). On the resistance experienced by spheres in their motion through gases. *Phys. Rev.*, 23(6):710–733.

[67] Ershov, K. S., Kochubei, S. A., Kiselev, V. G., and Baklanov, A. V. (2018). Decomposition pathways of titanium isopropoxide $Ti(OiPr)_4$: New insights from UV-photodissociation experiments and quantum chemical calculations. *J. Phys. Chem. A*, 122(4):1064–1070.

[68] Etgar, L., Zhang, W., Gabriel, S., Hickey, S. G., Nazeeruddin, M. K., Eychmüller, A., Liu, B., and Grätzel, M. (2012). High efficiency quantum dot heterojunction solar cell using anatase (001) TiO_2 nanosheets. *Adv. Mater.*, 24(16):2202–2206.

[69] Fang, J., Wang, Y., Kangasluoma, J., Attoui, M., Junninen, H., Kulmala, M., Petäjä, T., and Biswas, P. (2017). Cluster formation mechanisms of titanium dioxide during combustion synthesis: Observation with an APi TOF. *Aerosol Sci. Technol.*, 51(9):1071–1081.

[70] Fletcher, R. A., Ritchie, N. W. M., Anderson, I. M., and Small, J. A. (2011). Microscopy and microanalysis of individual collected particles. In Kulkarni, P., Baron, P. A., and Willeke, K., editors, *Aerosol Meas. Princ. Tech. Appl.*, pages 179–232. Wiley, 3rd edition.

[71] Formenti, M., Juillet, F., Meriaudeau, P., Teichner, S., and Vergnon, P. (1972). Preparation in a hydrogen-oxygen flame of ultrafine metal oxide particles - Oxidative properties toward hydrocarbons in the presence of ultraviolet radiation. *J. Colloid Interface Sci.*, 39(1):45–55.

[72] Frank, A. J., Kopidakis, N., and Lagemaat, J. V. D. (2004). Electrons in nanostructured TiO_2 solar cells: Transport, recombination and photovoltaic properties. *Coord. Chem. Rev.*, 248(13-14):1165–1179.

[73] Frenklach, M. (2002). Method of moments with interpolative closure. *Chem. Eng. Sci.*, 57(12):2229–2239.

[74] Frenklach, M. and Harris, S. J. (1987). Aerosol dynamics modeling using the method of moments. *J. Colloid Interface Sci.*, 118(1):252–261.

[75] Friedlander, S. and Wang, C. (2004). The self-preserving particle size distribution for coagulation by Brownian motion. *J. Colloid Interface Sci.*, 24(2):170–179.

[76] Friedlander, S. K. (1977). *Smoke, dust, and haze: Fundamentals of aerosol behavior*. John Wiley & Sons, New York.

[77] Fujishima, A. and Honda, K. (1972). Electrochemical photolysis of water at at a semiconductor electrode. *Nature*, 238:37–38.

[78] Fujiwara, K. and Pratsinis, S. E. (2017). Atomically dispersed Pd on nanostructured TiO_2 for NO removal by solar light. *AIChE J.*, 63(1):139–146.

[79] Girot, T., Devaux, X., Bégin-Colin, S., Le Caër, G., and Mocellin, A. (2001). Initial stages of the transformation of single-crystal anatase particles during high-energy ball milling. *Philos. Mag. A*, 81(2):489–499.

[80] Glumac, N. G., Skandan, G., Chen, Y. J., and Kear, B. H. (1999). Particle size control during flat flame synthesis of nanophase oxide powders. *Nanostructured Mater.*, 12(1):253–258.

[81] Gonzalez, R. C., Woods, R. E., and Eddins, S. L. (2004). *Digital image processing using MATLAB*. Pearson Education.

[82] Goodson, M. and Kraft, M. (2002). An efficienct stochastic algorithm for simulating nano-particle dynamics. *J. Comput. Phys.*, 183(1):210–232.

[83] Gopalakrishnan, R., McMurry, P. H., and Hogan, C. J. (2015). The electrical mobilities and scalar friction factors of modest-to-high aspect ratio particles in the transition regime. *J. Aerosol Sci.*, 82:24–39.

[84] Gopalakrishnan, R., Thajudeen, T., Ouyang, H., and Hogan, C. J. (2013). The unipolar diffusion charging of arbitrary shaped aerosol particles. *J. Aerosol Sci.*, 64:60–80.

[85] Grant, F. A. (1959). Properties of rutile (titanium dioxide). *Rev. Mod. Phys.*, 31(3):646—-674.

[86] Grcar, J. F. (1992). The Twopnt program for boundary value problems. Technical Report SAND91-8230.

[87] Grey, I. E., Li, C., Madsen, I. C., and Braunshausen, G. (1988). TiO_2-II. Ambient pressure preparation and structure refinement. *Mater. Res. Bull.*, 23:743–753.

[88] Gribb, A. A. and Banfield, J. F. (1997). Particle size effects on transformation kinetics and phase stability in nanocrystalline TiO_2. *Am. Mineral.*, 82:717–728.

[89] Grosschmidt, D., Bockhorn, H., Goodson, M., and Kraft, M. (2002). Two approaches to the simulation of silica particle synthesis. *Proc. Combust. Inst.*, 29(1):1039–1046.

[90] Guisbiers, G., Van Overschelde, O., and Wautelet, M. (2008). Theoretical investigation of size and shape effects on the melting temperature and energy bandgap of TiO_2 nanostructures. *Appl. Phys. Lett.*, 92(10).

[91] Hanaor, D. A. H. and Sorrell, C. C. (2011). Review of the anatase to rutile phase transformation. *J. Mater. Sci.*, 46(4):855–874.

[92] Harris, S. J. and Kennedy, I. M. (1988). The coagulation of soot particles with van der Waals forces. *Combust. Sci. Technol.*, 59(4-6):443–454.

[93] Holman, J. P. (1972). *Heat transfer*. McGraw-Hill, New York.

[94] Hu, L., Miao, Z., Zhang, Y., Zhang, H., and Yang, H. (2019). Numerical assessment on rotation effect of the stagnation surface on nanoparticle deposition in flame synthesis. *Materials (Basel).*, 12(9).

[95] Hulburt, H. M. and Katz, S. (1964). Some problems in particle technology. *Chem. Eng. Sci.*, 19(8):555–574.

[96] Hung, C.-H., Miquel, P. F., and Katz, J. L. (1992). Formation of mixed oxide powders in flames: Part I. TiO_2-SiO_2. *J. Mater. Res.*, 7(7):1861–1869.

[97] Iida, Y. and Ozaki, S. (1961). Grain growth and phase transformation of titanium oxide during calcination. *J. Am. Ceram. Soc.*, 44(3):120–127.

[98] Ishigaki, T., Li, Y.-L., and Kataoka, E. (2003). Phase formation and microstructure of titanium oxides and composited produced by thermal plasma oxidation of titanium carbide. *J. Am. Ceram. Soc.*, 86(9):1456–1463.

[99] Ishizuka, S., Kimura, Y., and Yamazaki, T. (2016). In situ FT-IR study on the homogeneous nucleation of nanoparticles of titanium oxides from highly supersaturated vapor. *J. Cryst. Growth*, 450:168–173.

[100] Johnson, R. F., Vandine, A. C., Esposito, G. L., and Chelliah, H. K. (2015). On the axisymmetric counterflow flame simulations: Is there an optimal nozzle diameter and separation distance to apply quasi one-dimensional theory? *Combust. Sci. Technol.*, 187(1-2):37–59.

[101] Jullien, R. (1984). Transparency effects in cluster-cluster aggregation with linear trajectories. *J. Phys. A*, 17:L771–L776.

[102] Jullien, R. (1987). Aggregation phenomena and fractal aggregates. *Contemp. Phys.*, 28(5):477–493.

[103] Kammler, H. K., Pratsinis, S. E., Morrison, P. W., and Hemmerling, B. (2002). Flame temperature measurements during electrically assisted aerosol synthesis of nanoparticles. *Combust. Flame*, 128(4):369–381.

[104] Kashima, K. and Sugiyama, H. (1990). Particle size control of TiO_2 ultrafine particles by CVD method. *Kagaku Kogaku Ronbunshu*, 16(3):551–556.

[105] Kasper, M., Siegmann, K., and Sattler, K. (1997). Evaluation of an in situ sampling probe for its accuracy in determining particle size distributions from flames. *J. Aerosol Sci.*, 28(8):1569–1578.

[106] Katzer, M., Weber, A. P., and Kasper, G. (2001). The effects of electrical fields on growth of titania particles formed in a CH_4-O_2 diffusion flame. *J. Aerosol Sci.*, 32(9):1045–1067.

[107] Kee, R. J., Miller, J. A., Evans, G. H., and Dixon-Lewis, G. (1989). A computational model of the structure and extinction of strained, opposed flow, premixed methane-air flames. *Symp. Combust.*, 22(1):1479–1494.

[108] Kho, Y. K., Teoh, W. Y., Mädler, L., and Amal, R. (2011). Dopant-free, polymorphic design of TiO_2 nanocrystals by flame aerosol synthesis. *Chem. Eng. Sci.*, 66(11):2409–2416.

[109] Kim, C. S., Nakaso, K., Xia, B., Okuyama, K., and Shimada, M. (2005). A new observation on the phase transformation of TiO_2 nanoparticles produced by a CVD method. *Aerosol Sci. Technol.*, 39(2):104–112.

[110] Knaup, J. M., Marx, J., and Frauenheim, T. (2014). Reduction of the TiO_{2-x} melting temperature induced by oxygen deficiency with implications on experimental data accuracy and structural transition processes. *Phys. Status Solidi - Rapid Res. Lett.*, 8(6):549–553.

[111] Kobata, A., Kusakabe, K., and Morooka, S. (1991). Growth and transformation of TiO_2 crystallites in aerosol reactor. *AIChE J.*, 37(3):347–359.

[112] Kormann, C., Hoffmann, M. R., and Bahnemann, D. W. (1991). Photolysis of chloroform and other organic molecules in aqueous TiO_2 suspensions. *Environ. Sci. Technol.*, 25(3):494–500.

[113] Korobeinichev, O. P., Shmakov, A. G., Maksyutov, R. A., Tereshchenko, A. G., Knyazkov, D. A., Bolshova, T. A., Kosinova, M. L., Sulyaeva, V. S., and Wu, J. S. (2012). Synthesis of mesoporous nanocrystalline TiO_2 films in a premixed H_2/O_2/Ar flame. *Combust. Explos. Shock Waves*, 48(1):49–56.

[114] Köylü, Ü. Ö., Faeth, G. M., Farias, T. L., and Carvalho, M. G. (1995). Fractal and projected structure properties of soot aggregates. *Combust. Flame*, 100(4):621–633.

[115] Kraft, M. (2005). Modelling of particulate processes. *KONA Powder Part. J.*, 23:18–35.

[116] Kruis, F. E., Fissan, H., and Peled, A. (1998). Synthesis of nanoparticles in the gas phase for electronic, optical and magnetic applications – a review. *J. Aerosol Sci.*, 29(5):511–535.

[117] Kuga, Y., Okauchi, K., Takeda, D., Ohira, Y., and Ando, K. (2001). Classification performance of a low pressure differential mobility analyzer for nanometer-sized particles. *J. Nanoparticle Res.*, 3(2-3):175–183.

[118] Kulkarni, P., Baron, P. A., Sorensen, C. M., and Harper, M. (2011). Nonspherical particle measurement: Shape factor, fractals, and fibers. In Kulkarni, P., Baron, P. A., and Willeke, K., editors, *Aerosol Meas. Princ. Tech. Appl.*, pages 509–547. Wiley, 3rd edition.

[119] Kusters, K. A. and Pratsinis, S. E. (1995). Strategies for control of ceramic powder synthesis by gas-to-particle conversion. *Powder Technol.*, 82:79–91.

[120] Lai, F. S., Friedlander, S. K., Pich, J., and Hidy, G. M. (1972). The self-preserving particle size distribution for Brownian coagulation in the free-molecule regime. *J. Colloid Interface Sci.*, 39(2):395–405.

[121] Lall, A. A. and Friedlander, S. K. (2006). On-line measurement of ultrafine aggregate surface area and volume distributions by electrical mobility analysis: I. Theoretical analysis. *J. Aerosol Sci.*, 37:260–271.

[122] Lall, A. A., Seipenbusch, M., Rong, W., and Friedlander, S. K. (2006). On-line measurement of ultrafine aggregate surface area and volume distributions by electrical mobility analysis: II. Comparison of measurements and theory. *J. Aerosol Sci.*, 37(3):272–282.

[123] Li, C., Shi, L., Xie, D., and Du, H. (2006). Morphology and crystal structure of Al-doped TiO_2 nanoparticles synthesized by vapor phase oxidation of titanium tetrachloride. *J. Non. Cryst. Solids*, 352(38-39):4128–4135.

[124] Li, J.-g. and Ishigaki, T. (2012). One-step Ar/O_2 thermal plasma processing of Y_2O_3:Eu^{3+} red phosphors: Phase structure, photoluminescent properties , and the effects of Sc^{3+} codoping. *J. Solid State Chem.*, 196:58–62.

[125] Li, S., Ren, Y., Biswas, P., and Tse, S. D. (2016). Flame aerosol synthesis of nanostructured materials and functional devices: Processing, modeling, and diagnostics. *Prog. Energy Combust. Sci.*, 55:1–59.

[126] Li, Y. and Ishigaki, T. (2002). Thermodynamic analysis of nucleation of anatase and rutile from TiO_2 melt. *J. Cryst. Growth*, 242:511–516.

[127] Li, Y.-L. and Ishigaki, T. (2004). Controlled one-step synthesis of nanocrystalline anatase and rutile TiO_2 powders by in-flight thermal plasma oxidation. *J. Phys. Chem. B*, 108(40):15536–15542.

[128] Li, Z. and Wang, H. (2003a). Drag force, diffusion coefficient, and electric mobility of small particles. I. Theory applicable to the free-molecule regime. *Phys. Rev. E*, 68(6):1–9.

[129] Li, Z. and Wang, H. (2003b). Drag force, diffusion coefficient, and electric mobility of small particles. II. Application. *Phys. Rev. E*, 68(6):1–13.

[130] Li Bassi, A., Cattaneo, D., Russo, V., Bottani, C. E., Barborini, E., Mazza, T., Piseri, P., Milani, P., Ernst, F. O., Wegner, K., and Pratsinis, S. E. (2005). Raman spectroscopy characterization of titania nanoparticles produced by flame pyrolysis: The influence of size and stoichiometry. *J. Appl. Phys.*, 98(7):074305.

[131] Liborio, L. and Harrison, N. (2008). Thermodynamics of oxygen defective Magnéli phases in rutile: A first-principles study. *Phys. Rev. B - Condens. Matter Mater. Phys.*, 77(10):1–10.

[132] Lindberg, C. S., Manuputty, M. Y., Akroyd, J., and Kraft, M. (2019a). A two-step simulation methodology for modelling stagnation flame synthesised aggregate nanoparticles. *Combust. Flame*, 202(204):143–153.

[133] Lindberg, C. S., Manuputty, M. Y., Buerger, P., Akroyd, J., and Kraft, M. (2019b). Numerical simulation and parametric sensitivity study of titanium dioxide particles synthesised in a stagnation flame. *J. Aerosol Sci.*, (In Press).

[134] Lindberg, C. S., Manuputty, M. Y., Yapp, E. K. Y., Akroyd, J., Xu, R., and Kraft, M. (2019c). A detailed particle model for polydisperse titanium dioxide aggregates. *J. Comput. Phys.*, 397:108799.

[135] Liu, C., Camacho, J., and Wang, H. (2018). Phase equilibrium of TiO_2 nanocrystals in flame-assisted chemical vapor deposition. *ChemPhysChem*, 19(2):180–186.

[136] Liu, X., Smith, M. E., and Tse, S. D. (2010). In situ Raman characterization of nanoparticle aerosols during flame synthesis. *Appl. Phys. B*, 100(3):643–653.

[137] Ma, H. K. (2014). Numerical study of the nanoparticle formation mechanism in a titania flame combustion synthesis process. *Aerosol Air Qual. Res.*, 14:251–259.

[138] Ma, H. K. and Yang, H.-A. (2010). Combustion synthesis of titania nanoparticles in a premixed methane flame. *J. Alloys Compd.*, 504(1):115–122.

[139] Manton, M. J. (1979). Brownian diffusion of aerosols to the face of a nuclepore filter. *Atmos. Environ.*, 13(4):525–531.

[140] Manuputty, M. Y., Akroyd, J., Mosbach, S., and Kraft, M. (2017). Modelling TiO_2 formation in a stagnation flame using method of moments with interpolative closure. *Combust. Flame*, 178:135–147.

[141] Manuputty, M. Y., Dreyer, J. A. H., Sheng, Y., Bringley, E. J., Botero, M. L., Akroyd, J., and Kraft, M. (2019a). Polymorphism of nanocrystalline TiO_2 prepared in a stagnation flame: formation of the TiO_2-II phase. *Chem. Sci.*, 10:1342–1350.

[142] Manuputty, M. Y., Lindberg, C. S., Botero, M. L., Akroyd, J., and Kraft, M. (2019b). Detailed characterisation of TiO_2 nano-aggregate morphology using TEM image analysis. *J. Aerosol Sci.*, 133:96–112.

[143] Marchand, R., Brohan, L., and Tournoux, M. (1980). TiO_2(B) A new form of titanium dioxide and the potassium octatitanate $K_2Ti_8O_{17}$. *Mater. Res. Bull.*, 15:1129–1133.

[144] Marchisio, D. L., Pikturna, J. T., Fox, R. O., Vigil, R. D., Scienza, D., Torino, P., and Duca, C. (2003). Quadrature method of moments for population-balance equations. *AIChE J.*, 49(5).

[145] Mazur, M., Wojcieszak, D., Kaczmarek, D., Domaradzki, J., Song, S., Gibson, D., Placido, F., Mazur, P., Kalisz, M., and Poniedzialek, A. (2016). Functional photocatalytically active and scratch resistant antireflective coating based on TiO_2 and SiO_2. *Appl. Surf. Sci.*, 380:165–171.

[146] McCormick, J. R., Zhao, B., Rykov, S. A., Wang, H., and Chen, J. G. (2004). Thermal stability of flame-synthesized anatase TiO_2 nanoparticles. *J. Phys. Chem. B*, 108:17398–17402.

[147] Mccusker, L. B., Von Dreele, R. B., Cox, D. E., Louër, D., and Scardi, P. (1999). Rietveld refinement guidelines. *J. Appl. Crystallogr.*, 32(1):36–50.

[148] McDonald, H. J. and Seltz, H. (1939). The heat capacities of titanium dioxide from 68–298°K. The thermodynamic properties of titanium dioxide. *J. Am. Chem. Soc.*, 61(9):2405–2407.

[149] McEnally, C. S., Köylü, Ü. Ö., Pfefferle, L. D., and Rosner, D. E. (1997). Soot volume fraction and temperature measurements in laminar nonpremixed flames using thermocouples. *Combust. Flame*, 109(4):701–720.

[150] McGraw, R. (1997). Description of aerosol dynamics by the quadrature method of moments. *Aerosol Sci. Technol.*, 27(2):255–265.

[151] McPherson, R. (1973). Formation of metastable phases in flame- and plasma-prepared alumina. *J. Mater. Sci.*, 8(6):851–858.

[152] Meakin, P., Donn, B., and Mulholland, G. W. (1989). Collisions between point masses and fractal aggregates. *Langmuir*, 5(2):510–518.

[153] Medalia, A. I. (1967). Morphology of aggregates. I. Calculation of shape and bulkiness factors; application to computer-simulated random flocs. *J. Colloid Interface Sci.*, 24(3):393–404.

[154] Mei, Z. G., Wang, Y., Shang, S. L., and Liu, Z. K. (2011). First-principles study of lattice dynamics and thermodynamics of TiO_2 polymorphs. *Inorg. Chem.*, 50(15):6996–7003.

[155] Memarzadeh, S., Tolmachoff, E. D., Phares, D. J., and Wang, H. (2011). Properties of nanocrystalline TiO_2 synthesized in premixed flames stabilized on a rotating surface. *Proc. Combust. Inst.*, 33(2):1917–1924.

[156] Meng, D. W., Wu, X. L., Sun, F., Huang, L. W., Liu, F., Han, Y. J., Zheng, J. P., Meng, X., and Mason, R. (2008). High-pressure polymorphic transformation of rutile to α-PbO_2-type TiO_2 at $\{0\ 1\ 1\}_R$ twin boundaries. *Micron*, 39(3):280–286.

[157] Menz, W. J. and Kraft, M. (2013). A new model for silicon nanoparticle synthesis. *Combust. Flame*, 160(5):947–958.

[158] Miller, J. A. and Kee, R. J. (1990). Chemical kinetics and combustion modeling. *Annu. Rev. Phys. Chem.*, 41:345–387.

[159] Miquel, P. F. and Katz, J. L. (1994). Formation and characterization of nanostructured V-P-O particles in flames: A new route for the formation of catalysts. *J. Mater. Res.*, 9(3):746–754.

[160] Mittemeijer, E. J. Scardi, P., editor (2004). *Diffraction analysis of the microstructure of materials*. Springer.

[161] Modak, A., Puduppakkam, K., Naik, C., and Meeks, E. (2013). Simulation of particle synthesis by premixed laminar stagnation flames. *Mater. Res. Soc. Symp. Proceeding*, 1506.

[162] Mood, A. M., Graybill, F. A., and Boes, D. C. (1974). *Introduction to the theory of statistics*. McGraw-Hill, New York, 3rd edition.

[163] Morgan, N. M., Patterson, R. I. A., and Kraft, M. (2008). Modes of neck growth in nanoparticle aggregates. *Combust. Flame*, 152(1-2):272–275.

[164] Murata, H., Kataoka, Y., Kawamoto, T., Tanaka, I., and Taniguchi, T. (2014). Photocatalytic activity of α-PbO_2-type TiO_2. *Phys. Status Solidi - Rapid Res. Lett.*, 8(10):822–826.

[165] Naicker, P. K., Cummings, P. T., Zhang, H., and Banfield, J. F. (2005). Characterization of titanium dioxide nanoparticles using molecular dynamics simulations. *J. Phys. Chem. B*, 109(32):15243–15249.

[166] Nakaso, K., Okuyama, K., Shimada, M., and Pratsinis, S. E. (2003). Effect of reaction temperature on CVD-made TiO_2 primary particle diameter. *Chem. Eng. Sci.*, 58(15):3327–3335.

[167] Navrotsky, A. (2011). Nanoscale effects on thermodynamics and phase equilibria in oxide systems. *ChemPhysChem*, 12(12):2207–2215.

[168] Nikraz, S. and Wang, H. (2013). Dye sensitized solar cells prepared by flames stabilized on a rotating surface. *Proc. Combust. Inst.*, 34(2):2171–2178.

[169] Nowotny, J., Bak, T., Nowotny, M. K., and Sheppard, L. R. (2008). Defect chemistry and electrical properties of titanium dioxide. 1. Defect diagrams. *J. Phys. Chem. C*, 112(2):602–610.

[170] Ogura, I., Hashimoto, N., Kotake, M., Sakurai, H., Kishimoto, A., and Honda, K. (2014). Aerosol particle collection efficiency of holey carbon film-coated TEM grids. *Aerosol Sci. Technol.*, 48(7):758–767.

[171] Oh, C. and Sorensen, C. M. (1998). Structure factor of diffusion-limited aggregation clusters: Local structure and non-self-similarity. *Phys. Rev. E*, 57(1):784–790.

[172] Okamoto, H. (2003). O-Ti (Oxygen-Titanium). *J. Phase Equilibria*, 22(4):515–515.

[173] Okuyama, K., Kousaka, Y., Tohge, N., Yamamoto, S., Wu, J. J., Flagan, R. C., and Seinfeld, J. H. (1986). Production of ultrafine metal oxide aerosol particles. *Am. Inst. Chem. Eng.*, 32(12):2010–2019.

[174] Okuyama, K., Ushio, R., Kousaka, Y., Flagan, R. C., and Seinfeld, J. H. (1990). Particle generation in a chemical vapor deposition process with seed particles. *AIChE J.*, 36(3):409–419.

[175] Oliver, P. M., Watson, G. W., Kelsey, E. T., and Parker, S. C. (1997). Atomistic simulation of the surface structure of the TiO_2 polymorphs rutile and anatase. *J. Mater. Chem.*, 7(3):563–568.

[176] Park, K., Kittelson, D. B., and McMurry, P. H. (2004). Structural properties of diesel exhaust particles measured by transmission electron microscopy (TEM): Relationships to particle mass and mobility. *Aerosol Sci. Technol.*, 38(9):881–889.

[177] Patterson, R. I., Singh, J., Balthasar, M., Kraft, M., and Wagner, W. (2006a). Extending stochastic soot simulation to higher pressures. *Combust. Flame*, 145(3):638–642.

[178] Patterson, R. I. A., Singh, J., Balthasar, M., Kraft, M., Norris, J. R., and Carlo, M. (2006b). The linear process deferment algorithm: A new technique for solving population balance equations. *SIAM J. Sci. Comput.*, 28(1):303–320.

[179] Pelaez, M., Nolan, N. T., Pillai, S. C., Seery, M. K., Falaras, P., Kontos, A. G., Dunlop, P. S., Hamilton, J. W., Byrne, J. A., O'Shea, K., Entezari, M. H., and Dionysiou, D. D. (2012). A review on the visible light active titanium dioxide photocatalysts for environmental applications. *Appl. Catal. B Environ.*, 125:331–349.

[180] Pich, J. (1964). Impaction of aerosol particles in the neighbourhood of a circular hole. *Collect. Czechoslov. Chem. Commun.*, 29(9):2223–2227.

[181] Pratsinis, S. E. (1988). Simultaneous nucleation condensation and coagulation in aerosol reactors. *J. Colloid Interface Sci.*, 124(2):416–427.

[182] Pratsinis, S. E. (1998). Flame aerosol synthesis of ceramic powders. *Prog. Energy Combust. Sci.*, 24(97):197–219.

[183] Pratsinis, S. E., Bai, H., Biswas, P., Frenklach, M., and Mastrangelo, S. V. R. (1990). Kinetics of titanium(IV) chloride oxidation. *J. Am. Ceram. Soc.*, 73(7):2158–2162.

[184] Pratsinis, S. E. and Vemury, S. (1996). Particle formation in gases: a review. *Powder Technol.*, 88:267–273.

[185] Pratsinis, S. E., Zhu, W., and Vemury, S. (1996). The role of gas mixing in flame synthesis of titania powders. *Powder Technol.*, 86(1):87–93.

[186] Ramkrishna, D. (1981). Analysis of population balance–IV. The precise connection between Monte Carlo simulation and population balances. *Chem. Eng. Sci.*, 36(7):1203–1209.

[187] Ranade, M. R., Navrotsky, A., Zhang, H. Z., Banfield, J. F., Elder, S. H., Zaban, A., Borse, P. H., Kulkarni, S. K., Doran, G. S., and Whitfield, H. J. (2002). Energetics of nanocrystalline TiO_2. *Proc. Natl. Acad. Sci.*, 99(Supplement 2):6476–6481.

[188] Ranz, W. E. and Marshall, W. R. J. (1952). Evaporation from drops. *Chem. Eng. Prog.*, 48(3):141–146.

[189] Riad, K. B., Wood-adams, P. M., and Wegner, K. (2018). Flame-made TiO_2(B). *Mater. Res. Bull.*, 106(June):276–281.

[190] R'Mili, B., Le Bihan, O. L. C., Dutouquet, C., Aguerre-Charriol, O., and Frejafon, E. (2013). Particle sampling by TEM grid filtration. *Aerosol Sci. Technol.*, 47(7):767–775.

[191] Rogak, S. N., Flagan, R. C., and Nguyen, H. V. (1993). The mobility and structure of aerosol agglomerates. *Aerosol Sci. Technol.*, 18(1):25–47.

[192] Rudyak, V. Y., Krasnolutskii, S. L., Nasibulin, a. G., and Kauppinen, E. I. (2002). Methods of measuring the diffusion coefficient and sizes of nanoparticles in a rarefied gas. *Dokl. Phys.*, 47(10):758–761.

[193] Rulison, A. J., Miquel, P. F., and Katz, J. L. (1996). Titania and silica powders produced in a counterflow diffusion flame. *J. Mater. Res.*, 11(12):3083–3089.

[194] Russell, A. (1955). The Rev. William Gregor (1761-1817), discoverer of titanium. *Mineral. Mag. J. Mineral. Soc.*, 30(229):617–624.

[195] Saggese, C., Cuoci, A., Frassoldati, A., Ferrario, S., Camacho, J., Wang, H., and Faravelli, T. (2016). Probe effects in soot sampling from a burner-stabilized stagnation flame. *Combust. Flame*, 167:184–197.

[196] Sato, H., Endo, S., Sugiyama, M., Kikegawa, T., Shimomura, O., and Kusaba, K. (1991). Baddeleyite-type high-pressure phase of TiO_2. *Science (80-.).*, 251(4995):786–788.

[197] Seto, T., Shimada, M., and Okuyama, K. (1995). Evaluation of sintering of nanometer-sized titania using aerosol method. *Aerosol Sci. Technol.*, 23(2):183–200.

[198] Shaddix, C. R. (1999). Correcting thermocouple measurements for radiation loss: A critical review. *Proc. 33rd Natl. Heat Transf. Conf.*

[199] Sham, T. K. and Lazarus, M. S. (1979). X-ray photoelectron spectroscopy (XPS) studies of clean and hydrated TiO_2 (rutile) surfaces. *Chem. Phys. Lett.*, 68(2):426–432.

[200] Sharma, G., Dhawan, S., Reed, N., Chakrabarty, R., and Biswas, P. (2019). Collisional growth rate and correction factor for TiO_2 nanoparticles at high temperatures in free molecular regime. *J. Aerosol Sci.*, 127:27–37.

[201] Shekar, S., Menz, W. J., Smith, A. J., Kraft, M., and Wagner, W. (2012). On a multivariate population balance model to describe the structure and composition of silica nanoparticles. *Comput. Chem. Eng.*, 43:130–147.

[202] Shen, P., Hwang, S.-L., Chu, H.-T., and Yui, T.-F. (2001). α-PbO_2-type TiO_2: From mineral physics to natural occurrence. *Int. Geol. Rev.*, 43(4):366–378.

[203] Shmakov, A. G., Korobeinichev, O. P., Knyazkov, D. A., Paletsky, A. A., Maksyutov, R. A., Gerasimov, I. E., Bolshova, T. A., Kiselev, V. G., and Gritsan, N. P. (2013). Combustion chemistry of $Ti(OC_3H_7)_4$ in premixed flat burner-stabilized H_2/O_2/Ar flame at 1 atm. *Proc. Combust. Inst.*, 34(1):1143–1149.

[204] Siegel, R. and Howell, J. R. (2001). *Thermal radiation heat transfer*. Taylor & Francis, 4th edition.

[205] Simons, P. Y. and Dachille, F. (1967). The structure of TiO_2 II, a high-pressure phase of TiO_2. *Acta Crystallogr.*, 23:334.

[206] Smoluchowski, M. (1917). Versuch einer mathematischen Theorie der Koagulationskinetik kolloider Lösungen [An attempt for a mathematical theory of coagulation kinetics of colloidal solutions]. *Zeitschrift für Phys. Chemie*, 92(1):129–168.

[207] Sorensen, C. M. (2011). The mobility of fractal aggregates: A review. *Aerosol Sci. Technol.*, 45(7):765–779.

[208] Sorensen, C. M. and Feke, G. D. (1996). The morphology of macroscopic soot. *Aerosol Sci. Technol.*, 25(3):328–337.

[209] Spektor, K., Tran, D. T., Leinenweber, K., and Häussermann, U. (2013). Transformation of rutile to TiO_2-II in a high pressure hydrothermal environment. *J. Solid State Chem.*, 206:209–216.

[210] Spurr, R. A. and Myers, H. (1957). Quantitative analysis of anatase-rutile mixtures with an x-ray diffractometer. *Anal. Chem.*, 29(5):760–762.

[211] Stokes, G. G. (1851). On the effect of the internal friction of fluids on the motion of pendulums. *Trans. Cambridge Philos. Soc.*, 9.

[212] Strobel, R., Baiker, A., and Pratsinis, S. E. (2006). Aerosol flame synthesis of catalysts. *Adv. Powder Technol.*, 17(5):457–480.

[213] Strobel, R. and Pratsinis, S. E. (2007). Flame aerosol synthesis of smart nanostructured materials. *J. Mater. Chem.*, 17(45):4743–4756.

[214] Sutherland, D. N. and Goodarz-Nia, I. (1971). Floc simulation: The effect of collision sequence. *Chem. Eng. Sci.*, 26(12):2071–2085.

[215] Takahashi, Y., Suzuki, H., and Nasu, M. (1985). Rutile growth at the surface of TiO_2 films deposited by vapour-phase decomposition of isopropyl titanate. *J. Chem. Soc. Faraday Trans. 1*, 81:3117–3125.

[216] Tammet, H. (1995). Size and mobility of nanometer particles, clusters and ions. *J. Aerosol Sci.*, 26(3):459–475.

[217] Teleki, A. and Pratsinis, S. E. (2009). Blue nano titania made in diffusion flame. *Phys. Chem. Chem. Phys.*, 11(19):3742–3747.

[218] Thajudeen, T., Jeon, S., and Hogan, C. J. (2015). The mobilities of flame synthesized aggregates/agglomerates in the transition regime. *J. Aerosol Sci.*, 80:45–57.

[219] The Mathworks (2016). MATLAB Image Processing Toolbox (2016b).

[220] Tian, M., Mahjouri-Samani, M., Eres, G., Sachan, R., Yoon, M., Chisholm, M. F., Wang, K., Puretzky, A. A., Rouleau, C. M., Geohegan, D. B., and Duscher, G. (2015). Structure and formation mechanism of black TiO_2 nanoparticles. *ACS Nano*, 9(10):10482–10488.

[221] Tolmachoff, E. D., Abid, A. D., Phares, D. J., Campbell, C. S., and Wang, H. (2009). Synthesis of nano-phase TiO_2 crystalline films over premixed stagnation flames. *Proc. Combust. Inst.*, 32(2):1839–1845.

[222] Tolmachoff, E. D., Memarzadeh, S., and Wang, H. (2011). Nanoporous titania gas sensing films prepared in a premixed stagnation flame. *J. Phys. Chem. C*, 115(44):21620–21628.

[223] Tournoux, M., Marchand, R., and Brohan, L. (1986). Layered $K_2Ti_4O_9$ and the open metastable TiO_2(B) structure. *Prog. Solid State Chem.*, 17:33–52.

[224] Tsantilis, S., Kammler, H. K., and Pratsinis, S. E. (2002). Population balance modeling of flame synthesis of titania nanoparticles. *Chem. Eng. Sci.*, 57(12):2139–2156.

[225] Tsantilis, S. and Pratsinis, S. E. (2004). Narrowing the size distribution of aerosol-made titania by surface growth and coagulation. *J. Aerosol Sci.*, 35(3):405–420.

[226] Ulrich, G. D. (1971). Theory of particle formation and growth in oxide synthesis flames. *Combust. Sci. Technol.*, 4(1):47–57.

[227] Ulrich, G. D., Milnes, B. A., and Subramanian, N. S. (1976). Particle growth in flames. II: Experimental results for silica particles. *Combust. Sci. Technol.*, 14(4-6):243–249.

[228] Ulrich, G. D. and Subramanian, N. S. (1977). Particle growth in flames III. Coalescence as a rate-controlling process. *Combust. Sci. Technol.*, 17(3-4):119–126.

[229] University of California San Diego (2014). The San Diego mechanism: Chemical-kinetic mechanisms for combustion applications.

[230] U.S. Department of the Interior and U.S. Geological Survey (2019). Mineral commodity summaries. Technical report.

[231] Vemury, S., Pratsinis, S. E., and Kibbey, L. (1997). Electrically controlled flame synthesis of nanophase TiO_2, SiO_2, and SnO_2 powders. *J. Mater. Res.*, 12(4):1031–1042.

[232] Waldmann, L. and Schmitt, K. H. (1966). *Thermophoresis and diffusiophoresis of aerosols*. Academic Press, New York.

[233] Wang, C. Y. (2008). Off-centered stagnation flow towards a rotating disc. *Int. J. Eng. Sci.*, 46(4):391–396.

[234] Wang, H., You, X., Joshi, A. V., Davis, S. G., Laskin, A., Egolfopoulos, F. N., and Law, C. K. (2007). USC mech version II: High-temperature combustion reaction model of H_2/CO/C_1-C_4 compounds.

[235] Wang, J., Li, S., Yan, W., Tse, S. D., and Yao, Q. (2011). Synthesis of TiO_2 nanoparticles by premixed stagnation swirl flames. *Proc. Combust. Inst.*, 33(2):1925–1932.

[236] Wang, Y., Kangasluoma, J., Attoui, M., Fang, J., Junninen, H., Kulmala, M., Petäjä, T., and Biswas, P. (2017a). Observation of incipient particle formation during flame synthesis by tandem differential mobility analysis-mass spectrometry (DMA-MS). *Proc. Combust. Inst.*, 36(1):745–752.

[237] Wang, Y., Liu, P., Fang, J., Wang, W.-N., and Biswas, P. (2015). Kinetics of sub-2 nm TiO_2 particle formation in an aerosol reactor during thermal decomposition of titanium tetraisopropoxide. *J. Nanoparticle Res.*, 17(3):147.

[238] Wang, Y., Sharma, G., Koh, C., Kumar, V., Chakrabarty, R., and Biswas, P. (2017b). Influence of flame-generated ions on the simultaneous charging and coagulation of nanoparticles during combustion. *Aerosol Sci. Technol.*, 51(7):833–844.

[239] Wegner, K. and Pratsinis, S. E. (2003). Nozzle-quenching process for controlled flame synthesis of titania nanoparticles. *AIChE J.*, 49(7):1667–1675.

[240] Wegner, K., Stark, W. J., and Pratsinis, S. E. (2002). Flame-nozzle synthesis of nanoparticles with closely controlled size, morphology and crystallinity. *Mater. Lett.*, 55(5):318–321.

[241] West, R. H., Beran, G. J. O., Green, W. H., and Kraft, M. (2007a). First-principles thermochemistry for the production of TiO_2 from $TiCl_4$. *J. Phys. Chem. A*, 111:3560–3565.

[242] West, R. H., Celnik, M. S., Inderwildi, O. R., Kraft, M., Beran, G. J. O., and Green, W. H. (2007b). Toward a comprehensive model of the synthesis of TiO_2 particles from $TiCl_4$. *Ind. Eng. Chem. Res.*, 46:6147–6156.

[243] West, R. H., Shirley, R. A., Kraft, M., Goldsmith, C. F., and Green, W. H. (2009). A detailed kinetic model for combustion synthesis of titania from $TiCl_4$. *Combust. Flame*, 156(9):1764–1770.

[244] Williams, D. B. and Carter, C. B. (2009). *Transmission electron microscopy: A textbook for materials science*. Springer.

[245] Willnet, I., Eichen, Y., and Frank, A. J. (1989). Tailored semiconductor-receptor colloids: Improved photosensitized H_2 evolution from water with TiO_2-β-cyclodextrin colloids. *J. Am. Chem. Soc.*, 111(5):1884–1886.

[246] Withers, A. C., Essene, E. J., and Zhang, Y. (2003). Rutile/TiO_2II phase equilibria. *Contrib. to Mineral. Petrol.*, 145(2):199–204.

[247] Wood, G. J. and Bursill, L. A. (1981). The formation energy of crystallographic shear planes in Ti_nO_{2n-1}. *Proc. R. Soc. London*, 375:105–125.

[248] Xing, Y., Köylü, Ü. Ö., and Rosner, D. E. (1996). Synthesis and restructuring of inorganic nano-particles in counterflow diffusion flames. *Combust. Flame*, 107(1-2):85–102.

[249] Xiong, Y. and Pratsinis, S. E. (1991). Gas phase production of particles in reactive turbulent flows. *J. Aerosol Sci.*, 22(5):637–655.

[250] Yang, G., Zhuang, H., and Biswas, P. (1996). Characterization and sinterability of nanophase titania particles processed in flame reactors. *Nanostructured Mater.*, 7(6):675–689.

[251] Yang, J., Huang, Y. X., and Ferreira, J. M. F. (1997). Inhibitory effect of alumina additive on the titania phase transformation of a sol-gel-derived powder. *J. Mater. Sci. Lett.*, 16(23):1933–1935.

[252] Yapp, E. K., Chen, D., Akroyd, J., Mosbach, S., Kraft, M., Camacho, J., and Wang, H. (2015). Numerical simulation and parametric sensitivity study of particle size distributions in a burner-stabilised stagnation flame. *Combust. Flame*, 162(6):2569–2581.

[253] Yeh, C. L., Yeh, S. H., and Ma, H. K. (2004). Flame synthesis of titania particles from titanium tetraisopropoxide in premixed flames. *Powder Technol.*, 145(1):1–9.

[254] Yoon, J. D., Park, K. Y., and Jang, H. D. (2003). Comparison of titania particles between oxidation of titanium tetrachloride and thermal decomposition of titanium tetraisopropoxide. *Aerosol Sci. Technol.*, 37(8):621–627.

[255] Zhang, H. and Banfield, J. F. (1998). Thermodynamic analysis of phase stability of nanocrystalline titania. *J. Mater. Chem.*, 8(9):2073–2076.

[256] Zhang, H. and Banfield, J. F. (2000). Understanding polymorphic phase transformation behavior during growth of nanocrystalline aggregates: Insights from TiO_2. *J. Phys. Chem. B*, 104(15):3481–3487.

[257] Zhang, H. and Banfield, J. F. (2002). Kinetics of crystallization and crystal growth of nanocrystalline anatase in nanometer-sized amorphous titania. *Chem. Mater.*, 14:4145–4154.

[258] Zhang, H. and Banfield, J. F. (2014). Structural characteristics and mechanical and thermodynamic properties of nanocrystalline TiO_2. *Chem. Rev.*, 114(19):9613–9644.

[259] Zhang, H., Chen, B., Banfield, J. F., and Waychunas, G. A. (2008a). Atomic structure of nanometer-sized amorphous TiO_2. *Phys. Rev. B*, 78(21):1–12.

[260] Zhang, P., Navrotsky, A., Guo, B., Kennedy, I., Clark, A. N., Lesher, C., and Liu, Q. (2008b). Energetics of cubic and monoclinic yttrium oxide polymorphs :Phase transitions, surface enthalpies, and stability at the nanoscale. *J. Phys. Chem. C*, 112:932–938.

[261] Zhang, Q. and Griffin, G. L. (1995). Gas-phase kinetics for TiO_2 CVD: hot-wall reactor results. *Thin Solid Films*, 263:65–71.

[262] Zhang, X., Jin, M., Liu, Z., Tryk, D. A., Nishimoto, S., Murakami, T., and Fujishima, A. (2007). Superhydrophobic TiO_2 surfaces: Preparation, photocatalytic wettability conversion, and superhydrophobic-superhydrophilic patterning. *J. Phys. Chem. C*, 111(39):14521–14529.

[263] Zhang, Y., Li, S., Yan, W., and Tse, S. D. (2012). Effect of size-dependent grain structures on the dynamics of nanoparticle coalescence. *J. Appl. Phys.*, 111(12).

[264] Zhang, Y., Li, S., Yan, W., Yao, Q., and Tse, S. D. (2011). Role of dipole-dipole interaction on enhancing Brownian coagulation of charge-neutral nanoparticles in the free molecular regime. *J. Chem. Phys.*, 134(8).

[265] Zhao, B., Uchikawa, K., McCormick, J. R., Ni, C. Y., Chen, J. G., and Wang, H. (2005). Ultrafine anatase TiO_2 nanoparticles produced in premixed ethylene stagnation flame at 1 atm. *Proc. Combust. Inst.*, 30(2):2569–2576.

[266] Zhao, B., Uchikawa, K., and Wang, H. (2007). A comparative study of nanoparticles in premixed flames by scanning mobility particle sizer, small angle neutron scattering, and transmission electron microscopy. *Proc. Combust. Inst.*, 31:851–860.

[267] Zhao, B., Yang, Z., Wang, J., Johnston, M. V., and Wang, H. (2003). Analysis of soot nanoparticles in a laminar premixed ethylene flame by scanning mobility particle sizer. *Aerosol Sci. Technol.*, 37(8):611–620.

[268] Zhao, H., Liu, X., and Tse, S. D. (2009). Effects of pressure and precursor loading in the flame synthesis of titania nanoparticles. *J. Aerosol Sci.*, 40(11):919–937.

[269] Zhao, W.-N., Zhu, S.-C., Li, Y.-F., and Liu, Z.-P. (2015). Three-phase junction for modulating electron-hole migration in anatase-rutile photocatalysts. *Chem. Sci.*, 6(6):3483–3494.

[270] Zhou, K., Wang, H. P., Chang, J., and Wei, B. (2015). Experimental study of surface tension, specific heat and thermal diffusivity of liquid and solid titanium. *Chem. Phys. Lett.*, 639:105–108.

[271] Zhou, Y. and Fichthorn, K. A. (2012). Microscopic view of nucleation in the anatase-to-rutile transformation. *J. Phys. Chem. C*, 116(14):8314–8321.

[272] Zhu, W. and Pratsinis, S. E. (1996). Flame synthesis of nanosize powders: Effect of flame configuration and oxidant composition. In *Nanotechnol. (ACS Symp. Ser. Vol. 622)*, chapter 4, pages 64–78. American Chemical Society.

Appendix A

Scope of collaboration in this thesis

Some of the elements in Chapters 4 and 6 of this thesis are the results of collaborative work with Casper Lindberg. This mainly concerns the stochastic population balance solver used to post-process the flame simulation solutions to resolve the particle morphology and phase composition. More details on this work have been published separately, e.g., Lindberg et al. [132] and Lindberg et al. [134]. In this thesis, only brief descriptions of the models and post-processing methodology are given.

Direct contributions of Casper Lindberg are the following:

1. Post-processing the flame solutions using the stochastic population balance solver for all cases (Chapters 4 and 6).
2. Generating the simulated TEM-like images for projected are analysis (Chapter 4).
3. Extending the detailed particle model type space to include particle phase and composition within the stochastic population balance solver (Chapter 6).
4. Implementing the size-dependent phase transformation models within the stochastic population balance solver (Chapter 6).

Appendix B

Experimental details

This appendix contains experimental details that supplement the work presented in Chapter 4 and 6. First, descriptions of the sampling system used for mobility size measurements and TEM sampling are given. Second, the time evolution of the particle size distributions from DMS measurements is presented. Third, the effects of dilution ratio on mobility size and number concentration (dilution tests) for DMS500 are shown. Next, the algorithm for the TEM image projection area analysis is outlined. Lastly, the temperature measurements for $\phi = 0.35$ flame and the flame distance estimation are discussed.

B.1 Sampling system

Figure B.1 shows the schematic of the sampling system used for mobility measurements and TEM sampling. The sampling line (1/4" OD) is integrated into the water cooled plate and a pinhole sampling orifice ($\sim$0.2 mm) is used to sample the gas at the stagnation plate. Before each measurement, the orifice is cleaned. In addition, the orifice is rotated away from the flame to prevent sampling and clogging of the orifice while the precursor flow is stabilising at the start of each measurement.

The line pressure is measured by two differential pressure transducers (Omega, PX653-10BD5V, range $\pm$25 mbar) at upstream (ΔP_1) and downstream (ΔP_2) from the orifice. The pressure drop at the orifice is estimated as $\Delta P_o = (\Delta P_1 + \Delta P_2)/2$. The dilution flow of 36 slpm is provided by the DMS500 (20 slpm) and a separate MFC (16 slpm). An external vacuum pump, in addition to the vacuum pump integrated with DMS500, is used to maintain the underpressure within the sampling line given the high dilution line. The underpressure of

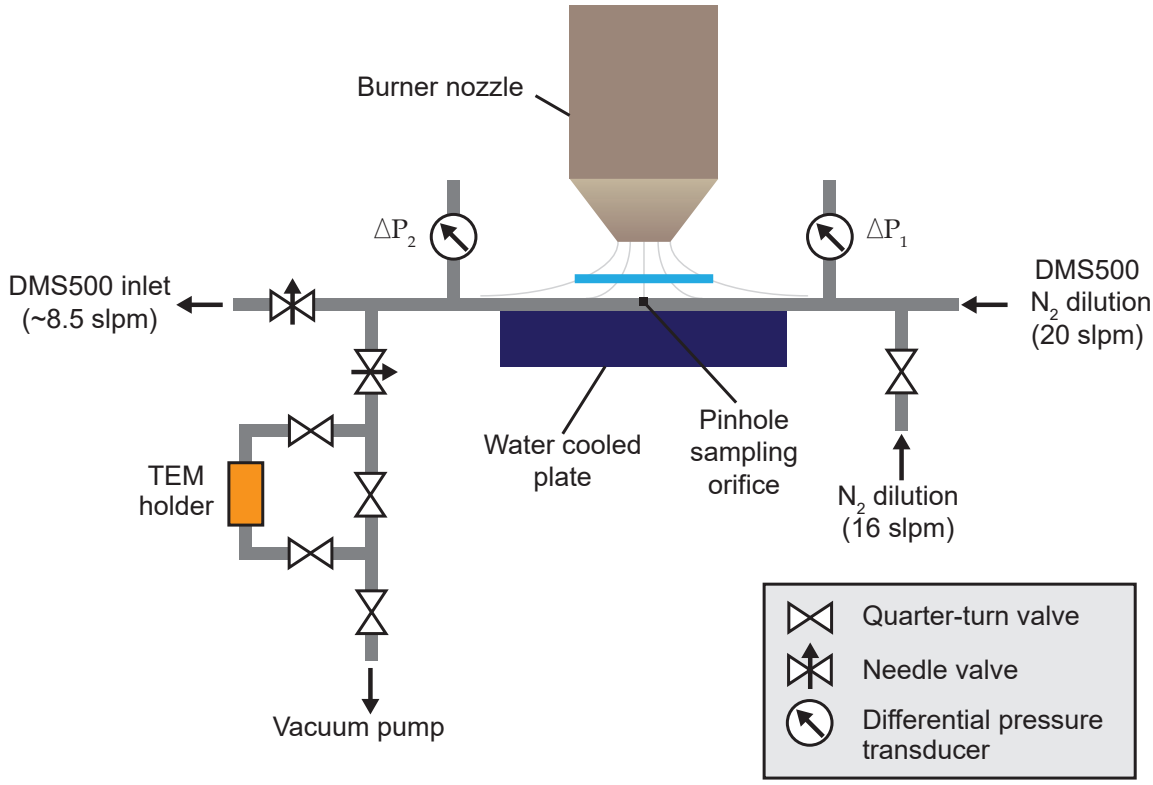

Figure B.1: *Schematic of an in situ sampling system with a pinhole orifice for particle mobility size measurements and TEM sampling.*

approximately 4 ± 0.5 mbar is maintained using two needle valves as shown in Fig. B.1. At the same time, the needle valves are used to control the sampling flow to DMS500 at approximately 8.5 slpm (recommended sample flow for DMS500).

When TEM samples are collected, the TEM is mounted on a holder placed downstream from the sampling orifice. The flow through the TEM grid is controlled by the two quarter-turn valves upstream and downstream from the holder. At the same time, the mobility size is recorded with the DMS500. The sampling time is 10 s from the moment a peak is observed by the DMS500.

B.2 DMS measurements

B.2.1 DMS500 setting

No restrictor is used with the DMS500 as the line pressure control is performed through the needle valves. A monomodal spherical calibration matrix is used (Monomodal M211 m2cqw222). The data rate is 10Hz with dilution correction turned off. All of the measurements reported in this thesis are from 10 s average (with stable reading). The sampling flow is maintained at 7.5–8.5 lpm (at DMS500 reference conditions: 0°C and 100 kPa). The second stage dilution is set at 20–40 to maintain sufficient signal except for the dilution tests.

B.2.2 Time-resolved PSD evolution

The DMS500 utilises multiple detectors in parallel which results in a fast time response compared to the conventional scanning DMA. Full particle size distributions (PSD) are measured at a maximum rate of 10 Hz. Therefore, the evolution of the PSD as a function of the sampling time can be easily resolved.

Typical particle size distributions from the measurements are shown in Fig. B.2. These measurements are from the dilution tests discussed in Section B.3 in which the dilution flow is varied while keeping a roughly constant pressure drop at the orifice. Figure B.2 shows the PSD evolution for 4 different dilution flows of 14, 19, 29, and 35 slpm. At the start of the measurement (sampling time = 0 s), the sampling tube is rotated such that the orifice is not exposed to the flame. After the flame is stabilised, the sampling tube is rotated towards the flame to start the sampling. As a result, particles are only observed at approximately 10 s. While the PSD is relatively stable during the sampling, the particle number (shown by the color scale) gradually decreases due to the orifice being clogged. In most cases, for 12 ml/h TTIP loading the sampling time is limited to 40-60 s before the DMS500 signal becomes too low. It is suspected that particle deposition on the wall of the orifice due to the thermophoresis is responsible for the clogging, gradually decreasing the orifice size and thus the sample volume (see Eq. B.2). Another possibility is that growth of film from unreacted precursor occurs on the orifice wall. This requires further investigation in the future.

The PSDs are subsequently fitted with lognormal distributions to obtain the median particle size ($\langle D_p \rangle$) for each measurement. The results are shown in Fig.B.3 together with the total particle number ($N_{\text{uncorrected}}$, before dilution correction) and the pressure drop across the orifice measured by the differential pressure transducers (ΔP_o). The data points with

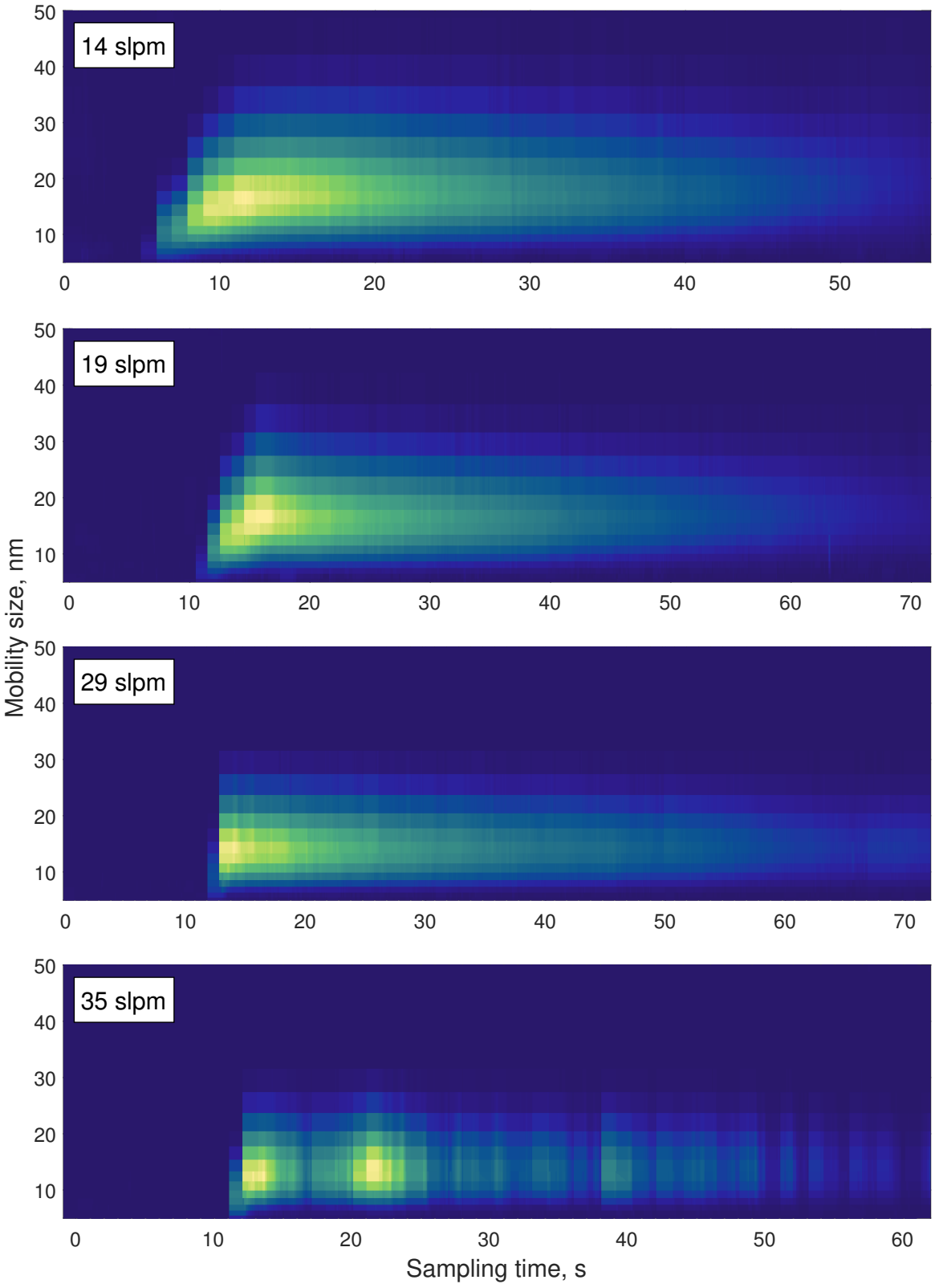

Figure B.2: *The particle size distribution from the DMS500 as a function of the sampling time. The measurements with dilution flow of 14, 19, 29, and 35 slpm are shown. The color scale reflects the number concentration (uncorrected for dilution).*

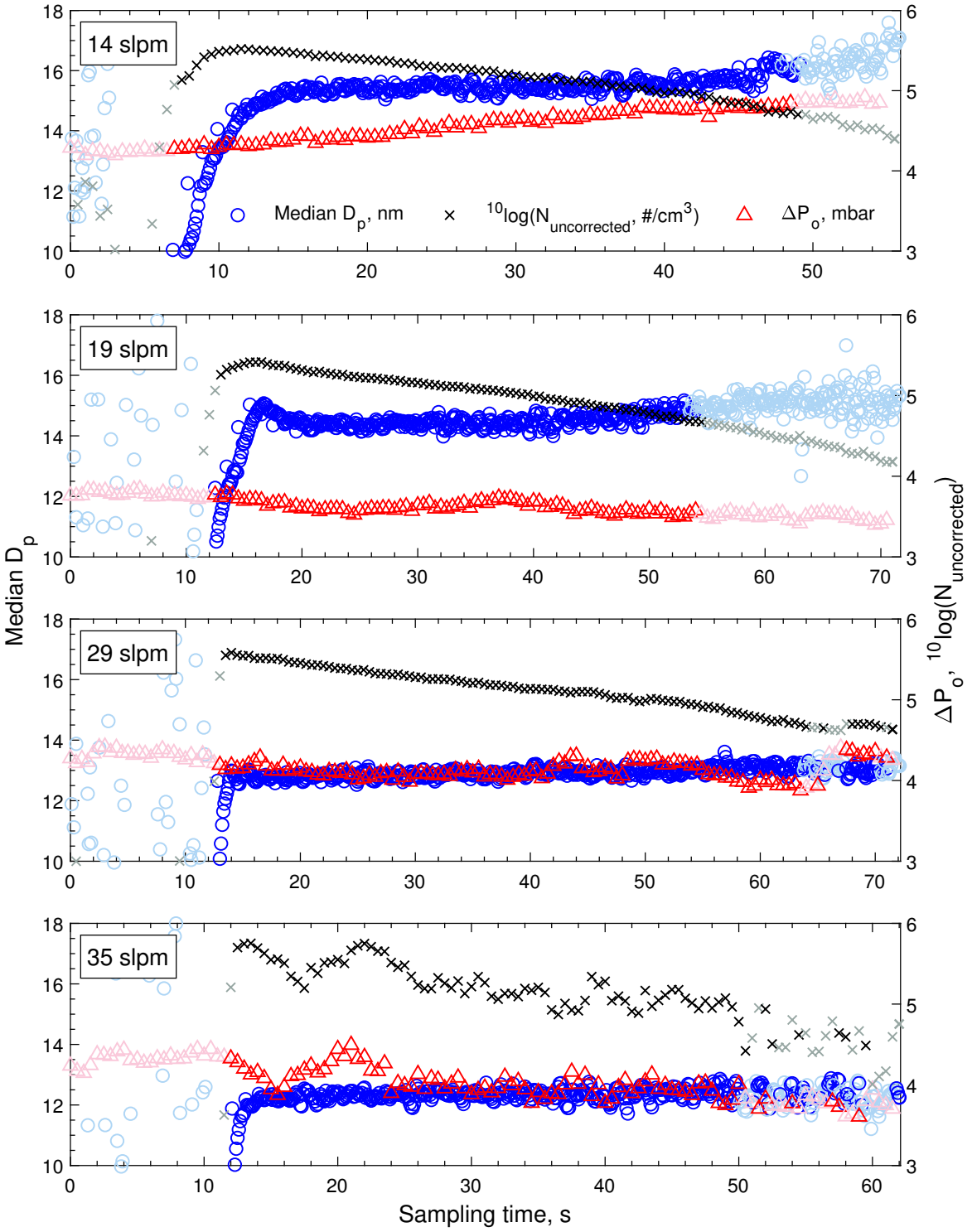

Figure B.3: *The median particle size (D_p) from lognormal fit and number concentration ($N_{\text{uncorrected}}$, uncorrected for dilution) from the DMS500 and the static pressure drop at the orifice (ΔP_o) as a function of the sampling time. The measurements with dilution flow of 14, 19, 29, and 35 slpm are shown. The data points with low DMS500 signal are shown in faded colors.*

low DMS500 signal ($N_{\text{uncorrected}} < 10^{4.5}$ cm^{-2}) are denoted with the faded symbols. As demonstrated qualitatively in Fig. B.2, Fig.B.3 shows the number concentration decreases gradually with increasing sampling time due to the orifice clogging for all dilution flows tested. However, the particle size remains relatively stable for high dilution cases (29 and 35 slpm flows). For low dilution cases, the particle size gradually increases with sampling time although only slightly (within approximately 1 nm for 14 slpm case). The significant increase of particle size at very low number concentration (faded colors) for 14 and 19 slpm cases is likely due to the background noise level. It is also noted that the pressure drop remains stable for high dilution cases but slightly increases over time with low dilution case (14 slpm). This is due to the temperature increase in the sampling line due to insufficient dilution, resulting in higher flow rates and subsequently higher pressure drop.

B.3 Sampling dilution tests

Given the large number density of particles sampled from the flame, sample dilution is necessary to minimise particle losses due to coagulation and deposition on the wall and the orifice. Sample dilution also cools and quenches the sampled gas to prevent further reactions. A thorough study on the dilution behaviour of a similar sampling system has been performed by Zhao et al. [267] who used a dilution flow of 29.5 l/min. The purpose of this section is to evaluate the sensitivity of the particle size and number density to the dilution ratio for the measurement conditions used in this work.

Here the dilution ratio is varied by changing the dilution volumetric flow rate, $L = 15$–38 l/min (STP), within the sampling line while maintaining a small static pressure drop, $\Delta P_o = P_{\text{atm}} - P_o$, approximately 4 ± 0.5 mbar across of the orifice. Each measurement is averaged over 5 seconds (with data acquisition rate of 10 Hz). This pressure drop is sufficiently small to avoid flame perturbation and large enough to prevent counterflow at the orifice due to pressure fluctuation during measurements. The total pressure drop, ΔP, is

$$\Delta P = \Delta P_o - \frac{\rho}{2A^2} L^2, \tag{B.1}$$

where the second term represents the dynamic pressure given as a function L, ρ, the mass density, and A, the flow cross section. For $L = 36$ l/min (flow rate used in this this work), the dynamic pressure is approximately 3.7 mbar. The sampled gas volumetric flow rate, L_s, is

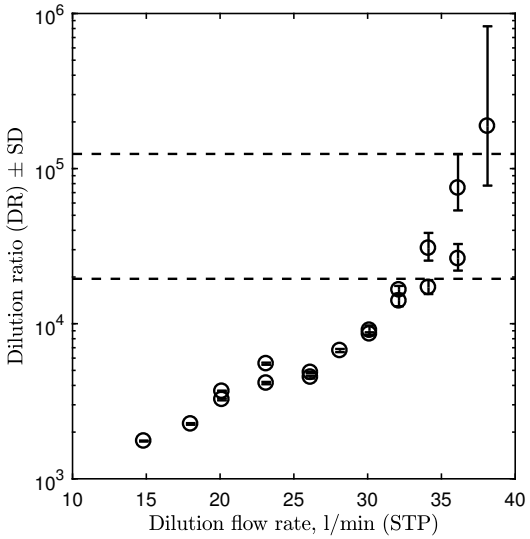

Figure B.4: *The calculated dilution ratio, DR, and standard deviation, SD, as a function of the dilution flow rate. The errorbar is calculated using the standard deviation of the pressure drop measurements. The dashed lines represent the range of DR for 36 l/min (STP) dilution flow rate given a fluctuation in the pressure drop in the range of 3.8–4.5 mbar.*

calculated using the relation for pressure loss due to laminar flow in a circular pipe,

$$L_s = \frac{f\pi d_o^4}{l\mu}\Delta P = k\Delta P, \tag{B.2}$$

where f is the friction factor, d_o is the orifice diameter, l, is the orifice length, μ is the gas viscosity. Assuming f, d_o, l, and μ are constant during the measurements, k was obtained from calibration using flow meters (≈ 7.6 ml·min^{-1}mbar^{-1}). The total dilution ratio, DR, is subsequently calculated similar to [267], i.e. DR $= 3.4L/L_s$ to account for the thermal expansion. The calculated DRs for all dilution flow rates tested are shown in Fig. B.4.

Figure B.5(a) shows the measured particle number density measured by the DMS500 as a function of DR for the $\phi = 0.35$ flame with 12 ml/h TTIP loading (detailed flame conditions given in Chapter 4). It is clear that the number density increases with DR for low dilution range, i.e. DR $< 10^4$. For DR $> 10^4$, the number density converges to approximately 1.1×10^8 cm^{-3} within the measurement uncertainty (shaded region in Fig. B.5(a)), suggesting that particle losses are sufficiently minimised. Figure B.5(b) shows the change in particle size as a function of DR. Increasing DR results in smaller particle size as particle losses, both through coagulation and deposition, result in a shift of particle size distributions towards a larger size. The particle size similarly converges to approximately 12.3 ± 0.25 nm at high dilution (DR $> 2 \times 10^4$) as indicated by the shaded region.

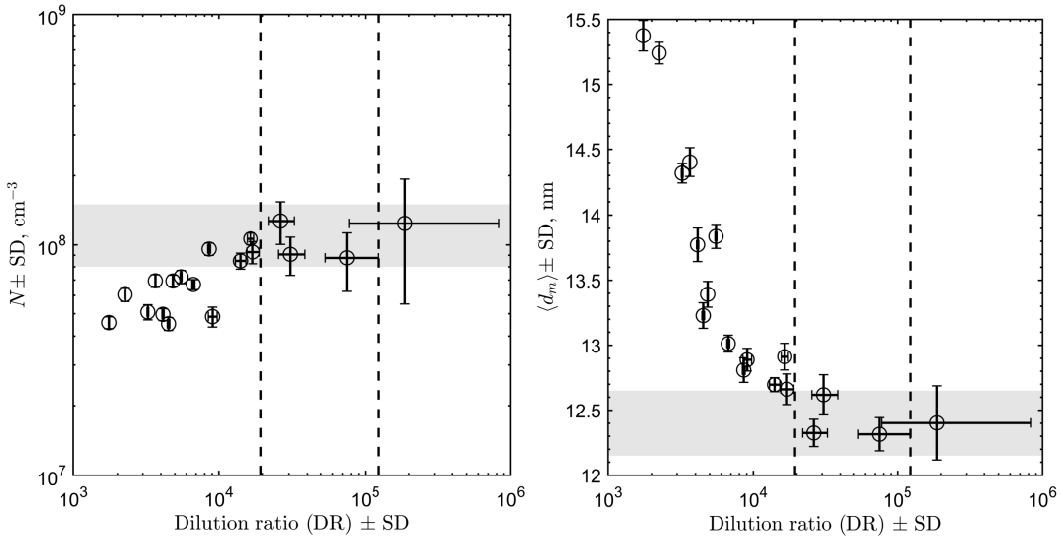

Figure B.5: *(a) Particle number density, N, and (b) median particle size, $\langle d_m \rangle$, and the respective standard deviations, SD, as a function of dilution ratio, DR, for $\phi = 0.35$ flame and 12 ml/h TTIP loading. The dashed lines represent the range of DR for 36 l/min (STP) dilution flow rate given a fluctuation in the pressure drop in the range of 3.8–4.5 mbar. The shaded regions indicate the converged values of N and d_m and the corresponding experimental uncertainties at high DR.*

Elsewhere in this thesis (Chapters 4 and 6), a dilution flow rate of 36 l/min and a static pressure drop fluctuation in the range of 3.8–4.5 mbar (due to the difficulty in controlling the pressure drop) were used. These conditions correspond to a DR of approximately 0.2–1.2×10^5. This range is indicated with the dashed lines in Figs. B.4 and B.5. Within this range, Fig. B.5 suggests that the particle number density and size are relatively insensitive to the dilution ratio.

B.4 TEM image analysis

For aggregate projected area analysis, the following semi-automated procedures were employed (see Fig. B.6 for illustration) using built-in functions in MATLAB Image Processing Toolbox [219]. The same procedure, except for step 2 (Filters), is used for the analysis of the simulated TEM-like images.

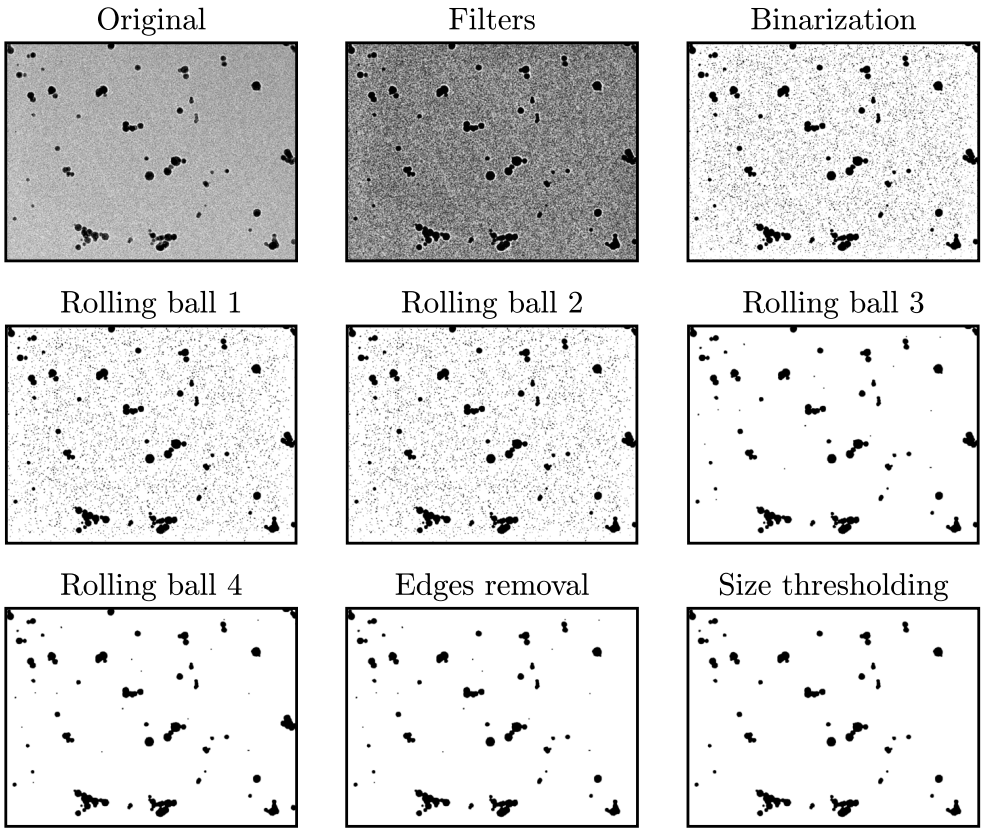

Figure B.6: *Snapshots of an analysed TEM image ($\phi = 1.67$, 30 ml/h TTIP loading rate) at different stages of the projected area analysis procedure.*

1. **Pre-processing**: Load image with *imread* function and remove TEM footer. The image location is specified by `locImage`.

```
% Load image
[Img, map]= imread(locImage);
% Crop footer
footer_found = 0;
for i = 1:size(Img,1)
    if sum(Img(i,:)) == 0 && footer_found == 0
```

```
        FooterEdge = i;
        footer_found = 1;
        Img_Cropped = Img(1:FooterEdge-1, :);
    end
end
if footer_found == 0
    Img_Cropped = Img;
end
```

2. **Filters**: Perform a contrast-limited adaptive histogram equalization (*adapthisteq* function) on 3×3 pixel tiles followed by a 2-D median filtering (*medfilt2* function) on 4×4 pixel tiles to enhance image contrast and reduce "salt and pepper" noise.

```
Img = adapthisteq(Img_Cropped,'NumTiles',[3 3]);
Img = medfilt2(Img,[4 4]);
```

3. **Binarization**: Create a binary image with adaptive image threshold calculated using local first-order image statistics around each pixel (*imbinarize* function). A dark foreground polarity and a sensitivity parameter of 0.05 were specified.

```
BW = imbinarize(Img,'adaptive','ForegroundPolarity' ...
    ,'dark','Sensitivity',0.05);
```

4. **Rolling ball 1-4**: Restructure connected black pixels with four successive rolling ball transformations (*strel* function, [81]) with increasing disk size of 0.6 (rolling ball 1), 0.8 (rolling ball 2), 1.2 (rolling ball 3), and 1.6 nm (rolling ball 4). The scale factor (px to nm) is specified by `px_nm`.

```
rb = [0.6 0.8 1.2 1.6];
for i = 1:4
    se = strel('disk',round(rb(i)/px_nm));
    if mod(i,2)==1
        BW = imclose(BW,se);
    else
        BW = imopen(BW,se);
    end
end
```

5. **Edges removal**: Remove pixel blobs that touch the image edges to exclude aggregates that are not completely within the image frame.

```
BW = removeEdges(BW);
function [BW] = removeEdges(BW)
    BWedge = BW;
    BWedge(2:size(BW,1)-1,2:size(BW,2)-1) = 1;
    [x,y] = find(BWedge == 0);
    p = length(x);
    q = 1;
    while q<=p
        if x(q)+1 <= size(BW,1)
            if BW(x(q)+1,y(q)) == 0
                p = p+1;
                x(p) = x(q)+1;
                y(p) = y(q);
                BW(x(q)+1,y(q)) = 1;
            end
        end
        if x(q)-1 >= 1
            if BW(x(q)-1,y(q)) == 0
                p = p+1;
                x(p) = x(q)-1;
                y(p) = y(q);
                BW(x(q)-1,y(q)) = 1;
            end
        end
            if y(q)+1 <= size(BW,2)
                if BW(x(q),y(q)+1) == 0
                p = p+1;
                x(p) = x(q);
                y(p) = y(q)+1;
                BW(x(q),y(q)+1) = 1;
            end
        end
            if y(q)-1 >= 1
                if BW(x(q),y(q)-1) == 0
```

```
            p = p+1;
            x(p) = x(q);
            y(p) = y(q)-1;
            BW(x(q),y(q)-1) = 1;
        end
    end
    q = q+1;
  end
end
```

6. **Size thresholding**: Remove structures with spherical equivalent diameter smaller than a specified threshold (`thresholdSize` = 2, 3, and 4 nm for 4, 12, and 30 ml/h loading rates, respectively).

```
BW = sizeThresholding(BW, thresholdSize, px_nm);
function [BW] = sizeThresholding(BW, thresholdSize,
  px_nm)
  CC = bwconncomp(abs(BW-1));
  [~,numParts] = size(CC.PixelIdxList);
  for k = 1:numParts
    area_pixelcount = length(CC.PixelIdxList{1,k});
    Aggregate_Area = area_pixelcount*px_nm^2;
    if Aggregate_Area <= 0.25*pi*(thresholdSize)^2
      BW(CC.PixelIdxList{1,k}) = 1;
    end
  end
end
```

7. Lastly, in the rare instance that the algorithm results in structures that are not particles (e.g., from clustered noise), these false particles are removed manually.

B.5 Temperature and flame distance measurements

Temperature measurement

The flame temperature profile was measured using a thin wire thermocouple ($d = 75$ μm, S-type, P10R-003, Omega Engineering) scanned along the flow direction with a motorised translational stage (Velmex). The scan speed was set to 0.5 mm/s in order to ensure a near steady-state measurement of the temperature. Due to deposition of particles on the wire when the precursor (TTIP) is used, this method is only suitable for undoped flames. Additionally, the maximum operating temperature is limited by the melting point of the thermocouple material (2041 K for Pt). Thus, the temperature measurement could only be performed for the lean flame ($\phi = 0.35$, $T_{\mathrm{ad}} = 2073$ K), as the rich flame temperature was too high ($\phi = 1.67$, $T_{\mathrm{ad}} = 2542$ K).

As the flame is stabilised by stretch (aerodynamically), the thermocouple wire easily "catches" or becomes the anchor point for the flame when the thermocouple wire is near the flame front (upstream). It was found that this could be minimised by placing the thermocouple slightly off-centered, approximately 3 mm from the centerline. In this condition, the flame disturbance is not observable compared to the fluctuation of the flame front. Two assumptions are made here: (1) the temperature is uniform radially at least up to 3 mm from the center which is reasonable given the flame diameter is roughly 3 cm and (2) the flame curvature is negligible and thus the flame front at 3 mm is taken to be the same as that at the centerline.

The actual flame temperature, T, is calculated from the measured temperature, T_{tc}, by taking into account the convective-radiative heat transfer of the thermocouple wire [198], i.e. the "radiation correction". Assuming a steady-state, this is given as

$$T = T_{\mathrm{tc}} + \varepsilon_{\mathrm{tc}} \sigma \left(T_{\mathrm{tc}}^4 - T_0^4 \right) \frac{d_j}{\kappa_g \mathrm{Nu}}, \tag{B.3}$$

where $\varepsilon_{\mathrm{tc}}$ is the thermocouple emissivity, σ is the Stefan-Boltzmann radiation constant, T_0 is the radiative sink temperature (surrounding temperature, 300 K), d_j is the thermocouple junction diameter (0.24 mm [149]), κ_g is the average gas thermal conductivity, and Nu is the thermocouple junction Nusselt number. The emissivity of the thermocouple (S-type, Pt/10%Rh-Pt) is given as a function of temperature as reported by Shaddix [198],

$$\varepsilon_{\mathrm{tc}} = -0.1 + 3.24 \times 10^{-4} T - 1.25 \times 10^{-7} T^2 + 2.18 \times 10^{-11} T^3. \tag{B.4}$$

The Nusselt number is calculated using the correlation for low Reynold number, Re, forced flow over a sphere as follows [188],

$$\mathrm{Nu} = 2 + 0.6\mathrm{Re}^{1/2}\mathrm{Pr}^{1/3}, \tag{B.5}$$

where Re is calculated based on the thermocouple junction diameter, i.e. $\mathrm{Re} = \rho_g u_g d_j/\mu_g$, Pr is the gas Prandtl number, i.e. $\mathrm{Pr} = c_p\mu_g/\kappa_g$. ρ_g, u_g, μ_g, and c_p are the mass density, velocity, dynamic viscosity, and specific heat of the gas phase, respectively. These and the average gas thermal conductivity, k_g, were obtained from the simulated gas species and velocity profiles with the energy equation solved for the flame mixture using the *k*inetics® software package as described in Chapter 3.

Figure B.7 shows the temperature profiles, before and after the radiation correction, for the undoped lean flame. The thermocouple measurement is able to capture the high temperature gradient at the edge of the combustion zone expected for a stretch stabilised stagnation flame. An uncertainty of ± 50 K is assigned to the temperature profiles due to the uncertainty in the parameters and estimated transport properties used for the correction [198, 149]. In addition, an estimated uncertainty of ± 0.2 mm is assigned due to the fluctuation of the flame front during the experiment.

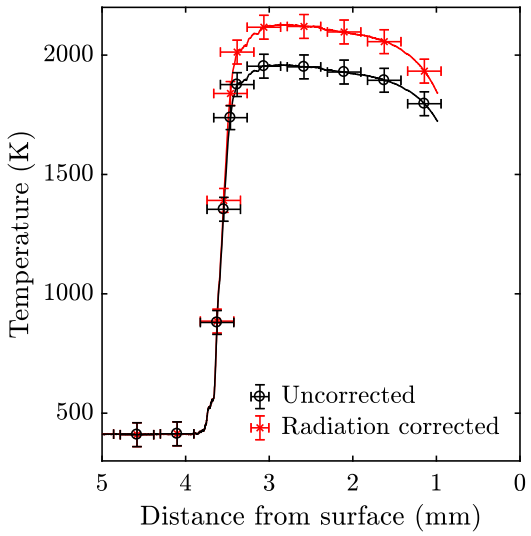

Figure B.7: *The temperature profiles, before and after the radiation correction, of the $\phi = 0.35$ undoped flame. The lines represent all data points while the symbols are every 240th points. The errorbars represent ± 0.2 mm and ± 50 K uncertainties.*

Flame distance estimation

Photographs of the undoped flames were taken with a digital camera (EX-ZR5000, Casio) in order to estimate the flame standing distance. This is needed because no temperature data for the rich flame ($\phi = 1.67$) was available. The photographs were taken with 20 ms exposure time and the data averaged over 4 photographs for each flame. Figure B.8 shows the averaged intensities (blue channel) along the burner centreline for the lean and rich flames. Herein the flame distance is approximated as the distance (upstream from the flame) at which the intensity is half of the maximum intensity as annotated in Fig. B.8.

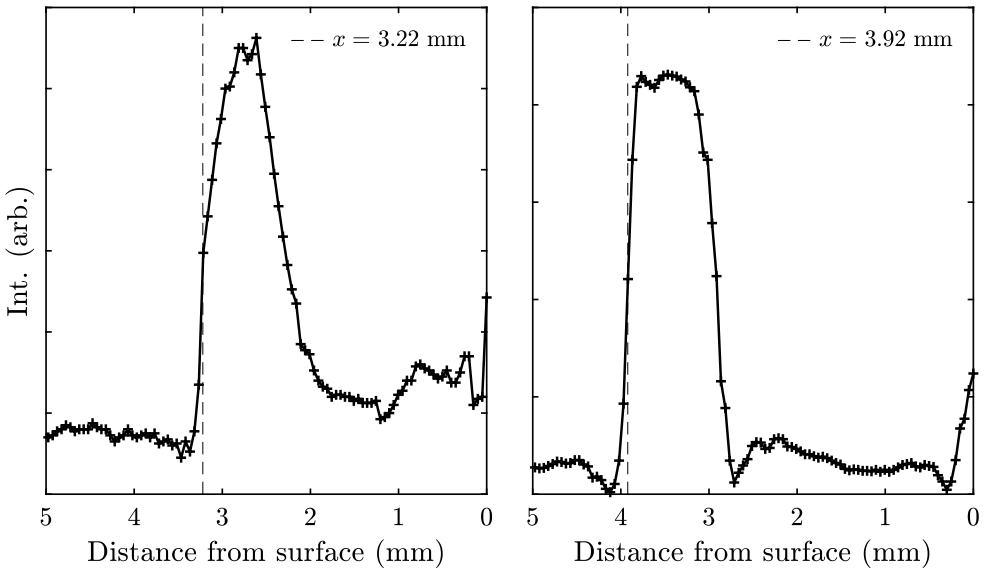

Figure B.8: *The blue channel intensities from the flame photographs along the burner centreline for the lean ($\phi = 0.35$, left) and rich flames ($\phi = 1.67$, right). The vertical dashed lines denote the distance at which the intensity is half of the maximum intensity, herein defined as the flame standing distance.*

Appendix C

Thermodynamic phase stability

This appendix presents the derivation of a thermodynamic formulation for the phase relative stability of nano-sized spherical crystallites by taking into account the surface effects. In addition, a careful attempt to reproduce the thermodynamic analysis of anatase-rutile stability by assuming an oxygen surface desorption proposed by Liu et al. [135] is given. It is shown that the main results reported in ref. [135] are not reproducible. Finally, an exploratory model of anatase-rutile stability is presented which contains a particle composition dependency. The model is able to reproduce the experimental data presented in Chapter 6 although important assumptions are made which warrant further investigation.

C.1 Size-dependent phase stability

The change of the free energy, dG, of a chemical system with n species as a function of temperature, T, and pressure, P, and number of chemical species, N, is given by

$$\mathrm{d}G = -S\mathrm{d}T + V\mathrm{d}P + \sum_{i=1}^{n} \mu_i \mathrm{d}N_i, \tag{C.1}$$

where S is the entropy, V is the volume, μ is the chemical potential.

Suppose a nanoparticle system is comprised of S solid components and F surrounding fluid components. The change of the free energy of the system is now

$$\mathrm{d}G = -\sum_{i=1}^{N_S+N_F} \bar{S}_i n_i \mathrm{d}T + \sum_{i=1}^{N_S+N_F} \bar{V}_i n_i \mathrm{d}(P+P_{\mathrm{exc}}) + \left(\sum_{i=1}^{N_S+N_F} \bar{\mu}_i \mathrm{d}n_i + \sum_{j=1}^{J} \gamma_j \mathrm{d}A_j + \sum_{k=1}^{K} \sigma_k \mathrm{d}l_k + \sum_{l=1}^{L} \mathrm{d}\lambda_l \right), \tag{C.2}$$

where $\bar{S}$ and $\bar{V}$ are the molar entropy and volume, n is the number of moles, A is the interface area, and P_{exc} is the excess pressure induced by the surface stress of solid particles. The total chemical potential is described by the last four terms on the right hand side: the bulk chemical potential (μ), the free surface energy (γ), the free energies associated of edges (σ) and corners (λ) [258]. For a system with constant temperature and pressure and neglecting the edges and corners, this can be written as follows,

$$\mathrm{d}G = \sum_{i=1}^{N_S+N_F} \bar{V}_i n_i \mathrm{d}P_{\mathrm{exc}} + \sum_{i=1}^{N_S+N_F} \bar{\mu}_i \mathrm{d}n_i + \sum_{j=1}^{J} \gamma_j \mathrm{d}A_j. \tag{C.3}$$

For a spherical particle of radius r, the excess pressure acting on the surface is equal to the difference between the surface pressure (P_S) and the fluid pressure (P_F), i.e. $P_{\mathrm{exc}} = P_S - P_F = \Delta P$, and is given by the Laplace-Young equation,

$$\Delta P = \frac{2f}{r}, \tag{C.4}$$

where f is the surface stress. The *surface stress* is the reversible work per unit area required to elastically stretch a surface. For solids, this is different from the *surface free energy* γ which is the reversible work per unit area involved in forming a surface by a process such as cleavage [43, 38]. The surface stress is related to the free surface energy via $f = \gamma + \partial\gamma/\partial\varepsilon$, where ε is the surface strain.

For a system with $N_S = 2$, the free energy associated with transformation of one molar of phase α to phase β is given by

$$\Delta G^{\circ}_{\alpha\to\beta} = \left(\bar{\mu}_\beta - \bar{\mu}_\alpha\right) + \left(\bar{V}_\beta \Delta P_\beta - \bar{V}_\alpha \Delta P_\alpha\right) + \left(\gamma_\beta A_\beta - \gamma_\alpha A_\alpha\right) \tag{C.5}$$

$$= \left(\bar{\mu}_\beta - \bar{\mu}_\alpha\right) + 2\left(\bar{V}_\beta \frac{f_\beta}{r_\beta} - \bar{V}_\alpha \frac{f_\alpha}{r_\alpha}\right) + \left(\gamma_\beta A_\beta - \gamma_\alpha A_\alpha\right), \tag{C.6}$$

and for a sphere, $A = 3V/r = 3M/\rho r$, where M is the molar mass,

$$\Delta G^{\circ}_{\alpha\to\beta} = \left(\bar{\mu}_\beta - \bar{\mu}_\alpha\right) + 2M\left(\frac{f_\beta}{\rho_\beta r_\beta} - \frac{f_\alpha}{\rho_\alpha r_\alpha}\right) + 3M\left(\frac{\gamma_\beta}{\rho_\beta r_\beta} - \frac{\gamma_\alpha}{\rho_\alpha r_\alpha}\right). \tag{C.7}$$

The explicit relationship between f and γ for TiO_2 is not known. For metals, surface stress is about one to two times surface free energy [43]. Thus, it is reasonable to assume that surface stress is t times the surface free energy, i.e. $f = t\gamma$ [255]:

$$\Delta G^{\circ}_{\alpha\to\beta} = \left(\bar{\mu}_\beta - \bar{\mu}_\alpha\right) + (2t+3)M\left(\frac{\gamma_\beta}{\rho_\beta r_\beta} - \frac{\gamma_\alpha}{\rho_\alpha r_\alpha}\right). \tag{C.8}$$

Finally, neglecting the volume change due to the transformation, i.e. $r_\alpha = r_\beta = r$, and substituting the molar chemical potential with standard Gibbs formation, ΔG°_f,

$$\Delta G^{\circ}_{\alpha\to\beta} = \Delta G^{\circ}_{f,\beta} - \Delta G^{\circ}_{f,\alpha} + (2t+3)\frac{M}{r}\left(\frac{\gamma_\beta}{\rho_\beta} - \frac{\gamma_\alpha}{\rho_\alpha}\right). \tag{C.9}$$

C.2 Surface desorption approach

Recently, Liu et al. [135] proposed a slight modification of Eq. C.9 to explain the anatase-rutile stability as a function of oxygen pressure. In their analysis, adsorption of surface oxygen is assumed to result in a mix of metallic Ti and TiO_2 on the surface. The purpose of this section is to reproduce the results reported in [135].

C.2.1 Thermodynamic formula

The expression for Gibbs free energy of the transformation of anatase to rutile, $\Delta G^{\circ}_{\mathrm{A}\to\mathrm{R}}$, is written as

$$\Delta G^{\circ}_{\mathrm{A}\to\mathrm{R}} = \Delta G^{\circ}_{f,\mathrm{R}} - \Delta G^{\circ}_{f,\mathrm{A}} + 2(2t+3)\frac{M}{d}\left(\frac{\gamma_{\mathrm{R/Ti}}}{\rho_{\mathrm{R}}} - \frac{\gamma_{\mathrm{A/Ti}}}{\rho_{\mathrm{A}}}\right), \tag{C.10}$$

where $\Delta G^{\circ}_{f,\mathrm{R}}$ and $\Delta G^{\circ}_{f,\mathrm{A}}$ are the Gibbs free energies of formation of rutile and anatase, $d = 2r$ is the crystalite size, ρ_{R} and ρ_{A} are the mass densities of rutile and anatase, $\gamma_{\mathrm{R/Ti}}$ and $\gamma_{\mathrm{A/Ti}}$ are the surface free energies of partially desorbed rutile and anatase.

The oxygen desorption reaction is written as a reversible equilibrium reaction

$$2\,O^- \rightleftharpoons O_2 + 2s^- \tag{C.11}$$

with equilibrium constant, K_p, related to the reaction Gibbs free energy, $\Delta G^\circ_{\text{des.}}$, given by

$$K_p = X_{O_2}\left(\frac{n_s}{1-n_s}\right)^2 = \exp\left(-\frac{\Delta G^\circ_{\text{des.}}}{RT}\right), \tag{C.12}$$

where X_{O_2} is the mole fraction of O_2 and n_s is the fraction of desorbed surface states. The reaction Gibbs free energy is estimated as following from the oxygen desorption enthalpy, $\Delta H^\circ_{\text{des., 298 K}}$, as

$$\Delta G^\circ_{\text{des.}}(T) = \Delta H^\circ_{\text{des., 298 K}} + \Delta H_s(T) - T\Delta S^\circ(T), \tag{C.13}$$

where the sensible enthalpy, ΔH_s, and entropy change, ΔS°, of the desorption reaction are estimated as

$$\Delta H_s(T) = \Delta H_{s,\text{Ti}}(T) + \Delta H_{s,O_2}(T) - \Delta H_{s,TiO_2}(T) \tag{C.14}$$

$$\Delta S^\circ(T) = S^\circ_{\text{Ti}}(T) + S^\circ_{O_2}(T) - S^\circ_{TiO_2}(T) \tag{C.15}$$

Finally, the surface free energies of partially desorbed rutile and anatase are written as

$$\gamma_{\text{R/Ti}} = n_s\gamma_{\text{Ti}} + (1-n_s)\gamma_{\text{R}} \tag{C.16}$$

$$\gamma_{\text{A/Ti}} = n_s\gamma_{\text{Ti}} + (1-n_s)\gamma_{\text{A}}, \tag{C.17}$$

where γ_{R}, γ_{A}, and γ_{Ti} are the surface free energies of rutile, anatase, and titanium metal, respectively.

C.2.2 Thermodynamic parameters

The Gibbs free energies of formation of anatase, $\Delta G^\circ_{f,\text{A}}$, and rutile, $\Delta G^\circ_{f,\text{R}}$ are given as parameterised functions, with coefficients in Table C.1, as follows (valid within $298 < T < 2000$ K) [255]:

$$f(T) = c_1 + c_2T + c_3T\log(T) + c_4T^2 + c_5/T$$

Table C.1: *Fitting coefficients for the free Gibbs energies of formation of anatase, $\Delta G^{\circ}_{f,\mathrm{A}}$, and rutile, $\Delta G^{\circ}_{f,\mathrm{R}}$.*

f	c_1	c_2	c_3	c_4	c_5
$\Delta G^{\circ}_{f,\mathrm{A}}$ (J/mol)	-9.41×10^{5}	2.655×10^{2}	-12.21	3.966×10^{-3}	-2.603×10^{5}
$\Delta G^{\circ}_{f,\mathrm{R}}$ (J/mol)	-9.46×10^{5}	2.472×10^{2}	-9.593	2.994×10^{-3}	-3.472×10^{5}

Oxygen desorption enthalpy, $\Delta H^{\circ}_{\mathrm{des.,298K}}$ is taken as 55 kcal/mol or 230.12 kJ/mol (from [222]).

$$\Delta H^{\circ}_{\mathrm{des.,\,298\,K}} = 230.12 \quad (\mathrm{kJ/mol}) \tag{C.18}$$

Sensible enthalpies, $\Delta H_s(T)$**, and entropies,** $S^{\circ}(T)$ of TiO_2, Ti, and O_2 are taken from JANAF webbook database [48]. The thermodynamic parameters are parameterised, with coefficients in Table C.2, as follows:

$$f(T) = c_1 + c_2 T + c_3 T\log(T) + c_4 T^2 + c_5/T$$

The fitted parameters are shown with the data from the JANAF table in Fig. C.1.

Table C.2: *Fitting coefficients for the sensible enthalpies, $\Delta H_s(T)$, and entropies, $S^{\circ}(T)$. Units for ΔH_s and S° are kJ/mol and J/mol, respectively.*

f	T (K)	c_1	$c_2\times10^{-2}$	$c_3\times10^{-3}$	$c_4\times10^{-6}$	c_5
$\Delta H_{s,\mathrm{Ti}}(T)$	300–1166	−31.65	32.05	−43.4	28.6	2.204×10^{3}
	1166–1939	-7.87×10^{-2}	5.76	−5.73	7.42	10.00
	1939–3000	−0.174	−9.36	18.1	−3.68	-4.56×10^{-4}
$S^{\circ}_{\mathrm{Ti}}(T)$	300–1166	−20.336	60.21	−78.5	24.65	6.297×10^{2}
	1166–1939	0.1174	43.05	−54.4	14.33	−10.00
	1939–3000	−9.998	34.12	−38.8	3.944	-2.50×10^{-2}
$\Delta H_{s,\mathrm{O_2}}(T)$	300–1100	−2.3387	−5.52	12.2	−3.2508	-4.652×10^{2}
	1100–3000	−13.9361	3.60	−0.2293	1.012	1.208×10^{3}
$S^{\circ}_{\mathrm{O_2}}(T)$	300–1100	1.863×10^{2}	27.85	−32.1	3.807	-2.9527×10^{3}
	1100–3000	2.05×10^{2}	18.83	−20.9	2.126	-7.56×10^{3}
$\Delta H_{s,\mathrm{TiO_2}}(T)$	300–2130	−20.54	3.76	3.98	2.51	1.27×10^{3}
	2130–3000	−0.6941	3.73	8.05	−1.574	−9.98
$S^{\circ}_{\mathrm{TiO_2}}(T)$	300–2130	−19.256	76.93	−91.0	12.63	-2.044×10^{3}
	2130–3000	−0.7714	62.94	−70.2	6.00	9.97

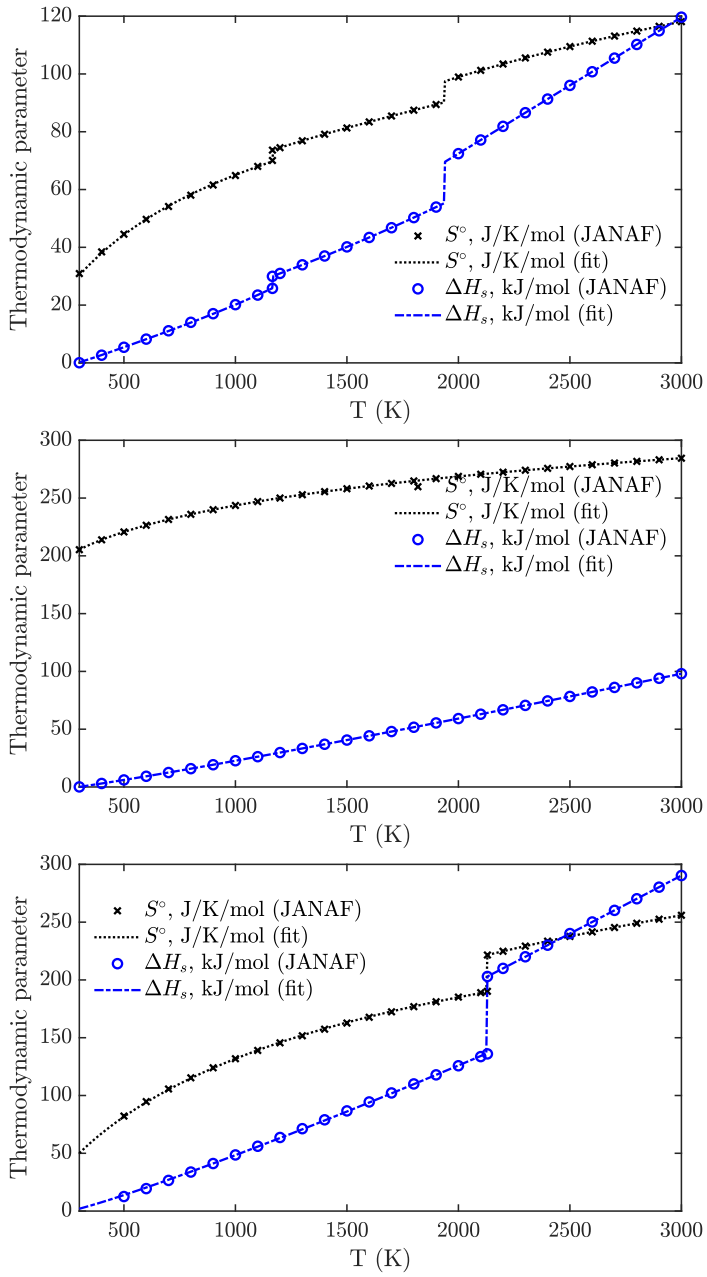

Figure C.1: *Thermodynamic parameters from JANAF and from fitting: (a) Ti, (b) O_2, and (c) TiO_2.*

Surface free energy of Ti, $\gamma_{\mathrm{Ti}}(T)$ is assumed to be equal to that of its liquid phase [270], given as the function of temperature:

$$\gamma_{\mathrm{Ti}}(T) = 1.64 - 2.38 \times 10^{-4}(T - 1943) \quad (\mathrm{J/m^2}) \tag{C.19}$$

Surface free energy of anatase, $\gamma_A(T)$, and rutile, $\gamma_R(T)$ is calculated as follows:

$$\gamma_A(T) = h_{A,\,0\,K} + \int_0^T c(T)dT - T\int_0^T \frac{c(T)}{T}dT \tag{C.20}$$

$$\gamma_R(T) = h_{R,\,0\,K} + \int_0^T c(T)dT - T\int_0^T \frac{c(T)}{T}dT, \tag{C.21}$$

where $h_{A,\,0\,K}$ and $h_{R,\,0\,K}$ are the surface enthalpies of anatase and rutile, taken as 1.93 and 1.34 J/m^2 [255]. The specific heat $c(T)$ is estimated with the Debye theory [54] from the low temperature measurements [60]. The expression of $c(T)$ is given by:

$$c(T) = 6.89\times10^{-4}\left(\frac{T}{T_D}\right)^3\int_0^{T_D/T}\frac{x^4e^x}{(e^x-1)^2}dx, \tag{C.22}$$

with Debye temperature, T_D, taken as 670 K [148]. The expression is fitted with a 22-order polynomial function, f, shown in Fig. C.2, which is valid within $0 < T/T_D < 5$:

$$c(T) = f(T) = \sum_{i=1}^{N=23} p(i)\left(\frac{T}{T_D}\right)^{N-i}. \tag{C.23}$$

This is consistent with the specific heat reported by Liu et al. [135] for selected temperatures:

$$f(T = 500\text{ K}) = 2.13\times10^{-4}\quad (\text{J/m}^2\text{/K}) \tag{C.24}$$

$$f(T = 1000\text{ K}) = 2.29\times10^{-4}\quad (\text{J/m}^2\text{/K}) \tag{C.25}$$

$$f(T = 1500\text{ K}) = 2.35\times10^{-4}\quad (\text{J/m}^2\text{/K}). \tag{C.26}$$

The polynomial fitting allows Eqs. C.20 and C.21 to be solved analytically.

Mass densities of anatase, $\rho_A(T)$, and rutile, $\rho_R(T)$ are given as functions of temperature with the assumption that the mass densities linearly decrease by 5% from 300 to 2000 K:

$$\rho_A(T) = 3780(1-0.05(T-300)/1700)\quad (\text{kg/m}^3) \tag{C.27}$$

$$\rho_R(T) = 4230(1-0.05(T-300)/1700)\quad (\text{kg/m}^3) \tag{C.28}$$

C.2.3 Remarks on the anatase-rutile stability

Similar to [Fig. 6 in 135], the isolines of the Gibbs free energy of transformation, i.e. $\Delta G^\circ_{A\to R} = 0$, are calculated as a function of oxygen mole fraction and the crystallite size.

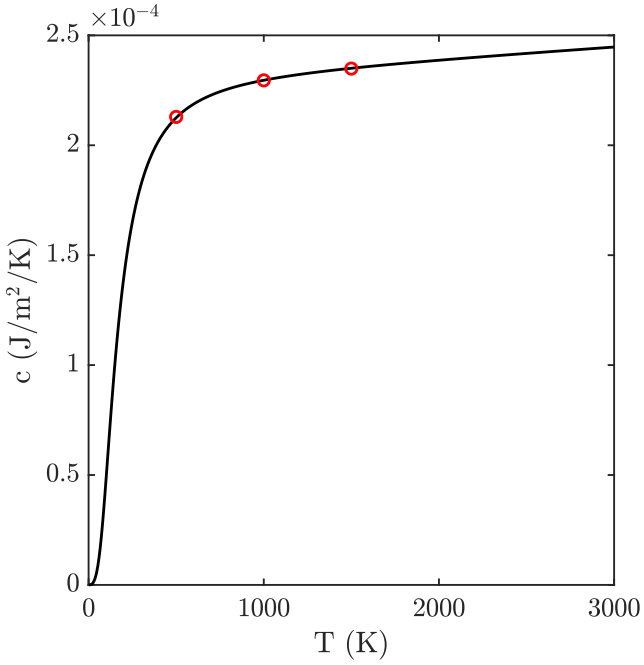

Figure C.2: *Fitted polynomial function of TiO_2 specific heat.*

The results are shown in Fig. C.3(a) while the original results reported by Liu et al. [135] are shown in Fig. C.3(b). The results are significantly different. However, it is not clear why there is such a discrepancy.

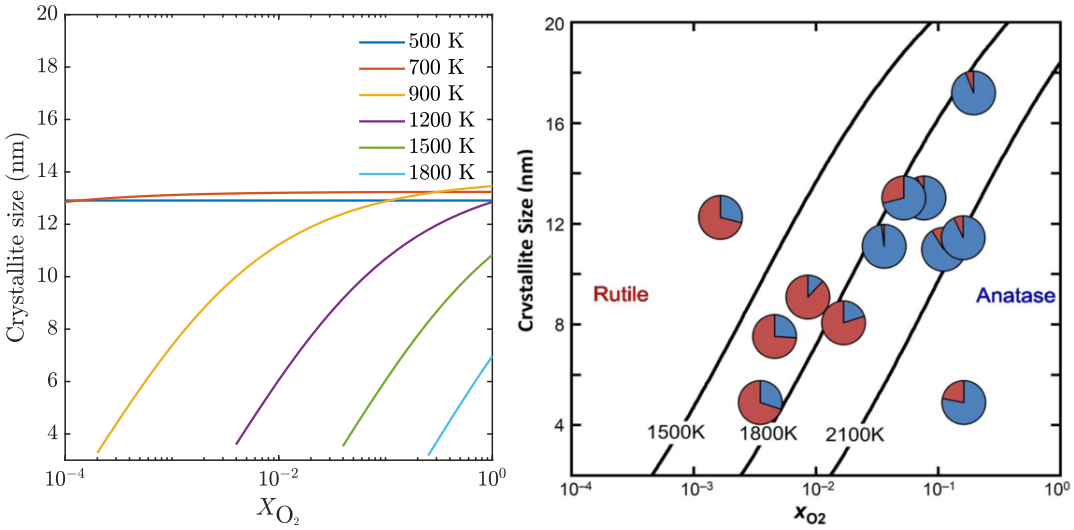

Figure C.3: *The Gibbs free energy of transformation isolines, i.e. $\Delta G^{\circ}_{A\rightarrow R}$, at several temperatures calculated (a) in this work, (b) by Liu et al. [135]. Reprinted with permission from John Wiley and Sons.*

Some important points are noted here:

- The authors' calculation of n_s for lean flame (T = 1500 K, $X_{O_2} = 0.01$) is markedly different from the calculation in this work using the thermodynamic quantities prescribed. The value cited is $n_s = 36\%$ whereas in this work, it is closer to 98%.
- There is a typo/mistake in Eq. (7) of [135]. It should be 1943 instead of 1043 K.
- There is a typo/mistake in Eq. (2) of [135]. It should be desorption reaction Gibbs free energy instead of anatase-rutile transformation Gibbs free energy.
- There is a mention of "The ratio of solid-to-liquid surface specific heat was taken to be 1.18." However, it is not clear how the authors used this in their analysis.
- Fig. 6 in [135] implies that at high oxygen concentration limit (i.e. $X_{O_2} = 1$), for example at $T = 1500$ K, the anatase-rutile crossover size is larger than 22 nm. This is incorrect as anatase-rutile crossover size should approximate the solution of Zhang and Banfield [255] at high oxygen limit (where no surface desorption occurs) which is $\sim$ 14 nm. The correct limit is observed in Fig. C.3(a).

C.3 Composition-dependent stability model

In Chapter 6, a size-dependent phase stability crossover model is introduced in the stochastic particle solver (Figs. 6.1 and 6.2). The model is used to test a hypothesis frequently proposed in the literature in which a crossover size exists below which anatase is thermodynamically more stable while rutile is more stable for larger particles (Section C.1). The crossover particle size is calculated from some intrinsic thermodynamic quantities assuming stoichiometric composition (TiO_2) of incipient particles. However, as discussed in Chapter 6 this hypothesis fails to explain the experimental observations. It is proposed that the non-stoichiometry of the early-stage particles influences the relative anatase-rutile stability (or equivalently, the crossover size) and is critical in understanding the crystal phase formation of TiO_2.

This section presents an exploratory model describing the anatase-rutile stability crossover which incorporates the particle composition (oxygen to titanium ratio or σ_O), i.e. a composition-dependent model, to explain the experimental data presented in Chapter 6. The model is implemented by introducing a σ_O-dependency on the crossover size parameter which is used in the stochastic particle solver (see Fig. 6.2). Here the growth parameter set 3 (Table 6.2) is assumed for this analysis.

Based on the comparison between the Gibbs free energy and the melting models, it was shown that a size-dependent transformation temperature is not very important. This is because

the particles have very narrow size distributions. Thus, the transformation temperature is imposed here as a constant similar to the Gibbs free energy model. Next, the crossover size d_{cross} is assumed to be a function of $\sigma_{\text{O},i}$. These can be written as follows,

$$T_{\text{trans},i} = \lambda_1 \tag{C.29}$$

$$d_{\text{cross},i} = F(\sigma_{\text{O},i}) \tag{C.30}$$

The explicit form of F is not known. Based on the composition-dependent hypothesis, the crossover size should increase with increasing σ_{O}, approaching the value predicted by thermodynamic analysis for stoichiometric composition ($\sigma_{\text{O}} = 2$). Here, F is approximated by a surrogate function $G(x)$ that fulfills the following conditions: (1) $G(x)$ is positive for $x > 0$, and (2) $G(x)$ increases with increasing x, i.e. $\mathrm{d}G/\mathrm{d}x > 0$. An error function based G is here used as the surrogate function,

$$F(x) \approx G(x) = \lambda_2 + \lambda_3 \text{erf}[\lambda_4(x - \lambda_5)] \quad \lambda_2, \lambda_3, \lambda_4, \lambda_5 \geq 0, \tag{C.31}$$

where λ_2, λ_3, λ_4, and λ_5 are the free parameters of the composition model.

The rutile fraction function in Eq. 6.13 for growth parameter set 3 is now written as

$$\text{f}_{\text{R}} = f_{\text{comp}}(y; z^{(3)}, \theta) \quad \text{where } \theta = [\lambda_1, \lambda_2, \lambda_3, \lambda_4, \lambda_5]. \tag{C.32}$$

The best fit parameter $\hat{\theta}_3 = [2000\ \text{K}, 9.1\ \text{nm}, 3.9\ \text{nm}, 120, 1.79]$ (using growth parameter set 3, i.e. $z^{(3)}$) is evaluated according to Eq. 6.14. The transformation temperature is 2000 K and the function $G(\sigma_{\text{O}})$ is given as

$$G(\sigma_{\text{O}}) = 9.1 + 3.9\text{erf}[120(\sigma_{\text{O}} - 1.79)] \ \ (\text{nm}), \tag{C.33}$$

which is shown in Fig. C.4(a). The function G has a sharp transition at $\sigma_{\text{O}} = 1.79$. However, as discussed above the absolute values of σ_{O} predicted in this model are strongly dependent on the model assumptions. Thus, the precise location of the transition in function G, σ_{O}^*, is uncertain. The physical mechanism responsible for this sharp transition is unclear and requires further investigation. One possible interpretation is that below a certain oxygen deficiency ($\sigma_{\text{O}} < \sigma_{\text{O}}^*$), one of the sub-oxides in the Magnéli series is formed [9]. These sub-oxides are line compounds in TiO_2 phase diagram and therefore only formed at specific compositions [172]. These sub-oxides are hypothesised to favour rutile formation due to the similarity between their crystal structures and rutile's and therefore results in a decrease in the

anatase-rutile crossover size. At larger σ_O, the crossover size or G in Fig. C.4(a) approaches 13 nm which is very close to the value calculated by Zhang and Banfield [255] (14 nm).

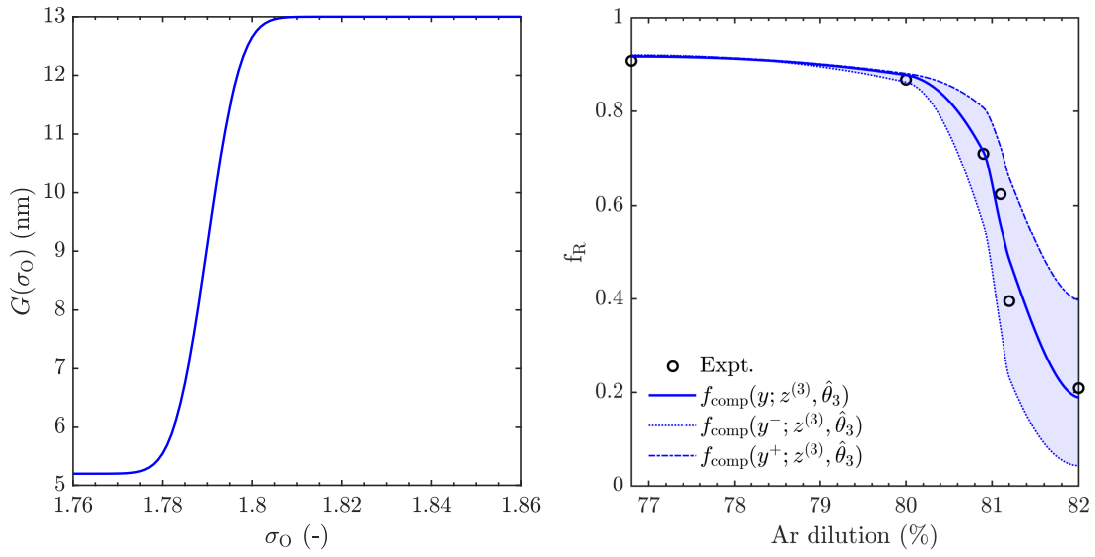

(a) ***(b)***

Figure C.4: *(a) The function G describing the crossover size dependency on σ_O (Eq. C.33) from the parameter estimation. (b) The measured and predicted rutile fractions as a function of Ar dilution for growth parameter set 3 (i.e. $z^{(3)}$) using the fitted parameter $\hat{\theta}_3$. Also shown are the rutile fractions assuming mixture equivalence ratio of 0.99 (y^-) and 1.01 (y^+) to indicate the uncertainty from the experimental flowrates.*

Figure C.4(b) shows the simulated rutile fractions with the best fitted parameters for the growth parameter set 3. The model shows an excellent agreement with the experimental data. In addition, the predicted rutile fractions for mixtures with equivalence ratios of 0.99 and 1.01 (assuming the same Ar dilution in Table 6.1) are shown. These represent the minimum uncertainty (shaded area) due to the fluctuation in the experimental flowrates. This suggests that the model is highly sensitive to the equivalence ratio, especially at higher Ar dilution, which may explain the narrow range of equivalence ratios in which anatase-rutile stability sensitivity has been reported before [108].

While the model presented here shows an excellent agreement with the experiments, a number of simplifying assumptions are made including the clustering mechanism, particle precursors, and reaction rates. This analysis highlights the need for a better chemical model that describes the early stage formation of particles for predicting the phase composition despite its apparent small impact on the particle size or morphology. For example, Ershov et al. [67] recently suggested that the TTIP decomposition mechanism proposed by [34] is missing an important pathway, i.e. the acetone abstraction pathway. This is especially important in this case as the

acetone abstraction reaction results in fewer oxidised species (with lower oxidation state of Ti) forming earlier, which then gradually oxidise in the flame. This would significantly affect the particle precursor concentration and in turn the composition of the incipient particles.

Further, some potentially important effects are not yet captured in the model discussed in this work. For example, the formation of the metastable phases suggests that the kinetic aspects of the phase transformation need to be considered. The effect of the oxygen defficiency on the transition temperature between non-crystalline and crystalline phases may also be important. Knaup et al. [110], using molecular dynamics simulations, show that the oxygen defficiency induces a significant reduction in the melting temperature of rutile. These effects shall be investigated in future work.